Experimental and Computational Study on Flow Measurement and Mixing Characterization in High-Temperature Gas-Cooled Reactors

by

Jiaxin Mao

A dissertation submitted in partial fulfillment
of the requirements for the degree of
Doctor of Philosophy
(Nuclear Engineering and Radiological Sciences and Scientific Computing)
in the University of Michigan
2024

Doctoral Committee:

Professor Annalisa Manera, Co-Chair
Associate Research Scientist Victor Petrov, Co-Chair
Assistant Professor Rohini Bala Chandran
Professor Elia Merzari, Penn State University
Professor Xiaodong Sun

Dedication

To **My family**, for the support, love, sacrifice, and patience.

ACKNOWLEDGEMENTS

Foremost, my deepest appreciation goes to my supervisors, Dr. Annalisa Manera and Dr. Victor Petrov, for their exceptional support, invaluable guidance, trust, and mentorship throughout my academic journey at the University of Michigan and the ongoing guidance on my path forward. Their profound knowledge, encouragement, and constructive feedback have been pivotal in shaping the trajectory of my research. Words cannot adequately convey the depth of my gratitude. I express my sincere thanks to the members of my thesis committee, Dr. Xiaodong Sun, Dr. Rohini Bala Chandran, and Dr. Elia Merzari, for their insightful comments, valuable suggestions, and the dedicated time they invested in reviewing and evaluating my work. A special expression of gratitude goes to Dr. Xiaodong Sun for his additional support and guidance in the development of my career.

Furthermore, I extend my profound gratitude to the Department of Energy for its pivotal role in providing the essential funding resources that significantly facilitated and accelerated the progress of my research. The invaluable experience gained through the NEAMS-IRP: 1.1 project has been a cornerstone in shaping my academic journey. I wish to express my heartfelt appreciation to Dr. Victor Coppo Leite, Dr. Cheng-Kai Tai, and Dr. Arsen S. Iskhakov for their exceptional contributions and incredible collaborations. Their expertise and dedication have not only enriched the research but have also been instrumental in broadening the scope and impact of my work.

Special gratitude is extended to my colleagues at the ECMFL group, both current and former, who have not only generously shared their ideas but also actively engaged in valuable discussions, providing unwavering support during the highs and lows of this transformative

academic journey. In particular, I want to express my sincere thanks to Arron Huxford, Zachary Welker, and Pei-Hsun Huang – steadfast allies whose support has been a constant beacon of encouragement throughout the entirety of my Ph.D. journey. Their camaraderie has added immeasurable richness to this experience, making it all the more memorable and meaningful.

In addition, I extend my heartfelt thanks to all of my friends whose companionship and camaraderie made my stay in Michigan an exceptionally delightful time. Their friendship added a vibrant and joyous dimension to my academic pursuits, creating cherished memories beyond the realms of research. I am grateful for the laughter, shared moments, and the support of these friends, who made my time in Michigan not only academically fulfilling but also personally enriching.

Last but not least, I am profoundly grateful to my family for their unwavering encouragement, boundless love, and unwavering understanding. Their steadfast support has not only served as a constant source of motivation but has also been the cornerstone of my resilience throughout this academic journey. I consider myself truly fortunate to have them by my side, providing a pillar of strength and unwavering encouragement as I navigated the challenges and triumphs of pursuing my Ph.D.

While the constraints of this acknowledgment prevent me from mentioning every individual by name, I wish to convey my deep and heartfelt gratitude to each person who played a pivotal role in shaping not only my academic journey but also providing invaluable support in various aspects of life. Your contributions have been instrumental in my growth and success. I look forward to the continued journey ahead and the prospect of crossing paths with you again. Until then, thank you for being an integral part of my life's endeavors. I will see you around.

TABLE OF CONTENTS

CHAPTER

LIST OF FIGURES

<u>**Figure**</u>

LIST OF TABLES

Table

LIST OF ABBREVIATIONS

CFD Computational Fluid Dynamics

DNS Direct Numerical Simulation

ECMFL Experimental and Computational Multiphase Flow Laboratory

GPU Graphics Processing Unit

HTGR High-Temperature Gas-cooled Reactor

LDV Laser Doppler Velocimetry

LDA Laser Doppler Anemometry

LES Large Eddy Simulations

NEUPs Nuclear Energy University Programs

PIRT Phenomena Identification and Ranking Table

PIV Particle Image Velocity

PSD Power Spectral Density

PWRs Pressurized Water Reactors

RANS Reynolds-Averaged Navier-Stokes

RKE Realizable $k - \epsilon$

RST Reynolds Stress Transport

SGDH Standard Gradient-Diffusion Hypothesis

SFR Sodium-cooled Fast Reactor

TKE Turbulent Kinetic Energy

TOF Time of Flight

LOFC Loss of Force Circulation

WMS Wire-Mesh Sensor

MiGaDome Michigan Multi-jet Gas-mixture Dome

HiRJet High-Resolution Jet

BWRs Boiling Water Reactors

NGNP Next Generation Nuclear Plant

ART-GCR Advanced Reactor Technologies Gas-Cooled Reactor

TRISO TRi-structural ISOtropic

SGS SubGrid-Scale

NRC Nuclear Regulatory Commission

PIRT Phenomena Identification and Ranking Table

SKE Standard $k - \varepsilon$

SST Shear-Stress Transport

RST Reynolds Stress Transport

URANS Unsteady Reynolds-Averaged Navier-Stokes

PCC Pressurized conduction Cooldown

ESBWR Economic Simplified Boiling Water Reactor

SFR Sodium-cooled Fast Reactor

TES Thermal Energy Storage

ECMFL Experimental and Computational Multiphase Flow Laboratory

DEHS Di-Ethyl-Hexyl-Sebacate

GPU Graphical Processing Unit

HPC High-Performance Computing

SEM Spectral Element Method

DFDE Double-Frame Double-Exposure

ASTFE American Society of Thermal and Fluids Engineers

POD	Proper Orthogonal Decomposition
SKELowRe	Standard $k - \varepsilon$ LowRe
KOmegaSST	$k - \omega(SST)$
SGDH	Simple Gradient Diffusion Hypothesis
LIH	Light Into Heavy
HIL	Heavy Into Light
GIF	Generation IV International Forum
IRP	Integrated Research Project

ABSTRACT

The High-Temperature Gas-cooled Reactor (HTGR), one of the six candidates for the advanced nuclear reactors in the Generation IV International Forum (GIF), has received great attention due to its enhanced safety, high thermodynamic efficiency, and suitability as energy source for high-temperature industrial processes such as hydrogen production. However, despite extensive advances in the development of this design, there remain thermal-hydraulic challenges that need to be addressed before commercialization.

One challenge is the measurement of the primary coolant flow. Currently, the primary helium coolant flow is not directly measured but rather inferred from either the energy balance of the turbine compressor or the helium circulator rotational speed. Though functional, both methods introduce large uncertainties; therefore, HGTR operation would benefit greatly from the development of a suitable gas flow meter. Such development is challenging due to the high flow rates (the gas velocities are in the range of $10 - 15\,m/s$ at the nominal operating conditions), high operating temperatures ($> 700^oC$), and high neutron flux and gamma fields in the reactor core. No commercially available flow meters are suitable for flow rate measurements in such a harsh environment.

Another challenge is related to the accurate prediction of the plant behavior during an extended Loss of Force Circulation (LOFC) accident, one of the Design Basis Accidents (DBAs) that have to be considered when licensing the design. During LOFC scenarios, the flow in the reactor pressure vessel reverts its direction, moving upwards. The extent to which the hot coolant jets exiting the core mix in the upper plenum will determine the heat removal rate, the occurrence of local hot spots, and the potential for thermal striping. In severe cases

or after repeated cycles, the striping can thermally fatigue the material of the upper plenum internals, leading to component failure. While 3D Computational Fluid Dynamic (CFD) models can be useful for an accurate prediction of thermal mixing and the occurrence of hot spots in the HTGR upper plenum, a shortage of high-resolution experimental data has hampered the validation of such models.

This thesis addresses the challenges mentioned above by 1): designing a novel acoustic flow meter and 2): conducting high-resolution experiments for mixing in large enclosures to establish a high-resolution database specifically designed for the validation of high-fidelity CFD models. The novel acoustic flow meter relies upon the principle of vortex-induced acoustics. Within the present dissertation, a combination of experiments and simulations was conducted to support the development and optimization of the flow meter design and to successfully demonstrate its proof of principle. To investigate the flow conditions relevant to mixing in the upper plenum and establish a database for CFD model validation, two experimental facilities were designed and constructed at the University of Michigan. Special care was dedicated to guaranteeing well-characterized boundary conditions, so that the data could be used for the validation of CFD codes. First, the Michigan Multi-jet Gas-mixture Dome (MiGaDome) facility, a $1/12^{th}$ scaled down from the upper plenum geometry of the Modular HTGRs design, was designed and built within the workscope of the present dissertation to investigate multi-jet interactions in a domed enclosure using optical measurements such as Laser Doppler Velocimetry (LDV) and Particle Image Velocity (PIV). Second, the High-Resolution Jet (HiRJet) facility was used to investigate the propagation of stratified fronts in a body of fluid. Wire-Mesh Sensor (WMS) units were used for high-resolution measurements of the time-dependent density field and characterization of the stratified front. High-resolution experimental data measured at these two facilities were used to shed light on the flow mixing in large enclosures with or without the presence of stratified density fronts. Extensive code validation has been conducted for RANS based turbulence models to assess and improve the performance of the computational models. The work in this thesis is

expected to benefit the advancement of HTGR designs by providing practical solutions and through enhanced computational tools.

CHAPTER I

Introduction and Background

1.1 Background

Nuclear energy has been an important component of the global energy supply, accounting for approximately 10% of the world's electricity generation [17]. It is a significant low-carbon energy source and the second-largest provider of low-carbon electricity after hydropower [18]. The appeal of nuclear energy is from its reliability as a continuous source of electricity, low operating costs, and the fact that it does not emit greenhouse gases during operation and is among the energy sources with the lowest greenhouse gas emissions associated with the full life cycle based on life cycle analyses [19].

The most commonly used nuclear reactors in the world currently are Pressurized Water Reactors (PWRs) and Boiling Water Reactors (BWRs) [20]. PWRs and BWRs have been widely adopted due to their established designs, proven track records, and their ability to generate electricity on a large scale efficiently [21]. Despite the successful applications of PWRs and BWRs, new types of reactors are actively being developed by the nuclear community, driven by the need to improve upon existing designs and address current challenges in the nuclear industry [22]. Among those newly developed reactor designs, the High-Temperature Gas-cooled Reactor (HTGR) design was promulgated in the Generation IV technology roadmap in 2002 as one of the Next Generation Nuclear Plant (NGNP) designs due to its compatibility with high-efficiency electricity production and nuclear-assisted hydrogen production [2].

A scheme of the HTGR design is shown in Figure 1.1. Reminiscent of a conventional reactor, the fission energy generated in the reactor core is carried out by the circulating coolant in the form of heat. The primary coolant then transfers the heat in the secondary loop to the secondary fluid that either drives the turbine for electricity or for other industrial applications.

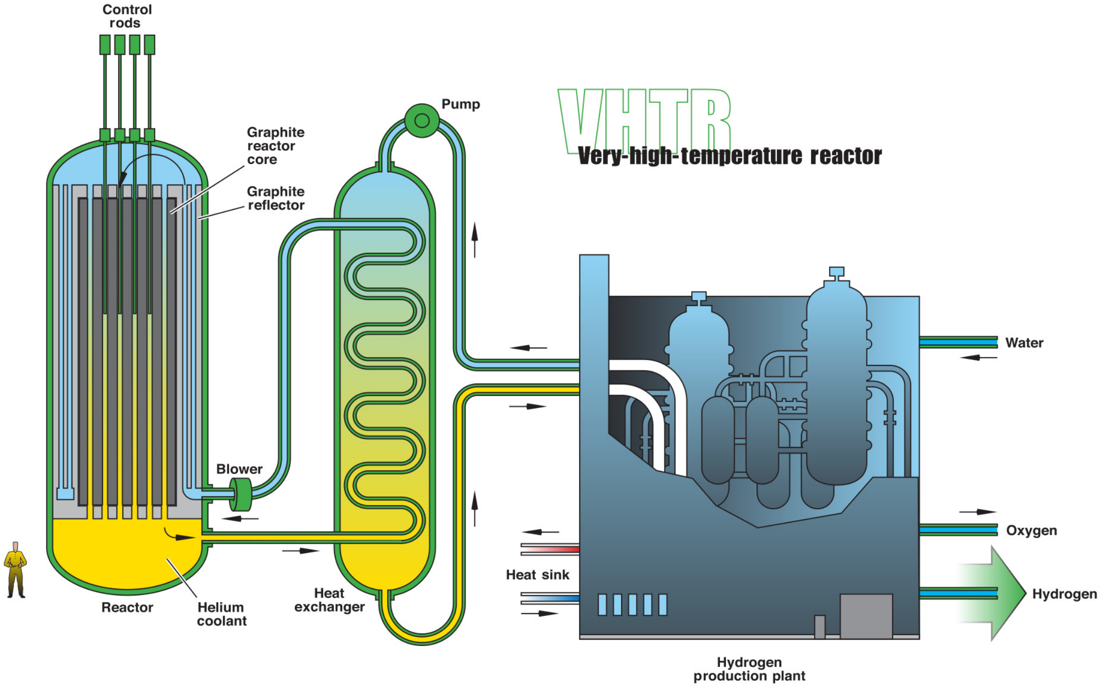

Figure 1.1: Very-high-temperature reactor scheme. Reprinted from [1].

The uniqueness of the HTGRs design relies on its cores design and coolant selection. The helium coolant has excellent heat transfer properties and does not react chemically with other substances, making it an efficient and safe choice for carrying away heat from the core. Using helium coolant allows for higher operating temperatures, which increases the efficiency of power generation compared to the light water reactor. Besides, HTGRs employ TRi-structural ISOtropic (TRISO) fuel particles, consisting of a small kernel of uranium dioxide fuel encapsulated in carbon and ceramic coatings layers. This design provides high fuel performance and enhanced containment of radioactive materials, improving safety. TRISO fuel particles are highly resistant to temperature and physical stresses, reducing the risk of fuel failure. The inherent properties of the fuel and coolant, such as their ability to handle high temperatures without relying on external cooling systems, contribute to the inherent safety of HTGRs [23].

One of the unique advantages of HTGRs is their ability to provide high-temperature heat for various industrial applications. The high outlet temperatures of the coolant enable the production of process heat, which can be utilized in industries like hydrogen production, district heating, and desalination. HTGRs also have the potential to be part of nuclear hybrid systems, where the excess heat generated by the reactor can be used for additional power generation or other applications. This flexibility allows for improved efficiency and energy utilization [24, 25, 26].

While HTGRs offer promising opportunities for improved safety and efficiency in nuclear energy, technical and economic challenges must be addressed before they can be widely deployed. HTGR designs continually evolve based on safety and other technical improvements, but also due to consumer demands and changes within the regulatory environment. There are several HTGR designs under development around the world [27, 28, 29]. The research and development (R&D) activities required to design and deploy HTGRs in the US are actively undergoing, under the lead of the Advanced Reactor Technologies Gas-Cooled Reactor (ART-GCR) program [30]. In order to provide analytical tools for the U.S. Nuclear Regulatory Commission (NRC) to verify the design and conduct licensing evaluation, a Phenomena Identification and Ranking Table (PIRT) exercise in major topical areas of HTGRs was conducted in 2007. The PIRT of each area helps identify and rank safety-relevant phenomena and assess the current knowledge base [31, 32]. The research activities under the instruction of this PIRT have been focused on those phenomena with high importance but medium-low knowledge levels. The most recent summary of the technical accomplishments can be found in [33]. A considerable amount of high-quality technical work has been focused on advanced fuel, graphite, and materials development.

Thermal hydraulics is also critical to HTGRs, to ensure proper reactor cooling, prevent overheating, and therefore ensure fuel integrity to avoid releasing radioactive materials during operational and accidental conditions. The PIRT panel of the accidents and thermal fluids (including Neutronics) has concentrated on the thermal fluid phenomena related to the HTGRs design. The most significant phenomena (those assigned an importance rank of “high” with the corresponding knowledge level of “low” or “medium”) in the thermal-fluids area include primary system heat transport phenomena, which impact fuel and component temperatures, reactor physics phenomena which impact peak fuel temperatures in many events, and postulated air ingress accidents that, however unlikely, could lead to major core and core support damage [31]. After the NRC PIRT assessment was released, the phenomena ranking determined the scope of the 29 Nuclear Energy University Programs (NEUPs) at various U.S. universities. An overview of the progress of these projects, along with a data platform of these projects, has been well-documented in [34].

Despite extensive advances in the development of the HTGR design, there remain thermal-hydraulic challenges that need to be addressed before commercialization. The present thesis aims at contributing to two of the identified challenges. The identified challenges in thermal hydraulics for HTGRs in this thesis include the need to develop reliable models for predicting heat transfer and fluid flow phenomena relevant during selected accident conditions, and the need for advanced instrumentation and sensors to monitor the behavior of the coolant and identify any anomalies or malfunctions.

Specifically, one challenge is the measurement of the primary coolant flow. As fuel configurations increase in complexity in contrast to many conventional reactor core designs, bypass and cross-flow through the graphite prismatic block introduce a high degree of uncertainty in the core flow distribution. Currently, the primary helium coolant flow is not directly measured but rather inferred from either the energy balance of the turbine compressor or the helium circulator rotational speed. Though functional, both methods introduce large uncertainties.

There are various types of flow meters that measure gas flow rates using different principles of operation. For example, conventional applications often incorporate mechanical flow meters, pressure-based flow meters, vortex flow meters, ultrasonic flow meters, optical flow meters, and magnetic flow meters. Despite the extensive variety in gas flow measurement systems, there are currently no methods and systems available for direct measurement of flow rate in applications involving high-velocity, high-temperature gas, particularly those that involve harsh environments. The key impediments in using commercial-off-the-shelf gas flow measurement methods in gas flow paths of these applications are (1) high flow velocities (10-15 m/s at the nominal operating conditions), (2) high operating temperatures ($> 700^oC$), and (3) either harsh chemical environments or high neutron flux and gamma field. As a result, there is a long-felt and unmet need for improved systems and methods for measuring gas flow, including systems and methods suitable for use in such harsh environments.

Another key area for the future design, development, and licensing of HTGRs is verifying and validating thermal hydraulics and heat transfer computational tools [33]. Validated tools are needed to analyze the behavior of the HTGRs during steady-state operations, abnormal conditions, and accident scenarios for which the plant must be licensed. Figure 1.2 shows the identified key phenomena, their corresponding scenarios of interest, and available experimental facilities. As can be seen from Figure 1.2, various experiments have been conducted or will be conducted to contribute to the general experimental datasets for the Verification and Validation (V&V) of simulation models for the HTGRs design. The most recent progress and advances in HTGR CFD and thermal fluid analysis have been summarised in [30]. However, it can be found from Figure 1.2, as well as from the reference [30, 34], that the mixing behavior in the upper plenum has not yet been sufficiently investigated.

The upper plenum mixing phenomenon becomes relevant for the determination of the plant behavior during an extended Loss of Force Circulation (LOFC) accident. Based on the HTGRs design, it is anticipated that the helium coolant streams heated in the reactor core will exhaust into the lower mixing plenum under normal operation conditions. The flow path

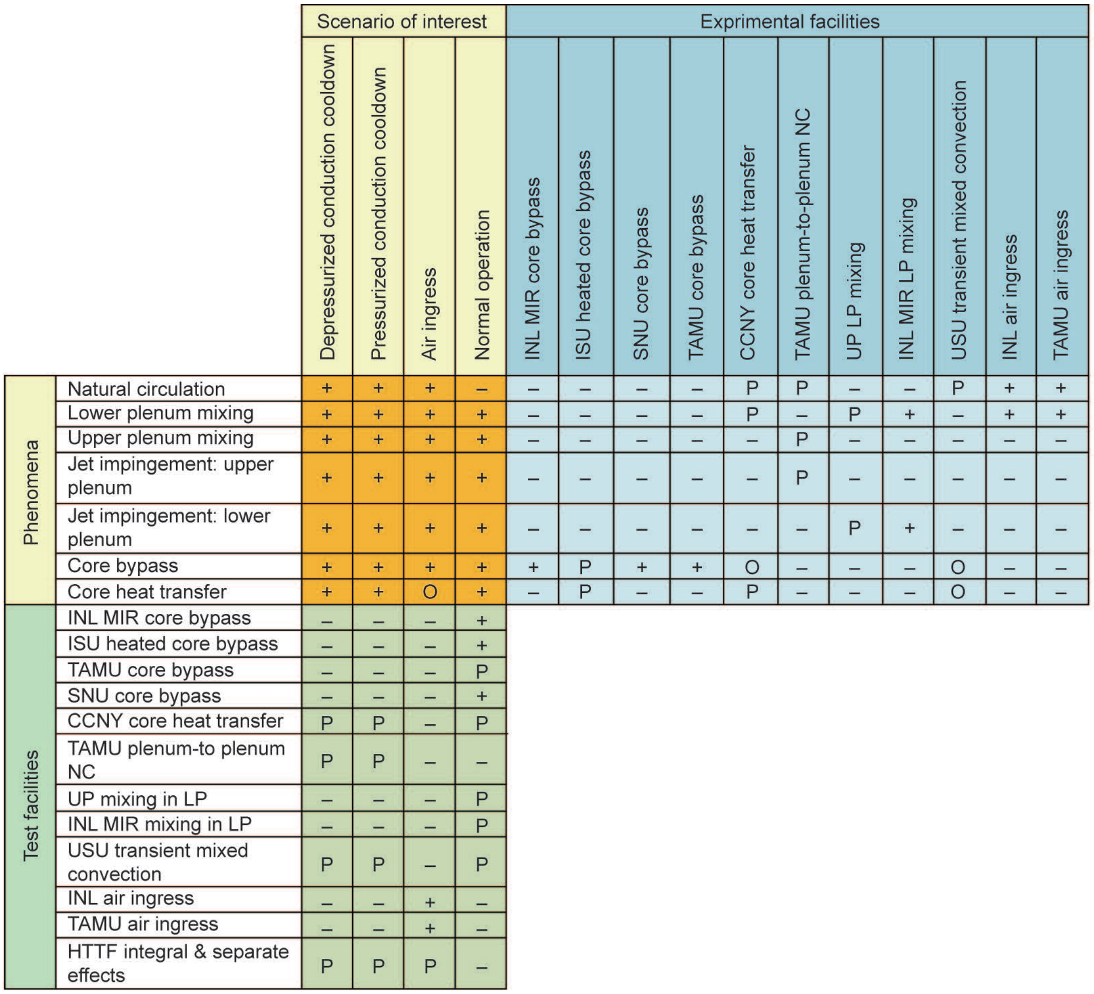

		Scenario of interest				Exprimental facilities										
		Depressurized conduction cooldown	Pressurized conduction cooldown	Air ingress	Normal operation	INL MIR core bypass	ISU heated core bypass	SNU core bypass	TAMU core bypass	CCNY core heat transfer	TAMU plenum-to-plenum NC	UP LP mixing	INL MIR LP mixing	USU transient mixed convection	INL air ingress	TAMU air ingress
Phenomena	Natural circulation	+	+	+	–	–	–	–	–	P	P	–	–	P	+	+
	Lower plenum mixing	+	+	+	+	–	–	–	–	P	–	P	+	–	+	+
	Upper plenum mixing	+	+	+	+	–	–	–	–	–	P	–	–	–	–	–
	Jet impingement: upper plenum	+	+	+	+	–	–	–	–	–	P	–	–	–	–	–
	Jet impingement: lower plenum	+	+	+	+	–	–	–	–	–	–	P	+	–	–	–
	Core bypass	+	+	+	+	+	P	+	+	O	–	–	–	O	–	–
	Core heat transfer	+	+	O	+	–	P	–	–	P	–	–	–	O	–	–
Test facilities	INL MIR core bypass	–	–	–	+											
	ISU heated core bypass	–	–	–	+											
	TAMU core bypass	–	–	–	P											
	SNU core bypass	–	–	–	+											
	CCNY core heat transfer	P	P	–	P											
	TAMU plenum-to plenum NC	P	P	–	–											
	UP mixing in LP	–	–	–	P											
	INL MIR mixing in LP	–	–	–	P											
	USU transient mixed convection	P	P	–	P											
	INL air ingress	–	–	+	–											
	TAMU air ingress	–	–	+	–											
	HTTF integral & separate effects	P	P	P	–											

Figure 1.2: Key thermal-fluids phenomena in HTGRs and the validation experiments for V&V. Symbol key: +, data directly validates key phenomenon; O, data partially applicable; –, not applicable; P, planned activity. Reprinted from [2].

of the coolant during normal operation is illustrated in Figure 1.3a. However, during such LOFC scenarios, the flow in the reactor pressure vessel reverts its direction, moving upwards, as shown in Figure 1.3b. As a result, the helium coolant that normally moves downward through the core and into the lower plenum will get reversed and flow upward through the core and into the upper plenum as hot jets/plumes. Depending on the decay power and the local heat fluxes, the gas flow could carry low or high momentum in different channels. Multiple jets exiting the top of the coolant channels will develop, coalesce, and impinge on the wall in the large enclosure of the upper plenum [35]. The extent to which the hot coolant jets mix in the upper plenum will determine the heat removal rate, the occurrence of local hot spots, and in the most severe conditions even material cracking due to the occurrence of thermal striping.

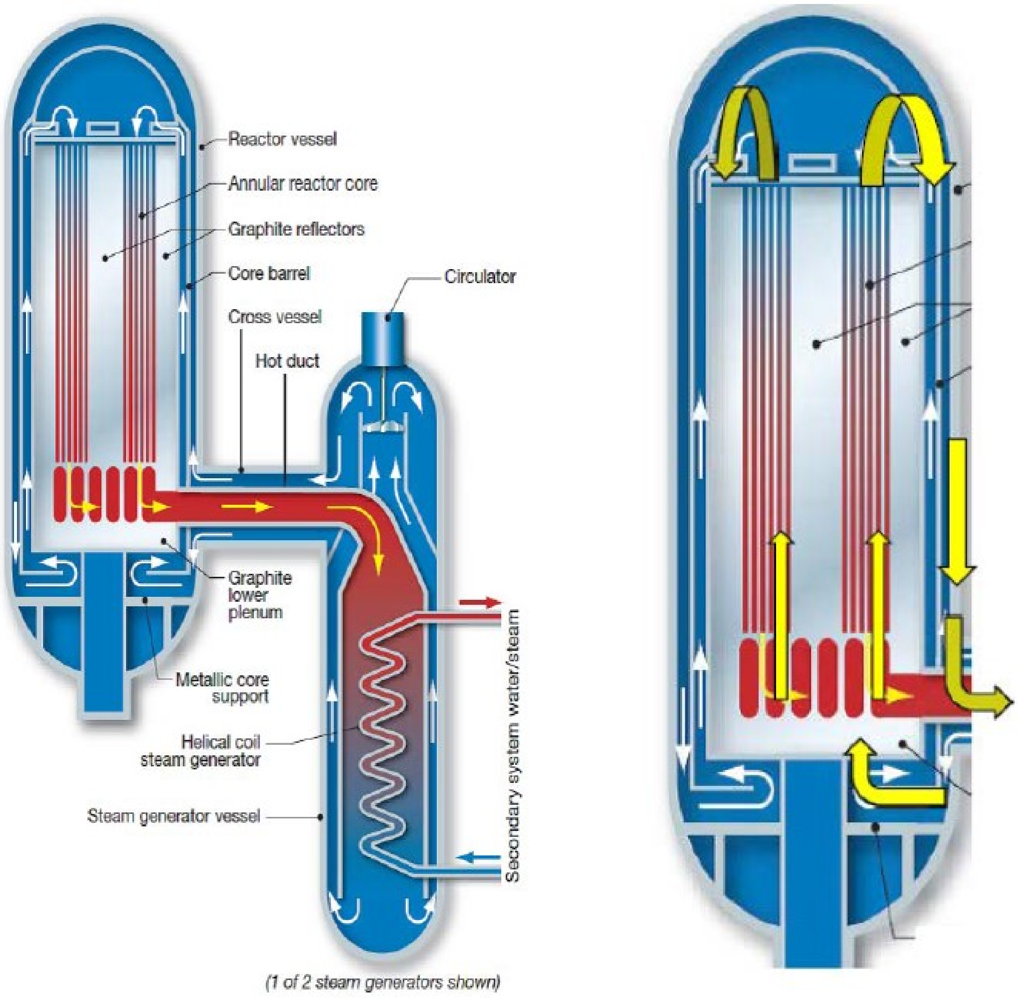

(a) Under normal operating conditions

(b) Under LOFC accident conditions

Figure 1.3: HTGR coolant flow pathways under normal operating conditions and LOFC accident. Reprinted from [3].

Accurately predicting the upper plenum mixing phenomenon can be challenging for nuclear reactor safety analysis tools due to the range of time and length scales that can differ by orders of magnitude. The combination of several phenomena, e.g. jet interaction and impingement, re-circulation, buoyant flows, and thermal stratification, significantly complicates the jet mixing behavior inside the large enclosure and challenges the existing system-level codes and Computational Fluid Dynamics (CFD) models. The ability of system-level and CFD codes to accurately model flow mixing in large enclosures is still under active investigation. High-resolution experimental data with well-controlled boundary conditions are required to support model development and validation.

1.2 Main Objectives of This Thesis

In light of the discussion above, this thesis aims at addressing the challenges mentioned above by 1): designing a novel acoustic flow meter and 2): conducting high-resolution experiments for mixing in large enclosures and providing high-resolution data specifically designed for the validation of high-fidelity CFD models.

The novel acoustic flow meter relies upon the principle of vortex-induced acoustics. A combination of experiments and simulations was conducted to develop the flow meter design and successfully demonstrate its proof of principle. The design proposed in this dissertation has been recently awarded a US patent.

To advance the understanding of flow mixing in the upper plenum and the model capability in predicting the related phenomena, two experimental facilities with well-defined boundaries were designed and constructed at the University of Michigan. First, the Michigan Multi-jet Gas-mixture Dome (MiGaDome) facility that is $1/12^{th}$ scaled down from the upper plenum geometry of the Modular HTGRs design was designed and built to investigate multi-jet interactions in a domed enclosure using optical measurements such as Laser Doppler Velocimetry (LDV) and Particle Image Velocimetry (PIV). Second, the High-Resolution Jet (HiRJet) facility was used to investigate the propagation of stratified fronts in a body of fluid. Wire-Mesh Sensor (WMS) units were used for high-resolution measurements of the time-dependent density field and characterization of the stratified front. High-resolution experimental data measured at these two facilities are used to shed light on the flow mixing in large enclosures with or without the presence of stratified density fronts.

The experiments from these two facilities have been accompanied by high-fidelity Direct

Numerical Simulations(DNSs), or Large Eddy Simulations(LESs) that were conducted by colleagues [36, 37] within an Integrated Research Project (IRP) (IRP-NEAMS-1.1: Thermal-Fluids Applications in Nuclear Energy) funded by the US Department of Energy and lead by Penn State University [38]. The newly obtained data from both high-resolution experiments and high-fidelity simulations were then combined to assess the performance of Reynolds-Averaged Navier-Stokes (RANS) based turbulence models. The work in this thesis is expected to benefit the advancement of HTGR designs by providing practical solutions and through enhanced computational tools.

1.3 Structure of This Thesis

Before delving into specific technical problems, Chapter II details measurement techniques and computational methods. The design and development of a novel acoustic flow meter will be covered in Chapter III. Following the overview of mixing in large enclosures and the introduction of experimental facilities in Chapter IV, Chapter V presents an in-depth discussion of the experimental findings from the separate-effect facilities. Chapters VI and VII focus on the planned validation of turbulence models, particularly in MiGaDome and HiRJET. The thesis concludes with a summary in Chapter VIII, discussing findings and suggesting avenues for future research.

CHAPTER II

Measurement Techniques and Computational Methods

This chapter introduces the key measurement techniques, computational models, and data processing approaches utilized in this thesis along with methods for uncertainty quantification. It is not meant to serve as a comprehensive review of all available advanced techniques, but rather as an explanation of the specific methods adopted to achieve the thesis objectives. Specifically, three cutting-edge experimental techniques will be covered: *Laser Doppler Velocimetry*, *Particle Image Velocimetry*, and the *Wire-Mesh sensor*. Following this, the predominant computational approaches will be outlined, from *Direct Numerical Simulation* to the *Reynolds-Averaging* approach.

2.1 Experiment Measurement Techniques

The experiments conducted in this thesis heavily involve the measurement of a fluid's flow rate, velocity field, and density field. The novel acoustic flow meter will be introduced in the next chapter. The other three advanced measurement methods, namely Laser Doppler Velocimetry (LDV), Particle Image Velocimetry (PIV), and Wire-Mesh Sensor (WMS), will be briefly discussed here.

2.1.1 Laser Doppler Velocimetry (LDV)

Laser Doppler Velocimetry (LDV), also known as Laser Doppler Anemometry (Laser Doppler Anemometry (LDA)), is a non-intrusive optical technique for one-dimensional velocity profiles [39]. A schematic that explains the working principle of LDV is shown in Figure 2.1.

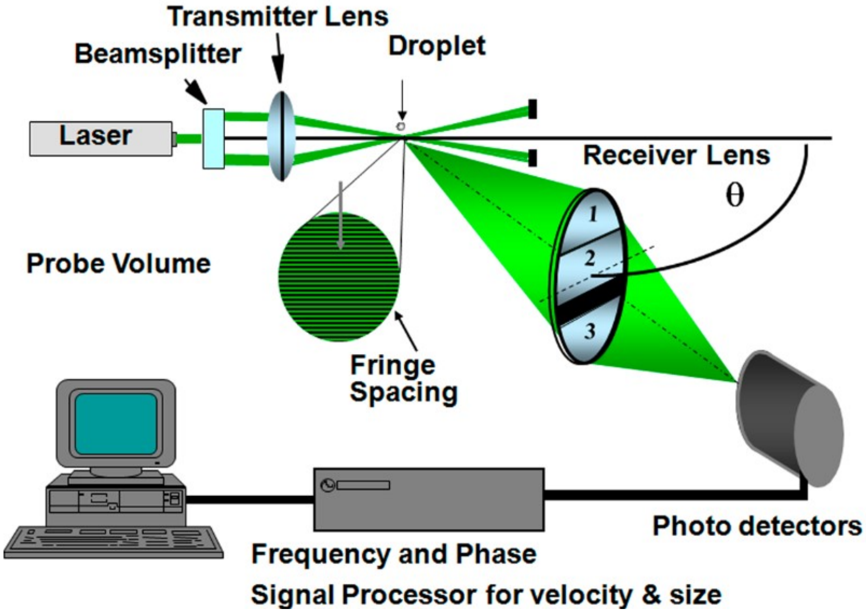

Figure 2.1: Working principle of LDV technique. Reprinted from [4].

An intersection point is created by crossing two collimated, monochromatic, and coherent laser beams, forming a compact measurement test volume. This convergence of beams results in the formation of fringe patterns within the measuring zone owing to the interference from the two coherent beams. When a particle, moving in conjunction with the fluid flow, enters this probing area, it refracts the incident laser beams in various directions. Depending on the setup, a photodetector can capture this scattered light either in the forward or backward orientation.

Due to the motion of the particle relative to the orientation of the laser beams and photodetector, the frequency of the scattered light undergoes a shift compared to the original beam, a phenomenon attributable to the widely accepted Doppler effect. This Doppler effect is experienced differently due to the angular disparity of the two simultaneous incident beams on the particle, leading to distinct Doppler shifts in the light beam towards the photodetector. Given that the incident beams are coherent, an interference occurs in the light scattered from the two beams. Consequently, the photodetector delivers a signal that is temporally modulated at the difference of the Doppler frequencies, a phenomenon termed the Doppler burst. This Doppler differential frequency can be linearly and explicitly connected to a velocity aspect of the moving particle [40].

2.1.2 Particle Image Velocimetry (PIV)

Particle Image Velocimetry (PIV) is a Time of Flight (TOF) measurement technique employed for flow field analysis [41]. Figure 2.2 is a schematic showing the typical set-up for PIV recording of two velocity components within the flow field (2C-2D PIV). The fundamental principle of PIV involves the use of a laser light sheet to illuminate the flow field, which is seeded with small tracer particles that follow the local fluid flow. The seeding particles are illuminated twice within a short time interval Δt and is recorded on two consecutive frames of a high-resolution digital camera.

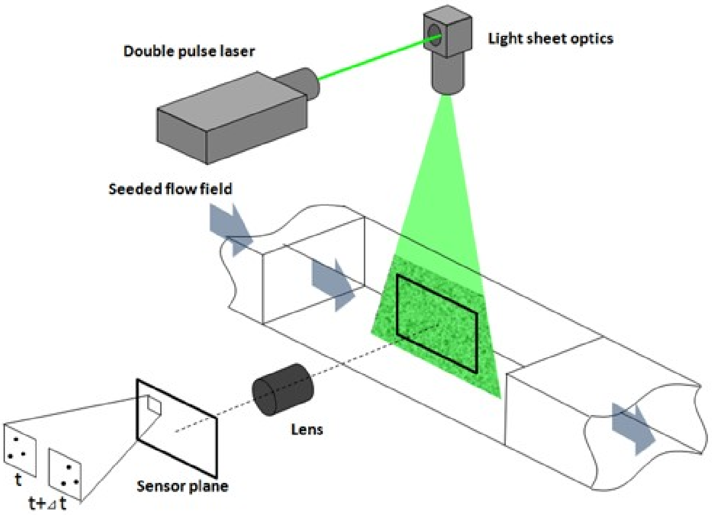

Figure 2.2: An illustration of a 2D PIV system setup. Reprinted from [5].

By following the statistical movement of the tracking particles, the local flow speed (in pixel/s) and direction can be obtained. The evaluation of the statistical movement is based on the cross-correlation of the two consecutive frames, as is demonstrated in Figure 2.3. The recorded flow region is divided into small interrogation windows. Depending on the recording frequency and flow speed (optimized using some pre-calculation or iterated measurements), the selected size of the windows (16x16, 32x32 pixels ...) must ensure that the bulk of the tracking particles remains in the same window after the short time Δt to obtain a valid cross-correlation. The localization of the correlation peak determines the average particle displacement within an interrogation window. The velocity components are calculated from the known time difference Δt and the measured displacement in each direction [42].

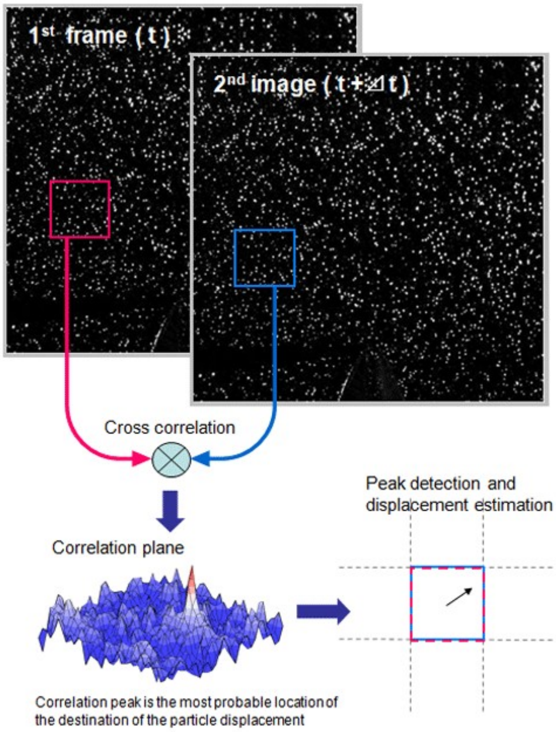

Figure 2.3: An illustration of a 2D PIV evaluation method. Reprinted from [5].

The successful application of the PIV requires that the containment of the flow must be optically accessible. As a result, acrylic or other transparent materials are often used. The camera's image through a solid surface often gets distorted due to the unmatched refraction of index between the solid boundaries and the flow, or the perspective distortions (from the curved boundaries, oblique viewing setups, and possibly inherent camera lens distortions).

A calibration procedure is needed correct this type of distortion. In addition, the calibration process also can serve as a procedure to provide references to scale the image into the real physical dimensions. This is achieved using the designed calibration targets (flat plates with equivalent grids) pre- or after-imaged in the region of interest to determine and correct perspective distortions and define the mm-scaling of images [42].

2.1.3 Wire-Mesh Sensor (WMS)

2.1.3.1 Working principle of the WMS

Wire-Mesh Sensors (WMSs) are designed for characterizing and visualizing gas-liquid two-phase flows and single-phase mixing processes. This state-of-the-art technique was pioneered by Prasser et al. [6] and can provide an instantaneous 2D void fraction/concentration field with high spatial and temporal resolutions.

The working principle of the wire-mesh sensor is based on the conductivity difference between the fluids/phases in the system. Figure 2.4 shows a simplified scheme of the sensor. The sensor consists of two perpendicularly oriented planes of parallel electrodes separated by a small gap in the direction of the flow [43]. Of the two perpendicular electrodes, one is called the transmitter, and another is called the receiver. The transmitter is activated during the operation with a rectangular driving voltage pulse. An electric field is thus formed around the transmitter. As the receiver electrode is kept in the ground state, a current proportional to the resistivity of the fluid between the electrodes will flow from the transmitter to the receiver electrode. The current passes the amplifier and then converts to a digital signal through the analog-to-digital converter (ADC). The magnitude of the recorded signal will be proportional to the conductivity of the fluids. Sequentially activating the transmitters in a time scale smaller than the flow time scale will record a 2D signal grid, thus providing a 2D instantaneous void fraction/concentration field, given that the concentration/void fraction is proportional to the conductivity of the fluids in the applications.

To convert the recorded digital signal into the real fraction/concentration field, a calibration process is necessary and achieved through two standalone measurements when the domain of interest is occupied with the individual fluids. For example, for the void fraction measurement in an air-water tube flow, measurements for the situations “tube completely filled with water” and “tube completely filled with air” are performed during the calibration procedure. The void fraction distribution from the experimental runs then can be established by relating the individual measured components to the calibration values assuming a proportionality of local void fraction and electrical conductivity [6].

Over the past two decades, the wire-mesh sensor technique has been widely used in numerous laboratories worldwide in applications spanning from single-phase mixing to two-phase or even three-phase measurements [44]. However, there are also extensive research activities since the pioneering work of Prasser et al. [6] that aim to improve the sensor’s capability and accuracy [43, 45, 46]. The most intuitively-understandable disadvantage of the WMS is its intrusive characteristic. This is especially important for a two-phase void fraction measurement when the wires cause interfacial deformation of the bubbles [47]. However, this effect is less dominant for single-phase mixing because the mixing process involves no phase change and depends mainly on turbulent and laminar diffusion. Another issue associated with the wire mesh sensor is the “cross-talk” between electrodes [6]. The cross-talk happens because the current can flow freely in the conductive field. When one of the transmitters is activated, a parasitic current from this instantaneously activated transmitter electrode to the neighboring transmitter electrodes will cause a non-zero potential of the non-activated transmitter electrodes. The corresponding receivers of these non-activated transmitters will also receive a false current. The same can happen when a parasitic current from this instantaneously activated transmitter electrode flows directly to the neighboring receivers. The main consequence of the cross-talk is leading to overshoot/undershoot in the final experimental data, thus compromising the accuracy of the measurement.

In the literature, several papers have reported using electrical potential field simulation to investigate the response of the WMS when measuring the two-phase bubbly flow [48, 49,

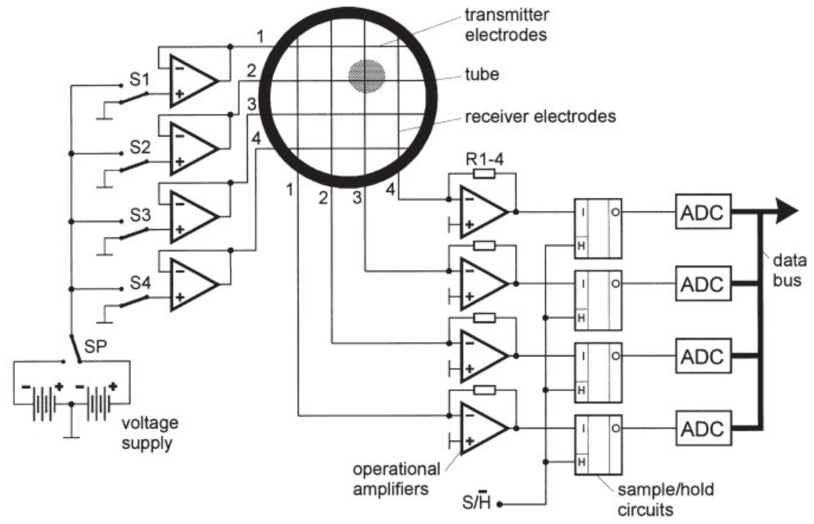

(a) Simplified scheme of the wire-mesh sensors

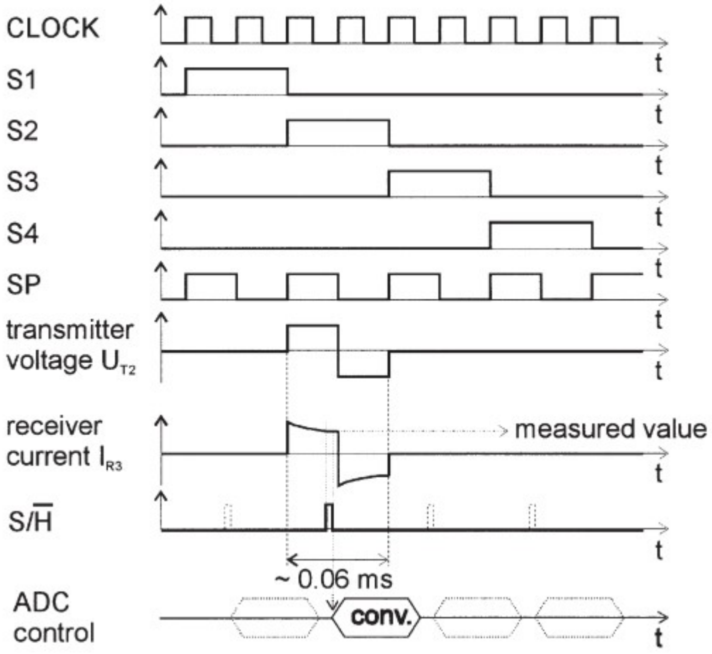

(b) Control signals and method of signal acquisition

Figure 2.4: Working principle of the wire mesh sensor. Reprinted from [6].

50, 51]. It was found that due to the presence of gas-liquid interfaces, the symmetry of the potential field in the periodic structure of the electrode grids has been disturbed [48]. A systematic character of overshoots of the conductance signal inside the fluid in a wire-mesh sensor has thus been observed. Even though the application of the wire mesh sensor to the single-phase mixing process has been widely seen and is well summarized by [44], to the author's best knowledge, there is currently no literature that has numerically investigated the signal response of WMS when measuring single-phase flow using the electrical potential field simulation.

Since this thesis will use WMS to measure density stratification, it is of great interest to have an electrical potential field simulation of the WMS when applied to such a scenario, which can inform the calibration process and improve the accuracy of the measurement.

2.1.3.2 Electrical field simulations of WMS in the application of thermal stratification

The working principle of the WMS as discussed indicates that the electric field is irrotational and temporally invariant during a single measurement cycle. As a result, the electrical potential field induced by the sensor electrodes within the conductive fluid can be determined by the Laplace equation, which can be expressed as:

$$\nabla \cdot (\sigma \nabla \phi) = 0 \tag{2.1}$$

Where σ and ϕ are the electrical conductivity and electric potential respectively.

Based on the intended application, a simplified model has been created to represent the real scenario while saving computational time. The computational model is shown in Figure 2.5. In this simplified model, the WMS consists of 4 vertical receivers (red color) and 16 horizontal transmitters (blue color). The diameter of all the wires is $D = 0.2$ mm, and the pitch distance between wires is $p = 1.5$ mm. The WMS geometry is immersed in a defined fluid domain of $l^* \times w^* \times h^* = 127 \times 127 \times 77$ (dimensions are normalized by the wire diameter).

Since the time scale of the flow is several orders of magnitude larger than the time scale of measurement, the simulation does not consider the flow of the fluid. Instead, the fluid domain is prescribed with a steady-state distribution of conductivity. As such, the six boundaries of the fluid domains have all been set to wall boundaries with electrical insulation conditions. The conductivity of the aluminum wires is set to be $\sigma_w = 3.78 \times 10^7$ S/m. To mimic the WMS measurement process, the transmitters were activated in sequence. The potential for the activated transmitter wire was set to unity while the other wires' potential was set to zero. During the activation of each transmitter, a steady-state electrical field was obtained with a residual below 10^{-10}.

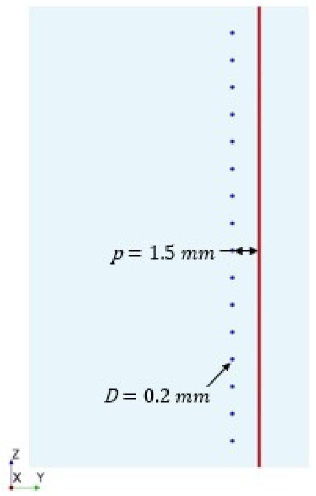

(b) Side view of the WMS (16x4).

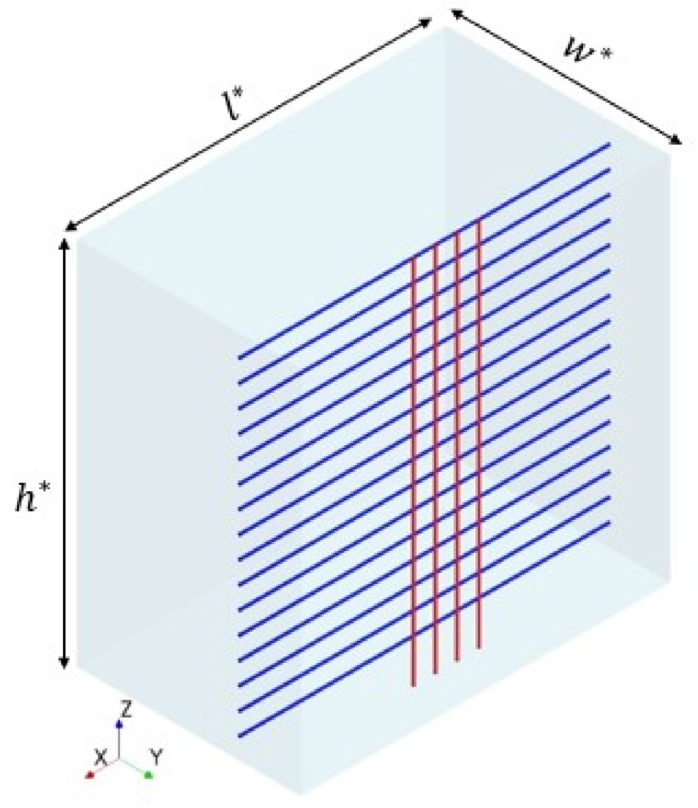

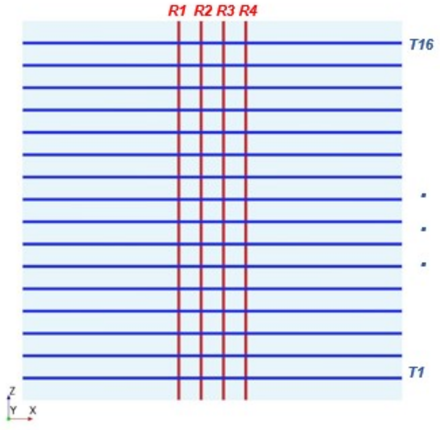

(a) Isometric of the computational model.

(c) Front view of the WMS (16x4).

Figure 2.5: A simplified computational model for the WMS in the application of measuring thermal stratification

As the stratification is gravity-oriented, the fluid domain has been assumed with a vertically distributed conductivity distribution. Two prescribed stratification scenarios are investigated. The first one has a smooth stratified front $\sigma_{sm}(z)$ in the vertical direction, shown in Figure 2.6a. The distribution of the smooth stratified front can be mathematically modeled with a sigmoid curve. The second case has a sharp stratification interface $\sigma_{sh}(z)$, shown in Figure 2.6b. The transmitters have been activated sequentially from $T1$ to $T16$ for each case. When one transmitter is activated, the current reading from the receiver corresponds to the conductivity at the cross point between the activated transmitter and the receiver. The current reading $I(z)$ from the receiver $R3$ has been extracted during each activation to examine the signal response of WMS. The calibration of the signal was achieved by running two uniform cases: the low-conductivity case with $\sigma_l = 0.001$ S/m and the high-conductivity case with $\sigma_h = 0.05$ S/m. The current readout from these two cases, namely $I_l(z)$ and $I_h(z)$, thus provide the calibration profiles. The measurement of the WMS from the simulation, then can be expressed as:

$$\sigma(z) = \frac{I(z) - I_h(z)}{I_l(z) - I_h(z)}(\sigma_l - \sigma_h) + \sigma_h \tag{2.2}$$

Figure 2.7 shows the WMS response to the two prescribed conductivity distributions regarding the concentration distribution. Note here the concentration is assumed to be proportional to the conductivity field. If such a condition can not be satisfied, it is necessary to have an additional conversion from conductivity to concentration based on the known relations. It can be seen from Figure 2.7a that WMS successfully captured the distribution with a smooth stratification. However, Figure 2.7b shows that an undershoot happened near the sharp interface (near transmitters $T11 - T14$). The undershoot of the concentration here corresponds to the overshoot of the conductivity, which means that the currents $I(z)$ monitored at these positions exceed the maximum reference calibration value $I_h(z)$. It is thus inferred that the sharp interface has altered the electrical field distribution. This speculation can be examined by looking at the electrical current density distributions, which is shown in Figure 2.8.

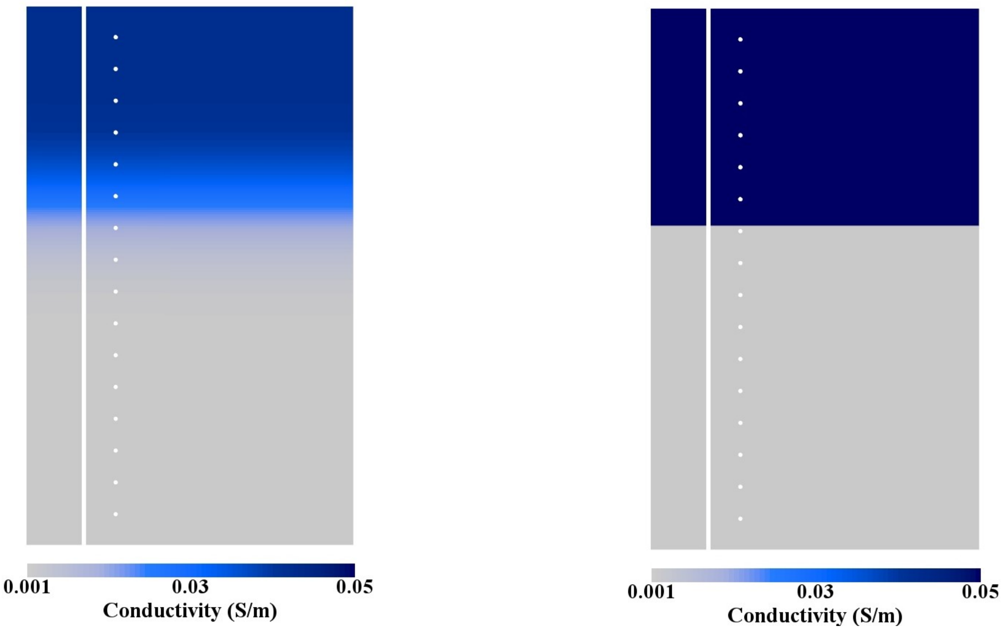

(a) Smooth conductivity distribution. (b) Sharp conductivity distribution.

Figure 2.6: Two prescribed conductivity distributions corresponding to the smooth and sharp stratified fronts, respectively. The observing plane passes the center of $R3$.

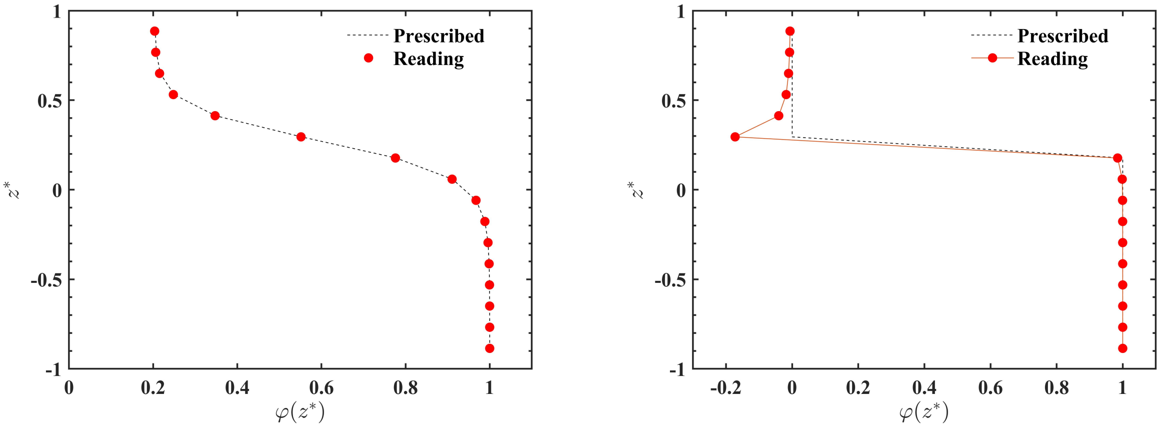

(a) WMS response to the smooth interface. (b) WMS response to the sharp interface.

Figure 2.7: WMS response to the two prescribed conductivity distributions.

Figure 2.8 compares the magnitude of the electrical current density $|\mathbf{J}|$ from the two studied cases with the calibration cases. The steady-state distribution of $|\mathbf{J}|$ was obtained when the transmitter $T11$ was activated. Figures 2.8a and 2.8b show the distributions from the two calibration cases where the conductivity is uniform across the field. Figure 2.8a shows no contour due to low conductivity. However, a horizontally-symmetrical current distribution is seen in Figure 2.8b for the uniform high-conductivity case. The electrical current flows from the high-potential transmitter to the receiver as the receiver has zero potential. But this also happens to the neighboring zero-potential transmitters due to cross-talk.

Figures 2.8c and 2.8d show electrical current density for the cases with $\sigma_{sm}(z)$ and $\sigma_{sh}(z)$, respectively. The magnitude from Figure 2.8c is lower than that from 2.8b since the magnitude of conductivity is generally smaller in this case. It can be seen from 2.8d that a clear boundary has formed between $T11$ and $T10$, where the sharp interface resides. This results in less cross-talk between transmitter $T11$ and the region below the interface. The electrical current thus diverts and redistributes more in the region above the interface where the conductivity is high. Stronger cross-talk is seen on $T11$ and $T12$ according to the contour colors. More current also flows into the receiver, leading to the overshoot of current in this case. The observed overshoot in this simulation agrees with the work in Ref. [48] in that the sharp interface had caused the overshoot by disturbing the symmetry of the electrical field.

Based on this electrical field simulation, it is learned that special care must be taken if a sharp interface is present when applying the WMS to measure single-phase mixing regarding the stratification phenomenon. More advanced algorithms or techniques may be developed later to eliminate this overshoot. In this thesis, by taking advantage of the fact that the overshoot happens only on one side of the interface where the conductivity is high, the overshoot can be corrected by resetting the final concentration values to the reference values. This practice will not change the physics but correct the abnormal distribution to a physics-bounded range without compromising accuracy.

2.2 Computational Methods

Fullfill Scientific Computing's literature review requirements

The behavior of fluid flow has been well-known to be governed by the conservation of mass, momentum, and energy. The set of conservation equations for incompressible flow, in Einstein's notation, is expressed as:

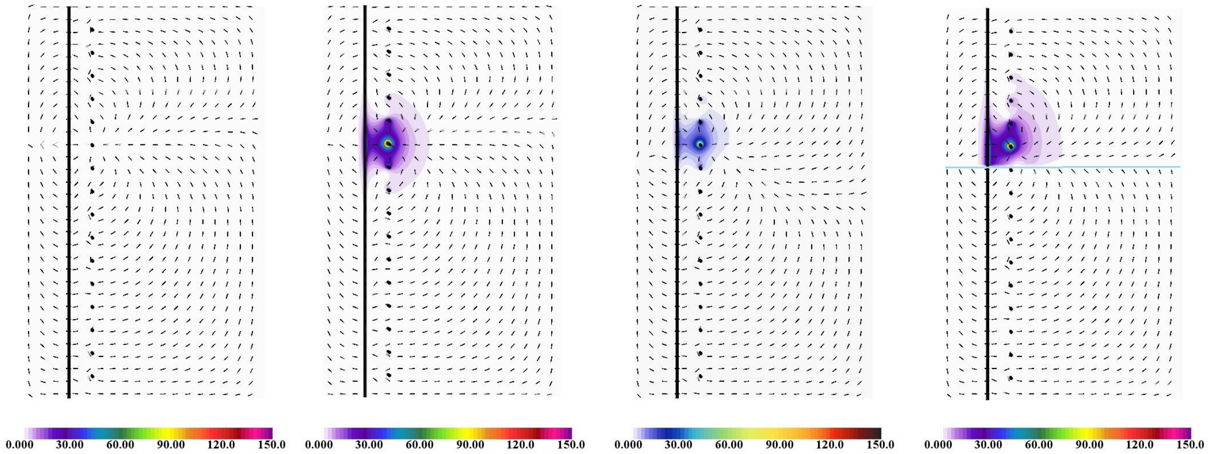

(a) $|\mathbf{J}| = f(\sigma_l)$ (b) $|\mathbf{J}| = f(\sigma_h)$ (c) $|\mathbf{J}| = f(\sigma_{sm}(z))$ (d) $|\mathbf{J}| = f(\sigma_{sh}(z))$

Figure 2.8: Contour of the electrical current density magnitude $|\mathbf{J}|$ when transmitter $T11$ is activated. The observing plane passes the center of $R3$. The vector field represents the electrical field with constant length. The horizontal line in (d) indicates the location of the interface.

The continuity equation:

$$\frac{\partial \rho}{\partial t} + \frac{\partial (\rho u_i)}{\partial x_i} = 0 \tag{2.3}$$

The momentum equations:

$$\frac{\partial (\rho u_i)}{\partial t} + \frac{\partial (\rho u_i u_j)}{\partial x_j} = -\frac{\partial p}{\partial x_i} + \frac{\partial}{\partial x_j}\left[\mu\left(\frac{\partial u_i}{\partial x_j} + \frac{\partial u_j}{\partial x_i}\right)\right] + \rho g_i \tag{2.4}$$

The energy equation:

$$\frac{\partial}{\partial t}(\rho C_p T) + \frac{\partial}{\partial x_j}(\rho C_p T u_j) = -\frac{\partial q_j}{\partial x_j} + q_v \tag{2.5}$$

where,

i and j denote the Cartesian coordinate directions, ρ is the density;

u_i is the velocity component in the i direction;

p is the pressure and μ is the molecular viscosity;

μ_t and α_t are the turbulent viscosity and turbulent thermal diffusivity, respectively;

g_i is the acceleration due to gravity in the i direction.

T is the temperature, q_j is the heat flux in the j direction, and q_v is the heat source;

Analytically solving the group of equations with equations of state and boundary conditions poses a challenge as the momentum equation is highly non-linear. As a result, analytical solutions exist only for particular cases, generally when the nonlinear convective terms vanish naturally [52]. However, when the flow gets more complex (turbulence, vortex, recirculation, stratification), as is often seen in real industrial applications, the non-linearity of the equations becomes dominant, and no analytical solutions can be obtained. This leads to the fact that Computational Fluid Dynamics (CFD) remains an indispensable tool for understanding the details of the complex flow in addition to experiments.

CFD discretizes the complete governing equations in space and time, resulting in a system of algebraic equations to be solved using an algebraic multigrid solver. In CFD three modeling approaches are primarily used, and these are categorized as Direct numerical simulation (Direct Numerical Simulation (DNS)), Large eddy simulation (Large Eddy Simulations (LES)), and Reynolds-averaged Navier–Stokes (RANS) models.

The main differences between the three methods are demonstrated in Figure 2.9. DNS is the most computationally intensive method. It resolves all the turbulence structures down to the smallest scales, with no turbulence modeling. It provides the most accurate insight into the physics of turbulent flows but is often limited in application due to its high computational cost; LES is a more intermediate method. LES resolves large, energy-containing structures in the flow while the effects of smaller, subgrid-scale structures are modeled. LES is less computationally intensive than DNS but more computationally intensive than RANS. It can provide both time-dependent and averaged results; RANS is the least computationally intensive method and is most commonly used in practical engineering applications. It models all of the turbulence in the flow and only resolves the mean flow features. As a result, it is much quicker and less computationally expensive than DNS or LES. However, it provides less detailed information about the flow. The specific realization of each method will be briefly discussed in the following subsections.

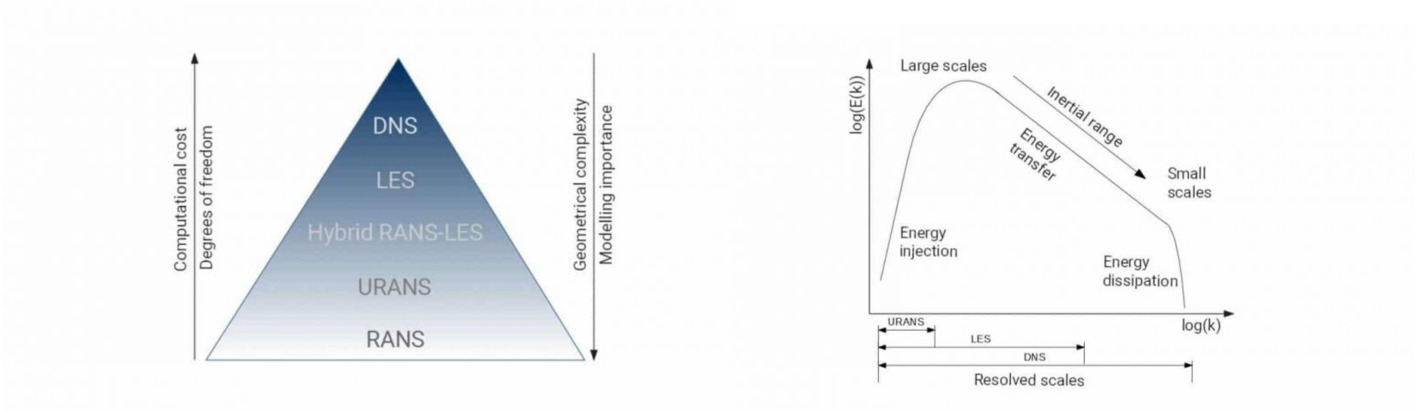

(a) Complexity vs cost.

(b) Resolved scales.

Figure 2.9: Turbulence models in CFD from RANS to DNS. Reprinted from [7].

2.2.1 Direct Numerical Simulation

Since no modeling effort is involved, the accuracy of DNS is solely determined by the discretization errors. Results from a turbulent channel flow have shown that the discretization errors are very small in DNS [53]. The key in DNS is that all scales of motion must be resolved. This includes the very small scales governed by the Kolmogorov length, time, and velocity scales, derived from dimensional analysis of the Navier-Stokes equations.

The Kolmogorov length (η) and time τ scales are given by:

$$\eta = \left(\nu^3/\varepsilon\right)^{1/4} \tag{2.6}$$

$$\tau = (\nu/\varepsilon)^{1/2} \tag{2.7}$$

where ν is the kinematic viscosity, and ε is the dissipation rate of turbulent kinetic energy.

DNS generally requires high spatial resolution (small Δx) and temporal resolution (small $\Delta \mathrm{t}$) to accurately resolve the Kolmogorov scales: $\Delta x \sim \eta$ and $\Delta \mathrm{t} \sim \tau$. These resolutions grow dramatically as Reynolds number Re increases: the number of grid points needed (N) scales with $\mathrm{Re}^{9/4}$, and the number of time steps needed τ scales with $\mathrm{Re}^{3/2}$.

2.2.2 Large Eddy Simulation

As indicated in Figure 2.9b, the energy-containing scales of turbulence, also known as the large scales, are resolved, and the effects of smaller scales are modeled. In the theory of turbulence [54], the larger eddies tend to be more coherent and have larger scales, and the mean flow and geometry influence them. These large scales contain most of the turbulent energy and are the most important for mixing and transport. The smaller scales, on the other hand, are more universal, isotropic and are responsible for dissipating the energy from the larger scales. LES models these small scales since they do not have a significant effect on the larger, energy-containing scales and modeling them reduces computational cost significantly as compared to directly simulating all scales as in DNS.

LES is realized by applying spatial filtering to the conservation equations. The filter separates the velocity field into resolved (grid) and modeled (sub-grid) components. Example of the filtered incompressible Navier-Stokes equations of motion can be expressed as [55]:

$$\frac{\partial \bar{u}_i}{\partial t} + \bar{u}_j \frac{\partial \bar{u}_i}{\partial x_j} = -\frac{1}{\rho}\frac{\partial \bar{p}}{\partial x_i} + \frac{\partial}{\partial x_j}\left(\nu \frac{\partial \bar{u}_i}{\partial x_j}\right) + \frac{1}{\rho}\frac{\partial \tau_{ij}}{\partial x_j}. \tag{2.8}$$

with

$$u_i = \bar{u}_i + u_i' \text{ and } p = \bar{p} + p' \tag{2.9}$$

where $\bar{u}_i$ and $\bar{p}$ are the resolvable scale part and u_i' and p' are the subgrid-scale part.

The residual stress tensor τ_{ij} resulting from the filtering accounts for interactions between the resolved and modeled scales. Modeling the unclosed stress tensor τ_{ij} leads to the SubGrid-Scale (SGS) models. A recent review on the subgrid-scale modeling for large-eddy simulation can be found in Ref. [56].

The filter width (or scale) is a feature of Large Eddy Simulation (LES) that determines which scales of turbulence will be resolved and which will be modeled. It's typically linked to the grid size in the discrete representation of the flow field. The selection of a suitable filter width is still a subject of research in LES. The choice can depend on various factors, including the specific characteristics of the flow, available computational resources, and a balance between accuracy and efficiency. The Taylor microscale is often adopted when designing meshes for LES [57], which is defined as

$$\lambda = \sqrt{10v\frac{k}{\varepsilon}} \tag{2.10}$$

where k is the turbulent kinetic energy and ε is the rate of energy dissipation.

With the continual increase in computational power, high-fidelity simulations using LES and DNS have become increasingly important to nuclear thermal hydraulics for the fundamental understanding of turbulent flow and heat transfer phenomena and for further development and validation of engineering CFD models. Several review papers summarizing high-fidelity simulations relevant for nuclear reactor safety and design purposes can be found in [58, 59, 60, 61].

2.2.3 Turbulence Modeling

2.2.3.1 Reynolds Averaging

Introduced by Reynolds in 1895 [62], Reynolds averaging is a statistical approach that decomposes the solution variable $\varPhi$ in the instantaneous Navier-Stokes equations into the sum of the mean component ϕ and its fluctuating component ϕ'. A detailed decomposition process can be found in [63]. The resultant Navier-Stokes equations, called Reynolds-Averaging Navier-Stokes equations, in terms of the mass, momentum, and temperature/concentration variables expressed in tensor notation, can be written as:

$$\frac{\partial \rho}{\partial t} + \frac{\partial}{\partial x_i}\left(\rho U_i\right) = 0 \tag{2.11}$$

$$\frac{\partial}{\partial t}\left(\rho U_i\right) + \frac{\partial}{\partial x_j}\left(\rho U_i U_j\right) = -\frac{\partial p}{\partial x_i} + \frac{\partial}{\partial x_j}\left[\mu\left(\frac{\partial U_i}{\partial x_j} + \frac{\partial U_j}{\partial x_i}\right)\right] + \frac{\partial}{\partial x_j}\left(-\rho\overline{u_i'u_j'}\right) + \rho g_i \tag{2.12}$$

$$\frac{\partial\left(\rho c_p T\right)}{\partial t} + \frac{\partial\left(\rho c_p T U_i\right)}{\partial x_i} = -\frac{\partial\left(p U_i\right)}{\partial x_i} + \frac{\partial}{\partial x_i}\left[k\frac{\partial T}{\partial x_i} - \rho c_p\overline{T'u_i'}\right] \tag{2.13}$$

$$\frac{\partial\left(\rho\varphi\right)}{\partial t}+\frac{\partial\left(\rho\varphi U_i\right)}{\partial x_i}=\frac{\partial}{\partial x_i}\left[\mathit{\Gamma}\frac{\partial\varphi}{\partial x_i}-\rho\overline{\varphi' u_i'}\right]+S_\varphi \tag{2.14}$$

The RANS equations are identical to the instantaneous NS equations except for the additional turbulent flux term that appears in the momentum and the temperature/concentration equations. Constitutive relations are needed for the closure of the equations.

2.2.3.2 Eddy-viscosity models

Based on the analogy between the molecular gradient-diffusion process and turbulent motion, eddy-viscosity models adapt the Boussinesq approximation. The Reynolds stress tensor is thus molded as the product of eddy viscosity and the mean strain-rate tensor. The mathematical format is shown below.

$$-\rho\overline{u_i' u_j'}=\mu_t\left(\frac{\partial u_i}{\partial x_j}+\frac{\partial u_j}{\partial x_i}\right)-\frac{2}{3}\delta_{ij}\rho k \tag{2.15}$$

For the introduced turbulent eddy viscosity coefficient μ_t, additional transport equations for scalar quantities are solved. For the next, several widely used turbulence models will be introduced.

Standard $k-\varepsilon$ model

As the base of the $k-\varepsilon$ model family, the Standard $k-\varepsilon$ (Standard $k-\varepsilon$ (SKE)) model is the simplest but complete two-equations model popular for industrial applications. For the Standard $k-\varepsilon$ model, the transport equations for the turbulent kinetic energy k and the turbulent dissipation rate ε are solved and can be written as:

$$\frac{\partial}{\partial t}(\rho k)+\frac{\partial}{\partial x_i}\left(\rho k U_i\right)=\frac{\partial}{\partial x_j}\left[\left(\mu+\frac{\mu_t}{\sigma_k}\right)\frac{\partial k}{\partial x_j}\right]+G_k+G_b-\rho\varepsilon-Y_m+S_k \tag{2.16}$$

$$\frac{\partial}{\partial t}(\rho\varepsilon)+\frac{\partial}{\partial x_i}\left(\rho\varepsilon U_i\right)=\frac{\partial}{\partial x_j}\left[\left(\mu+\frac{\mu_t}{\sigma_\varepsilon}\right)\frac{\partial\varepsilon}{\partial x_j}\right]+C_{1\varepsilon}\frac{\varepsilon}{k}\left(G_k+C_{3\varepsilon}G_b\right)-C_{2\varepsilon}f_2\rho\frac{\varepsilon^2}{k}+S_\varepsilon \tag{2.17}$$

where,

G_k is the turbulent production by the mean velocity gradient;

G_b is the turbulent production by buoyancy;

Y_m denotes the contribution of expansion in the case of compressible turbulence, which is often negligible;

$C_{1\varepsilon} = 1.44, C_{2\varepsilon} = 1.92$, $f_2 = 1$, $\sigma_k = 1$; Literature shows that the model coefficient $C_{3\varepsilon}$ within $0.3 \sim 1$ does not affect the simulation results. But no general agreement has been reached on the specification of its value. The methods to calculate $C_{3\varepsilon}$ implemented in STAR-CCM+ can be found in [64];

S_k and S_ε are user-defined source terms.

The closure for turbulent eddy viscosity μ_t is then given by

$$\mu_t = \rho C_\mu f_\mu \frac{k^2}{\varepsilon} \tag{2.18}$$

where the coefficient $C_\mu = 0.09$ and $f_\mu = 1$.

The SKE model is also often called the high-Reynolds number approach since it was originally developed for the high-Reynolds number flow, and the near-wall region is modeled with wall functions.

Standard $k - \varepsilon$ Low-Re model

A modification to account for the blocking effects of the wall includes using a low-Reynolds number approach or a two-layer approach. The low-Reynolds number approach for the SKE model implemented in STAR-CCM+ is called the Standard $k - \varepsilon$ Low-Re model.

This model applies damping functions to the model coefficients to mimic the decrease of turbulent mixing near the walls so that no wall functions are needed to model the viscous- and buffer layer. The damping functions are incorporated into f_2 in Eq. 2.17 and f_μ in Eq. 2.18, with the following formula:

$$f_2 = 1 - 0.3 \exp\left(-Re_t^2\right) \tag{2.19}$$

$$f_\mu = 1 - \exp\left[-\left(0.091\sqrt{Re_d} + 0.0042 Re_d + 0.00011 Re_d^2\right)\right] \tag{2.20}$$

where turbulent Reynolds number $\mathrm{Re}_t = k^2/(v\varepsilon)$ and wall-distance Reynolds number $Re_d = \sqrt{k}d/v$, with d the distance to the wall.

Realizable $k - \varepsilon$ model

A relatively recently-developed variation of the SKE model, called the Realizable $k - \epsilon$ (RKE) model, takes exactly the same form for the k equation as that in the SKE model but with different model constants. The ε equation has a different form as the following:

$$\frac{\partial}{\partial t}(\rho\varepsilon) + \frac{\partial}{\partial x_j}(\rho\varepsilon u_j) = \frac{\partial}{\partial x_j}\left[\left(\mu + \frac{\mu_t}{\sigma_\varepsilon}\right)\frac{\partial \varepsilon}{\partial x_j}\right] + \rho C_1 S\varepsilon - \rho C_2 \frac{\varepsilon^2}{k + \sqrt{\nu\varepsilon}} + C_{1\varepsilon}\frac{\varepsilon}{k}C_{3\varepsilon}G_b + S_\varepsilon \tag{2.21}$$

where,

$$C_1 = \max\left[0.43, \frac{\eta}{\eta + 5}\right], \quad \eta = S\frac{k}{\varepsilon}, \quad S = \sqrt{2S_{ij}S_{ij}} \tag{2.22}$$

$$C_{1\epsilon} = 1.44, \quad C_2 = 1.9, \quad \sigma_k = 1.0, \quad \sigma_\epsilon = 1.2 \tag{2.23}$$

The eddy viscosity is also computed from Eq. 2.18 but with C_μ being non-constant. The formula for the C_μ is

$$C_\mu = \left(4.04 + \sqrt{6}\cos\left[\frac{1}{3}\cos^{-1}(\sqrt{6}W))\right]\frac{k\sqrt{S_{ij}S_{ij} + \varOmega_{ij}\varOmega_{ij}}}{\epsilon}\right)^{-1} \tag{2.24}$$

where,

$$W = \frac{S_{ij}S_{jk}S_{ki}}{\left(S_{ij}S_{ij}\right)^{3/2}}, S_{ij} = \frac{1}{2}\left(\frac{\partial u_j}{\partial x_i} + \frac{\partial u_i}{\partial x_j}\right), \Omega_{ij} = \frac{1}{2}\left(\frac{\partial u_j}{\partial x_i} - \frac{\partial u_i}{\partial x_j}\right) \tag{2.25}$$

The term "realizable" refers to the fact that this model satisfies certain mathematical constraints on the Reynolds stresses, which results in a generally better performance in predicting separated flows and flows with complex secondary flow features [65, 66].

SST $k - \omega$ model

The Shear-Stress Transport (SST) k- ω model determines the turbulent eddy viscosity based on the turbulence kinetic energy k and the specific dissipation rate ω ($\omega = \varepsilon/k$). The transport equations for the two turbulent quantities are the following:

$$\frac{\partial}{\partial t}(\rho k) + \frac{\partial}{\partial x_i}\left(\rho k v_i\right) = \frac{\partial}{\partial x_j}\left[\left(\mu + \sigma_{k,\omega}\mu_t\right)\frac{\partial k}{\partial x_j}\right] + G_{k,\omega} + G_{b,\omega} - Y_k + S_k \tag{2.26}$$

$$\frac{\partial}{\partial t}(\rho \omega) + \frac{\partial}{\partial x_i}\left(\rho \omega v_i\right) = \frac{\partial}{\partial x_j}\left[\left(\mu + \sigma_{\omega}\mu_t\right)\frac{\partial \omega}{\partial x_j}\right] + G_{\omega} + D_{\omega} - Y_{\omega} + S_{\omega} \tag{2.27}$$

where,

$G_{k,\omega}$ is the turbulent production by the mean velocity gradient;

$G_{b,\omega}$ is the turbulent production by buoyancy;

G_ω is the generation of the turbulent dissipation rate ω;

D_ω is the cross-diffusion term;

Y_k and Y_ω are the dissipation terms for k and ω, respectively;

$\sigma_{k,\omega}$ and σ_ω are model coefficients;

$S_{k,\omega}$ and S_ω are user-defined source terms.

The eddy viscosity is computed based on the k to ω ratio, with a coefficient as a low-

Reynolds-number correction and blending function:

$$\mu_t = \frac{\rho k}{\max\left[\frac{\omega}{\alpha^*}, \frac{SF_2}{a_1}\right]} \tag{2.28}$$

$$\alpha^* = \frac{0.072/3 + \rho k/6\mu\omega}{1 + \rho k/6\mu\omega}, F_2 = \tanh\left(\left(\max\left[2\frac{\sqrt{k}}{0.09\omega y}, \frac{500\mu}{\rho y^2\omega}\right]\right)^2\right) \tag{2.29}$$

where y is the distance to the next surface.

Reynolds Stress Transport (Reynolds Stress Transport (RST)) model

Instead of linking the Reynolds stress tensor to the mean velocity gradient, the Reynolds Stress Transport (RST) models directly calculate the components of the Reynolds stress tensor by solving their governing transport equations, thus accounting for the anisotropy. The transport equation for the Reynolds stress tensor is given as:

$$\frac{\partial}{\partial t}(\rho \mathbf{R}) + \frac{\partial}{\partial x_i}(\rho \mathbf{R} U_i) = \frac{\partial}{\partial x_j}\left[\left(\mu + \frac{\mu_t}{\sigma_k}\right)\frac{\partial \mathbf{R}}{\partial x_j}\right] + \mathbf{G}_{\mathbf{k},\mathbf{R}} + \mathbf{G}_{\mathbf{b},\mathbf{R}} - \frac{2}{3}\mathbf{I}\Upsilon_M + \underline{\phi} - \rho\underline{\varepsilon} + \mathbf{S}_{\mathbf{R}} \tag{2.30}$$

where,

$\mathbf{G}_{\mathbf{k},\mathbf{R}}$ is the turbulent production by the mean velocity gradient;

$\mathbf{G}_{\mathbf{b},\mathbf{R}}$ is the turbulent production by buoyancy;

Υ_M is the dilatation dissipation term;

$\underline{\phi}$ is the pressure strain tensor term;

$\underline{\varepsilon} = \frac{2}{3}\varepsilon\mathbf{I}$ is the turbulent dissipation rate tensor, with the isotropic turbulent dissipation rate obtained from a transport equation analogous to the $k - \varepsilon$ model;

$\mathbf{S}_{\mathbf{R}}$ is user-defined source term;

σ_k is the model coefficient and the turbulent viscosity μ_t is computed with an additional model coefficient C_μ as:

$$\mu_t = \rho C_\mu \frac{k^2}{\varepsilon} \tag{2.31}$$

2.3 Conclusions

In this chapter, the main measurement techniques and computational models involved in this thesis have been presented. The working principle of particle image velocimetry, laser Doppler velocimetry, and wire-mesh sensor have been explained. Besides, an electric-magnetic field simulation for applying a wire-mesh sensor in a stratification environment has been conducted. The simulation demonstrated the applicability of a wire-mesh sensor for measuring smooth stratification. Overshoot has been observed from the simulation when applying a wire-mesh sensor for sharp stratification, but this can be accounted for. For the computational models, realizations of direct numerical and large eddy simulation were first discussed. The classical Reynolds-averaging method, with various turbulence models, is then introduced. It must be noted that this thesis will only use the high-fidelity data from the direct numerical and large eddy simulations performed by colleagues [36, 37]. The main objectives of the computational methods will be the application and validation of RANS models.

CHAPTER III

Design of a Novel Acoustic Flow Meter

3.1 Introduction

One of the concerns is that the primary coolant flow, which is helium, is not directly measured in HTGRs. It is calculated indirectly using the coolant circulator shaft speed signal, the circulator performance curves, and the equation of state of the working fluid [67]. However, this indirect prediction inevitably leads to increased uncertainty in the quantity of interest as circulator performance curves include highly non-linear dynamics, particularly at low-power/low-flow-rate conditions. As a critical factor in the measurement of core heat removal, core flow rate needs to be monitored more efficiently and accurately. Consideration of all commercial flow meters has been effectively eliminated due to the high flow rate ($10 - 15\, m/s$ at the nominal operating conditions), high operating temperatures ($> 700^oC$), and high neutron flux and gamma fields in the reactor core. As a result, there is a long-felt and unmet need to develop a flow meter suitable for use in harsh environments given the characteristics of the HTGR s, which originates using acoustic emission to measure the flow rate. After numerous explorations, the corrugated pipe has been selected as the design basis for the flow meter. It is a corrugated flexible plastic pipe. When held and swung in the air, the tube will whistle with a clear tone, which will change according to the swinging speed. Its whistling ability was first discussed in Ref. [68], and a following experimental exploration was reported in Ref. [69].

A sketch illustrating this phenomenon is reported in Figure 3.1. When gas flows into a corrugated pipe, flow separation occurs on the upstream edge of each cavity, leading to the generation of a vortex flowing downstream. The vortex that sheds from the upstream edge and breaks on the downstream wall induces an unsteady force periodically, which is the source of the sound in the mainstream. This sound source provides acoustic energy to the mainstream, resulting in a longitudinal acoustic wave. This pressure oscillation controls the vortex shedding in return, consequently forming a self-sustained acoustic change. According to the observation in Ref. [70], the audible frequency was correlated to the natural harmonics of the tube. Later, however, researchers concluded that the whistling was due to the feedback mechanism from the flow-acoustic interaction, and the frequency was not necessarily the same as the pipe resonance frequency.

Nowadays, corrugated pipes have been widely existing in industries due to their inherent character of being globally flexible and locally rigid, for example, offshore natural gas production systems, vacuum cleaners, and even heat exchangers. Besides, due to its musical characteristics, it is also popular as an amusing musical toy [71]. Numerous literature is also available about the study of corrugated pipes, and a thorough literature review is presented in Ref. [72]. However, significant research work on the corrugated pipe so far has concentrated mainly on revealing the whistle principle and avoiding unexpected noise [73] [74] [75]. To utilize the flow-frequency relationship to build a gas flow meter has never been of discussion to the best of the author's knowledge. The essential advantage of using a sound pipe is that it does not require significant modifications to reactor core internals. The actual sensing can be accomplished without interfering with the flow and potentially on the outside surface of the reactor pressure vessel. It could simplify the reactor core's internals and enhance reactor safety. In addition, as new-generation reactors are scaled down to smaller sizes to save on construction costs, such a simple pipe design could be useful considering its simplicity.

This chapter first exploited the possibility of experimentally using the corrugated pipe for an acoustic flow meter. The details of the experiments are presented in the next section, along with the proposed acoustic flowmeter prototype. Then the Unsteady Reynolds-Averaged Navier-Stokes (URANS) simulation with STAR-CCM+ v13.04.010, as a design and optimization tool, was also validated against the experimental data. The last section concludes with a summary of experimental and computational findings and then identifies future work.

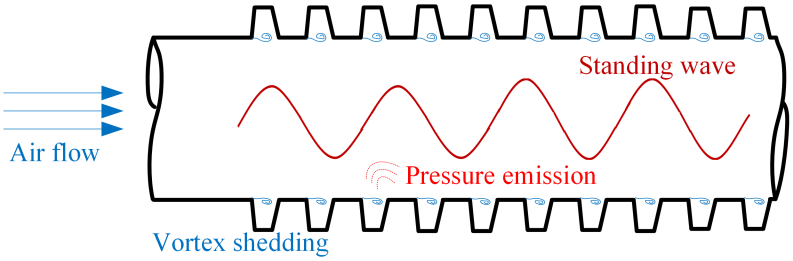

Figure 3.1: Demonstration of flow-acoustic interaction inside the corrugated pipe.

3.2 Experimental Investigation

3.2.1 Experimental Facility

An experimental facility was constructed as a starting point to understand the corrugated pipe's behavior. The sketch of the experimental setup is reported in Figure 3.2. The test facility was equipped with an air compressor that sent compressed air to the test section. A flow meter (ENDRESS+HAUSER PROMASS 63M) was installed to measure the flow rate and gas temperature between the air compressor and test section. The flow rate was changed by adjusting the valve before the flow meter. The end of the test section was open to the room environment. The sound signal was obtained from the miniDSP UMIK1 microphone (NATAL-MR-PN-8748133), which transferred the signal to the computer for analysis. In addition, an oscilloscope and a smartphone with an instant spectrum analysis application (dB meter) were utilized for the assistance of on-site spectrum visualization during experimental runs.

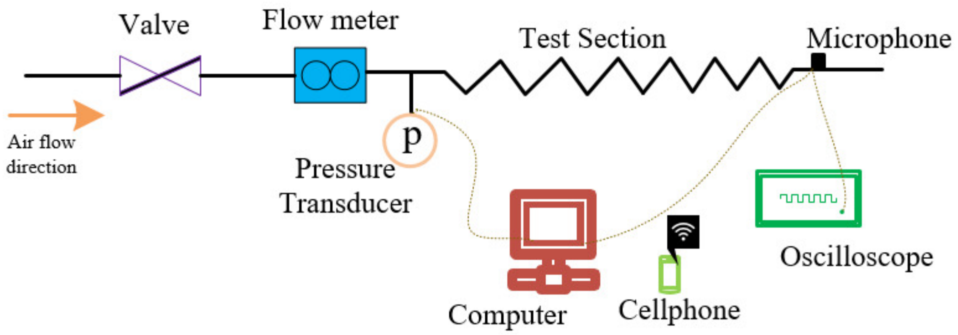

Figure 3.2: Sketch of the experimental setup.

A corrugated pipe with a length of 1194 mm was selected after a series of preliminary performance tests using various corrugated pipes. The tests have shown that longer pipes had clearer tonal sounds or characteristic frequencies than shorter pipes. The corrugated pipe was made of polyethylene and had a 25.4 mm outer diameter. Its cavity width and height were 2 mm and 1.7 mm, respectively, with a 4 mm pitch. Since the edge was too small to be measured, it was assumed to be a sharp edge. The test section consisted of a rigid PVC pipe with a 25.4 mm inner diameter containing the corrugated pipe inside to avoid bending and deformation. Photos of the corresponding geometry of the corrugated pipe are reported in Figure 3.3.

3.2.2 Steady-state Experiment on the Corrugated Pipe

The experimental campaign was conducted by adjusting the valve to control the mass flow rate. For each run, signals were recorded for 10 seconds after establishing stable flow conditions. A typical recorded signal and its frequency spectrum for flow rate $\dot{m} = 4.898 \times$

Figure 3.3: Snapshots of the corrugated pipe.

$10^{-3}\,kg/s$ is shown in Figure 3.4. The spectrum shows a single large peak frequency, f, of 1.420 kHz. The measurement uncertainty for the flow rate is LES s than 0.5%, according to the flow meter specification. Each measurement under the same flow rate was repeated three times to consider the influence of the gas temperature variation. Figure 3.5 demonstrates the obtained peak frequency versus flow rate relationship. The first flow rate recorded here corresponds to the first audible frequency, and the Reynolds number is estimated to be $Re = 10,055$. When the flow rate develops, the peak frequency does not increase smoothly. As shown in Figure 3.5, several plateaus are present. It is understandable if considering that as the velocity increases, the impingement of the vortex on edge is stronger, strengthening the emitted acoustic source, and thus providing enough energy for an acoustical wave to jump into the next level of pipe harmonics.

To design a flow meter, this non-monotonic relationship between flow rate and frequency needs to be eliminated later through optimization to achieve higher measurement resolution. Investigation to predict this frequency-jumping phenomenon in the corrugated pipe has led to various theories as summarized in Ref. [72]. In short, most of them related the jumping with the pipe harmonics. One of the often-used models from Ref. [76] formulated the frequency as

$$f_n = \frac{nc}{2L'} \frac{(1-M^2)}{1+\left(\frac{d_c}{R_{\text{int}}}\right)\left(\frac{l_c}{p_c}\right)\left(1+\frac{d_c}{2R_{\text{int}}}\right)}\,, \tag{3.1}$$

where n is the nth harmonic mode, c is the speed of sound, $L' = L + 1.2R_{int}$ with L the corrected tube length and R_{int} the internal radius of the tube. l_c is the length of corrugation, d_c is the depth of corrugation, p_c is the pitch of corrugation, M is the Mach number, respectively. It was proposed that if $M^2 \ll 1$, then Eq. (3.1) can be approximated as:

$$f_n = 0.89 \frac{nc}{2L'} \,. \tag{3.2}$$

Based on the formula in Eq. (3.2), the histogram for the peak frequency from the measurements is plotted and shown on the left of Figure 3.6. The frequency bins here have been selected corresponding to the nth modes. From the histogram, the first audible frequency locates in between the 8th and 9th modes. In addition, there is no frequency observed between the 12th and 13th modes as well as between 26th and 29th modes. A similar phenomenon was also reported in Ref. [77]. This discontinuity on the mode number here can signify that the proposed model needs further improvement, as the currently available models predict that the modes are continuous. However, the resolution in the plateau regions is of greater concern to develop a flow meter. What is optimistic here is that within the plateau, a slight increment of frequency is still happening, which is better illustrated by the plot on the right of Figure 3.6. It shows the gradient of peak frequency to the flow rate for the points only in the plateau regions. Even though the gradient does not maintain the same value as the flow rate increases, it is noticeable that the average of the gradient is around 19, as indicated by the horizontal line, and the gradient has been positive for all the measured points. This observation also qualitatively agrees with what has been reported in Ref. [78], Ref. [79] and Ref. [80].

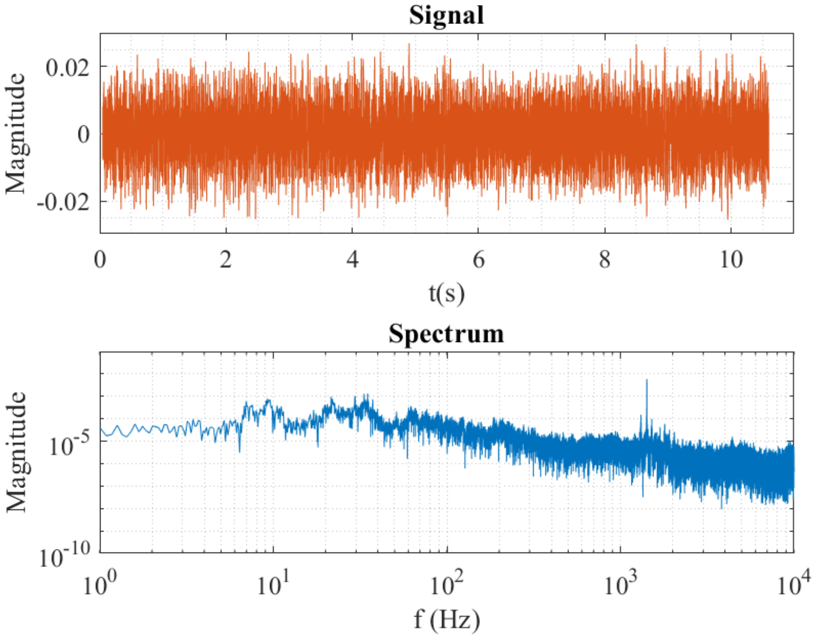

Figure 3.4: Signal and spectrum at $\dot{m} = 4.898 \times 10^{-3}\, kg/s$.

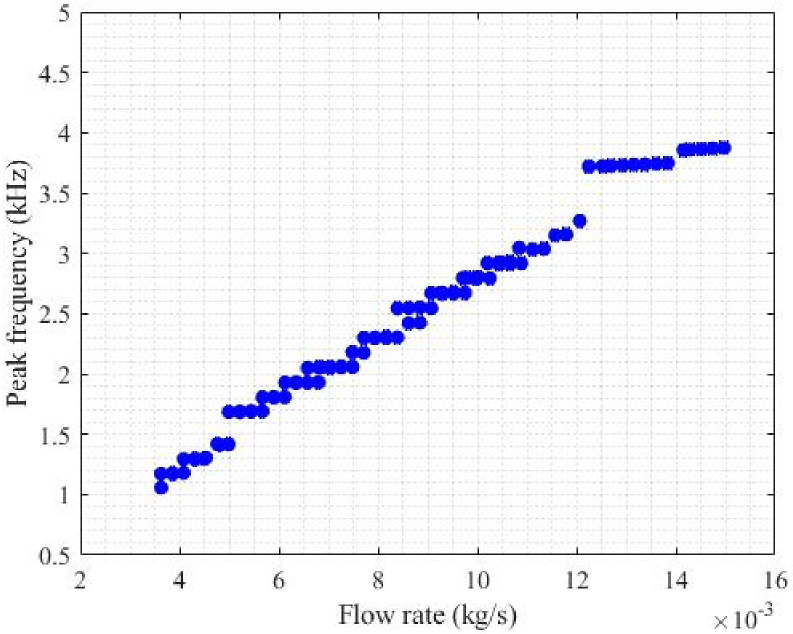

Figure 3.5: Peak frequency-flow rate relationship.

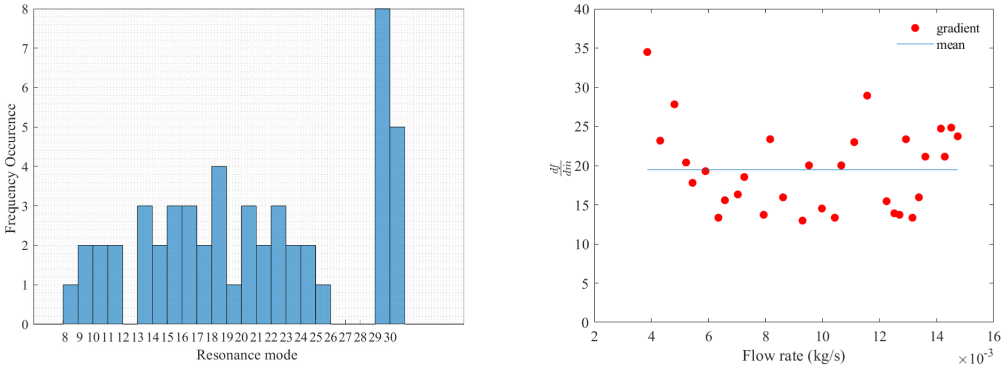

Figure 3.6: Histogram (left) and the gradient (right).

3.2.3 Transient Experiment on the Corrugated Pipe

To examine the transient acoustic-flow characteristics, we performed the experiment by continuously operating the valve to get the frequency spectrum. The sound signal was recorded for one minute with the growth of the flow rate. Then a short-time Fourier transform was adapted to analyze the signal. Figure 3.7 shows the sound signal in the frequency domain. Here, the increase in time corresponds to the growth of the flow rate. Like the steady-state experiment, though overall the peak frequency increases in time, plateaus still show up for specific periods (certain flow ranges). Besides, as can be observed from the spectrum, instead of having only a single dominant frequency at one flow rate, one or two higher mode frequencies also follow the same trend as the most dominant frequency. After around 0.9 minutes, the frequency remains the same magnitude, which is caused by the air supply reaching the maximum flow rate. The overall response of the corrugated pipe to flow change here made a good example of applying it to the transient scenario. As a closing mark, the observation has indicated a good flow-frequency response for the corrugated pipe. Yet, it is necessary to improve the resolution by either tuning the geometry parameters or combing the corrugated pipe with an additional setup.

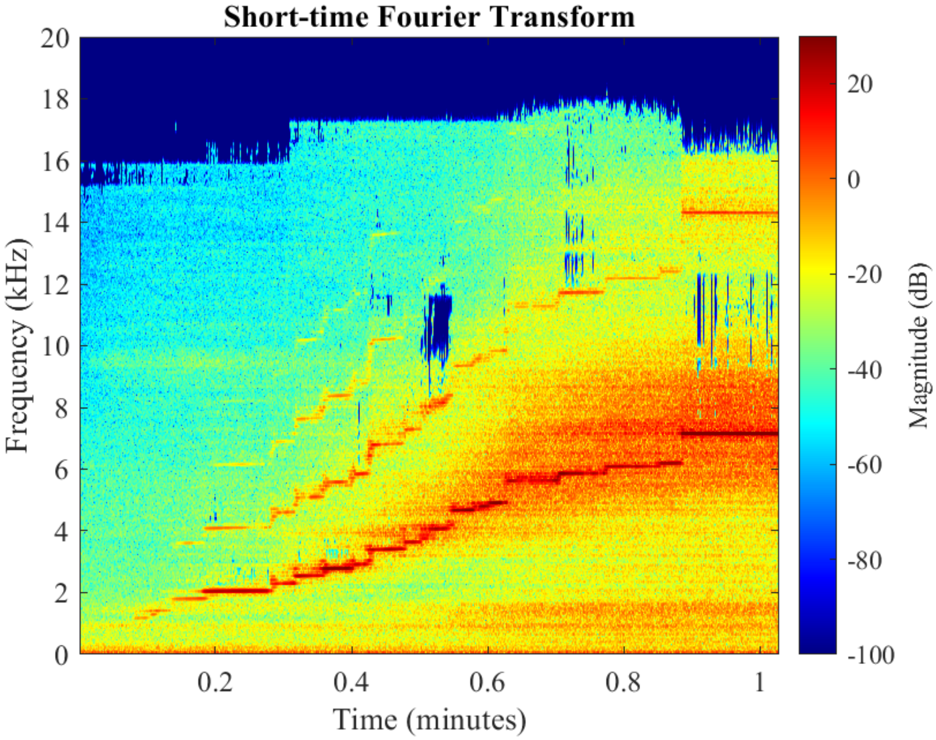

Figure 3.7: Full frequency spectrum.

3.2.4 Prototype of the Acoustic Flow Meter

According to Ref. [81], adding a smooth pipe upstream or downstream of the corrugated pipe will have a significant effect on the peak frequency. This phenomenon has also been discussed in Ref. [76] where the author found that a higher flow was required to initiate the whistle after adding a longer smooth pipe before the corrugated pipe, and no whistling would happen when the smooth front pipe was longer than 100 mm. To investigate the influence of the upstream and downstream extensions of the corrugated pipe on the whistling frequency, we connected a 787 mm smooth pipe with the same diameter to the exit of the corrugated pipe, then performed a set of runs for different flow rates. The comparison has shown a change in peak frequency due to the presence of the smooth pipe. The maximum relative change was about 7.7%. Though in Ref. [81], a more dramatic change has been observed.

The influence of the smooth pipe on the whistling can come from several factors. First, since the whistle is caused by the coupling between pipe acoustical resonance and vortex shedding, adding a longer tube will effectively increase the resonance length. On the other hand, this will also influence the velocity profile near the wall region. As vortex formation, shedding, and impinging on the edge of the cavity rely heavily on the velocity profiles, changing the velocity profile will alter the source strength, thus the whistle frequency. It then suggests separating the corrugated pipe from the piping system. A tube-in-tube configuration is thus proposed here as an optimization, as illustrated in Figure 3.8. The corrugated section needed to generate the acoustic wave is mounted inside the main circulation pipe. An undisturbed inlet will be established in this way, and the corrugated section (necessary to establish an acoustic wave) will be independent of the piping system.

To experimentally prove the feasibility of this tube-in-tube configuration, a straw-shaped corrugated pipe fixed with two holders was fit into a pipe with 25.4 mm outer diameter. Figure 3.9 shows snapshots of those components. The left photo shows the straw-shaped corrugated pipe, which was commercially available. It has a 10 mm inner diameter, and the total length is about 150 mm. The pitch is approximately 4.72 mm for the single cavity, and the height is about 1.5 mm. These dimensions were from a caliper with a resolution of 0.01 mm. The pipe with 25.4 mm outer diameter was used as the outer tube, and the corrugated pipe was mounted into the outer tube by using the 3D printed supports shown on the right of Figure 3.9. The whole piece together represents the very first design of the acoustic flow meter. Validation of the independence from the system for this geometry was accomplished through measurements with varying lengths of the upstream and downstream smooth pipes.

Two smooth pipes with a length of 1232 mm and 610 mm were selected to conduct the measurements. The first steady-state measurements were performed with the 1232 mm pipe upstream of the test section. The second set of measurements had the additional 610 mm pipe installed upstream. For the third set of measurements, the 610 mm pipe was then taken to the exit of the test section. Since the flow stability and room temperature were of significance to the measurement uncertainty, the first set of measurements was repeated six times on different days to yield an experimental uncertainty bar. Figure 3.10 presents the peak frequencies measured within a single plateau region for all three setups. The diamond symbol represents the first setup, and the square symbol represents the second setup, with the solid circle standing for the last design. It can be seen from the plot that the frequency grows with the increase in flow rate, and the measured data locates within the line bounds formed by the diamond symbols. Since the maximum relative variation in the bound is LES s than 1%, it concludes that this geometry has suitable system-independent property.

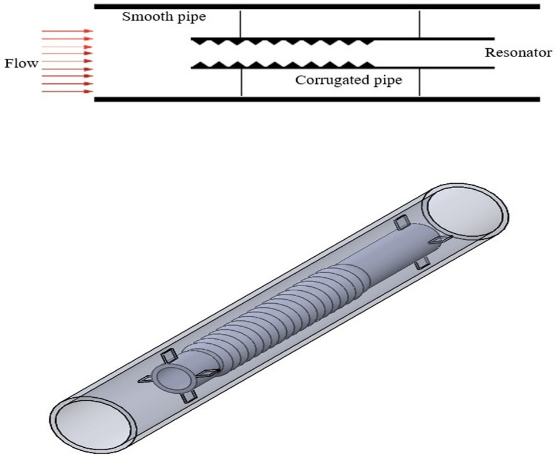

Figure 3.8: Sketch and 3D CAD model of the tube-in-tube configuration.

Figure 3.9: Snapshots of the original design of the acoustic meter.

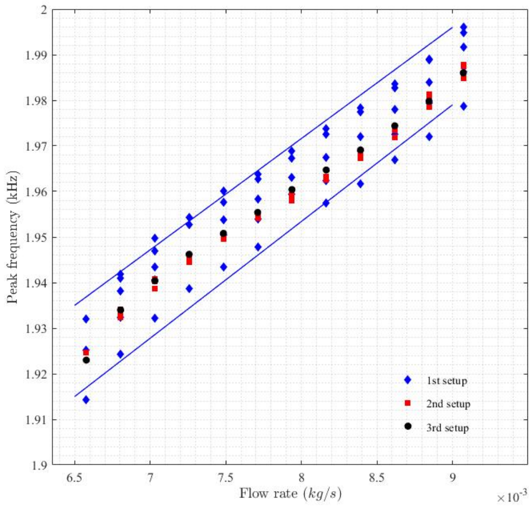

Figure 3.10: Experimental data for the prototype flow meter.

3.3 URANS Simulations of the Corrugated Pipe

To mature the design of the acoustic meter, a suitable tool is needed to optimize the frequency-flow relationship, such as removing the ”plateau.” Experiment investigation here becomes not as powerful as Computational Fluid Dynamics (CFD) simulations if considering the time, effort needed for manufacturing, and other factors. However, even though Large-Eddy Simulation (LES) often gives relatively high accuracy, as shown in Ref. [82] and Ref. [83], the time and computational resources that the LES simulation method often consumes make it expensive as a design tool during the preliminary design phase. Instead, the focus here is shifted to the URANS simulation.

Recently, modeling of friction loss in a corrugated pipe using RANS simulation was validated against empirical formulas, and experiments [84]. A hybrid computational aeroacoustic method was also reported in Ref. [85], where the SST $k-\omega$ model was combined with vortex sound theory to estimate acoustic source power from a single cavity in a pipe flow. Later, this method was modified for better prediction of the acoustic power [86]. There is currently no direct validation for URANS simulation on a full-length corrugated pipe. Thus, a CFD simulation of the flow in a corrugated pipe has been performed to investigate whether

URANS simulation can capture this whistling phenomenon.

3.3.1 Geometry, Boundaries, and Mesh

The corrugated pipe geometry provided in Ref. [82] was used for the simulation (see Figure 3.11 for the geometry specifications of the single cavity of the corrugated pipe). The diameter of the inner pipe was 25.4 mm. The depth and width of each cavity were 3.11 mm, and 4.68 mm, respectively. The pitch of the cavity was 5.3 mm, and the total pipe length was 614 mm. A total of 116 cavities were present in the corrugated section.

A 2-Dimensional (2D) axisymmetric computational domain was used to save computational resources, as shown in Figure 3.12. The inlet boundary condition was set as mass flow inlet, while the outlet was set as outlet boundary. The SST $k-\omega$ model was employed for the simulation. The case with an average inlet velocity equal to 18 m/s was selected since this case has also been simulated through LES simulation in Ref. [82]. The corresponding mass flow rate for this 2D model was estimated to be 0.00158 kg/s. The mesh convergence study was conducted for only ten corrugations by imposing periodic boundary conditions across the domain. Firstly, four steady-state cases with increased global mesh refinement were carried out. The base sizes for the four cases were $0.5mm, 0.25mm, 0.125mm$, and $0.0625mm$, respectively. Four line probes at different radial locations were used to monitor the axial pressure distribution. Figure 3.13 shows the pressure distribution along the axial direction at $y = 0.010\,\mathrm{m}$ and $y = 0.002\,\mathrm{m}$, respectively, with the original point on the inlet center axis. Good mesh convergence is observed. Since the acoustic modeling has a high demand on the mesh resolution, the finest mesh (case 4 with 0.0625 mm cell size) was selected for the follow-up simulation. In addition, since the edge area of the cavity is the source of pressure fluctuation, additional local refinement was implemented in the proximity of the cavities to have a high enough mesh cutoff frequency. The finalized mesh is presented in Figure 3.14.

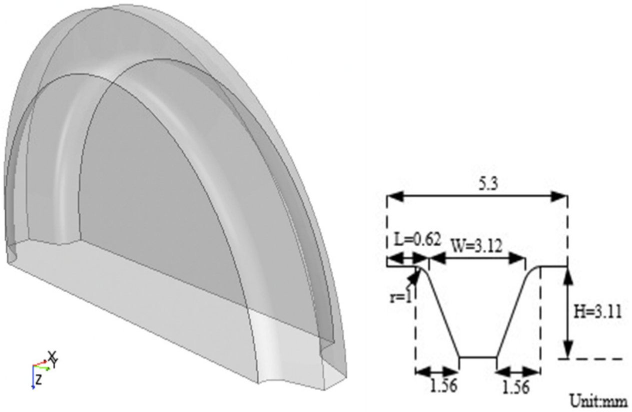

Figure 3.11: Single cavity geometry and its main parameters.

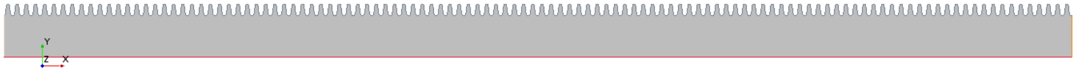

Figure 3.12: Computational domain and boundary conditions.

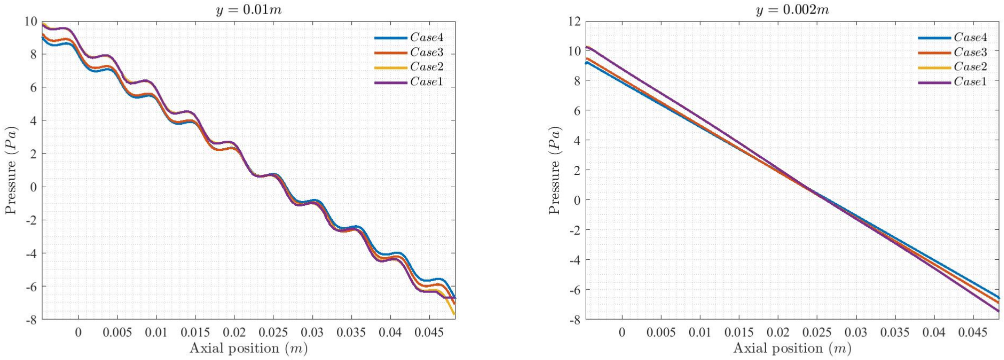

Figure 3.13: Mesh convergence study.

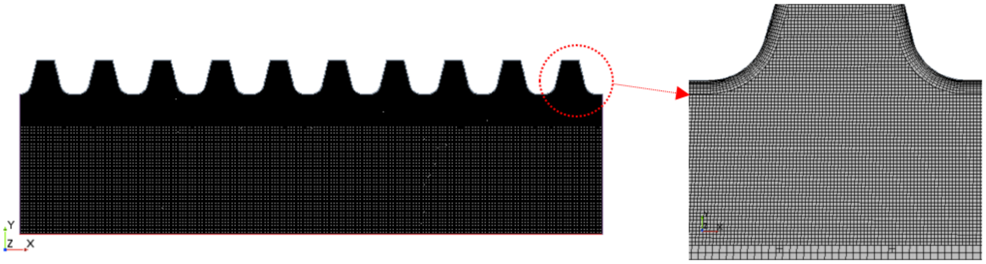

Figure 3.14: Snapshots of the mesh.

3.3.2 Transient Simulation and Results

The transient simulation was conducted with an interrogation time step of 10^{-6}s and a second-order scheme. Three point-probes were defined to monitor the pressure variation in the middle of the pipe ($y = 0.0137\,\text{m}$, $y = 0.0115\,\text{m}$, and $y = 0\,\text{m}$ respectively). In addition, the same line probes used for the mesh convergence study were used to show the axial pressure distributions at different radial locations. The simulation was run for 0.25 s. In Figure 3.15 the pressure contours and the pressure distributions along the pipe at three different times are reported. The evolution of pressure distribution indicates the periodical change of pressure within the corrugated pipe.

The time traces of the pressure at one of the probes are reported in Figure 3.16. A periodical pressure fluctuation can be observed. The frequency spectrum was obtained by using the fast Fourier transform analysis (see the right of Figure 3.16). The computed frequency peak is 1.678 kHz, which is smaller than the measured frequency in the experiment (1.978 kHz). But it is observed that this computed frequency lies between the sixth and seventh modes, and the measurement is on the eighth mode (see table in Ref. [82]). This preliminary case indicates that the simulation can capture the primary physical phenomenon well. In consideration of having the simulation more aligned with the actual facility reported in Ref. [82] and also avoiding the nonphysical inlet and outlet boundaries, two boxes were added to the pure corrugated geometry before further conducting the validation. The new simulation was then conducted with three different flow rates.

Figure 3.17 shows the pressure variation and frequency spectrum from the three new cases with slightly longer simulation time. It is observed that, for the new $U = 18\,\text{m/s}$ case, the spectrum shows two dominant frequencies (1.579 kHz and 1.811 kHz). The presence of the second dominance frequency hints that this velocity was in the transition of exciting flow into higher resonance mode. However, since the LES simulation given in Ref. [82] reported only one dominant frequency and the experiment also recorded the most dominant frequency, the comparison of this second peak is not feasible here. With the other two cases only having one dominant frequency (1.080 kHz and 0.830 kHz, respectively), the dominant frequency comparison is summarized in Table 3.1. The conclusion here is that the 2D URANS simulation can reproduce the velocity-frequency trend but tends to predict a lower frequency compared to LES simulation and experiments. This is expected as the 2D modeling plus the RANS averaging will underestimate the energy generated by the vorticity near the wall, thus providing a lower acoustical source.

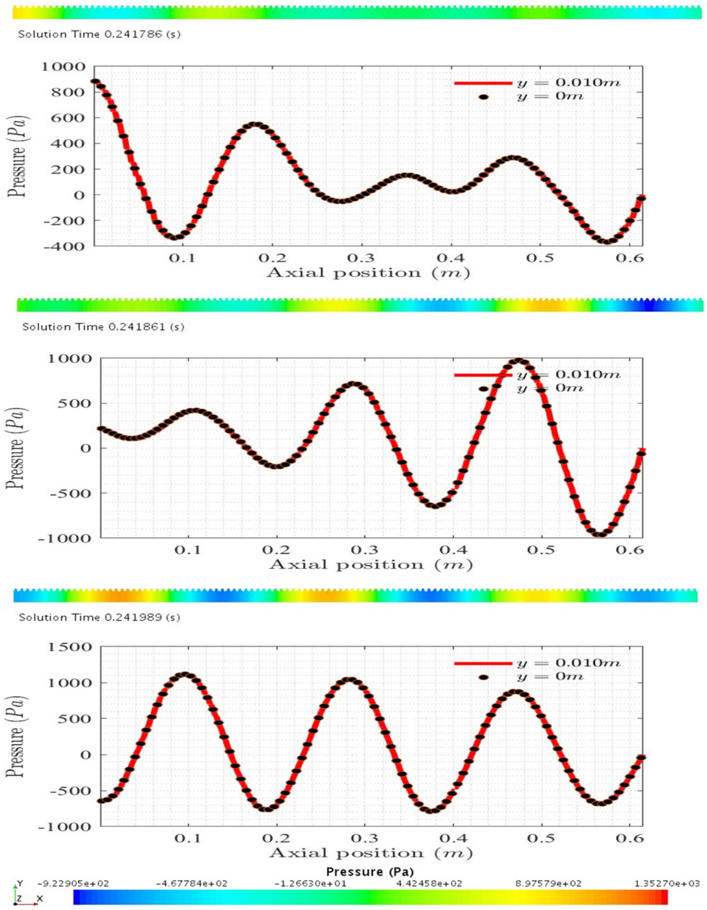

Figure 3.15: Pressure distribution along the pipe at three different times.

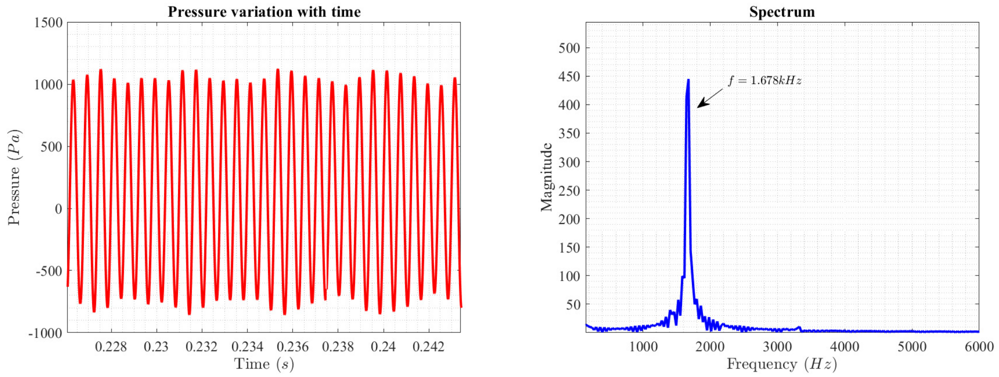

Figure 3.16: Pressure time trace and spectrum from one of the probes.

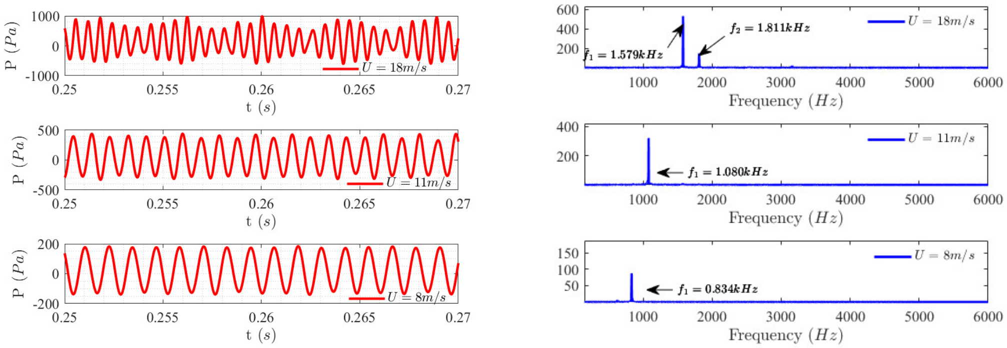

Figure 3.17: Velocity-frequency relationship.

Table 3.1: Comparison of the velocity-frequency relationship with literature.

Case	**URANS**(kHz)	**LES** (kHz) **[82]**	**EXP** (kHz)**[82]**
U=18m/s	1.579	1.978	1.968
U=11m/s	1.080	1.273	1.230
U=8m/s	0.830	0.980	0.990

3.4 URANS Simulations of the Prototype Geometry

Simulations of the proposed prototype flow meter have also been conducted to validate the model further. Figure 3.18 shows the modeled geometry and mesh. Note instead of modeling the whole tube-in-tube configuration, this simulation was only focused on the inner straw shape geometry. A 2D axisymmetric computational domain was meshed with a base size of 0.2mm and a local refinement at the cavity region. The transient simulations were for 0.3s with a time step size of $10^{-5}s$. Due to the simplification of the model, the mass flow rate for the inlet was calculated based on pressure and mass balance. The simulation results, in comparison with the experimental data, are summarized in Table 3.2. The results re-confirm that URANS generally underpredicts the frequency while showing a good velocity-frequency trend. Improving the accuracy of URANS simulation needs further exploration of the 3D model with various turbulence models. However, it can be concluded that URANS simulation can capture the main physical phenomenon of whistling in the corrugated pipe.

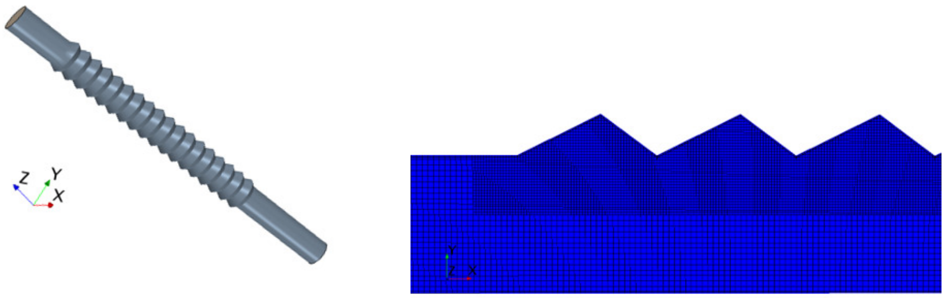

Figure 3.18: Geometry and mesh for the prototype flowmeter design.

Table 3.2: Comparison of the velocity-frequency relationship with experimental data.

Flow rate ($10^{-3} kg/s$)	**URANSfrequency** (kHz)	**EXP frequency** (kHz)
6.80	1.668	1.942
7.26	1.684	1.954
7.70	1.692	1.964
8.15	1.708	1.974
8.61	1.744	1.984
9.06	1.766	1.995

3.5 Conclusions and Outlook

A system based on corrugated pipes has been considered a potential candidate for designing an acoustic flow meter for high-temperature gas-cooled reactors. Preliminary experiments and simulations have been carried out to explore the viability of such a system. This experimental study has shown that the peak frequency of the acoustic wave emitted by the pipe increases with the airflow rate, but not monotonically, as there are specific flow rate ranges in which the frequency presents plateaus. In addition, it has also been confirmed that adding a smooth pipe downstream or upstream of the corrugated section will cause a shift in the acoustic wave frequency under the same air flow rate conditions. A prototype of the acoustic flow meter thus has been proposed based on the experimental observations. In addition, URANS simulation has been validated against experimental data as well as LES simulations. It has been shown that URANS simulation has successfully captured the physics of whistling and showed a good velocity-frequency dependence. However, simulation accuracy needs further improvement as it tends to underpredict the peak frequency. Future work will focus on a more systematic experimental campaign and optimize the flow meter geometry to improve its low-frequency response. In addition, attention will be paid to seeking possibilities using machine learning to predict the flow rate based on the frequency spectrum rather than peak frequency.

CHAPTER IV

Mixing in Large Enclosures: Overview

4.1 Introduction

Accurately predicting mixing in the upper plenum of HTGR is important to assess reactor safety during LOFC accident scenarios. The mixing phenomenon in the upper plenum has long been a challenge for existing system-level codes due to deficiencies in the three-dimensional closure models, approximations in the numerical solutions, nodalization effects, and imperfect knowledge of boundary and initial conditions [87]. As for CFD codes, RANS modeling is widely used for industrial applications, but the performance and accuracy of RANS models has to be assessed for the particular physics under investigation. Previous research has shown room for improvement in CFD RANS prediction of jet spreading and impingement, recirculation, buoyant flows, and thermal stratification [88] [89] [90]. More spatially-resolved CFD methods like Large Eddy Simulation (LES) are often too computationally expensive for industrial applications. Therefore, it is essential to develop advanced and efficient analysis codes to improve the accuracy of reactor safety analyses and reduce modeling uncertainties.

Mixing in large enclosures has been challenging for several other advanced reactor designs. This is why, under the NEAM IRP project [8], entitled "Center of Excellence for Thermal-Fluids Applications in Nuclear Energy: Establishing the knowledge base for thermal-hydraulic multiscale simulation to accelerate the deployment of advanced reactors – IRP-NEAMS-1.1:

Thermal-Fluids Applications in Nuclear Energy," mixing in large enclosures has been identified as one of the four industrially driven challenging problems, as shown in Figure 4.1.

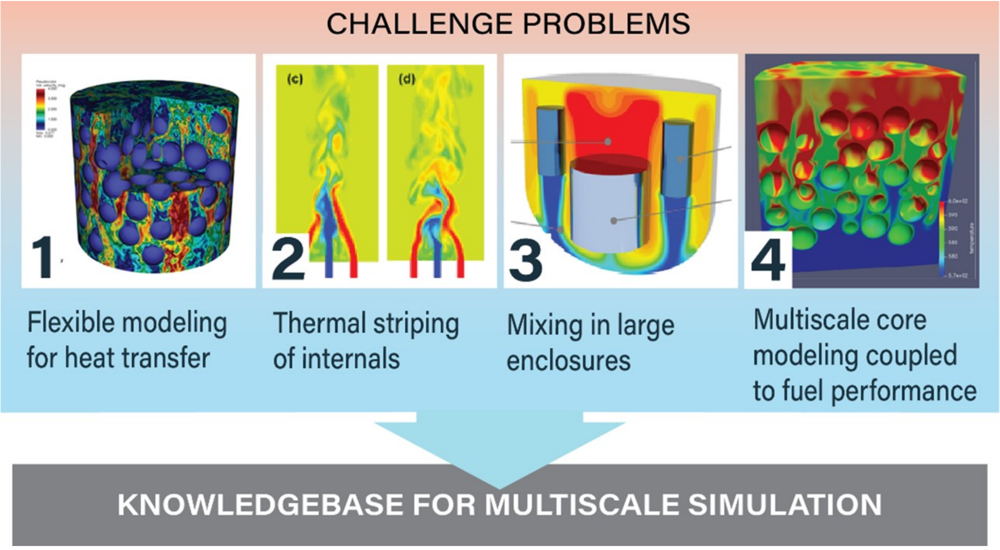

Figure 4.1: Identified four challenge problems under the NEAM IRP project [8].

The Working Package 3 (CP3) [9] of this project aims to develop a multi-fidelity (multi-scale) set of models for mixing in large enclosures. Given the complexity of this phenomenon, the project has proceeded with a hierarchical modeling framework that breaks down the reactor-system level physics into multiple levels of sub-physics problems targeting specific physics and interactions, as shown in Figure 4.2. The hierarchical approach aims to ensure model robustness by relying on unit physics and sub-system level validation exercises. The work scope has, therefore, been split into two categories: one focusing on the interaction of single/multiple jets in a plenum and another focusing on thermal stratification. For each research category, it is proposed to use the results of high-resolution experiments and LES/DNS in combination with machine learning techniques to inform the development of lower-fidelity models.

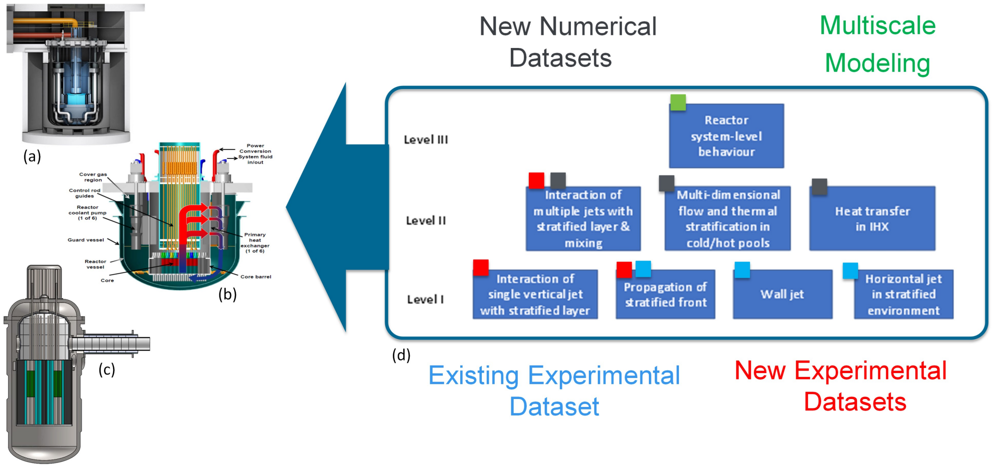

Figure 4.2: IRP CP3 hierarchical approach for data-driven model development [9].

4.2 Background on mixing in large enclosures

As several processes are involved in jet interactions in large enclosures, a progressive review of the individual fundamental flow dynamics with increased complexity will assist in understanding the overall mixing process. The most fundamental phenomenon decomposed from large enclosure mixing may begin with single jet impingement into the top wall.

Since jet impingement is frequently used in the industry for cooling, drying, annealing, and tempering, it has been an area of interest for extensive research efforts. Several review papers have documented this topic in detail, e.g., [91], [92]. For a single jet impingement into a surface (flat or curved), the flow structure is often categorized into three distinct flow regions: *free jet region*, *stagnation flow region*, and *wall jet region*, as shown in Figure 4.3. Various parameters are decisive to characterize the flow features such as the Reynolds number, the nozzle to plate distance, the inlet velocity profile, and the turbulence intensity.

The jet emanating from the inlet has a velocity and temperature profile determined by the upstream flow and the inlet geometry. Flat velocity profiles with less turbulence are created with a slot shape or a contraction nozzle. In contrast, parabolic velocity profiles with moderate turbulence are seen for the pipe-shaped nozzle [93] [94]. Experimental study of a confined impinging water jet in Ref. [95] suggests that the nozzle exit velocity profile

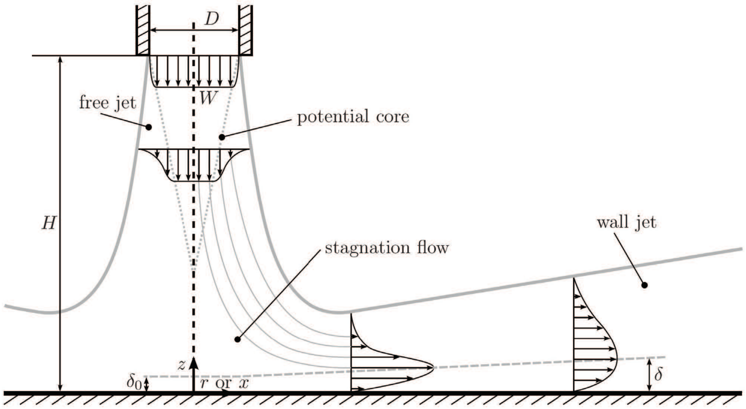

Figure 4.3: Flow regions of a single impinging jet, reprinted from [10].

is strongly influenced by the fluid dynamics in the stagnation zone at confinement heights between $0 < H/D < 1$.

The free jet region is defined as the region where the emerging jet is sufficiently far from the impingement surface that the flow is unaffected by the impingement. This region may not exist if the inlet/surface spacing is less than two diameters, when the elevated static pressure in the stagnation region influences the flow immediately at the nozzle exit. However, if a sufficient distance is allowed, three distinct sub-zones can be identified in the free jet. First, a potential core zone is present, characterized by the fact that the average velocity equals the inlet velocity. After the potential core region, the axial velocity decays quickly, and turbulence intensity increases because of entrainment of the surrounding fluid in the transition zone. A fully-developed region will be finally reached (after 25 jet diameters) where both the first- and second-order statistics become self-similar [96]. In the stagnation region, flow is strongly affected by the wall. The streamwise momentum diminishes dramatically while the horizontal momentum increases as the flow divert. Static pressure rises as well in this region, and according to [10] this region generally has a distance of approximately 1.2 jet diameters from the wall surface. After the flow impingement, the flow behaves as in the wall jet region where the bulk fluid moves laterally outward parallel to the wall.

Impinging jets on curved surfaces are less investigated in terms of heat transfer and main flow parameters compared to flat-plate configurations [97] [98]. The flow structure for a jet impinging on a concave surface is shown in Figure 4.4. A so-called *Taylor-Görtler* vortex that enhances momentum and energy transfer on the surface is produced by the centripetal force due to surface curvature [99]. Most studies on curved surfaces mainly focused on heat and/or mass transfer measurements, while flow field data were seldom mentioned [100]. Cornaro et al. [101] provided visualization of a round jet impinging on cylindrical surfaces. The effects of nozzle-to-surface spacing, surface curvature, and Reynolds number on vortex development have been investigated using the smoke wire flow visualization technique. Choi et al. [102] provided flow field measurements for jet impingement cooling on a semicircular concave surface using a Laser Doppler Anemometer.

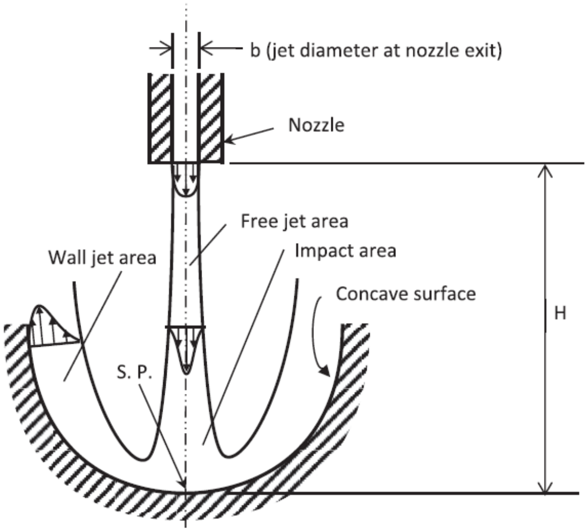

Figure 4.4: Single impinging jet onto a concave surface, reprinted from [11].

When the jet is issued into a confined space, the same regions described for single jet impingement still exist, as shown in Figure 4.5. The difference is that a counter-rotating vortex pair will be present when the wall jet turns back toward the confined wall [91]. According to flow visualization studies in [103, 104], the center of the vortex tends to move away from the jet center, and more quiescent fluid will be entrained into the confined region when the Reynolds number, inlet diameter, and nozzle-to-surface distance increase.

A more complex flow structure is present for a system of multiple impinging jets in a confined space, primarily because of the consequential interactions between jets. Interactions

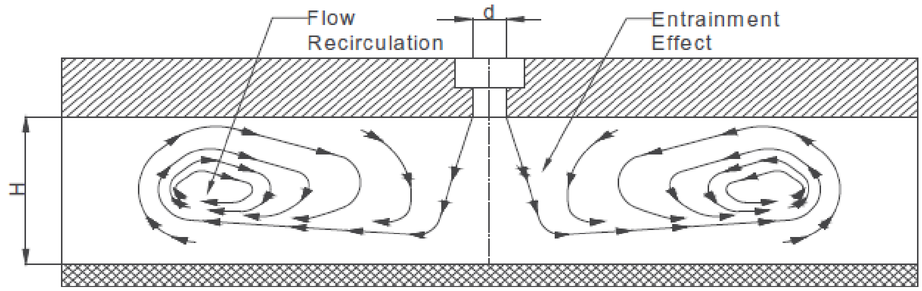

Figure 4.5: Recirculation from confined impinging jet, reprinted from [12].

between twin impinging jets are sketched in Figure 4.6. When the jet spacing is small and the inlet/surface spacing is large, the inference first happens between the shear layers after jets are issued from the inlets. Secondly, the vortex pairs from the post-impingement flow interact with each other between the jet spacing, from which a 'fountain effect' will be formed. The interaction between the fountain and the two jets was found to increase with decreasing jet spacing, according to flow visualizations of multiple jet impingement reported in [105].

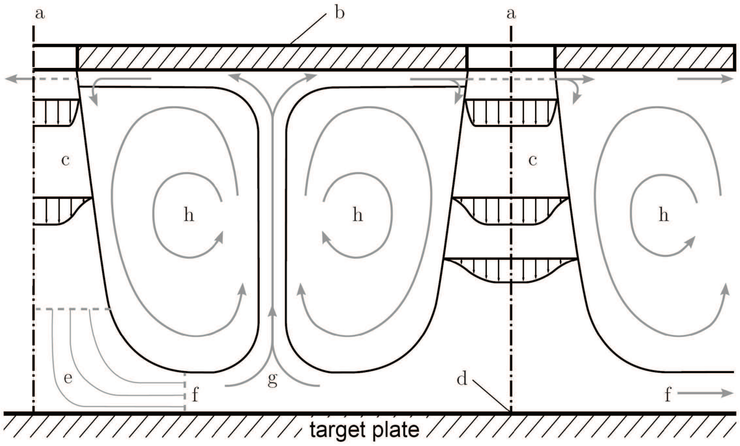

Figure 4.6: Schematic illustration of twin-jet impingement flow, reprinted from [13].

In addition, the post-impingement flow (also known as "spent air" in the cooling industry), tends to accumulate in the confined space, depending on the exit configuration. An accumulated crossflow will be generated, and the strength of the crossflow is determined by the path of the "spent air." Significant jet deflection will happen because of the crossflow mass flux [106].

Even though the physics of jet flows has been well investigated in the literature, there is a lack of high-resolution experimental data that can be used for comprehensive validation of CFD models. A non-exhaustive summary of the experimental investigations with available flow data can be found in Tables 4.1-4.3. Most available experimental investigations on jets flows rely on the Hot Wire Anemometer Probe (HWAP) or Laser Doppler Velocimetry (LDV), which are point-wise measurements. Such experiments have provided valuable data, including one-dimensional velocity profiles and lumped heat transfer coefficients, for validating turbulence models [93]. Nevertheless, the underlying reasons for the model discrepancy are rarely revealed as limited by the available flow field information.

In support of model development and validation, high-resolution experimental data with well-controlled boundary conditions are required. Mixing in large enclosures is of interest in the nuclear field for normal or accidental conditions of various reactor types. Examples include, among others, the occurrence of steam jets into the containment after a main steam line break in light water reactors [107], steam condensation and mixing in the suppression pool and isolation condenser pool of Gen-III+ designs like for the Economic Simplified Boiling Water Reactor (ESBWR) [108], and thermal mixing in the lower plenum of HTGRs [109]. Several past experiments have focused on the phenomenon of mixing in large enclosures for specific reactor designs or reactor safety systems. For example, an experimental study of gas mixing processes and heat transfer augmentation by a forced jet in a large cylindrical enclosure with an isothermal bottom heating/cooling surface for the AP-600 reactor containment design can be found in [110]; experiments on the PANDA facility conducted at the Paul Scherrer Institut (PSI) have studied buoyant jets with horizontal injection into large containment [111] for LWRs applications; reference [112] provided scaled-down experimental facility designs for reactor lower and upper plenums that aimed to study the flow mixing of a Pressurized conduction Cooldown (PCC) scenario. Researchers at Texas A& M University have performed flow experiments in a facility representing the core and upper plenum of the

Modular HTGR design [35], which is most related to the work presented in this dissertation. The Particle Image Velocimetry (PIV) technique was used to study single jet and plume injection while measuring velocity fields under various Reynolds numbers. In general, it is found that previous studies focused on relatively high Reynolds numbers. Most of the existing experiments are also mostly focused on the thermal effects, and detailed investigations are missing with regard to the velocity field and the turbulent parameters that play a vital role in the mixing process, as well as in validating turbulence models.

Table 4.1: Experimental data reported in the literature for free impinging jet on flat surfaces.

Literature	Nozzle	$\mathrm{Re}\times10^{-3}$	H/D	Technique	region
Cooper et al. [100]	pipe	$23, 70$	$2, 4, 6, 10$	HWP	free jet, wall jet
Yao et al. [113]	pipe	10	9	HWP	free-jet, wall jet
Kim [114]	pipe	$30, 40, 50$	$2, 4, 6, 8, \infty$	SFHP	all three regions
Tummers et al. [115]	pipe	23	2	LDV , PIV	stagnation, wall jet
El Hassan et al. [116]	pipe	$1.26, 2.45$	2	LDV	free jet, wall jet
Meslem et al. [117]	orifice	1.36	4.5	PIV	free jet, wall jet

Table 4.2: Experimental data reported in the literature for jet impinging on concave surface.

Literature	Nozzle	Re	H/D	Technique	region
Choi et al. [102]	pipe	$47, 100$	2	LDV	centerline

Table 4.3: Experimental data reported in the literature for confined impinging jet.

Literature	Nozzle	Re	surface	H/D	Technique
Loureiro and Silva Freire [118]	pipe	$47, 100$	flat	2	LDV
Guo et al. [119]	orifice	$1000 - 9000$	flat	$2, 4, 8$	SPIV
Baydar and Ozmen [120]	round nozzle	$30,000 - 50,000$	flat	$0.2 - 6$	HWA

4.3 Background on thermal stratification

Thermal stratification occurs when two types of streams with different temperatures come into contact and establish a temperature gradient [121, 122]. Two representative examples of thermal stratification are shown in Figure 4.7. For both examples, fluid with high temperature T_2 is in contact with fluid with a lower temperature T_1; in between the two fluids, a layer with a temperature gradient is present.

(a) Example of sharp stratification (b) Example of smooth stratification

Figure 4.7: Examples of stratification with different gradients. Note the black line does not reflect the real temperature distribution in the layers.

In the HTGR design, during loss of forced circulation events, stratification is layered with the hottest gases (lowest density) residing adjacent to the ceiling of the upper plenum [3, 34]. The thermal stratification phenomenon is also relevant in several other reactor designs and is particularly important in pool-type Sodium-cooled Fast Reactor (SFR) and in the water pools that are part of Gen III/III+ passive safety systems. In the pool-type SFR design, a reactor trip with a postulated loss of flow event would cause stratification to form in the upper plenum [123]. In the protected loss of flow scenario, colder sodium coolant rising from the core into the hotter fluid in the upper plenum would lead to thermally stratified layers forming between the core and the inlet to the intermediate heat exchanger. In the unprotected loss of flow scenario where the reactor does not scram successfully, hotter sodium coolant would rise from the core into the colder fluid in the upper plenum instead [124]. Research also indicates that significant thermal stratification is likely to exist after the steam blowdown in the suppression pool of BWRs [125].

Even though stratification phenomena have been shown to considerably increase the performance of the Thermal Energy Storage (TES) of a solar heating system [126], it is a great safety concern in nuclear reactors. Depending on the specific scenarios, the presence of thermal stratification in reactor components could lead to non-appreciable mixing, undesired thermal loading on structures, and possibly block the natural circulation path. As a result, thermal stratification has been of great research interest in the nuclear field. Two review papers that summarize experimental and numerical methods for thermal stratification can be found in [122, 127]. It is found that even though previous work has laid an extensive knowledge base on density stratification, access to high-resolution experimental data on stratification for the validation of CFD models remains scarce [37].

4.4 Construction of Validation Experiments

As research efforts are undertaken to advance the understanding of this mixing phenomenon, this thesis aims to support the further validation and development of CFD models to enhance the prediction of multi-jet mixing in large enclosures [128, 129, 36, 130] and stratification [131, 15, 16] with high-resolution experiments under the IRP CP3 project. Following the proposed work scope of the IRP CP3 project, this thesis includes two separate effect facilities that are used to provide high-resolution validation experiments for mixing in large enclosures. The MiGaDome facility, a 1/12th scaled representation of the Modular HTGR upper plenum, is used to study single/multiple jets in the plenum. The HiRJet facility is used to study the thermal stratification phenomenon.

For the MiGaDome facility, high-resolution two-dimensional velocity and turbulent statistics fields suitable for developing a multi-fidelity (multi-scale) set of models for mixing in large enclosures have been provided by utilizing the means of the Particle Image Velocimetry (PIV) technique. For the HiRJet facility, with the aid of the advanced Wire-Mesh Sensor (WMS) technique, the time-dependent density distribution on a 2D plane in the test section has been captured with high spatial and high temporal resolution. The experimental campaign aims to establish a high-resolution database to characterize stratified front propagation at medium Reynolds numbers and validate numerical simulations. The two experimental facilities will be introduced in the next section.

4.5 Separate-Effect Experimental Facilities

4.5.1 Michigan Multi-jet Gas-mixing Dome (MiGaDome) Facility

The Michigan Multi-jet Gas-mixture Dome (MiGaDome) facility was designed and built in the Experimental and Computational Multiphase Flow Laboratory (ECMFL) at the University of Michigan, based on the model that was geometrically scaled down from the Modular HTGR upper plenum with a length ratio of 1/12. Figure 4.8 shows the full view of the facility.

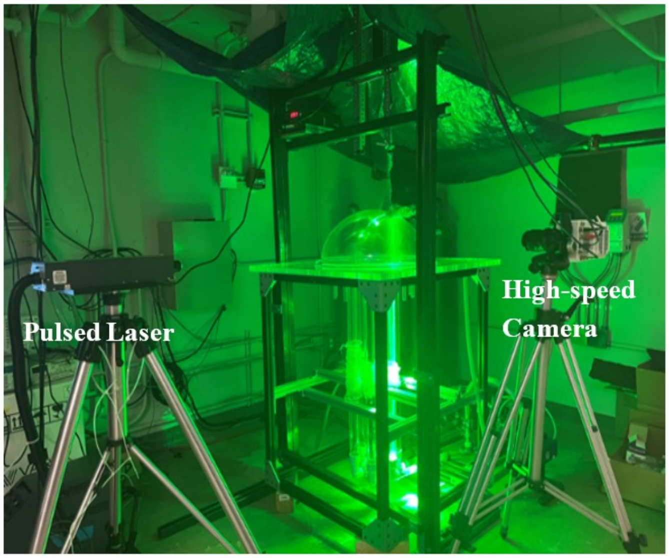

Figure 4.8: Full view of the MiGaDome facility.

The CAD and the dimensions of the test section are shown in Figure 4.9. Six inlets of $44.45mm$ inner diameter simulating the coolant channels in 66 fuel blocks of the prototype reactor are designed to maintain the hexagonal array pattern and the flow area ratio. The 12 outlets of $12.7mm$ inner diameter, modeling the gaps in the Modular HTGRs, are in the periphery region. The locations of inlets and outlets were determined based on the effective diameter of the active core. A transparent dome as the enclosure represents the upper plenum thermal protection. As determined by the scaling analysis, the inner diameter of the clear dome is 495.3mm, while the inner height of the dome is 228.6mm. More details about the scaling analysis can be found in [132]. On the upstream of inlets, 909.32mm long straight pipes are connected to develop the flow.

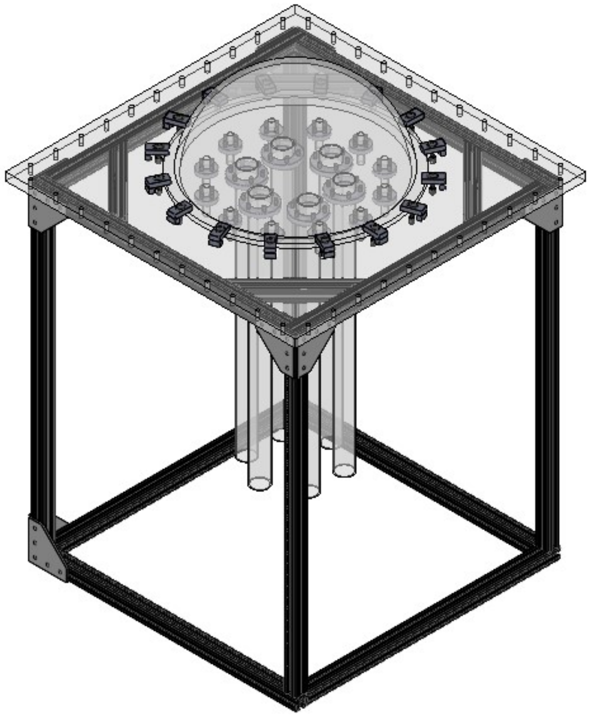

(a) CAD of the test section.

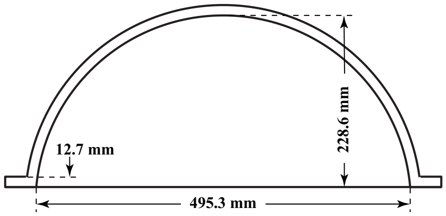

(b) Dome dimensions (mm).

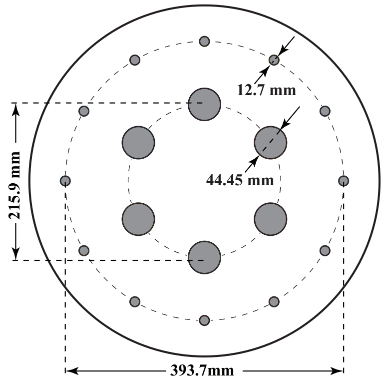

(c) Inlets/outlets dimensions (mm).

Figure 4.9: CAD of the test section and its related dimensions.

Figure 4.10 shows the gas supply system for the facility. Each inlet branch has been equipped with a K-type thermocouple and a pressure transducer to monitor the inlet temperature and pressure. In addition, six mass flow controllers (ALICAT MCR Series) are connected to the flow branches to control the mass flow rate, which provides flexibility for studying various jet injection patterns.

The flow field in the test section is captured using a 2D Particle Image Velocimetry (PIV) system. Application of PIV measurement to the gas flow has been successfully demonstrated

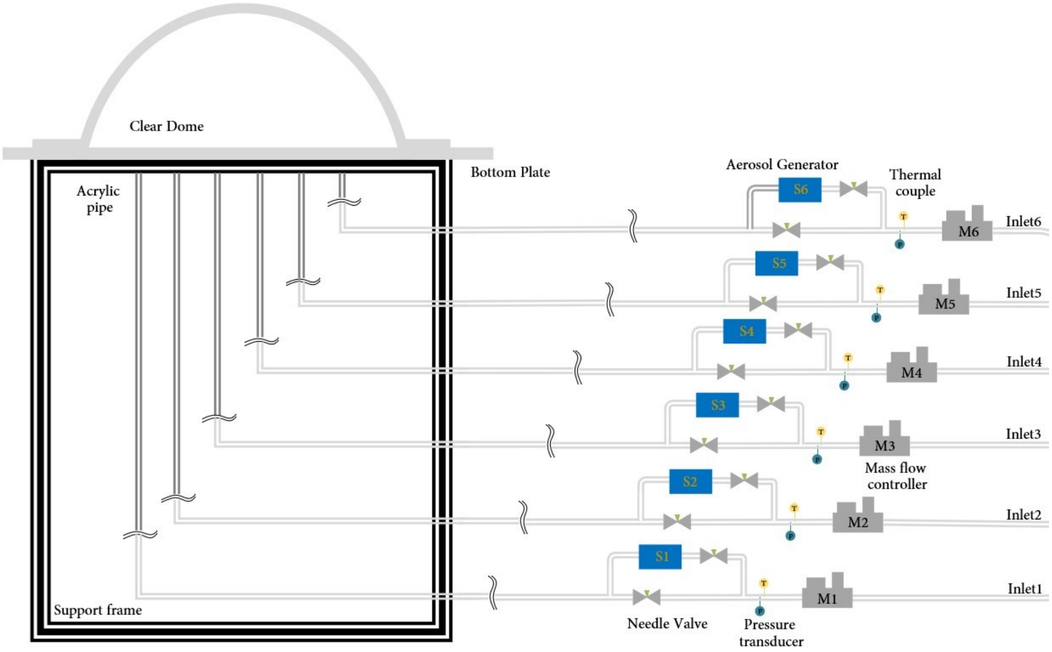

Figure 4.10: Schematic of the gas supply for the MiGaDome facility.

in Ref. [133, 134, 135]. Laser Dopper Velocimetry (LDV) is also utilized to monitor velocity profiles at the inlet boundary. The 2D PIV system uses a high-speed 4MP CMOS camera (Phantom VEO 440L), with 10μm pixel size, 12-bit depth, and up to 1100fps at full resolution. The CMOS camera imagines the field of interest from the side with the tripod support, as shown in Figure 4.8. A Scheimpflug adaptor is mounted between the lens and the camera to facilitate better imaging. A New Wave Research 532nm Nd: YAG double-pulsed laser (Solo III-15) has also been deployed to illuminate the flow field. Synchronization between the camera and the pulsed laser is established through the BNC 555 Pulse/Delay generator, which has eight signal channels and functions as a master clock. The Laskin nozzle aerosol generator from LaVision that generates a polydisperse aerosol in the sub-micrometer range creates seeding particles. The tracing particles are generated using the Di-Ethyl-Hexyl-Sebacate (DEHS) liquid, which is non-toxic, offers good light scattering, and evaporates over time. The scaling and calibration of the raw images are achieved by using a calibration target with a grid of equidistant marks. Finally, the PIV data is processed using LaVision DaVis software.

The Artium Technologies LDV system consists of a transmitter, a receiver probe, a processing engine set, and burst processor acquisition manager software. The wavelength of the LDV laser is 532nm, and the formed fringe spacing is 2.6μm. In the measurement, the probe can be placed at different axial locations and move along the radial direction in 0.1mm increments across the pipe's inner diameter with the support of the translation stages. Figure 4.11 shows the setup of the two optical systems.

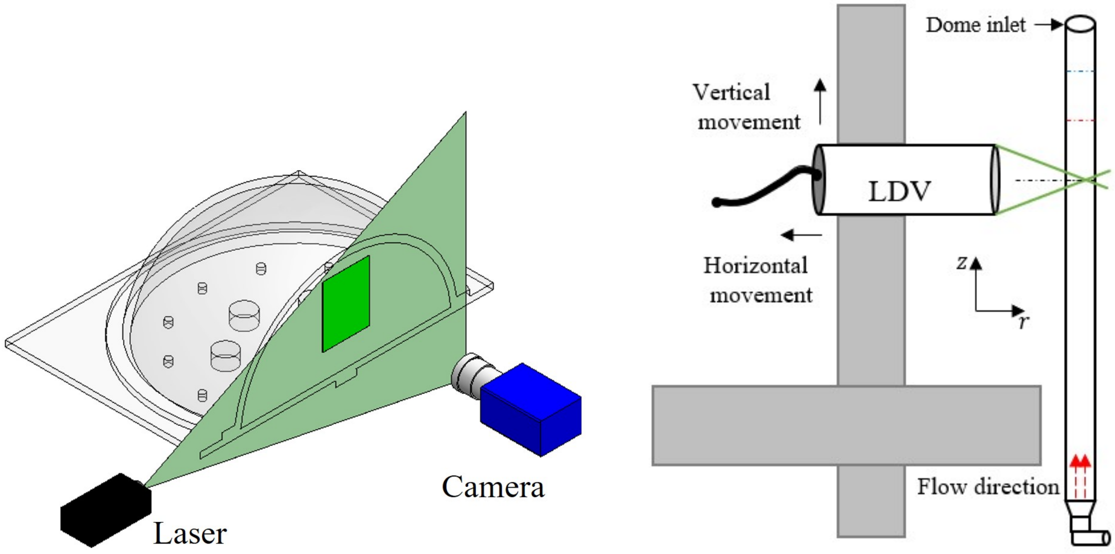

(a) PIV (b) LDV

Figure 4.11: Demonstation of the measurement systems.

4.5.2 High-Resolution Jet (HiRJet) Facility

The HiRJet facility, depicted in Figure 4.12, was established at the University of Michigan to investigate stratified fronts at intermediate Reynolds numbers [136]. The setup includes an acrylic tank (58.42 cm x 60.96 cm x 60.96 cm) with six nozzles (38 mm inner diameter), three on each side. Connected by 1.8 m long pipes, these nozzles serve as inlets or outlets. In this study, the middle side nozzle is the inlet, and the bottom nozzle serves as the outlet, with other nozzles sealed during experiments. For more details, see Ref. [136, 90]. The HiRJet facility has undergone enhancements following the findings of [90]. Notably, the tank has been reconstructed with a sealed lid, ensuring a consistent water level. Additionally, the large WMS has been substituted with a newly designed (64x16) configuration to mitigate noise and overshoot. Furthermore, a small WMS has been introduced at the tank outlet to monitor outlet boundary conditions. Dr. Vineet Vishwakarma spearheaded these updates and conducted the corresponding measurements. This section revisits the experimental facility to provide the reader with a comprehensive understanding of the experimental setup and measurement techniques.

To create a stratified environment, two fluids with different densities were used in the experiment instead of using heating elements as in [137, 138, 139]. With this approach, heat losses can be avoided, and the facility does not need to be insulated, which allows the use of optical measurement techniques as well and eliminate the uncertainties associated with heat losses estimations. The tank was pre-filled with a fluid with a given density, while a second fluid with a different density was injected from the side nozzle into the tank. Depending on the density difference between injection and tank fluid, an upper-directed plume or a lower-directed plume develops in the tank. In both cases, a propagating stratified front develops in the vertical direction.

The stratified front propagation was monitored using a WMS system, relying on the fluid's local electrical conductivity. This system provides a 2D density distribution with a spatial resolution of 8.1 mm and a frequency of 100 Hz. The large WMS inside the tank (in blue) recorded density distribution on a 2D plane, positioned 285 mm off the jet centerline to minimize disturbance. A smaller WMS (in green), located 202.7 mm upstream of the inlet, monitored inlet density. These sensors are referred to as the ”large WMS” and the ”inlet WMS”. The inlet flow rate was measured with a Coriolis flow meter, and a Laser Doppler Velocimetry (LDV) system was employed to measure velocity in the acrylic pipe section upstream of the inlet WMS.

Tap water and sugar solution were selected as the two working fluids in the experiment, and the density difference was created by varying the sugar concentration. The densities

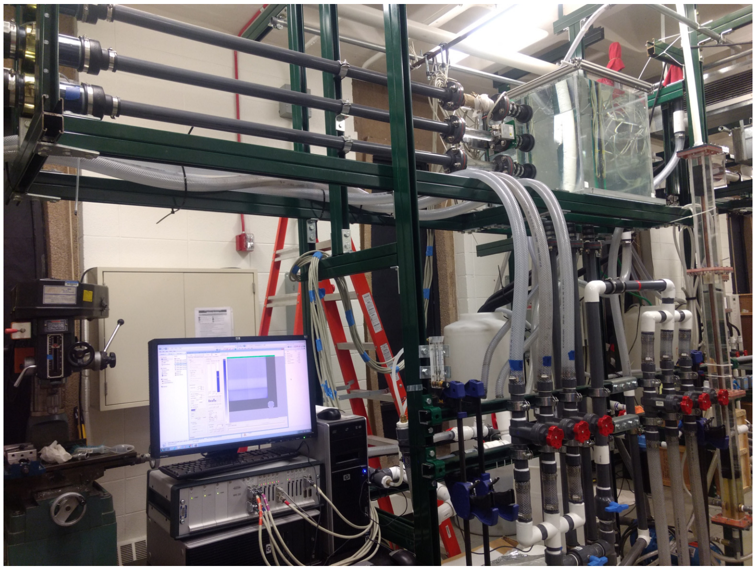

(a) Full view of the HiRJet facility

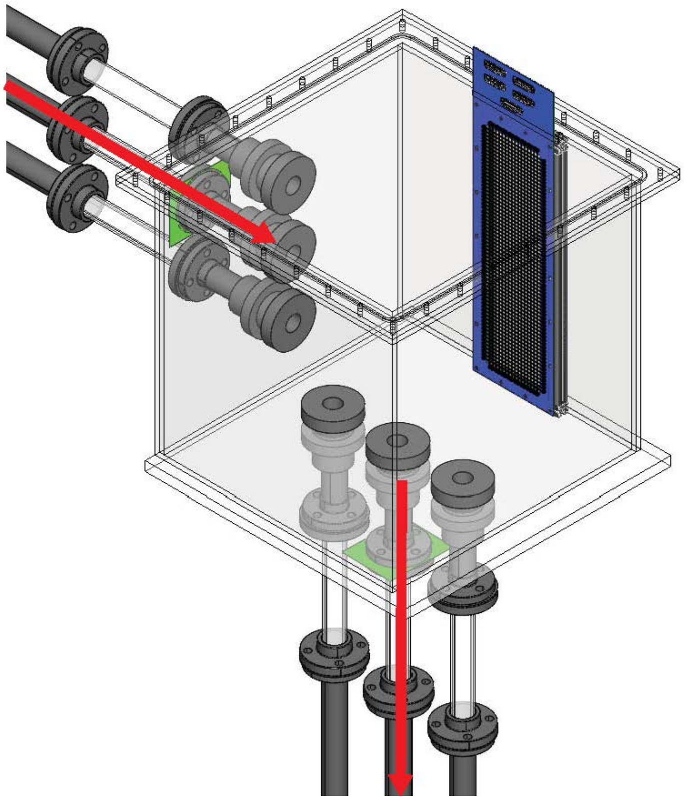

(b) Schematics of the acrylic tank and wire-mesh sensors. Large WMS -blue; Inlet WMS - green. Note the information from the additional WMS at the outlet is not used in this experiment.

Figure 4.12: Views of the HiRJet facility.

and viscosities of the fluids were measured to provide adequate flow properties for the CFD simulations. The density of the fluids was measured using a 100 mL flask and a high-accuracy scale. These values were verified by measuring the Degrees Brix number using a Digital Refractometer (Sper Scientific 300037). Furthermore, the viscosities of the fluids were measured via an Ostwald Viscometer. Knowing the density and viscosity of one liquid (tap water) and the density of the second liquid (DI + sugar solution), one can calculate the viscosity of the second liquid via Equation 4.1:

$$\mu_x = \mu_w \frac{\rho_x}{\rho_w} \frac{t_x}{t_w} \tag{4.1}$$

where μ is the dynamic viscosity, ν is the kinematic viscosity, ρ is the density, and t is the time it takes the fluid to flow through the capillary under the influence of gravity. The subscripts w and x denote tap water and sugar solution, respectively. By closely monitoring the boundary conditions and measuring the fluid properties, accurate boundary conditions can be provided for the CFD simulations.

4.6 High-fidelity simulations

Both experiments have been accompanied by high-fidelity DNS /LES simulations that have been conducted by colleagues under the IRP CP3 project. The high-fidelity simulations were conducted using the state-of-the-art CFD code NekRS, an open-source code based on the Spectral Element Method (SEM) [140]. NekRS can leverage Graphical Processing Unit (GPU) in modern High-Performance Computing (HPC) facilities to achieve considerable speedup compared to its predecessor Nek5000, which is advantageous for large-scale simulations. The readers are referred to Ref. [36] and Ref. [37] for the details of the high-fidelity simulations.

4.7 Conclusions

In this chapter, a framework for studying mixing in large enclosures under the NEAM IRP project has been briefly discussed. The main focus is on the interaction of single/multiple jets in a plenum and the propagation of stratified fronts. The backgrounds for the jet impingement and mixing in large enclosures and thermal stratification are then introduced. It was found that the high-resolution experimental data for the concerned phenomena was still scarce. It is proposed to use the results of high-resolution experiments and LES/DNS, in combination with machine learning techniques, to feed the development of lower-fidelity models. The second part of this thesis, following the proposed framework of working package 3 of the NEAM IRP project, is to conduct validation experiments that can provide high-resolution data for code validation and development. Two separate effect facilities, the MiGaDome, and the HiRJet facilities, are then discussed. High-fidelity simulations have also been conducted in parallel with the two experimental facilities to expand the database by colleagues under this project. The experimental findings, along with the validation of turbulence models using RANS simulations, will be introduced in the following chapters.

CHAPTER V

Experimental Database from the Separate-effect Facilities

This chapter delves into the discussion of high-resolution experimental datasets focused on mixing in large enclosures, originating from the MiGaDome and HiRJet facilities. The measurements at the MiGaDome facility initiated with single jet injection and progressively increased in complexity by introducing additional jets. Notably, density effects were incorporated through the study of two jets with different densities. This effort resulted in the establishment of a comprehensive database encompassing first- and second-order statistics tailored to the velocity field. Concurrently, the HiRJet facility contributed measurements involving various density differences and injection orientations. The outcome was the creation of a dedicated database specifically focused on the transient stratification process. The datasets from both facilities serve a crucial role in model validation and development within the scientific community. Throughout the remainder of this chapter, significant scientific findings derived from the high-resolution data will be highlighted and thoroughly discussed.

5.1 MiGaDome: Single jet injection

5.1.1 Region of Interest and Test Matrix

This study investigates isothermal single jet injection configuration to provide insight into the fundamental flow physics of jet spreading and mixing within the plenum. Compressed air is utilized as the working fluid. We use a Cartesian coordinate system to describe and reference the measured flow field, with the coordinate system's origin centered at the jet's inlet, as illustrated in Figure 5.1. The velocity components in the horizontal and vertical directions are denoted as $(x, \overline{U}), (y, \overline{V})$, and the corresponding velocity fluctuations are u' and v', respectively. The 2D field of view in the experiment is located above the jet inlet. In particular, data from the XY plane are of interest to observe the jet spreading and mixing, and the relative locations are shown in Figure 5.1. Note only a partial area above the jet inlet was covered in the measurement as a balance between the measurement spatial resolution and the image size.

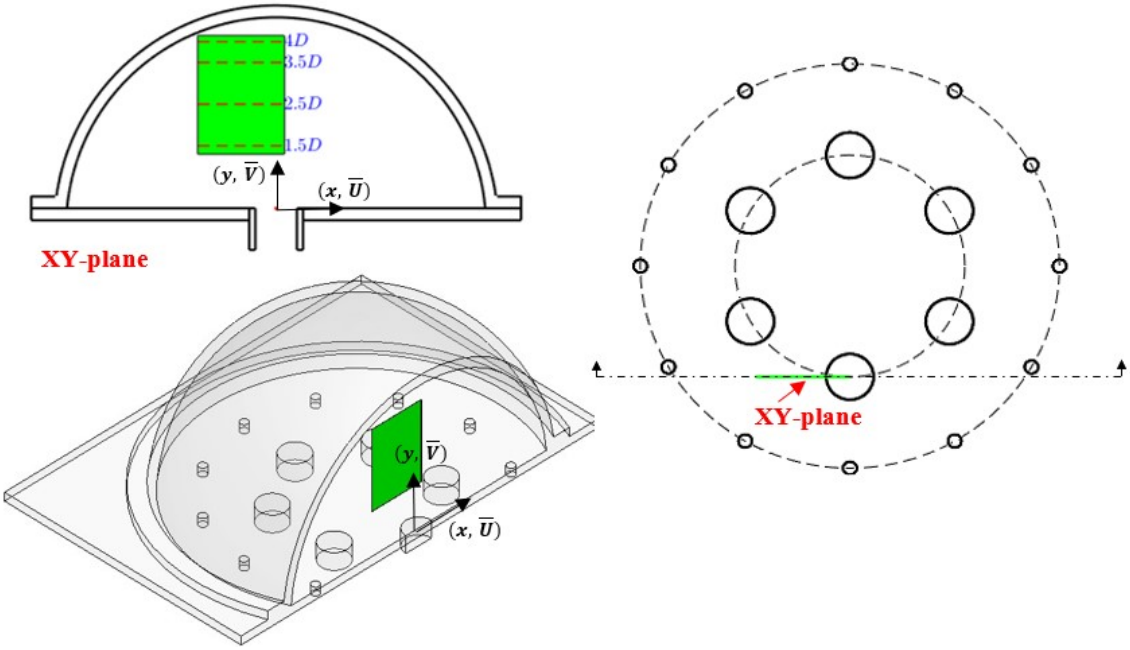

Figure 5.1: Region of interest and coordinate system.

The PIV system parameters, along with the flow field variables, are summarized in Table

5.1. A single jet injection for several Reynolds numbers is studied. The flow field was measured with the Double-Frame Double-Exposure (DFDE) technique with a low recording rate, enabling time-independent sampling of each image pair. In contrast, the interframe rate was relatively high to capture particle movement efficiently.

Table 5.1: Detailed PIV imaging parameters and flow conditions.

Parameter	Re1022	Re2038	Re4097	Re6021
Jet injection	Single	Single	Single	Single
Recording rate (Hz)	15	15	15	15
Interframe rate (Hz)	300	1500	3000	4500
Reynolds number	1022 ± 48	2038 ± 63	4097 ± 91	6021 ± 116
Flow rate ($10^{-3}\,kg/s$)	0.6490	1.298	2.596	3.835
Flow uncertainty ($10^{-3}\,kg/s$)	±0.0212	±0.0246	±0.0269	±0.0284
Temperature (°C)	22.4 ± 0.2	22.4 ± 0.2	21 ± 0.2	22.5 ± 0.2

5.1.2 Data Processing and Uncertainty

The recorded PIV image pairs were processed in LaVision's DaVis 10.1.2 using a multi-pass approach with an initial interrogation window of 96 × 96 pixel^2 with 50% overlap for the first pass and a final interrogation of 24×24 pixel^2 with a 75% overlap for the last four passes. Based on these settings and the locations of the PIV equipment, velocity fields with spatial resolutions of 1.49 mm were obtained. Turbulent statistics were computed by appropriate ensemble averaging. A detailed description of the processing method can be found in [141] and [142]. The identifiable uncertainty sources from data sampling and processing included the flow controller unsteadiness σ_{f}, the drag of seeding particles σ_{d}, peak-locking σ_{p} and random error σ_{r} [142]. Finally, errors were combined to generate uncertainty bands using the root-sum-square method.

5.1.3 Results and Discussion

5.1.3.1 Inlet velocity profile

The velocity distributions, along with the intensity profiles, are of significance when specifying boundary conditions for modeling and simulation of the facility. An LDV system measured the velocity profile within the inlet pipe at a distance of $y/D = 3.42$ upstream of the dome inlet. Figure 5.2 shows the normalized velocity to centerline velocity $\overline{V}_c$ and the relative velocity intensity profiles. A theoretical fully-developed laminar profile and a fully-developed turbulent profile are also plotted as references. The turbulent fully-developed profile was obtained from a pipe flow simulation for the experimental Reynolds number of 4097 utilizing STAR-CCM+ v15.06.007.

Note that measurement near the wall was not achieved due to the low signal-to-noise ratio and the high-velocity gradient. Nevertheless, these measured points for each case are sufficient to extract the velocity profile through proper data fitting. As can be seen from Figure 5.2a, the flow quickly develops into a fully developed profile with Reynolds numbers above 4097. Figure 5.2b shows that for all the cases, the relative velocity fluctuation is the lowest near the pipe center and gradually rises when approaching the wall.

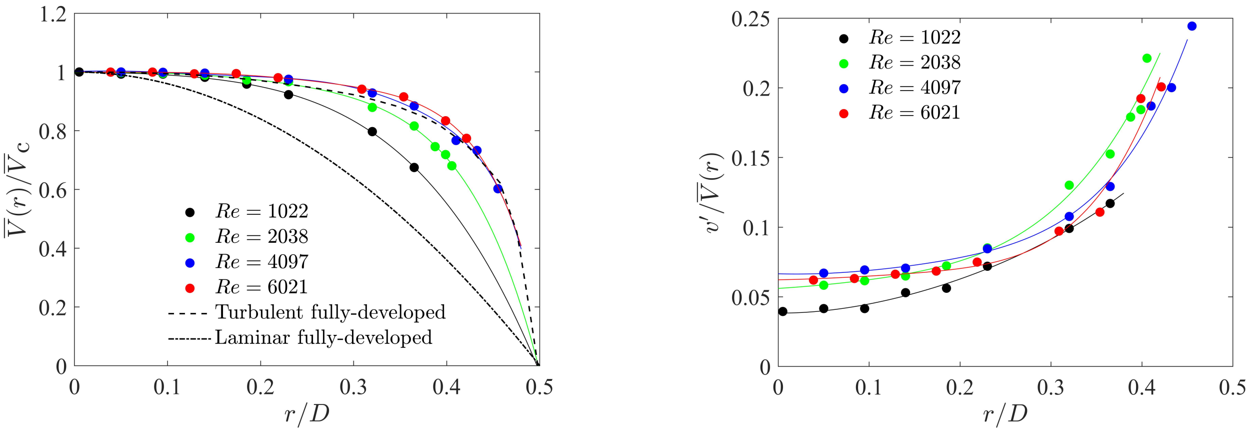

(a) Normalized velocity profile

(b) Relative intensity

Figure 5.2: Velocity profiles for different Reynolds numbers from LDV measurement with a distance of $y/D = 3.42$ from the dome inlet.

5.1.3.2 Flow pattern and first-order statistics

Figure 5.3 shows the velocity magnitude contours normalized by the inlet velocity obtained for four different Reynolds numbers (Re $= 1022, 2038, 4097, 6021$). The flow stream vectors are also shown through equally-sized arrows. A quantitative comparison of the velocity profiles at different elevations is presented in Figure 5.4. Examining the velocity contour of case $Re = 1022$, it can be observed that a core region with high momentum is present. In this case, the bulk flow barely mixes with the surroundings after leaving the inlet since the momentum is mainly dissipated through molecular diffusion effects. As a result, the momentum is mostly preserved in the streamwise direction, and low horizontal velocity is seen at $y/D = 1.5$. When the flow gets close to the dome ceiling, suppression of the streamwise velocity due to the presence of the dome diverts the flow, and the horizontal velocity $\bar{U}$ increases significantly at $y/D = 4$. As a result, a strongly curved streamline can be observed in the after-impingement region.

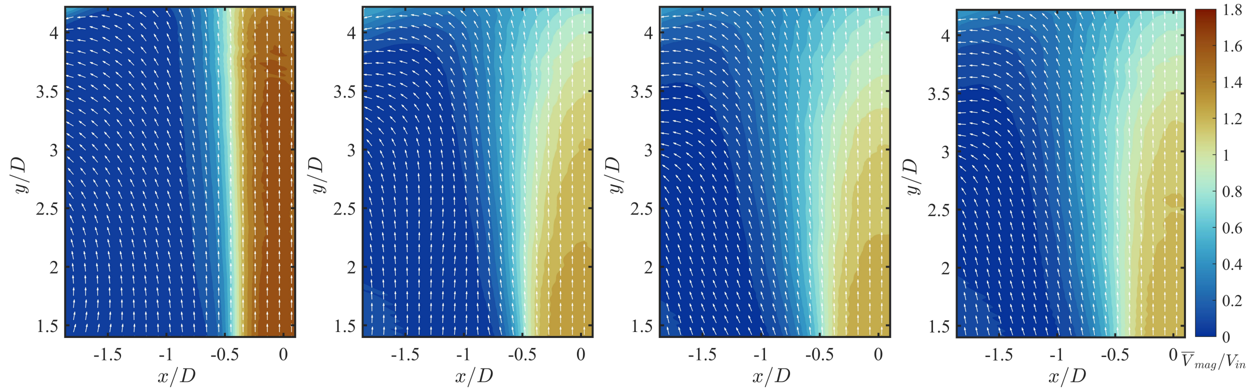

(a) $Re = 1022$ (b) $Re = 2038$ (c) $Re = 4097$ (d) $Re = 6021$

Figure 5.3: Normalized velocity magnitude $\overline{V}_{mag}$ fields for different Reynolds numbers.

As the Reynolds number increases, mixing is enhanced through the entrainment of the surrounding fluid due to turbulence. Therefore, the crosswise spreading of the jet increases with increasing Reynolds number. As a result, broader streamwise velocity profiles are seen compared to the case $Re = 1022$. However, it is observed that the profiles show asymptotic behavior as the Reynolds number approaches $Re = 6021$, especially close to the top of the dome. This trend is likely to occur because the jet cannot spread freely near the dome's ceiling, and the entrainment is restricted since the surrounding fluid is subjected to the curved surface. Because of the strong spreading in turbulent cases, the curved streamline structure also expands further away from the jet center. The curvature strength can be assessed by looking at the vorticity field $\overline{\omega}_z$, which is defined as:

$$\overline{\omega}_z = \frac{\partial \overline{U}}{\partial y} - \frac{\partial \overline{V}}{\partial x} \tag{5.1}$$

The normalized vorticity fields are shown in Figure 5.5. In the shear layer region, due to the large velocity gradient, strong vorticity is observed. As the Reynolds number increases, the vorticity is dissipated radially from the shear layer region to the surrounding fluid.

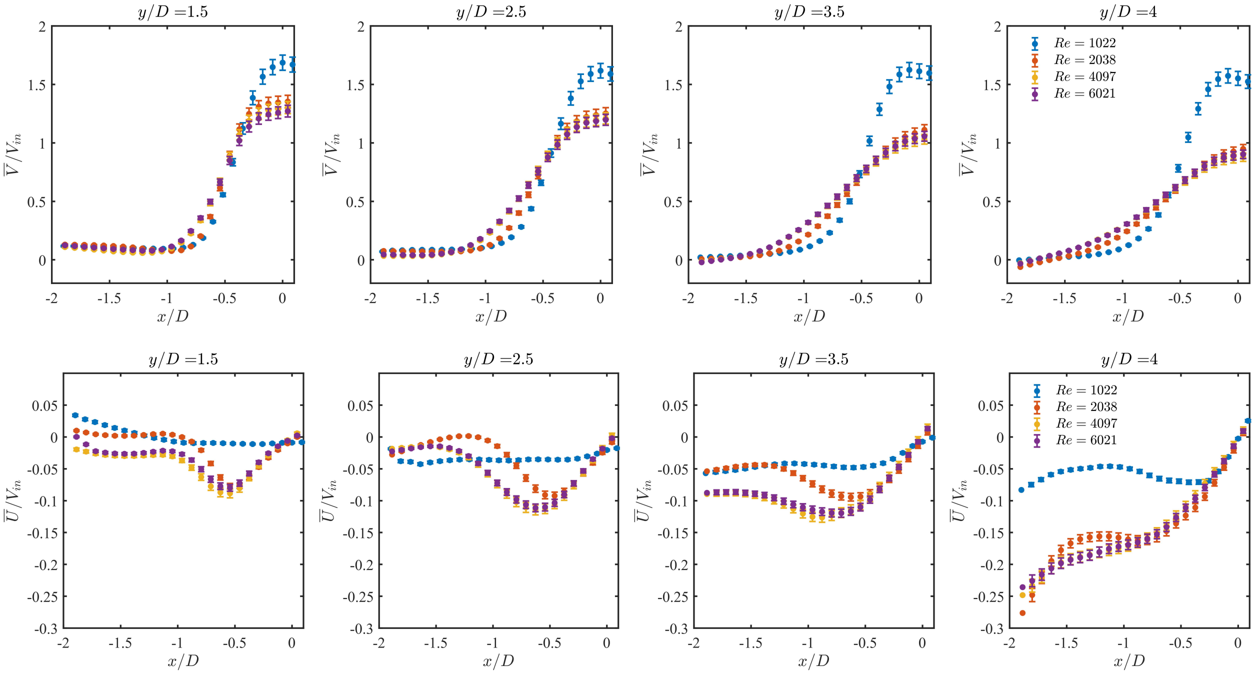

Figure 5.4: Streamwise and crosswise velocity profiles at different distances from the inlet.

For jet flow, the half-width is defined as the radial position where the velocity has dropped to half the centerline velocity. As the jet spreads downstream from the inlet, the half-width will increase with speed regulated by the strength of the mixing process, i.e. stronger mixing leads to larger spreading. For the present work, the half-width $x_{1/2}$ is defined as the horizontal

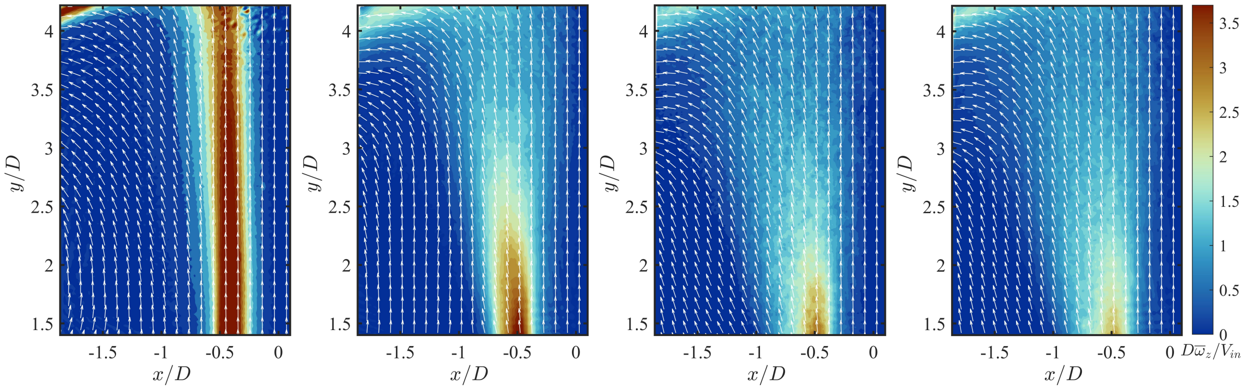

(a) $Re = 1022$ (b) $Re = 2038$ (c) $Re = 4097$ (d) $Re = 6021$

Figure 5.5: Vorticity fields $\overline{\omega}_z$ normalized by the inlet velocity and diameter.

position where the velocity magnitude is half its maximum. The growth of the jet half-width with downstream distance in the XY plane is plotted in Figure 5.6.

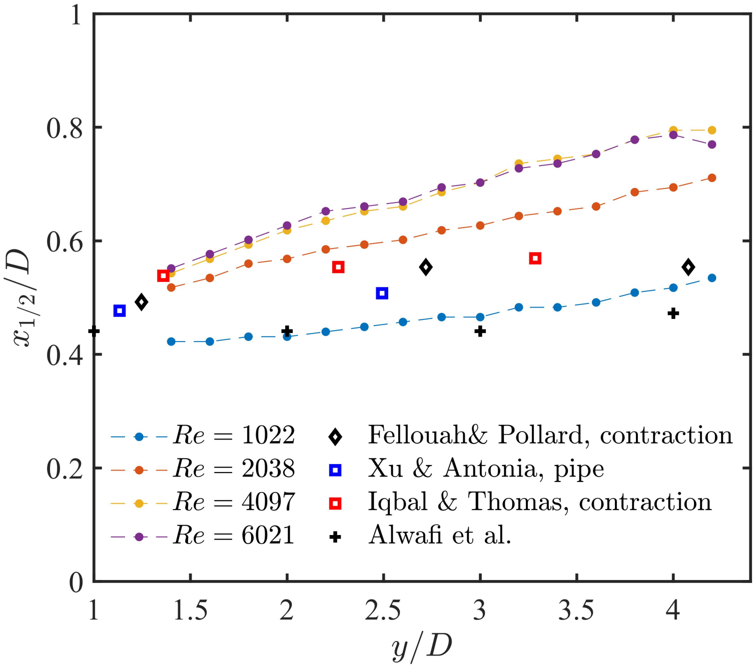

Figure 5.6: Jet half-width downstream of the inlet.

As shown in Figure 5.6, the overall half-width grows with increasing Reynolds number. The jet's mixing or spreading rate can be inferred from the slope of the increasing half-width. Compared to the free jet references (Iqbal & Thomas[143], Fellouah & Pollard [144], and Xu & Antonia [145]), and impinging jet with higher H/D in a dome from Alwafi et al. [35], all of which show nearly-flat half width in the near field, the jet half-width in the current experiment is observed to increase linearly, even for the low Reynolds number ($Re = 1022$). This indicates that a stronger entrainment of the surrounding fluid is present due to the small size of the confinement, yielding therefore a higher mixing rate.

5.1.3.3 Second-order statistics

Figure 5.7 and Figure 5.8 below show the second-order turbulent statistics normalized by the square of the inlet velocity. The streamwise and crosswise Reynolds normal stresses are presented in Figure 5.7. For the low Reynolds injection case ($Re = 1022$), the statistical fluctuation in the crosswise direction is negligible compared to the other three cases. However, a strong streamwise fluctuation is observed in the shear layer, especially near the dome surface (e.g. $y/D = 4$). This fluctuation is likely caused by the impingement on the dome surface. For turbulent flow ($Re = 2038$, 4097, 6021), it can be observed that the streamwise Reynolds normal stress is, in general, greater than the crosswise Reynolds normal stress along the streamwise direction. As the jet evolves downstream and y/D increases, a re-distribution of the Reynolds normal stresses is observed. First, near the inlet region ($y/D = 1.5$), a sharp peak is present for both the streamwise and crosswise Reynolds normal stresses. The peaks are near the jet's boundary layer, where turbulence mixing occurs strongly. As the downstream distance from the inlet increases, the sharp-peak profile gradually diminishes due to spreading. Getting close to the dome ceiling, it is found that the central region of the jet has stronger fluctuations, and a flatter profile is observed for the Reynolds normal stresses. As the Reynolds number increases, a more even distribution is observed. The Reynolds shear stress presented in Figure 5.8 shows a preserving shape along the downstream. For each case, a negative peak indicating flow entertainment through counter-clockwise rotations is present.

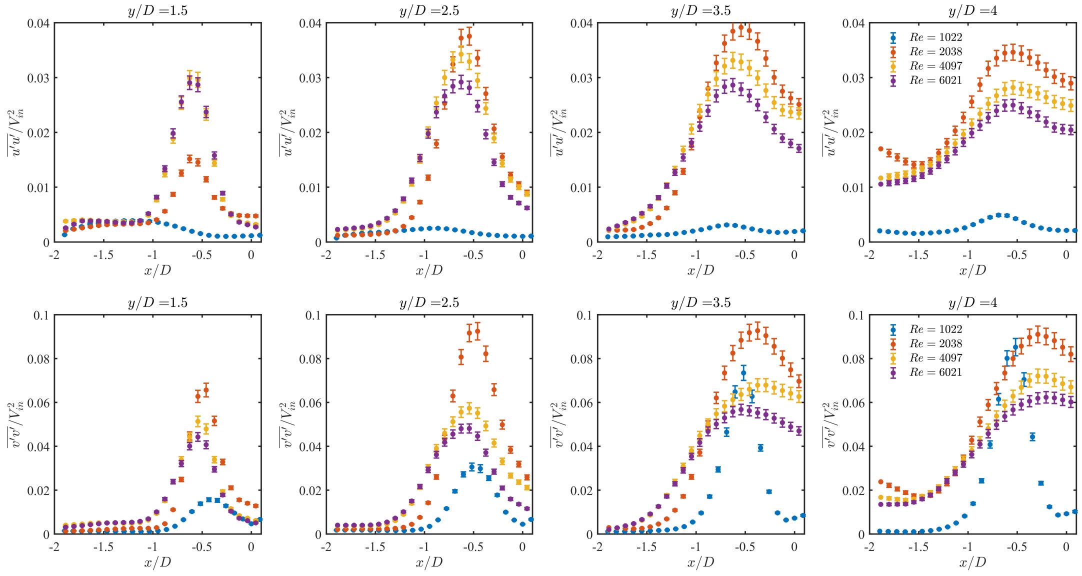

Figure 5.7: Profiles of Reynolds normal stresses normalized by the square of inlet velocity V_{in}.

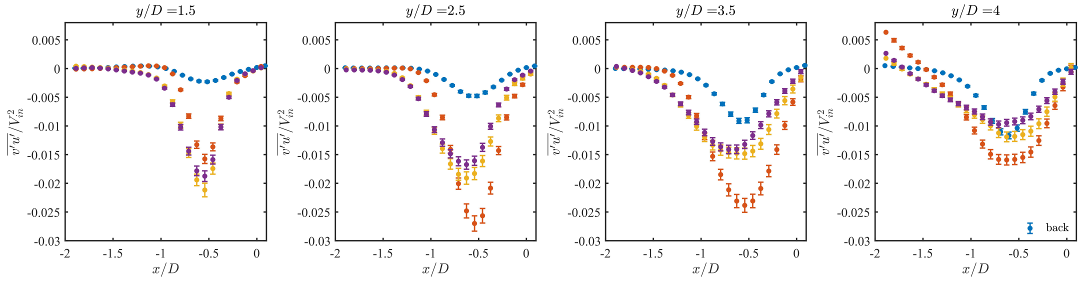

Figure 5.8: Profiles of Reynolds shear stress normalized by the square of inlet velocity V_{in}.

5.1.3.4 2D Budgets for Momentum Equations

Based on the measured statistics, the budgets for the governing momentum equations can be reconstructed in the experiment's 2D measurement plane. A budget analysis of the Reynolds-averaged momentum equation is significant in revealing the effect of turbulence on the flow distribution, thus advancing model development. Using the Cartesian coordinate system and the notations mentioned in subsection 5.1.1, the Reynolds-averaged momentum equations on the XY plane are expressed as the following:

- x-component of the steady-state incompressible Reynolds-averaged Navier-Stokes equation:

$$\begin{aligned}\overbrace{(\underbrace{\bar{U}\frac{\partial \bar{U}}{\partial x}+\bar{V}\frac{\partial \bar{U}}{\partial y}}_{2D}+\bar{W}\frac{\partial \bar{U}}{\partial z})}^{\text{convection}} = &\overbrace{-\frac{1}{\rho}\frac{\partial \bar{P}}{\partial x}}^{\text{pressure gradient}} \\ &+\nu\overbrace{(\underbrace{\frac{\partial^2 \bar{U}}{\partial x^2}+\frac{\partial^2 \bar{U}}{\partial y^2}}_{2D}+\frac{\partial^2 \bar{U}}{\partial z^2})}^{\text{molecular diffusion}}+\overbrace{(\underbrace{\frac{\partial \overline{u'u'}}{\partial x}+\frac{\partial \overline{u'v'}}{\partial y}}_{2D}+\frac{\partial \overline{u'w'}}{\partial z})}^{\text{turbulent diffusion}}+\overbrace{g_x}^{\text{Gravity}}\end{aligned} \tag{5.2}$$

- y-component of the steady-state incompressible Reynolds-averaged Navier-Stokes equation:

$$\begin{aligned}\overbrace{(\underbrace{\bar{U}\frac{\partial \bar{V}}{\partial x}+\bar{V}\frac{\partial \bar{V}}{\partial y}}_{2D}+\bar{W}\frac{\partial \bar{V}}{\partial z})}^{\text{convection}} = &\overbrace{-\frac{1}{\rho}\frac{\partial \bar{P}}{\partial y}}^{\text{pressure gradient}} \\ &+\nu\overbrace{(\underbrace{\frac{\partial^2 \bar{V}}{\partial x^2}+\frac{\partial^2 \bar{V}}{\partial y^2}}_{2D}+\frac{\partial^2 \bar{V}}{\partial z^2})}^{\text{molecular diffusion}}+\overbrace{(\underbrace{\frac{\partial \overline{u'v'}}{\partial x}+\frac{\partial \overline{v'v'}}{\partial y}}_{2D}+\frac{\partial \overline{v'w'}}{\partial z})}^{\text{turbulent diffusion}}+\overbrace{g_y}^{\text{Gravity}}\end{aligned} \tag{5.3}$$

where ρ, P, ν, and g are density, pressure, viscosity, and directional gravity acceleration. $\overline{W}$ and w' are the out-of-plane average velocity and velocity fluctuation, respectively. For both equations, the LHS represents convection. The four terms on the RHS are pressure gradient, molecular diffusion due to viscosity, turbulent diffusion due to Reynolds stresses, and gravity force. As is limited by the measurement technique, the contribution from the out-of-plane velocity to each term cannot be included in this analysis, nor the budgets of pressure gradient and gravity. As a result, only a portion of each term has been computed (see the terms within the bracket in Eq. 5.2 and Eq. 5.3). The normalized absolute contributions from the 2D convection ($\frac{D}{V_{in}^2}|\overline{V}\frac{\partial \overline{U}}{\partial y}+\overline{U}\frac{\partial \overline{U}}{\partial x}|$), the 2D turbulent diffusion ($\frac{D}{V_{in}^2}|\frac{\partial \overline{u'u'}}{\partial x}+\frac{\partial \overline{v'u'}}{\partial y}|$), and the molecular diffusion $(\frac{D}{V_{in}^2}|\nu(\frac{\partial^2\overline{U}}{\partial y^2}+\frac{\partial^2\overline{U}}{\partial x^2})|)$ to the governing equations for case $Re = 4097$ are presented in Figure 5.9. Note all the terms have been non-dimensionalized by the length scale D and velocity scale V_{in}. As inferred from the magnitude, the molecular diffusion contribution is small compared to the other two terms and is thus negligible. However, the turbulent diffusion and convection are of comparable magnitude. The convection becomes significantly dominant close to the dome ceiling, where the impingement diverts the flow. In this region, turbulent diffusion is suppressed. The contribution of turbulence diffusion becomes most effective in regions where a high gradient of the Reynolds stresses is present. This can be observed in the region between $y/D \approx 1.5 \sim 3$ for both equations, where the jet is less affected by the dome.

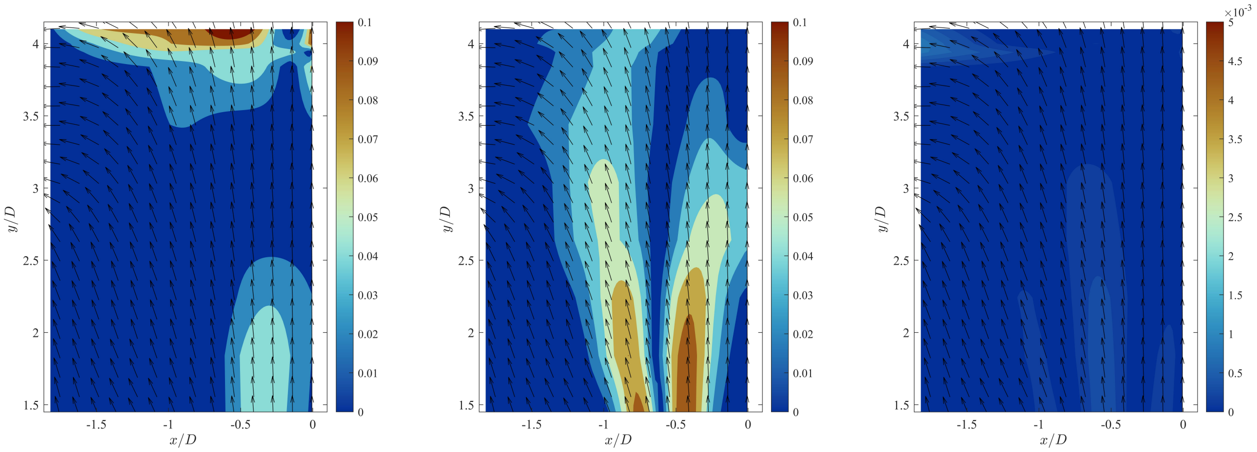

(a) Crosswise 2D momentum budgets: convection, turbulent diffusion, and molecular diffusion

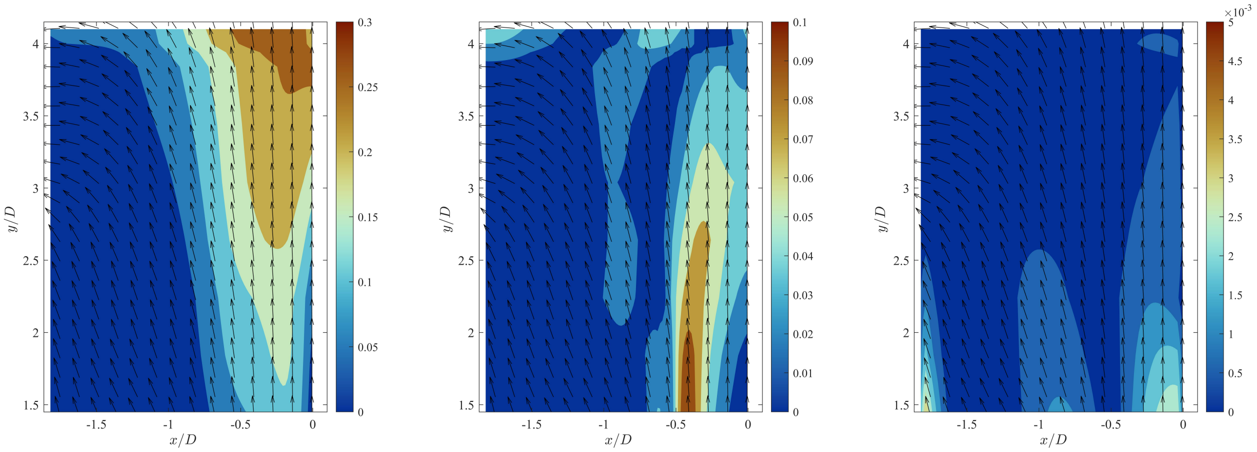

(b) Streamwise 2D momentum budgets: convection, turbulent diffusion, and molecular diffusion

Figure 5.9: Dimensionless absolute contribution of 2D budgets to momentum equations.

5.1.4 Conclusions

The present study investigated the flow mixing in the MiGaMDome facility under uniform-density conditions using the PIV measurement technique. High-resolution experimental data with well-defined boundary conditions suitable for CFD validation have been reported. First-order and second-order statistics have been presented and discussed to analyze the details of the local mixing process and turbulent characteristics under the effects of jet spreading and jet impingement within the upper plenum enclosure. Results from the single jet injection have shown that the normalized statistics of the jet reach asymptotic behavior as the Reynolds number increases. By investigating the 2D budgets for the momentum equation, it is observed that the contribution of turbulent diffusion is minor near the enclosure's surface, where strong convection is present due to impingement.

5.2 MiGaDome: Two jets interactions

5.2.1 Test Matrix and Region of Interest

In this study, the turbulent mixing of two jets with/without density effect is studied. The region of interest is shown in Figure 5.10. As is shown in Figure 5.10a, two inlets (in red color) are used, while the other four inlets (in gray color) remain at zero flow rate. All the outlets are open to the ambient during the experiment. The 2D measurement plane is located at the region that crosses the two jet inlets (green line). Figure 5.10b shows the front view of the measured plane. The origin of the coordinate system is set to be at the center between the two inlets. x, y, z refer to the lateral, streamwise, and spanwise (i.e. out-of-plane) directions, respectively. The corresponding mean velocity components and velocity fluctuation components are denoted as $\overline{U}, \overline{V}, \overline{W}$ and u', v', w'.

Experiments were first conducted under Reynolds number of $Re = 4097$ and $Re = 6021$ using compressed air, with three different injection cases. Reynolds number is based on the inlet jet diameter D and the air viscosity ν at ambient pressure and reference temperature

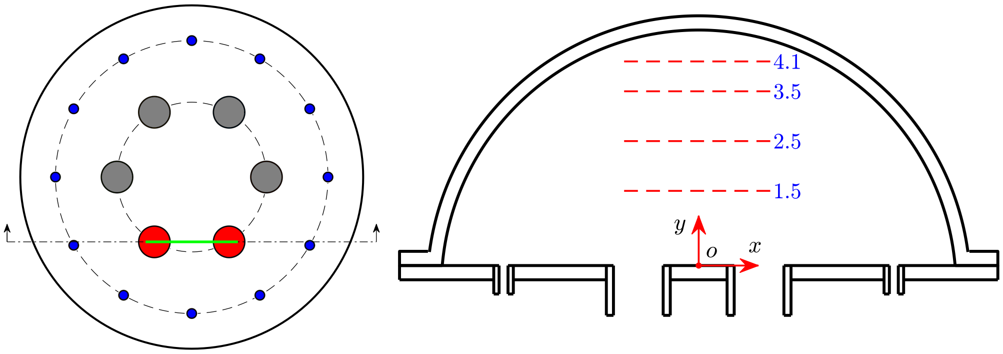

(a) Top view (b) Front view

Figure 5.10: Views of the measurement plane.

21^oC. The three cases are summarized in Table 5.2. For case TJa and TJc, both inlets have the same Reynolds number, while the second case TJb has uneven injection ($Re = 6021$ v.s. 4097). Based on the LDV measurement, a fully developed velocity profile has been reached for both Reynolds numbers before entering the dome [146]. The values of turbulent intensity at the center of the pipe, according to the measurement from LDV , are 7.8%($Re = 6021$) and 8.7%($Re = 4097$), respectively. The turbulent dissipation rate ε and Kolmogorov length scale η_k is also provided to specify the inlet conditions. The calculation of the two quantities is based on the integral pipe length scale of pipe flow to provide an estimation of the relative values when needed for specifying the inlet boundaries [147, 148]. For each case, the flow field was recorded with a frequency of $15Hz$. The recorded PIV image pairs were processed in LaVision's DaVis 10.1.2 using a multi-pass approach with an initial interrogation window of 96×96 pixel^2 with 50% overlap for the first pass and a final interrogation of 24×24 pixel^2 with a 75% overlap for the last four passes. Based on these settings and the locations of the PIV equipment, velocity fields with spatial resolutions of 1.49 mm were obtained.

The aforementioned setup aims to explore the fundamental physics of two-jet interactions under uniform scenarios. However, it is anticipated that a more complex flow pattern will be present when considering the density effect. An experimental examination of the flow with jets of different densities would greatly help advance the understanding of the mixing

Table 5.2: Test matrix and inlet boundary conditions

Case	TJa	TJb	TJc
Jet mean inlet velocity V_o (m/s)	1.401	1.401 v.s. 2.071	2.071
Inlet turbulent intensity $I = v'/V_o$	8.7%	8.7% v.s. 7.8%	7.8%
Reynolds number $Re = V_o D/\nu$	4097	4097 v.s. 6021	6021
Estimated dissipation rate $\epsilon = v'^3/D(\mathrm{m}^2/\mathrm{s}^3)$	0.041	0.041 v.s. 0.095	0.095
Kolmogorov scale $\eta_K = (\nu^3/\epsilon)^{1/4}$ (mm)	0.62	0.62 v.s. 0.5	0.5
Temperature ($^{\circ}C$)		21.5	

behavior. The buoyant jet flow in the large enclosure is characterized by the Reynolds number (Re) and Grashof number (Gr). In this work, the Reynolds number is defined using the flow properties and gas velocity for each inlet. The plenum Grashof number is defined based on the plenum height H_p:

$$\mathrm{Gr} = \frac{g \cdot H_p^3 \bar{\rho} \mathit{\Delta} \rho}{\bar{\mu}^2} \tag{5.4}$$

where $\mathit{\Delta}\rho$ is the density difference between the inlet gas and ambient gas, $\bar{\rho}$ is the average density, and $\bar{\mu}$ is the average viscosity.

To conduct the experiment with density differences, three different gases are used, including compressed air, argon, and helium. The same two inlets, as indicated in Figure 5.10, are used to investigate the interaction between jets of density difference. During the experiment, the dome was kept quiescent with ambient air first. Then, the injection of both inlets happened at the same time by opening the mass flow controller. The right inlet (referred to as Inlet #2) is supplied with air, and the gas supply for the left inlet (referred to as Inlet #1) varies from argon to helium. The experimental conditions are summarized in Table 5.3. The investigation includes two Gr numbers: cases TJDDb and TJDDc have $Gr = 2.3 \times 10^{-8}$ created by using argon against air, while cases TJDDd and TJDDe have $Gr = 5.2 \times 10^{-8}$ created by using helium against air.

Measurement was conducted again with a frequency of $15Hz$, and the data were processed in LaVision's DaVis 10.1.2 using a similar method as mentioned in the uniform injection scenario. For the experiment with density variations, measuring the density field could

Table 5.3: Experimental condition for two jets with density difference

Case	Inlet#1				Inlet#2 (air)			
TJDD	Gas	$\boldsymbol{\rho^*}$	$\boldsymbol{\mu^*}$	$\boldsymbol{Re^*}$	$\boldsymbol{\rho\,(kg/m^3)}$	$\boldsymbol{\mu(10^{-5}Pa\cdot s)}$	$\boldsymbol{Re}$	**Gr($\mathbf{10^8}$)**
b	Ar	1.38	1.21	1	1.20	1.81	4097	2.3
c	Ar	1.38	1.21	1.38	1.20	1.81	4097	2.3
d	He	0.14	1.08	0.12	1.20	1.81	4097	5.2
e	He	0.14	1.08	0.24	1.20	1.81	4097	5.2

* Normalized based on the air properties.

not be achieved since the MiGaDome facility is not equipped with the necessary measurement technique. Instead, the analysis will focus on the flow field. Future work necessitates incorporating measurement techniques like PILF to provide the density field essential for a better understanding of the interaction between buoyant jets. Nevertheless, the current measurement of the flow field aims to establish a foundation for further exploration by offering valuable insights into the effect of density differences, along with providing data readily usable for code validation.

5.2.2 Results and Discussion

In this subsection, the flow visualization, frequency analysis, and flow statistics for the three uniform cases (TJa, TJb, TJc) will first be discussed. Then, the effect of the density variation will be briefly discussed by examining the pattern of the averaged flow field from the four non-uniform cases (TJDDb, TJDDc, TJDDd, TJDDe).

5.2.2.1 Visualization of the Instantaneous Flow Field

Figure 5.11 shows the snapshots of the instantaneous velocity field at three different times for the three cases. The magnitude has been normalized by the inlet velocity V_o of $Re = 6021$. The three vertical lines in each snapshot indicate the location of the inlet centers and the center of origin. For each case, the main jet streams break up and recover due to the entrainment with the surroundings and the impingement into the top curved surface. Intense turbulent mixing is observed for all three cases, with spanwise vortices of various sizes developed in the observed plane.

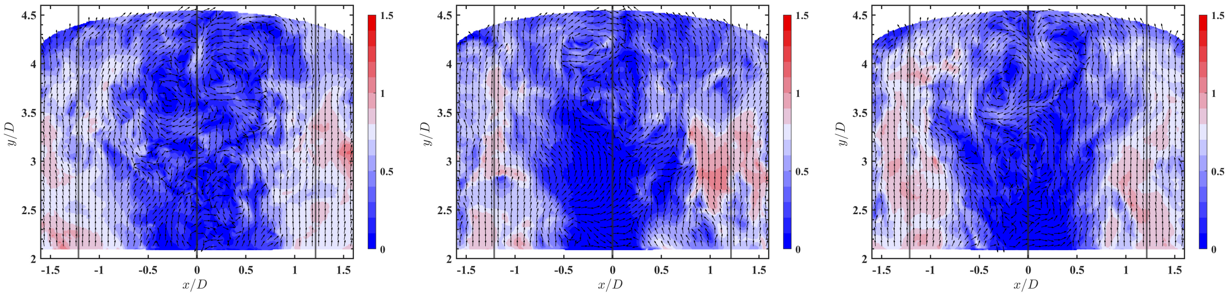

(a) TJa, $t_1 = t_o$ (b) TJa, $t_2 = t_o + 3s$ (c) TJa, $t_3 = t_o + 6s$

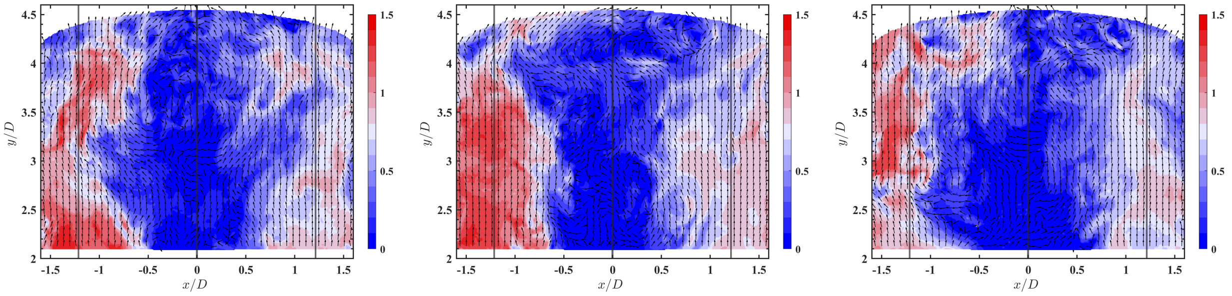

(d) TJb, $t_1 = t_o$ (e) TJb, $t_2 = t_o + 3s$ (f) TJb, $t_3 = t_o + 6s$

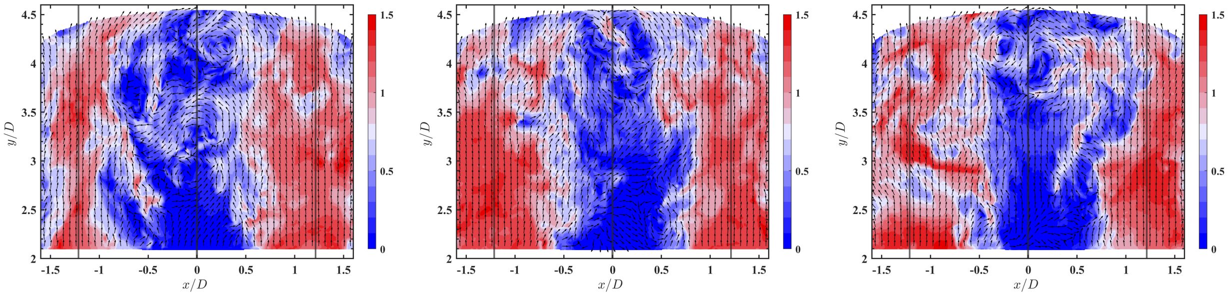

(g) TJc, $t_1 = t_o$ (h) TJc, $t_2 = t_o + 3s$ (i) TJc, $t_3 = t_o + 6s$

Figure 5.11: Instantaneous velocity field, normalized by the inlet velocity V_o of $Re = 6021$. Note the three cases were recorded with random t_o. The arrows are the directional velocity vectors.

The structures corresponding to vortexes can be identified using the Q-criterion. The Q-criterion used to capture vortices is defined as the second invariant of the velocity gradient tensor:

$$Q = \frac{1}{2}\left(\|\boldsymbol{\Omega}\|^2 - \|\boldsymbol{S}\|^2\right) \tag{5.5}$$

where $\boldsymbol{\Omega}$ and $\boldsymbol{S}$ are the rotation-rate and strain-rate tensors, respectively. Positive values of Q are indicative of locations where the vorticity dominates over viscous stress. It must be noted that limited by the 2D measurement, the Q-criterion could only be computed on a 2D frame and thus is not representative of all the vortex structures existing on the observing plane. Nevertheless, important quantitative information regarding the turbulent energy transfer process can still be observed. Figure 5.12 shows the two consecutive instantaneous contours of positive Q values for case TJa, while the other two cases bear similar distribution. Note the superimposed vector field represents the instantaneous velocity fluctuations. As can be seen from Figure 5.12, unstable eddies of different sizes (see some indicated by numerical labels) are breaking up and re-forming in the dynamic process. For example, process 1 witnessed the transport of a small eddy in the flow, while process 2 involved the break-up of a large eddy into small ones. Processes 3 and 4 showed some eddies with intermediate sizes. This observed dynamic process of the turbulent eddies clearly illustrates the turbulent energy redistribution, i.e., energy cascade [149].

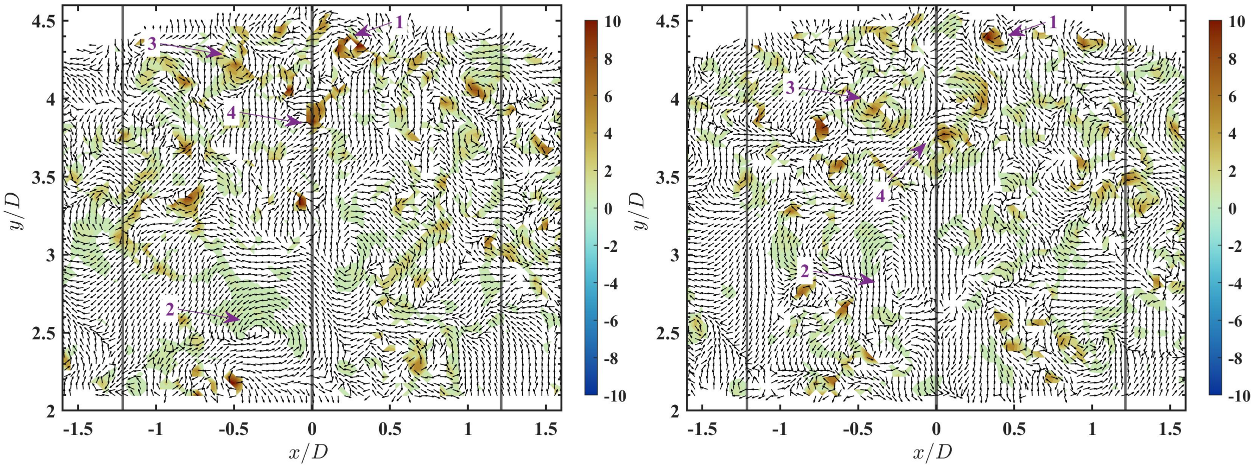

(a) TJa, $t_1 = t_o$ (b) TJa, $t_2 = t_o + 1/f$

Figure 5.12: Instantaneous vorticity contours indicated by the positive Q values for case TJa.

5.2.2.2 Power Spectrum Desensity

To help identify periodicities in the transient flow field, Power Spectral Density (PSD) analysis of the time series of the instantaneous flow field has been conducted. The PSD approach and its success in revealing the flow dynamics have been discussed at a great length in literature [150] [142][90]. Welch's method [151] is employed for the analysis here since this method reduces the noise in the frequency spectrum (in exchange for the loss of frequency resolution) and provides convergent estimates of the power spectral densities [90]. Since the measurements were carried out with a $15Hz$ recording frequency, the maximum resolved frequency can only reach $7.5HZ$, according to the Nyquist theorem [152]. Identification of periodical oscillations with frequencies higher than the cutoff frequency would require time-resolved measurements that will be carried out in future work. Figure 5.13 shows the PSD at several locations for all three cases. The frequency is presented using the Strouhal number, which is defined as:

$$St = fD/\overline{V_i} \tag{5.6}$$

where $\overline{V}_i$ is the inlet average velocity, and D is the inlet diameter. It can be seen that clear peaks are present at the center $x/D = 0$ for the uniform case TJa and TJc, while no peak is observed for the uneven injection case TJb. The values of the peak St number at $x/D = 0$ are 0.0144 and 0.0120, respectively. Moving away from the plane center, the peak diminishes quickly for both cases, i.e., at the jet center $x/D = 1.21$ no obvious peak is seen. The fact that no low-frequency oscillation is seen for the uneven injection case is favorable. For the mixing in the reactor upper plenum during the aforementioned HTGR s accident scenario, it is expected that the hot jets/plums issued into the plenum will also have different momentum. However, an exclusive conclusion cannot be drawn here until further time-resolved experiments are conducted.

5.2.2.3 Averaged velocity and Reynolds stresses

From the snapshots of the instantaneous flow field, mean flow statistics that are suitable for CFD validation can be obtained through ensemble averaging [153] [154]. Sufficient sample sizes $(3051 - 9151)$ for each case have been taken to ensure that the averaged results are independent of the number of snapshots obtained, as indicated by the convergence plots.

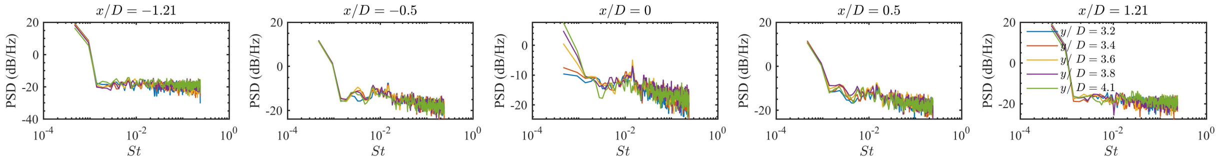

(a) TJa

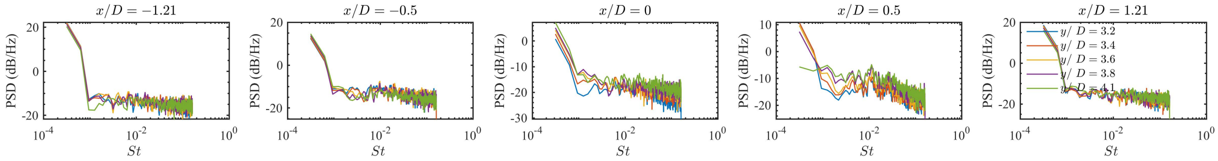

(b) TJb

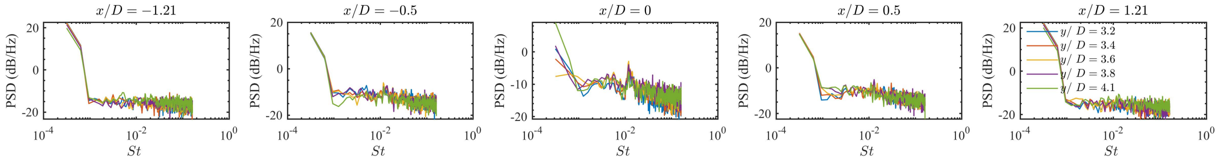

(c) TJc

Figure 5.13: Power spectrum density of the streamwise velocity at several $(x/D, y/D)$ locations. The Strouhal number $St = fD/\overline{V_i}$ (for case TJb, the inlet velocity V_i was based on $Re = 6021$).

The results from the convergence plot are not shown in this work for brevity and the reader is referred to [153] for the detailed evaluation method. The uncertainty quantification also follows the same procedure mentioned in [153, 146]. The uncertainty of the flow rate was estimated to $\pm 2.7 \times 10^{-5} kg/s$ based on the specification of the flow controller. The identifiable uncertainty sources from data sampling and processing included the flow controller unsteadiness σ_{f}, the drag of seeding particles σ_{d}, peak-locking σ_{p} and random error σ_{r}. Errors were combined to generate uncertainty bands using the root-sum-square (RSS) method.

Figure 5.14 shows the averaged vector fields for the three cases. The velocity magnitude has been normalized by the inlet velocity of $Re = 6021$, and the vector fields are shown using equal-length arrows. As can be seen for each case, the jet issued from the inlet moves upwards towards the dome surface as y/D increases. The flow between the jets also has been entrained to move upwards. Near the dome top, the flow direction from being perpendicular to the wall changes gradually to being nearly parallel to the wall. For the two uniform injection cases TJa and TJc, the wall jets collide and result in an increase in local pressure and separation of the fluid from the surface, forming a fountain down-wash flow. A pair of large vortices have been generated between the fountain flow and the jets. The penetration of the fountain flow, i.e. the location of the stagnation point caused by the impingement between the fountain flow and the entrained upward flow, becomes smaller as the Reynolds number increases, as can be inferred from the vector fields of case TJa and TJc. For the uneven injection case TJb, since the left jet has a higher Reynolds number, the wall jets' impingement has been impelled to the location closer to the right jet, forcing a small region of recirculation instead of the fountain flow.

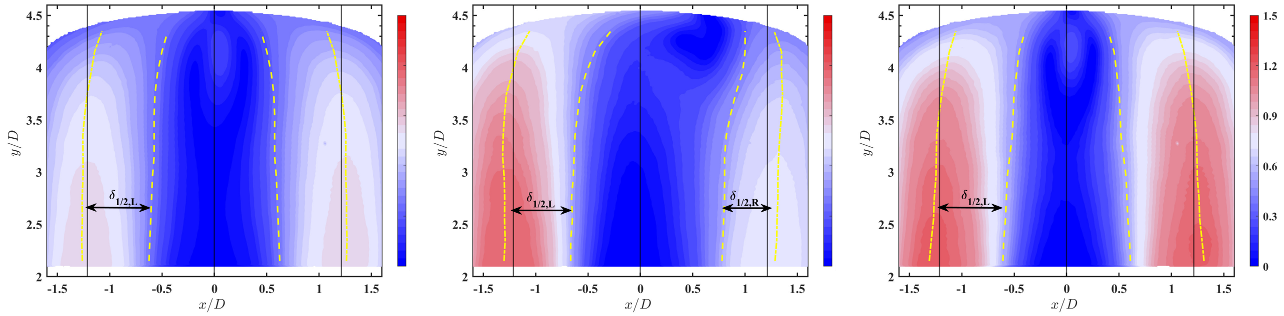

(a) Mean velocity contours. From left to right: TJa, TJb, TJc.

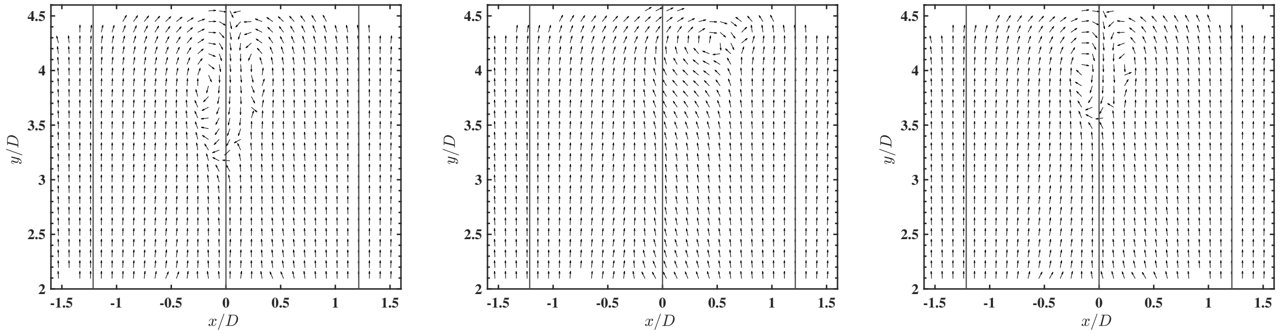

(b) Mean velocity vectors. From left to right: TJa, TJb, TJc.

Figure 5.14: The averaged velocity field for the three cases, normalized by the inlet velocity V_o of $Re = 6021$. Top: mean velocity contours; Bottom: velocity directional vectors.

In each contour, the distribution of the jet's maximum velocity is indicated by the yellow dash-dot line, and the location where the jet's velocity drops to half the local jet's maximum velocity is indicated by the dashed yellow line. It can be seen that the maximum streamwise velocity happens off the center of the jet for all three cases. Specifically, all the cases first have shown a distribution closer to the outer mixing layers near the jet inlets, which could have been caused by the fact that the outer mixing layer is near the outlet nozzles. As y/D increases, the maximum velocity gradually shifts towards the inner mixing layer. This trend differs from the observation in the experiments of free twin jets that maximum velocity gradually shifts towards the outer mixing layer [155]. This difference trend is mainly attributed to the geometric effect of the concave surface.

The distribution of jet half-width $\delta_{1/2}$, which is defined as the location where the mean streamwise velocity is equal to half the local jet maximum mean velocity, can be inferred from the distance between the two yellow lines. Jet half-width is often used to characterize the spreading rate of the jet [146][156] [149]. For the turbulent free-round jets, the jet half-width was found to grow linearly as the distance from the inlet nozzle increased [149]. For the free twin jets, the flow becomes well mixed after two jets merge into one stream [155]. Figure 5.15 shows the jet half-width in the inner mixing layer for the three cases. The jet half-width for case TJa increases slightly and then decreases gradually along the jet trajectory, while a drop of the jet half-width is first seen for case TJc. Both cases show a limited spreading in the inner mixing layer due to the small jet spacing and the suppression of the fountain flow. The asymmetrical case TJb has shown that the half-width of the high-momentum jet increases while the half-width of the low-momentum jet decreases dramatically near the recirculation.

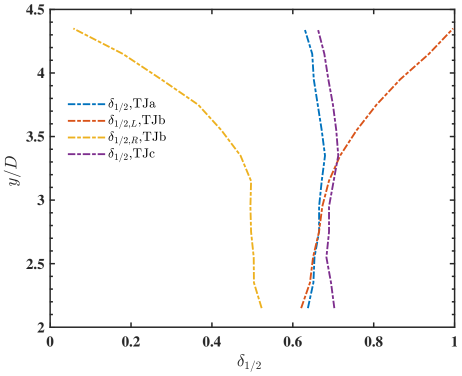

Figure 5.15: Jet half width in the inner mixing layer, normalized by the jet inlet diameter D.

Figure 5.16 shows the streamwise and the lateral velocity profiles at several y/D locations.

The profiles have been normalized by the inlet velocity V_o of $Re = 6021$. Double peaks are seen for the streamwise velocity at $y/D = 2.5$. Due to the existence of the fountain flow in both cases TJa and TJc, negative streamwise velocity values are present in the profiles at $y/D = 4$. The lateral velocity peaks at the shear layers, where the lateral momentum exchange dominates. At $y/D = 4$, the right peak of the lateral velocity profile for case TJb has been shifted towards the center under the effect of the clockwise recirculation.

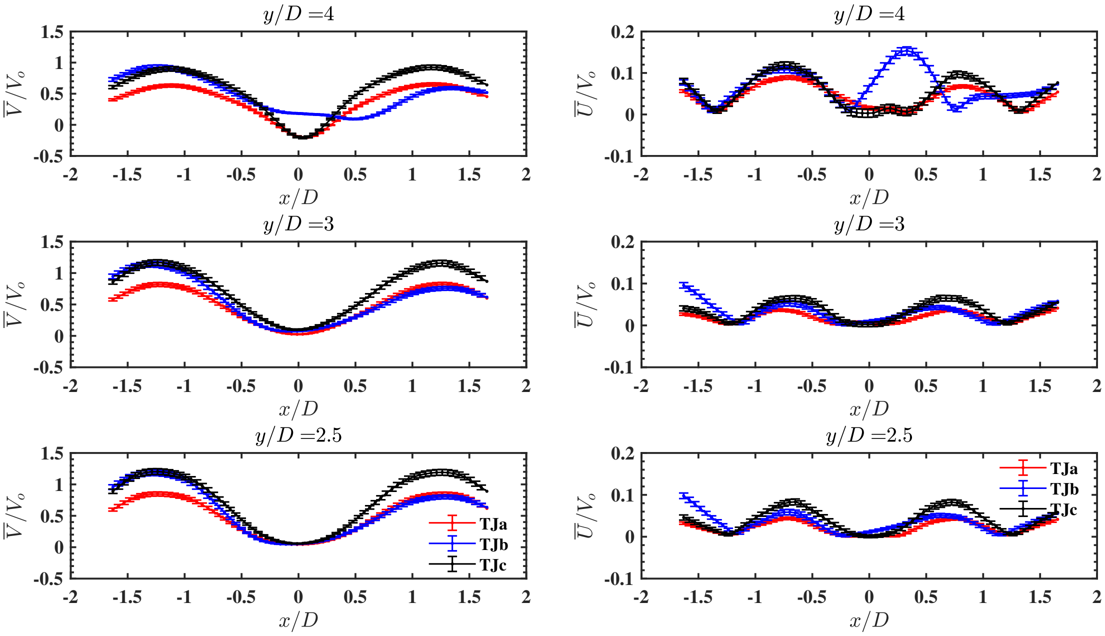

(a) Streamwise velocity (b) Transverse velocity

Figure 5.16: Velocity profiles at various y/D locations.

Mixing phenomena depend strongly on the intensity of turbulent fluctuations and the convection of these fluctuations. As a result, the prediction of turbulent statistics is as important as that of the mean flow statistics. Figure 5.17 shows the profiles of Reynolds normal stresses that present turbulent fluctuations along the streamwise and the lateral directions, and the profiles of the Reynolds normal stress that indicates the convection of the fluctuation. All the profiles have been normalized by the square of the inlet velocity V_o of $Re = 6021$.

For both streamwise Reynolds normal stress and lateral Reynolds normal stress, the magnitude increases as the Reynolds number increases (see profiles between TJa and TJc).

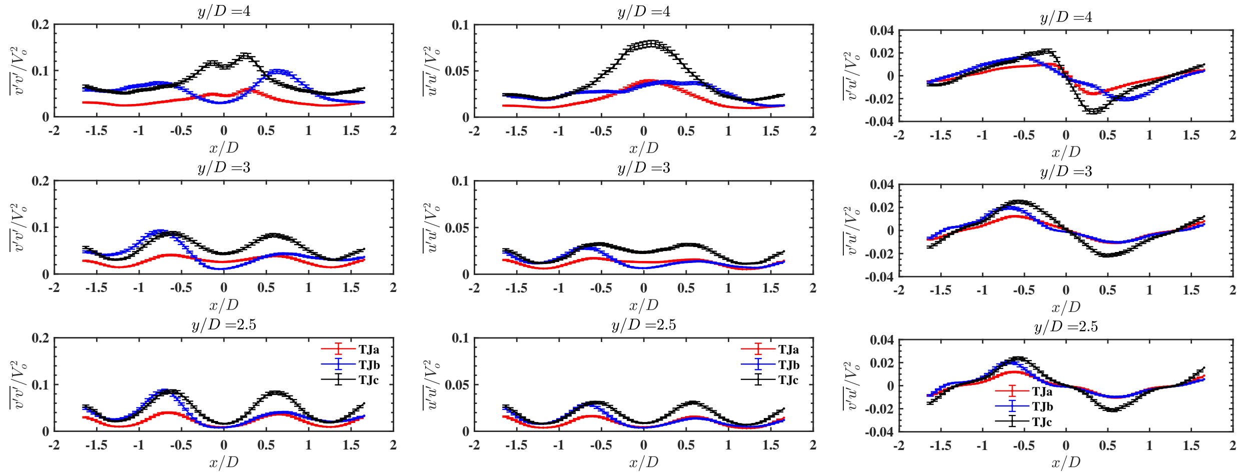

(a) Streamwise Reynolds stress (b) Lateral Reynolds stress (c) Reynolds shear stress

Figure 5.17: Second-order statistics profiles at various y/D locations.

Before reaching the fountain flow region, the profiles (($y/D = 2.5$ and $y/D = 3$) peak at the shear layers region, which is similar to the turbulent free round jets [157]. At $y/D = 4$, the largest values of both Reynolds normal stresses for case TJa and TJc are seen in the central region where the fountain flow presents, indicating the high degree of unsteadiness of the fountain flow. Without the fountain flow, the values of the Reynolds normal stresses for case TJb are the highest near the recirculation region. The profiles of Reynolds shear stress for all three cases show two peaks of opposite signs. This is because clockwise entrainment of the flow happens in the inner shear layer of the left jet, while counter-clockwise entrainment of the flow happens in the inner shear layer of the right jet.

5.2.2.4 Spatial cross-correlation and integral length scale

Complete validation of Reynolds-averaging-based turbulence models requires the knowledge of turbulent parameters, for example, turbulent kinetic energy k and turbulent dissipation rate ε for $k-\varepsilon$ models. Limited by the 2D PIV measurement technique, the out-of-plane flow information is not available in the measurements. If assuming the turbulence flow is dominant in the streamwise direction and the Reynolds normal stresses in the lateral direction and out-of-plane direction to be of the same order, the turbulent kinetic energy may be assumed as $k = \frac{1}{2}\left(2\overline{u'u'} + \overline{v'v'}\right)$. However, direct computing turbulent dissipation rate requires information on all the nine squared velocity gradients and three cross-product velocity gradients for three-dimensional flow, in addition to the fine spatial resolution that resolves to the Kolmogorov scale [158]. Instead, based on the equilibrium turbulence arguments [159] [160][161], the rate of turbulent dissipation can be determined by $\varepsilon = A\frac{k^{3/2}}{\ell}$, where ℓ is the integral length scale and A is a proportionality constant of order 1. The integral length scale is considered to be characteristic of the largest motions of a turbulent flow and can be determined from the two-point spatial correlation of velocity fluctuations. The spatial velocity cross-correlation in Einstein notation can be expressed as [54] [162]:

$$R_{ij}\left(\boldsymbol{x},\boldsymbol{\sigma}\right) = \frac{\overline{\boldsymbol{v_i'}\left(\boldsymbol{x}\right)\boldsymbol{v_j'}\left(\boldsymbol{x}+\boldsymbol{\sigma}\right)}}{\sqrt{\overline{\boldsymbol{v_i'^2}\left(\boldsymbol{x}\right)}}\sqrt{\overline{\boldsymbol{v_j'^2}\left(\boldsymbol{x}\right)}}}. \tag{5.7}$$

where $\boldsymbol{v_i'}$ refers to the velocity fluction in ith direction, $\boldsymbol{x}$ is the location of the reference point and $\boldsymbol{\sigma}$ the spatial separation from the reference point. Figure 5.18 below shows the streamwise and lateral two-point spatial correlation at several points for case TJa. For each contour, the two-point correlation is maximum at the reference point when $\sigma = 0$ leads to auto-covariance. As the spatial separation σ increases, the magnitude of the two-point spatial correlation decreases since the turbulent fluctuations at the reference point is less correlated to fluctuations at the observing point. Looking at both the left corner contours of R_{yy} and R_{xx}, a roughly round structure is observed, indicating isotropic turbulence at this reference point. The vertically-elongated structures in the contours of R_{yy}, and the horizontally-elongated structures in the contours of R_{yy}, on the other hand, represent anisotropic turbulent fluctuations.

The integral length scale ℓ can then be computed as the integral of the spatial velocity cross-correlation over the spatial separation [35]:

$$\ell_{ii}(\boldsymbol{x}) \equiv \int\limits_0^\infty R_{ii}\left(\boldsymbol{x},\boldsymbol{\sigma}\right)d\boldsymbol{\sigma} \tag{5.8}$$

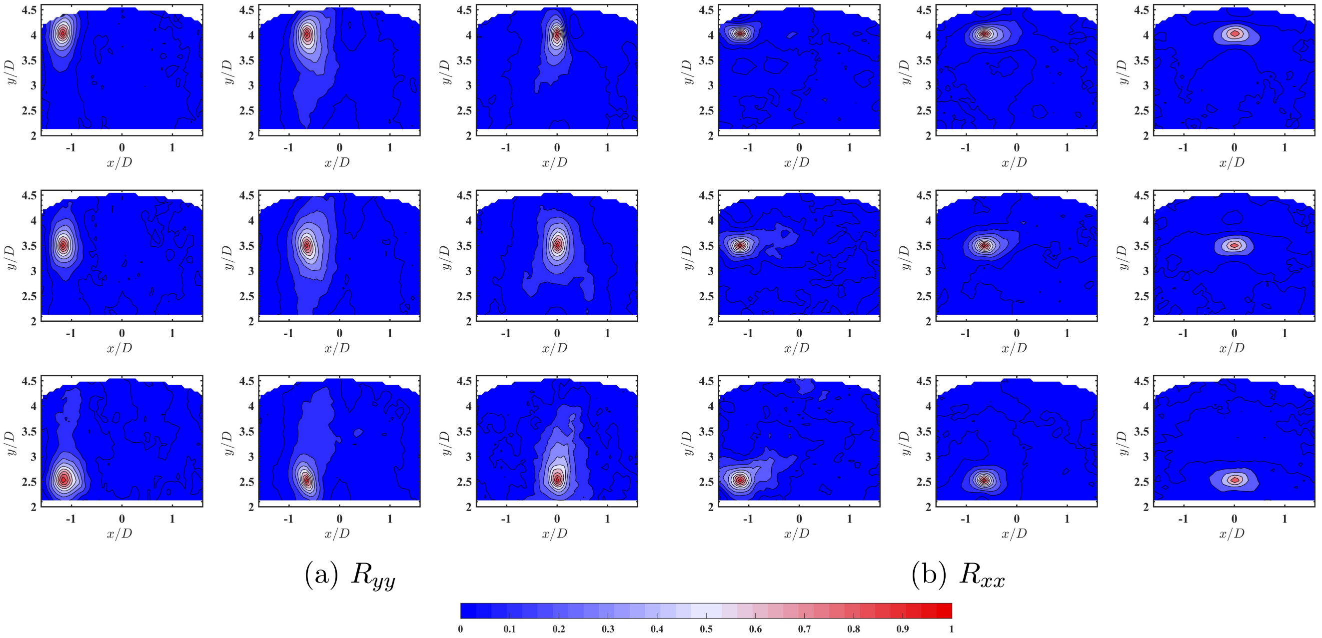

(a) R_{yy} (b) R_{xx}

Figure 5.18: Two-point cross-correlation contours at various points for case TJa. From left to right: x/D =-1.21, -0.7, 0; From bottom to top: y/D =2.5, 3.5, 4.

Figure 5.19 shows the directional integral length scales at different elevations for the three cases. It can be seen from Figure 5.19 (a)-(c) that the streamwise integral length scale l_{yy} falls in the range of $0.4D \sim D$. The distribution of l_{yy} shows a double-peak profile. As y/D increases, l_{yy} shows a decreasing trend in the center. The lateral integral length scale l_{xx} is in the range of $0.3D \sim 0.8D$. A single peak at the center at $y/D = 2.5$ is seen for l_{xx} but gets smoothed at $y/D = 3.5$ and $y/D = 4$.

5.2.2.5 Density effect on the flow pattern

Figure 5.20 illustrates the velocity field of cases involving density differences. The averaged velocity contour is normalized by the average velocity of the air inlet V_o and the inlet diameter D. The equal-length arrow indicates the flow direction. For cases TJDDb ($Re^* = 1, Gr = 2.3 \times 10^{-8}$) and TJDDc ($Re^* = 1.38, Gr = 2.3 \times 10^{-8}$), argon (left) and air (right) were injected. Consequently, the left inlet has a higher density and, therefore, lower velocity than the right inlet when $Re^* = 1$ (case TJDDa). This asymmetry shifts the wall jet impingement location to the left side of the center, resulting in two asymmetric recirculation

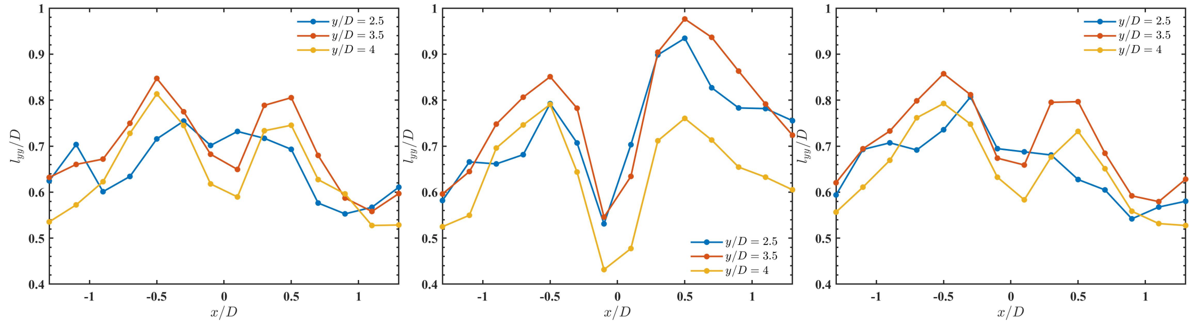

(a) TJa, l_{yy}/D (b) TJb, l_{yy}/D (c) TJc, l_{yy}/D

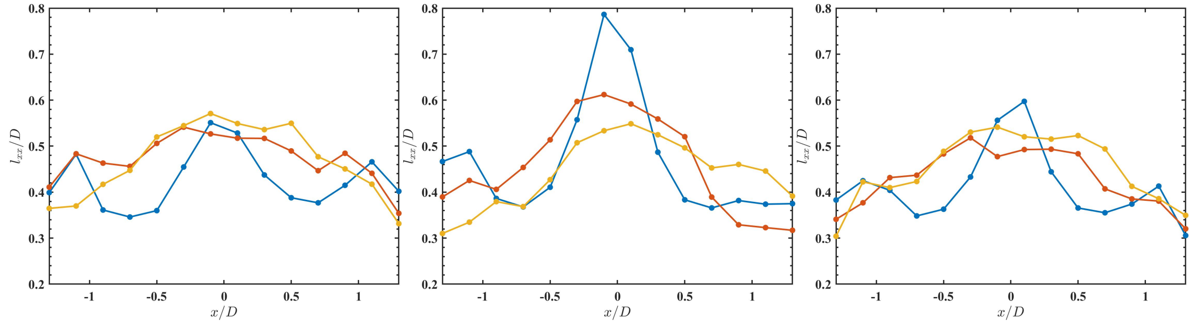

(d) TJa, l_{xx}/D (e) TJb, l_{xx}/D (f) TJc, l_{xx}/D

Figure 5.19: The profiles of the directional integral length scales at $y/D = 2.5, 3.5, 4$ for the three cases, normalized by the inlet jet diameter D.

zones and the deflection of the buoyant argon jet. The larger recirculation zone on the right side causes additional momentum transport from the buoyant argon jet to the air jet, as indicated by the flow direction of the arrows. As the normalized Reynolds number Re^* increases further for the buoyant argon jet in case TJDDc ($Re^* = 1.38$), the wall jet impingement location shifts to the right side of the center, leading to a deflection observed for the air jet. When the Gr number increased, that is for cases TJDDd ($Re^* = 0.12, Gr = 5.2 \times 10^8$) and TJDDe ($Re^* = 0.24, Gr = 5.2 \times 10^8$), the pattern of recirculation has differed considerably. With helium (left) and air(right) injected, the helium jet has a significantly lower density than the air jet. The gradient of density between the two jets has caused the recirculation to lean more toward the helium jet.

In the uniform environment, the interaction of the two jets was found to cause low-frequency periodicities near the downwash fountain flow. PSD analysis that was used to study the uniform cases is employed here to examine the effect of density difference on the

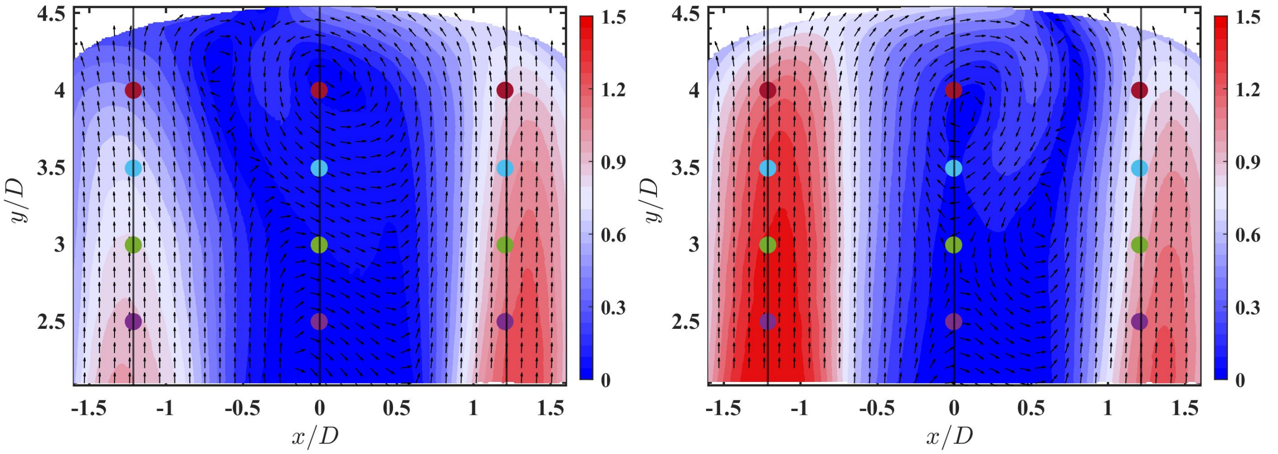

(a) TJDDb ($Re^* = 1, Gr = 2.3 \times 10^8$)

(b) TJDDc ($Re^* = 1.38, Gr = 2.3 \times 10^8$)

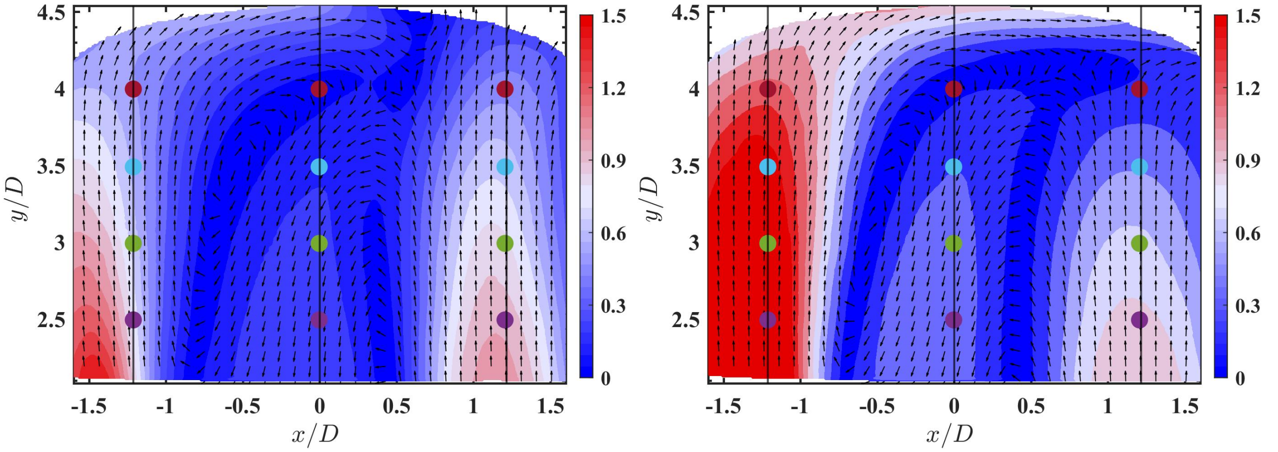

(c) TJDDd ($Re^* = 0.12, Gr = 5.2 \times 10^8$)

(d) TJDDe ($Re^* = 0.24, Gr = 5.2 \times 10^8$)

Figure 5.20: The averaged velocity field, normalized by the same inlet velocity $V_o = 1.4 m/s$. The contour represents the velocity magnitude, and the equal-length arrow shows the flow direction. Dots indicate the location for PSD analysis

periodicities. The locations that were used for the analysis have been indicated by the dots in Figure 5.20. Figure 5.21 shows the PSD spectrum for the four cases at several selected locations. It can be inferred from Figure 5.20 that the low-frequency oscillation is present for the cases with density variations.

For case TJDDb, multiple dominant peaks have been observed. Peaks ***a*** and ***b*** shown in the subplot of TJDDb are near the dome top for the argon jet, where the deflection happens. Peaks ***c*** and ***d*** shown in the subplot of TJDDb are near the bottom of the air jet, where the air jet is influenced greatly by the large recirculation flow. For case TJDDc, the dominant peaks are mostly seen for the air jet (Peaks ***a,b,c*** the subplot of TJDDc) since the air jet side is more subjected to the effect of wall jet impingement in this scenario. For case TJDDd, no dominant frequencies are apparent, while for case TJDDe, the overall power contained in the spectrum for the helium jet is significantly higher than that of the air jet. In general, it can be seen that the flow pattern becomes more intricate when the density effect is evolved, though a more systematic study with the density field involved is necessitated in further work to fully understand the flow dynamics.

5.2.3 Conclusions and Future Work

In this work, flow mixing in the MiGaDome facility that is 1/12th scaled-down from the HTGRs upper plenum has been investigated using two jets. PIV measurements were first conducted for three cases: TJa (Re=4097), TJb (Re=4097 v.s. 6021), and TJc (Re=6021). Then additional measurements with density variation were conducted for four cases (TJDDb, TJDDc, TJDDd, and TJDDe)

The analysis was first conducted for the three uniform injection cases. From the snapshots of the instantaneous vector field, intense turbulent mixing with spanwise vortices of various sizes is observed for all three cases. A PSD analysis on the instantaneous flow field with a $7.5Hz$ cutoff frequency has shown low-frequency fluctuations of $St = 0.0144$ and $St = 0.0120$ at the center between two jets for the uniform injection cases TJa and TJc, respectively.

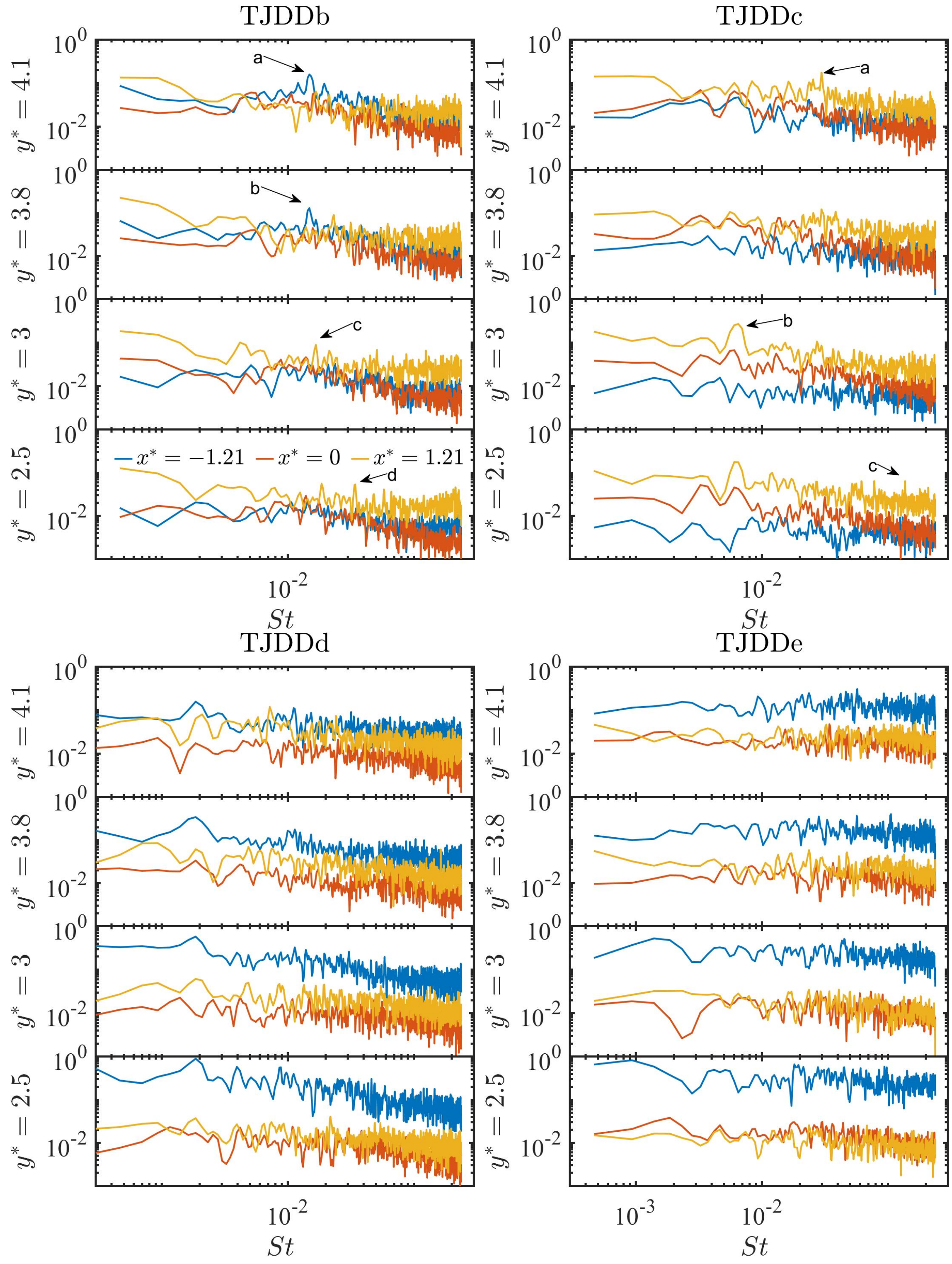

Figure 5.21: PSD analysis of cases with density variations at selected locations.

Time-averaged flow fields obtained through ensembling averaging show that a down-wash fountain flow has formed due to the wall jet impingement for the uniform injection cases, while a clockwise recirculation has formed for the uneven injection case TJb. The mixing between the two jets has also been characterized by looking into the jet half-width in the inner mixing layer. Turbulent fluctuations are quantified by plotting the distribution of the Reynolds stresses, with the finding that the largest turbulent fluctuations/Reynolds normal stresses are in the fountain flow region. Lastly, the turbulent integral length scales are also calculated based on the two-point spatial cross-correlation. For all the cases, the streamwise integral length scale l_{yy} falls in the range of $0.4D \sim D$, and the lateral falls in the range of $0.3D \sim 0.8D$.

The effect of the density on the flow pattern was then analyzed by examining the four cases with density variations. The flow pattern becomes more intricate when the density effect is evolved. Though a more systematic study with the density field involved is necessitated in further work to fully understand the flow dynamics, the obtained data for the cases with density variation has become a valuable validation source. Recently, the experimental data has been selected as the benchmark data for the first annual nuclear thermal hydraulics competition held by the American Society of Thermal and Fluids Engineers (ASTFE) [163].

5.3 MiGaDome: Multi-jet interactions

5.3.1 Test Matrix and Region of Interest

This study investigated three different injection configurations: three adjacent jets (MJa), six jets of the same Reynolds number (MJb), and six jets of two different Reynolds numbers (MJc), the patterns of which are shown in Fig. 5.22. The 2D field of view in the experiment is located above one of the jet inlets, which is the same as the measurement in Fig 5.1. The experiments were conducted in a uniform-density environment using compressed air. The PIV system parameters, along with the flow field variables, for the three studied cases are summarized in Table 5.4.

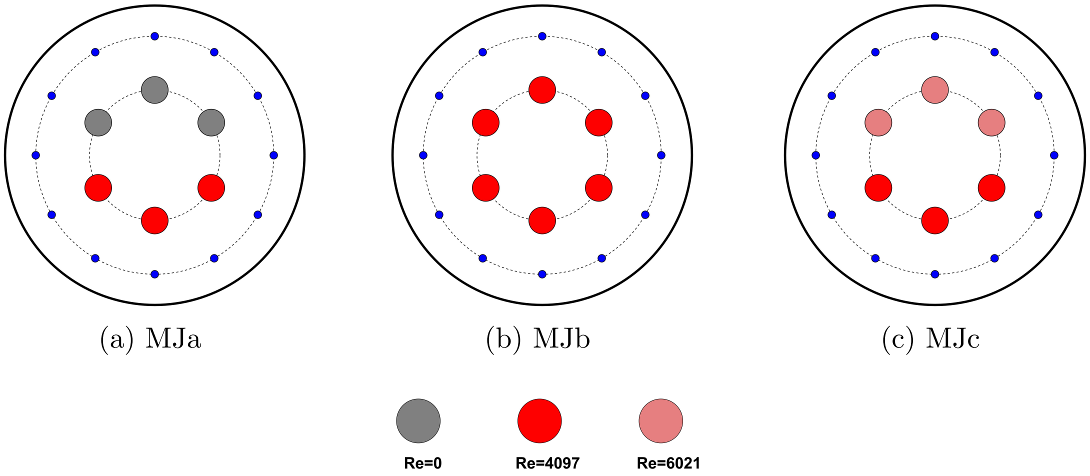
(a) MJa

(b) MJb

(c) MJc

Figure 5.22: Schematics of the multi-jet injection schemes.

Table 5.4: PIV imaging parameters and flow conditions for multi-jet injections.

Parameter	MJa	MJb	MJc
Jet injection	Three	Six	Six
Recording rate (Hz)	15	15	15
Interframe rate (Hz)	3000	3000	3000
Temperature (°C)	21	22	22

5.3.2 Results and Discussion

5.3.2.1 comparison of the flow pattern

Figure 5.23 shows the velocity field of the three cases. It can be seen that a downward fountain flow, which was observed in the two jets scenarios, has also been shown for cases MJa and MJb. However, the influence of the downward fountain flow has different effects on the jet core for the two cases. For case MJa (three jets), a recirculation zone has been established between the jet core and the fountain flow. Instead, the downward fountain flow directly impinges with the upward flow engulfed by the jet core for case MJb (six jets). This difference is expected when considering the following: the spreading of the injected jet momentum in this confined volume is restricted by the degree of freedom. In the scenario of three neighboring jets (MJa), the entrained upward flow by the jet core can escape from the observation plane and into the out-of-plane region above the unused inlets, where a low-pressure zone is established compared to the jet-occupying region. The downward fountain flow thus can easily entrain the fluid and form a recirculation region next to the jet core. For the scenario of six jets (MJb), the out-of-plane freedom has been eliminated by the presence of the additional jets. The engulfed upward flow then more likely stays in the observed plane and competes with the downwash flow.

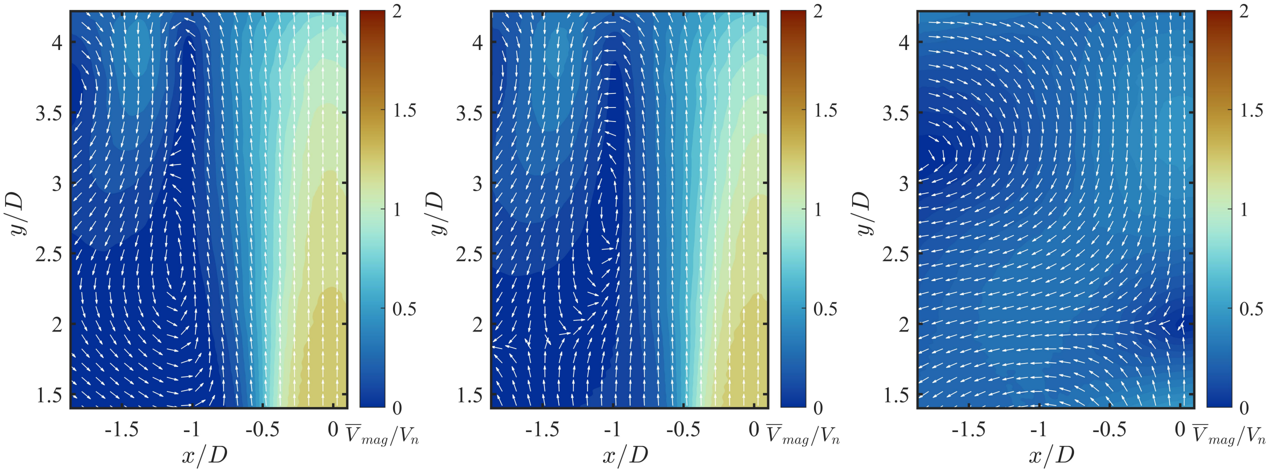

(a) MJa (b) MJb (c) MJc

Figure 5.23: Velocity contours of the multi-jet cases.

For the uneven six-jet injection case MJc, the flow pattern distinctly differs from case MJa and MJb, as is shown in Figure 5.23c. No jet core with high momentum is observed in the measurement plane in this scenario. It is observed that a downward flow dominates and suppresses the upward flow in the lower region of the plane, causing a direct impingement between fluids.

Reasons leading to this special flow pattern can be explained by reviewing the two jets case TJb, which is present in Figure 5.14. As has been shown in Figure 5.14, when one side of the jet has higher momentum compared to another one, the wall jet formed after the higher-momentum jet will impel the flow into the region above the lower-momentum jet. This multi-jet scenario has multiplied this effect since one side of the inlets has higher momentum than the other ($Re = 6021$ vs $Re = 4097$). Because half of the inlets have higher injection momentum, the flow from the high-momentum inlets will intrude into the side with low jet injection momentum. As a result, the flow field has demonstrated a suppressed jet core and a reversed flow from the dome top on the observed plane.

5.3.2.2 POD analysis of the flow field

To gain an insight into the turbulence structures of the flow, modal decomposition methods can be applied to visualize the spatial coherent structure of the turbulent eddies. Identification and modeling of these coherent structures are essential for understanding transport and flow mechanisms in the flow field [164]. Here the Proper Orthogonal Decomposition (POD) is employed. Details of the principle and implementation of this method can be found in [165]. In brief, POD decomposes the instantaneous vector field representing turbulent fluid motion into a spatially dependent set of deterministic modes, as is demonstrated in Equation 5.9.

$$\boldsymbol{v}'(\boldsymbol{x},t) = \sum_{k=1}^{\infty} a_k(t)\mathit{\Phi}_k(\boldsymbol{x}) \tag{5.9}$$

where $\mathit{\Phi}_k(\boldsymbol{x})$ represents the deterministic mode and $a_k(t)$ is the time coefficient. Each mode has an associated eigenvalue λ_k that ranks the modes according to their contribution to the total variance, which in this case, is the kinetic energy of the velocity fluctuations. One general practice when applying the POD is ordering the eigenvalue λ_k from the largest to the smallest so that the modes that contribute the most to the kinetic energy can be easily identified. Based on this technique, the 2D instantaneous velocity fluctuations from the PIV measurement are decomposed into sets of spatial modes.

Figure 5.24 reports the first four modes for the three cases. For each mode on the contour, the coherent structure can be interpreted as synchronized fluctuation or anti-correlated velocity fluctuations. Regions where the spatial mode has the same sign represent a synchronized fluctuation, while regions with the opposite sign mean the anti-correlated velocity fluctuations at both measurement points [165].

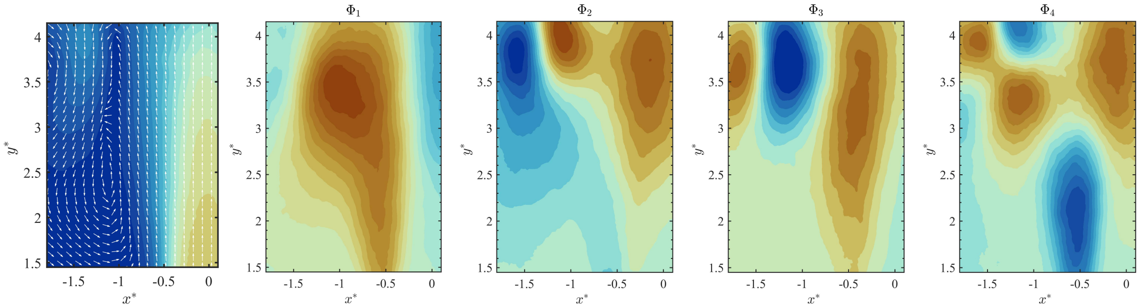

(a) MJa, averaged flow field and the first 4 POD modes.

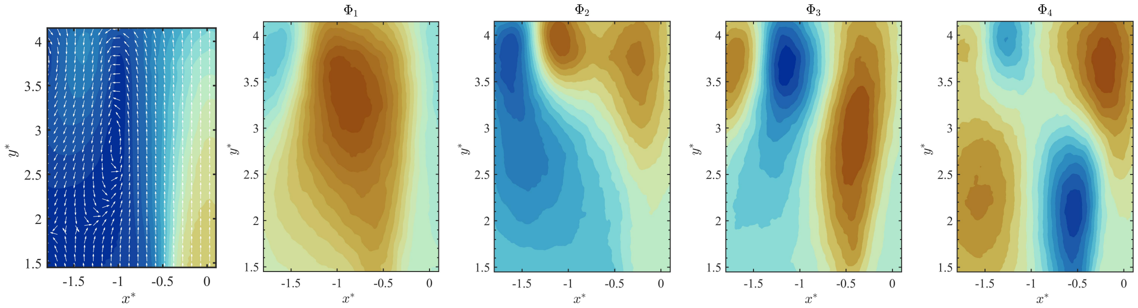

(b) MJb, averaged flow field and the first 4 POD modes.

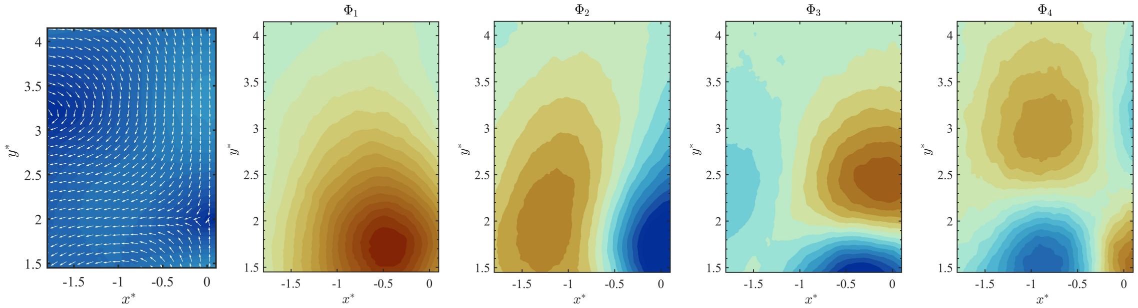

(c) MJc, averaged flow field and the first 4 POD modes.

Figure 5.24: Averaged flow field and the first 4 POD modes of the multi-jet cases.

Comparing Cases MJa (Figure 5.24a) and MJb (Figure 5.24c), it can be seen that the coherent structures are similar. A dominant large coherent structure is represented in the $1st$ mode $\varPhi_1$ for the two cases. This large structure indicates the strong synchronized fluctuation in the region between the downward fountain flow and the upward jet core. It also shows that the large structure of mode $\varPhi_1$ extends further into the left corner in case MJb compared to case MJa, indicating a stabilization effect of the recirculation in the left corner of case MJa. In addition, various coherent structures can be observed in higher modes. The second and third dominant modes $\varPhi_2$ and $\varPhi_3$ show an alternative pattern near the top region, which results from the shear layer instability and turbulence transportation after impingement.

The large structure in mode Φ_1 of case MJc, is centered in the lower region of the contour where the jet-to-jet impingement happens. The fading color away from the lower region indicates a synchronized fluctuation in the whole measurement plane. The strong jet-to-jet impingement is also responsible for the other smaller alternative coherent structures in higher modes.

The contribution of each mode and the cumulative contribution from the modes to the overall fluctuations are plotted in Figure 5.25. Similar modal energy distribution and cumulative modal energy distribution are shown for both cases MJa and MJb, since the flow pattern and fluctuation patterns are quite similar. The modal energy distribution for the first few modes from case MJc accounts for more total kinetic energy as compared to the other two cases. As a result, the cumulative modal energy distribution for the first 20 modes from case MJc also shows a higher value. This means fewer modes are needed when one wants to reconstruct the flow field with certain energy reserved (for example, 50% energy reserved) for case MJc compared to other cases.

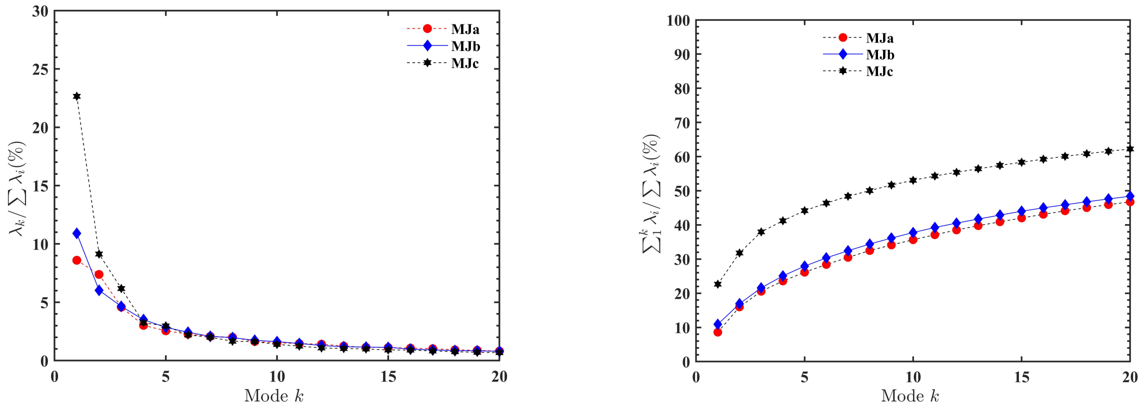

(a) POD modal energy distribution

(b) POD cumulative modal energy distribution

Figure 5.25: Modal energy distribution of the first 20 modes for the multi-jet cases

5.3.3 Conclusions

In the present study, the flow mixing under three different injection configurations: three adjacent jets (MJa), six jets of the same Reynolds number (MJb), and six jets of two different

Reynolds numbers (MJc), have been investigated experimentally using the 2D PIV technique. The obtained flow fields from the three cases have been analyzed. It has been shown that the flow field of interest for the three-jet injection case is similar to the flow of the six-jet injection when all the inlets have the same Reynolds number. The flow pattern from case MJc, however, differs from the other cases due to jet-to-jet impingement. POD analysis shows similar coherent structures in the first few dominant modes for cases MJa and MJb, and the modal energy contribution to the total turbulent kinetic energy also has a similar distribution. The coherent structures in the first few dominant modes for case MJc are different from the other cases as the main fluctuation, in this case, is centered near the jet-to-jet impingement region. Besides, a higher cumulative modal energy contribution in the first 20 modes is seen in MJc compared to the other two cases.

5.4 HiRJet : Propagation of stratified front

To further provide CFD-grade experimental data on stratification and eliminate the unnecessary geometrical effects as mentioned in Ref.[166], the High-Resolution Jet (HiRJet) facility at the University of Michigan has been designed and is currently in operation. With the aid of the advanced Wire-Mesh Sensor (WMS) technique, the time-dependent density distribution on a 2D plane in the test section has been captured with a high-spatial and high-temporal resolution. An experimental campaign was performed to establish a high-resolution database to characterize stratified front propagation at medium Reynolds numbers and validate the numerical simulations. High-fidelity Direct Numerical Simulations (DNS) are also conducted parallelly for this HiRJet facility by North Carolina State University (NCSU) to complement the experimental campaign and expand the knowledge basis on stratification from the high-fidelity data [15]. So far, a total of eight cases of different conditions have been collected by Dr. Vineet Vishwakarma. A more detailed analysis of the experiments can be found in [167]. In this thesis, two of the cases are selected as representative of the stratification process and will be used for validating CFD simulations, which will be discussed in detail in Chapter VII.

5.5 Conclusions and Future Work

The primary objective of the research effort presented in this chapter was to create high-resolution experimental datasets focusing on mixing in large enclosures and thermal stratification, utilizing the MiGaDome and HiRJet facilities.

In the MiGaDome facility, a comprehensive exploration of various injection schemes was conducted. Findings from single air jet injections revealed that the normalized statistics of the jet exhibit asymptotic behavior as the Reynolds number increases. Analysis of the 2D budgets for the momentum equation indicated a minor contribution of turbulent diffusion near the enclosure's surface, where strong convection occurs due to impingement. For two jets without density variations, time-averaged flow fields obtained through ensemble averaging pointed out to the formation of a down-wash fountain flow due to wall jet impingement in even injection cases, while an anticlockwise recirculation was found to form in the case of uneven injection (TJb). An initial examination of density effects on two-jet interactions showcased increased complexity in the flow pattern with evolving density effects. Regarding multiple jets, it was observed that the flow field for the three-jet injection case resembles that of the six-jet injection when all inlets have the same Reynolds number. For HiRJet, the study focused on the propagation of stratified fronts with different injection schemes, resulting in eight test cases. Two of these cases will be employed to validate CFD simulations, elaborated in Chapter VII.

Several future investigations are recommended to enhance the understanding of mixing in large enclosures. Firstly, the region of interest for measuring the MiGaDome facility has primarily focused on a vertical plane. It would be of great interest to study cross-flow between jets through measurements on a horizontal plane as well. Secondly, for the frequency study in the MiGaDome facility, future work necessitates time-resolved measurements to increase the cutoff frequency. This will allow for the study of the flow and identification of oscillations beyond the current cutoff frequency, if permitted by the hardware. Lastly, a more systematic study on flow mixing with density effects in the MiGaDome facility, incorporating both velocity and density field measurements, would be of great importance to further understand the flow dynamics. For the HiRJet facility, future work necessitates expanding the database to include a broader range of flow rates and density variations.

CHAPTER VI

Validation of Turbulence Models: MiGaDome

6.1 Introduction

While the focus of the present dissertation was on the establishment of a high-fidelity experimental database, preliminary efforts were dedicated to the validation of CFD RANS models as well. In this chapter, we will use experimental results from a single jet injection in the MiGaDome facility, along with high-fidelity LES simulations [14], to assess the performance of RANS models.LES can provide essential reference data and a wealth of information in addition to the high-resolution experimental data, which is limited to 2D measurements [60]. We have chosen the isothermal single-jet case as the reference case due to its relative simplicity compared to other more complex multi-jet cases. This relatively simple configuration can serve as a solid foundation for further extending the validation framework into more complex cases once validated. We will investigate and compare the profiles of both first-order and second-order turbulence statistics from RANS with both the experiment and LES. The combination of high-resolution experiments and LES/DNS can provide detailed physical insight into the shortcomings of RANS models.

6.2 Test Matrix

Measurements on the MiGaDome facility have been conducted with various injection schemes, as summarized in Chapter V. In this context, the single-jet injection with $Re = 4000$ has been selected to illustrate the framework of combining high-resolution experiments with high-fidelity simulations for benchmarking RANS simulations. The flow rate, along with the fluid properties, is summarized in Table 6.1. The LES simulation was performed using NekRS, and a detailed description can be found in [14].

Both first- and second-order statistics predicted by the LES simulation have demonstrated excellent agreement compared to experiments. It is therefore assumed that the out-of-plane information from the LES, not captured by the experiments due to the limitations of the 2D PIV technique, is trustworthy and can be used to benchmark the RANS simulations.

Table 6.1: Flow rate and fluid properties for the turbulent single jet

Re	4000
$\dot{m}$	$2.596 \times 10^{-3} kg/s$
ρ	$1.194 kg/m^3$
μ	$1.823 \times 10^{-5} Pa \cdot s$

6.3 Computational Domain and Mesh Independence Study

The computational domain is constructed from the 3D CAD model of the MiGaDome facility using STAR-CCM+, as illustrated in Figure 6.1. This domain primarily comprises a dome-shaped volume with extrusions, featuring 6 inlets and 12 outlets. In the simulation, only the highlighted inlet, as shown in Figure 6.1b, will be utilized to specify velocity and turbulence intensity. The 12 small outlets are designated as pressure outlets, while the other boundaries are set as walls.

The origin of the coordinate system is at the inlet center and located on the bottom plate, consistent with the experimental setup. The y direction points in the anti-gravity direction, while the z direction points toward the nearest outlet.

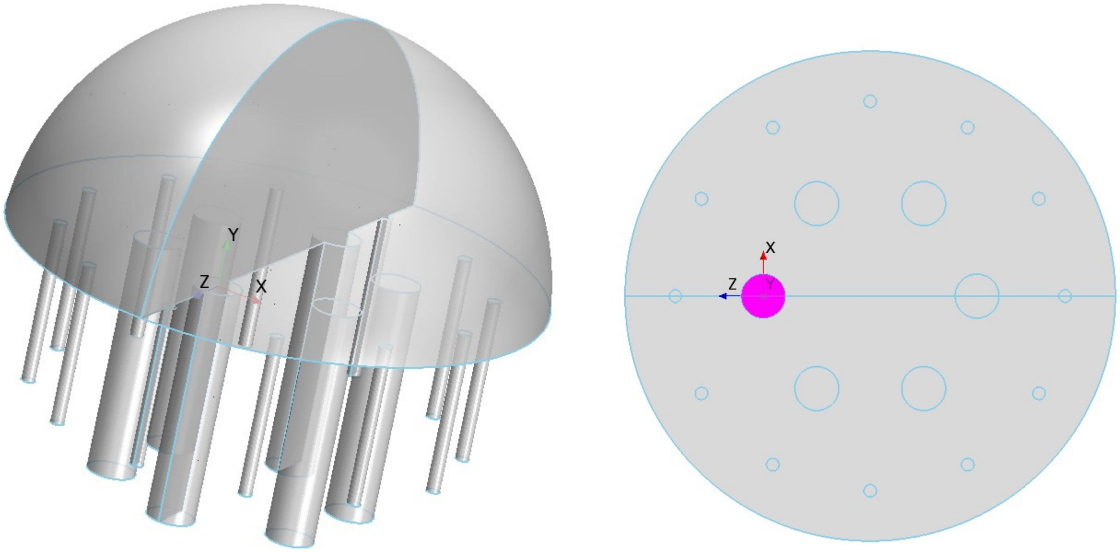

(a) Angled view (b) Bottom view

Figure 6.1: Computational model and the coordinate system for MiGaDome enclosure, with (a) Angled view and (b) Bottom view to show inlet and outlets. The inlet has been highlighted with light red color.

A mesh sensitivity study was conducted using three different mesh configurations. These meshes were generated by gradually refining the base size, as summarized in Table 6.2. For the mesh convergence study the RST model was used together with fully developed inlet flow boundary conditions. Fully developed inlet profiles were obtained by running a separate round pipe simulation with periodic boundary conditions. Figure 6.2 displays velocity, turbulence kinetic energy, and turbulent dissipation rate profiles obtained for various mesh sizes. The results indicate that both first- and second-order quantities are independent of mesh size when a value less than 2mm is chosen. Therefore, the mesh configuration with $\Delta x = 1.5$mm was selected for the simulations. Figure 6.3 provides details of the mesh.

Table 6.2: MiGaDome mesh information

Mesh Number	Δx(mm)	Number of Cells (Millions)
1	2.5	1.67
2	2	2.77
3	1.5	5.86

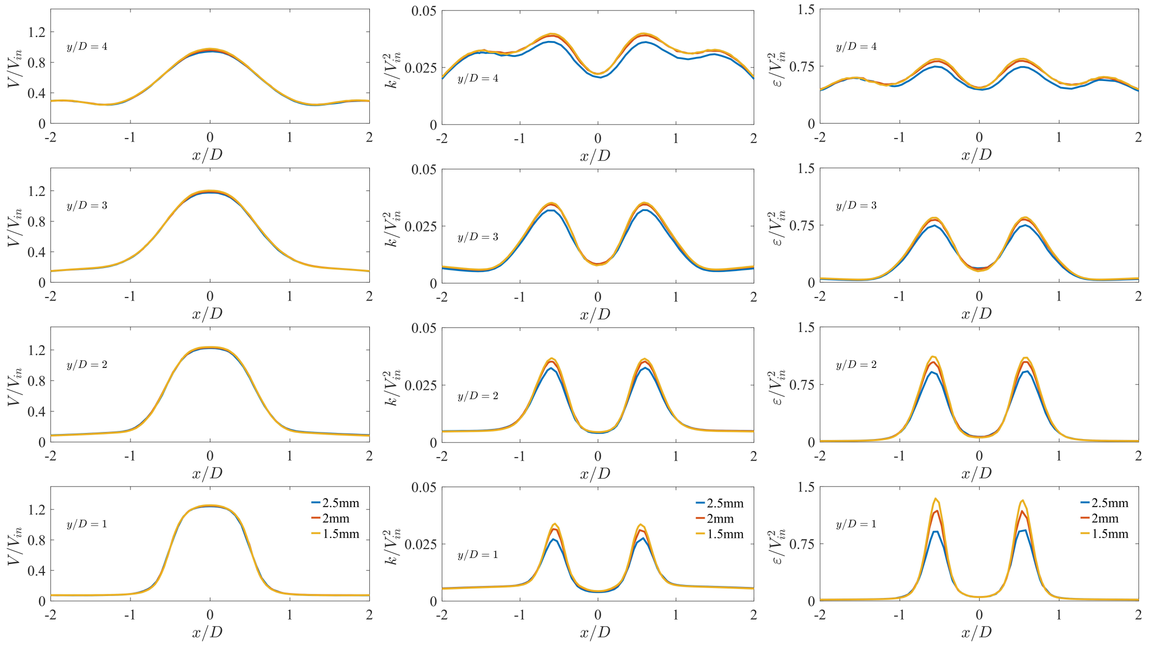

(a) Velocity (b) TKE (c) TDR

Figure 6.2: Profiles of normalized velocity, Turbulent Kinetic Energy (TKE), and Turbulent Dissipation Rate (TDR) for different grid sizes.

6.4 Inlet Conditions and Turbulence Models

Reliable turbulent boundary conditions at the inlet of the computational domain are essential to complete the simulations. As demonstrated by the measurements [141], a fully developed flow is achieved before the dome inlet. Consequently, a fully developed velocity profile is enforced at the inlet boundary. Regarding the inlet turbulence, the turbulent intensity is set based on the inlet LDV measurement [141], and the turbulent length scale is established at $0.07D$, referring to both the measurement results and the typical turbulent length scale in pipe flow.

The performance of several widely used turbulence models has been investigated, including the Standard $k-\varepsilon$ LowRe (SKELowRe) model, the Realizable $k-\varepsilon$ (RKE) model, the Reynolds Stresses Transport (RST) model, and the $k-\omega(SST)$ (KOmegaSST) model. Each simulation employed a steady-state solver with the default model setup, except for the KOmegaSST model, where the Low-Re Damping option was activated. Data collection for

(a) Overview

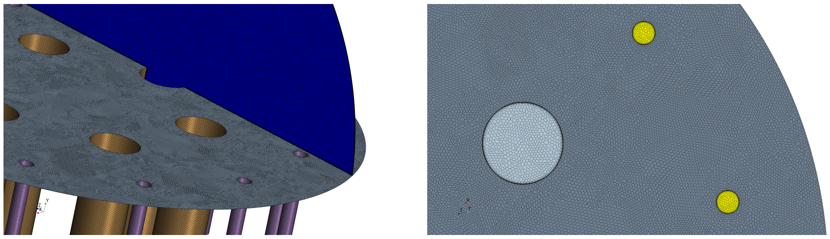

(b) View of the dome (c) View of the inlet

Figure 6.3: Views of the mesh details.

statistics was carried out until the residuals exhibited no further changes, and the residual values dropped below 10^{-6}.

6.5 Results and Discussion

6.5.1 Visualization of the velocity field

Firstly, a visualization of the flow field in the MiGaDome enclosure is presented in Figure 6.4. Figure 6.4a shows the steady-state flow distribution in the MiGaDome enclosure on two orthogonal planes as computed with the SKELowRe model. The vector field is visualized through the black vectors, and a mean velocity contour on the $z/D = 0$ plane is also present to visualize the jet core. Note that the simulations performed using other RANS models present similar qualitative distributions; thus, only one simulation result is present here to explain the phenomenon of what occurs in the enclosure.

The vector field in Figure 6.4a reveals the formation of multiple recirculation zones in the enclosed space. Due to the asymmetrical positioning of the inlet relative to the enclosure, the sizes and locations of these recirculation zones vary depending on the observation plane. On the $z/D = 0$ plane, the jet exhibits symmetry in both $+x$ and $-x$ directions. The two recirculation zones on either side of the jet are symmetrically distributed, so only one side is depicted in Figure 6.4a. However, given the inlet closer proximity to the outlet in the $+z$ direction, a smaller recirculation zone is observed on the $+z$ side compared to the $-z$ side. This prediction qualitatively aligns with the LES results, as illustrated in Figures 6.4b and 6.4c.

6.5.2 Planes of interest

Taking into account the asymmetrical features, two planes are chosen for a more in-depth investigation of the RANS models predictions. The first plane is situated at $z/D = 0$, as depicted in Figure 6.5a. Another plane is positioned at $y/D = 3$, providing a top view of the jet, as shown in Figure 6.6a. Both velocity contours are derived from the SKELowRe model to enhance visualization. To facilitate further comparison, several line profiles will be extracted from these two planes, as indicated in the velocity contours. For the $z/D = 0$ plane, the profiles are obtained from locations $y/D = 1.8, 2.5, 3, 3.5$. On the $y/D = 3$ plane, the profile locations follow an azimuthal direction ($\theta = 0, \pi/4, \pi/2, 3\pi/4, \pi$), with $\theta = 0$ aligning with the $+z$ axis.

The first selected plane provides a clear depiction of how the jet develops with increasing height, entraining the surrounding flow and spreading as it ascends. This observation aligns with the velocity profiles from both the experiment and LES, as illustrated in Figure 6.5b. On the second selected plane, the asymmetry of the jet is evident due to the influence of different recirculation zones. Velocity profiles at various θ from LES on this plane are

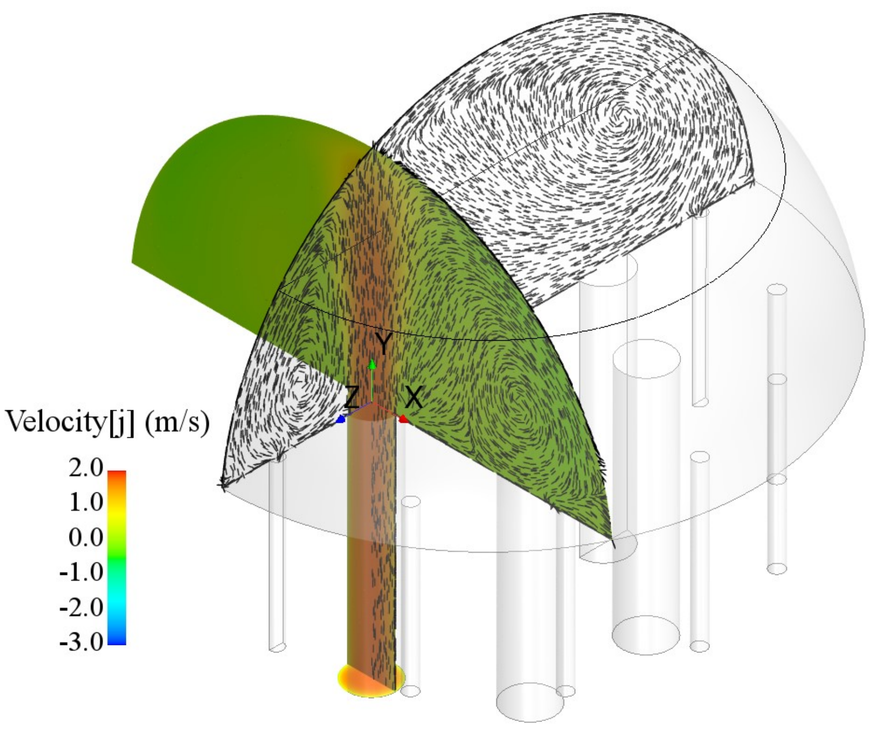

(a) An angled view of the mixing in MiGaDome enclosure at two planes with vector field and velocity contour from simulation using SKELowRe model.

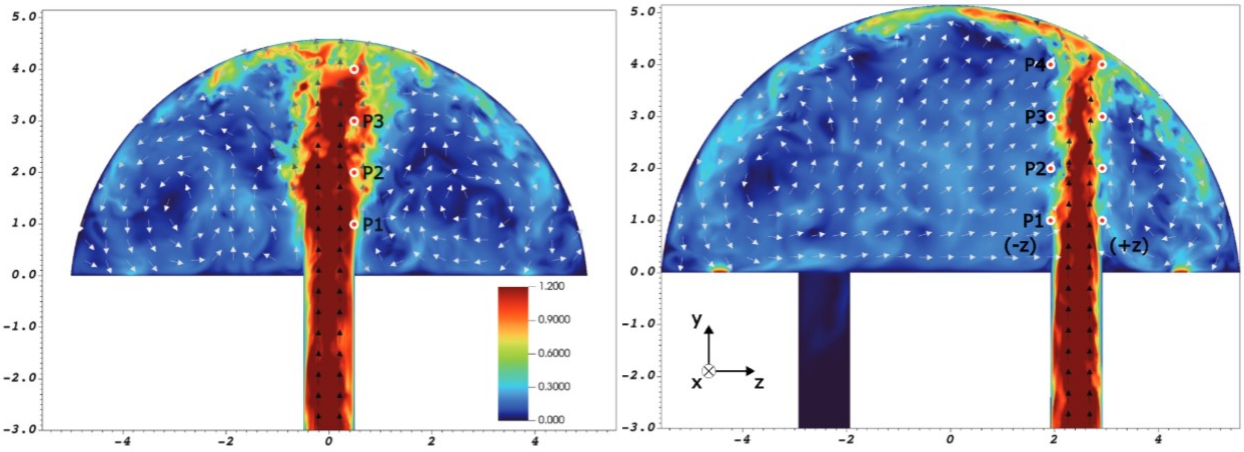

(b) Velocity vector at the $z/D = 0$ plane from LES.

(c) Velocity vector at the $x/D = 0$ plane from LES.

Figure 6.4: Visualization of the mixing in MiGaDome enclosure from simulation using SKELowRe model and its qualitative comparison with LES. Note the contours for the LES simulation represent an instantaneous snapshot of the velocity, and the average velocities are shown using constant length-vectors [14].

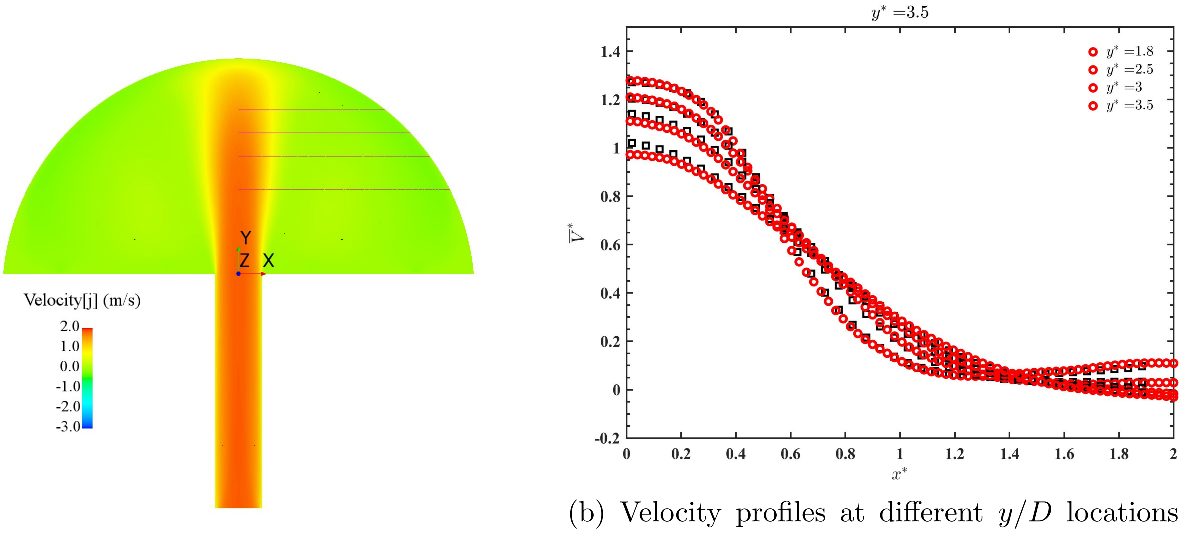

(a) Velocity contour on the $z/D = 0$ plane from SKELowRe model.

(b) Velocity profiles at different y/D locations from experiment (Black square) and LES (Red circle).

Figure 6.5: Velocity contour on the $z/D = 0$ plane from SKELowRe model and profiles at several y/D locations from experiment and LES. The profiles have been normalized by the inlet velocity and the inlet diameter.

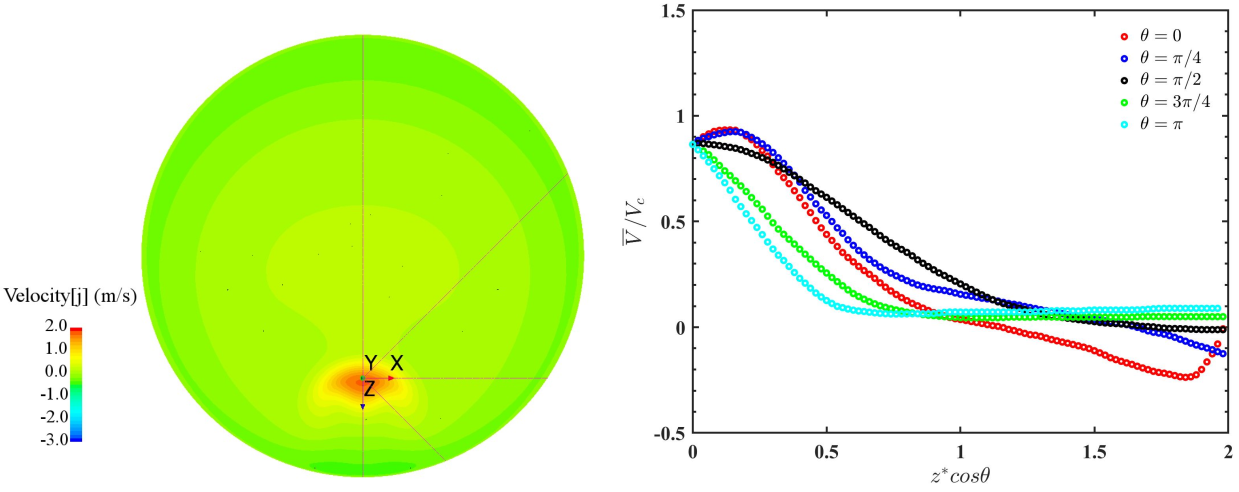

(a) Velocity contour on the $y/D = 3$ plane from SKELowRe model.

(b) Velocity profiles at different locations from LES.

Figure 6.6: Velocity contour on the $y/D = 3$ plane from SKELowRe model and profiles from LES at several different azimuthal angles θ locations ($\theta = 0$ is aligned with $+z$ axis). The profiles have been normalized by the centerline velocity and the inlet diameter.

displayed in Figure 6.6b. It is important to note that these profiles have been normalized by the centerline velocity. Examining the profiles at $\theta = 0$ and $\theta = \pi/4$ reveals a noticeable shift in the locations of maximum velocity away from the jet center, moving more towards the outlets. As the angle θ increases, the location of maximum velocity gradually re-centers into the pipe center.

6.5.3 Validation data from experiment and LES

The validation of RANS models utilizes both experimental and LES data. The experimental data were measured solely on the $z/D = 0$ plane, allowing for the direct extraction of velocity and Reynolds stress information at lines $y/D = 1.8, 2.5, 3, 3.5$ on this plane for comparison. In contrast, LES simulations provide information on both observing planes. The RANS models are validated by comparing the profiles with both the experiment and LES data. Before delving into RANS validation, a preliminary comparison between the experiment and LES has been conducted to establish the reliability of the LES data.

The normalized velocity profiles on the $z/D = 0$ plane at several y/D locations are presented in Figure 6.5b. Additionally, Figure 6.7 presents the profiles of second-order Reynolds normal stresses on the same plane at different y/D locations. These profiles have been normalized by the square of the inlet average velocity. Notably, the results from LES exhibit good agreement with the experimental data. To quantitatively assess the difference between the experiment and LES, a normalized error, denoted as σ, is defined:

$$\sigma(\%) = \frac{\sqrt{\sum_{i=1}^{n} (\ f_i - F_i)^2}}{\sqrt{\sum_{i=1}^{n} F_i^2}} \tag{6.1}$$

Where f_i represents the point-wise data from the simulation, and F_i represents the corresponding point-wise data from the experiment. Table 6.3 presents the normalized error resulting from the profiles comparison. As the out-of-plane Reynolds normal stress $\overline{w'w'}$ is unavailable in the experiment, the σ_k for turbulent kinetic energy is estimated by assuming

$\sigma_{\overline{u'u'}} = \sigma_{\overline{w'w'}}$. The values of σ_k are then computed using error propagation, and the results are displayed in Table 6.3.

The findings reveal that the maximum difference between the experiment and LES is below 2.97% for the first-order velocity profiles, while the maximum difference for the second-order Reynolds stress profiles is LESs than 8.51%. It is important to note that these computed differences are derived solely from the line profiles on the $z/D = 0$ plane, as constrained by the available experimental data. It is assumed that the profiles from LES on the $y/D = 3$ plane carry a similar magnitude of errors compared to the experiment.

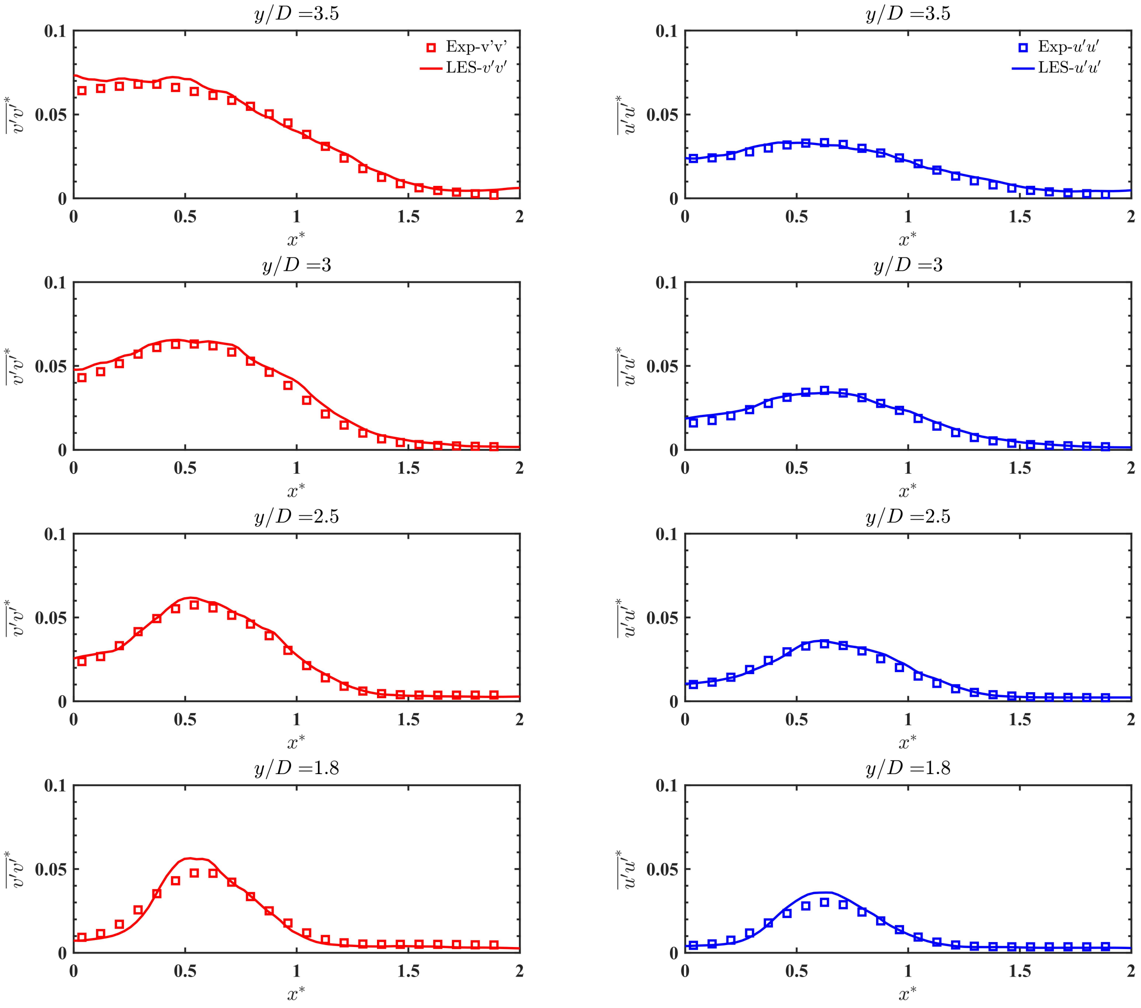

(a) Streamwise Reynolds normal stress. (b) Lateral Reynolds normal stress.

Figure 6.7: Comparison between experiment and LES on the profiles of Reynolds normal stresses at several y/D locations on the $z/D = 0$ plane. The profiles have been normalized by the square of the inlet average velocity and the inlet diameter.

Table 6.3: Normalized errors of first- and second-order quantities between experiment and LES.

Profile Location	$y* = 1.8$	$y* = 2.5$	$y* = 3$	$y* = 3.5$
$\sigma_V(\%)$	2.26	1.67	2.52	2.97
$\sigma_{\overline{v'v'}}(\%)$	4.24	6.22	8.05	7.17
$\sigma_{\overline{u'u'}}(\%)$	6.37	8.19	8.51	6.70
$\sigma_k(\%)$	8.49	11.30	12.54	10.29

6.5.4 Validation of RANS models on the velocity profiles

The comparison of velocity profiles from RANS with the aforementioned data is presented in Figure 6.8. The profiles on the $z/D = 0$ plane obtained with RANS models are compared to both experiments and LES, while the profiles on the $y/D = 3$ plane are compared to LES only. All the profiles have been normalized by the inlet velocity and the jet inlet diameter.

Comparing CFD to PIV experiments and LES across the four turbulence models reveals that the Realizable $k-\varepsilon$ model and the Standard $k-\varepsilon$ Low-Re model consistently provide the best predictions for the velocity profiles on both planes. In contrast, the $k-\omega(SST)$ and RST models tend to deviate from the reference data. Employing the same quantification method using Eq. 6.1, the maximum disagreement is examined, and the results are summarized in Table 6.4. The mean errors on the computed velocity profiles are minimal when using the Standard $k-\varepsilon$ Low-Re model (6.6% on the $z/D = 0$ plane and 5.3% on the $y/D = 3$ plane). The mean errors on the two observing planes from the Realizable $k-\varepsilon$ model are only slightly higher than those from the $k-\varepsilon$ Low-Re model, at 7.3% and 7.9%, respectively. However, the mean errors from the $k-\omega(SST)$ and RST models are generally more than twice as large as those from the Standard $k-\varepsilon$ Low-Re model.

Table 6.4: Error from velocity profile comparison.

	y^*				Mean	θ^*				Mean
	1.8	2.5	3	3.5		0	0.25π	0.75π	π	
SKELowRe	3.8	6.5	7.5	8.5	6.6	5.3	5.4	6.4	4.2	5.3
RKE	8.1	9.2	6.5	5.5	7.3	13.7	4.7	6.8	6.5	7.9
RST	12.4	14.4	15.7	16.2	14.7	13.6	9.4	9.1	19.4	12.9
KOmegaSST	11.6	19.6	20.4	17.4	17.2	8.1	14.8	28.6	29.4	20.2

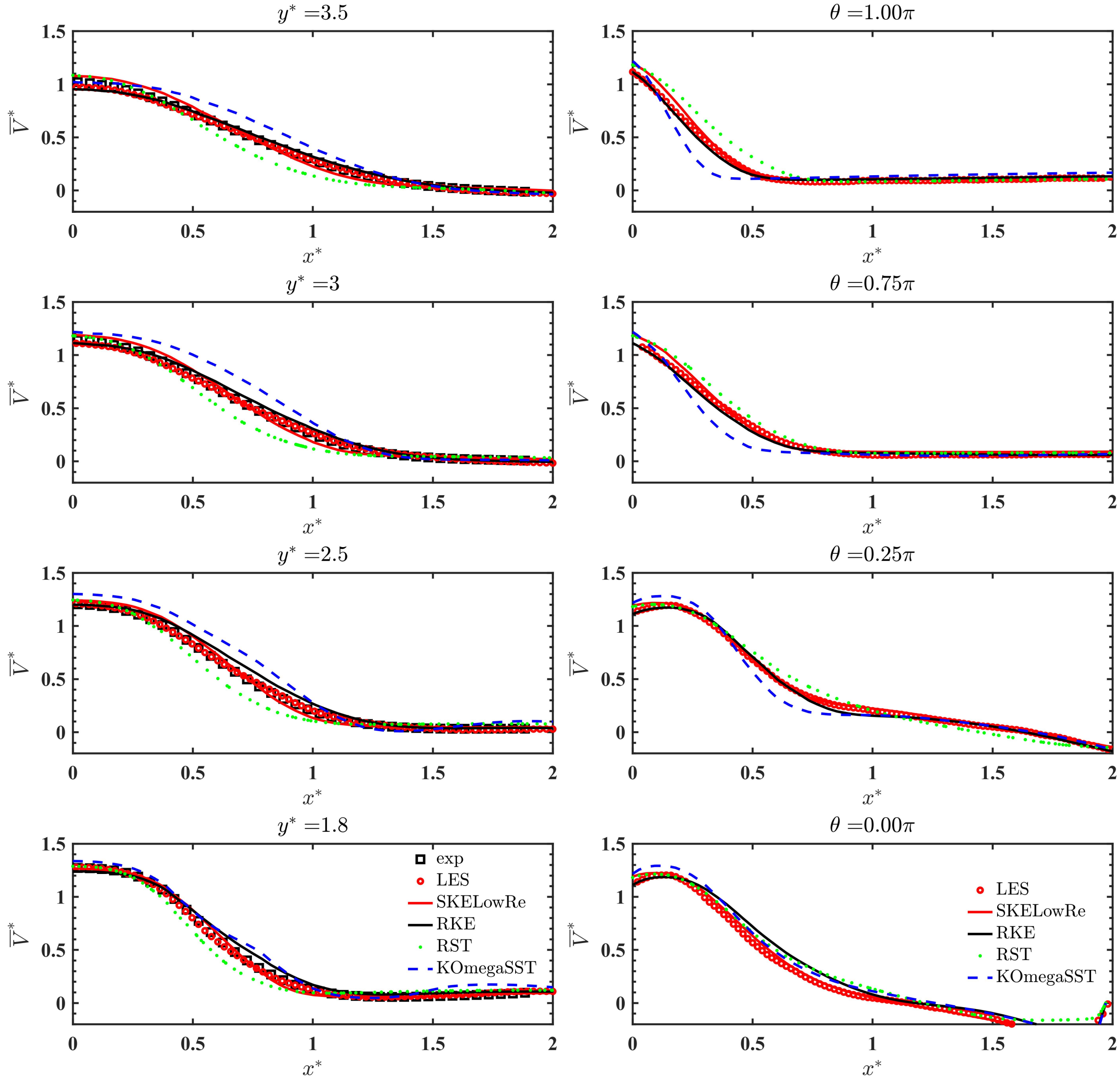

Figure 6.8: Velocity profile comparison with experiments and LES.

6.5.5 Validation of RANS models on the turbulent kinetic energy profiles

A comparison of the turbulent kinetic energy profiles on the $z/D = 0$ plane, and the root-mean-square of streamwise Reynolds normal stresses on the $y/D = 3$ plane are reported in Figure 6.9. It can be seen from Figure 6.9 that, although RANS models correctly predicted the qualitative behaviour of the profiles, the magnitude is substantially lower than what is computed from the LES simulation, with the turbulent kinetic energy and normal stresses being significantly underestimated.

The quantification of the error is summarized in Table 6.5. For the second-order statistics, the errors from the four turbulence models are of the same level. Nevertheless, the lowest mean error on the $z/D = 0$ plane is predicted by the RST model, with a value of 36%. The lowest mean error on the $y/D = 3$ plane is 48.4%, predicted by the Standard $k - \varepsilon$ Low-Re model.

Table 6.5: Error from turbulent kinetic energy/root-mean-square velocity flucturation profile comparison.

	y^*				Mean	θ^*				Mean
	1.8	2.5	3	3.5		0	0.25π	0.75π	π	
SKELowRe	47.2	47.0	46.3	41.6	45.5	42.9	48.7	52.6	49.2	48.4
RKE	44.42	42.61	33.7	23.3	36.0	53.7	53.6	47.7	45	50.0
RST	39.1	41.6	42.6	40.0	40.8	55	62.6	56.1	50.9	56.2
KOmegaSST	56.3	58.3	53.2	36.3	51.0	50.9	54.8	62.1	62.0	57.5

6.6 Conclusions and Future Work

In this chapter, the database from both high-resolution experiments and high-fidelity LES simulation has been used to validate the CFD RANS models. An isothermal single-jet case has been simulated using four turbulent models: Standard $k - \varepsilon$ Low-Re model, Realizable $k - \varepsilon$ model, Reynolds stresses transport model, and $k - \omega(SST)$ (Low-Re Damping) model.

The LES data were first compared to the experimental data. The quantitative comparison demonstrated the high accuracy of the LES data. An assumption was then made about the

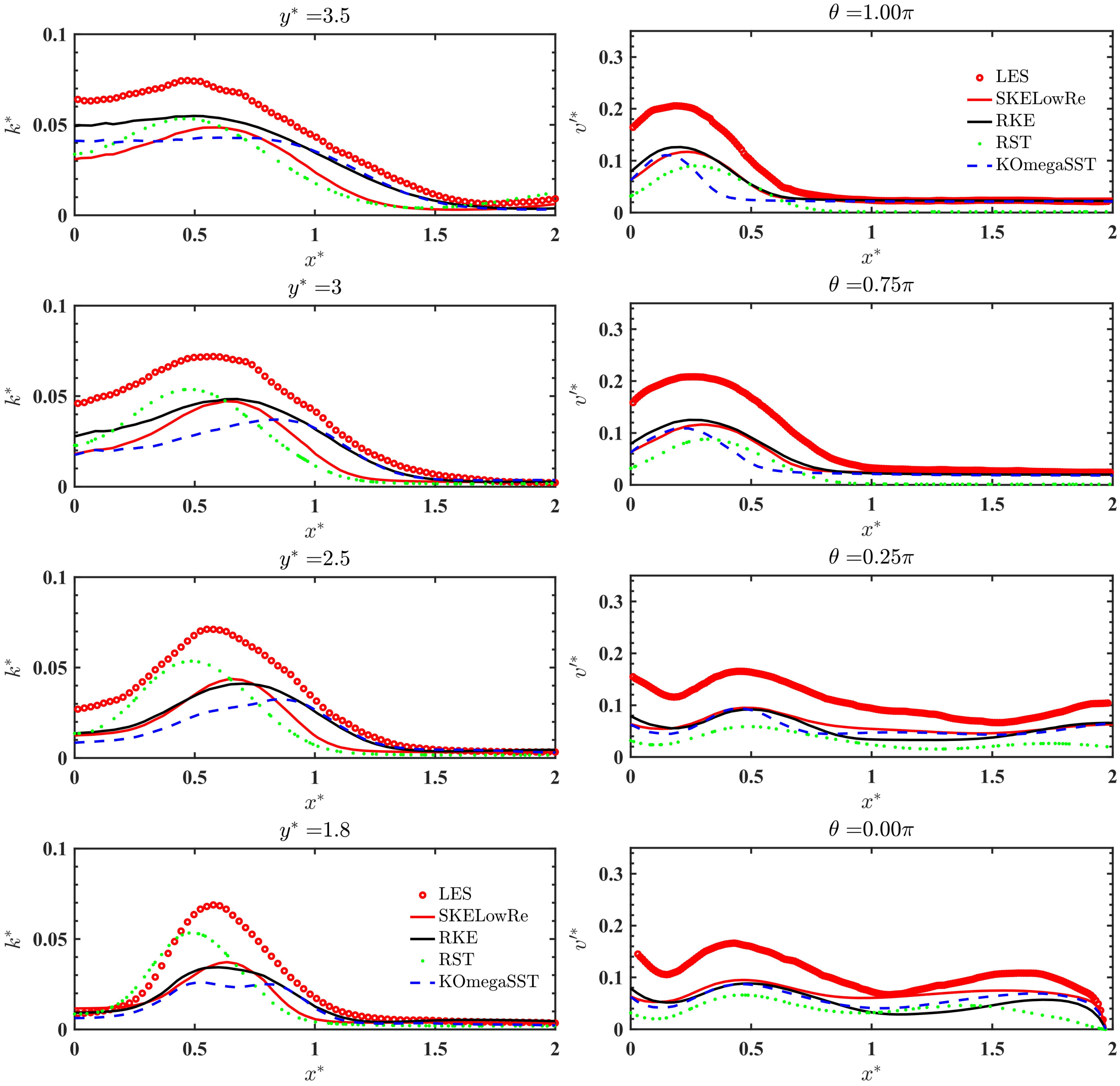

Figure 6.9: Turbulent kinetic energy comparison

reliability of the LES on the unvalidated region. The database from both the experiment and high-fidelity simulation was then used to validate the four turbulence models.

Velocity profiles and the turbulent kinetic energy profiles from two planes were extracted and compared quantitatively to the database. The results from the turbulence models, in general, show reasonable trends. However, an error quantification showed that the velocity profile has been best predicted by the Standard $k - \varepsilon$ Low-Re model, with only 6.6% error on the $z/D = 0$ plane and 5.3% error on the $y/D = 3$ plane. The largest deviation is seen for the $k - \omega(SST)$ (Low-Re Damping) model. For the turbulence kinetic energy, the four turbulence models predicted the profiles with similar magnitude of error. The lowest mean error on the $z/D = 0$ plane is predicted by the RST model, with a value of 36%. The lowest mean error on the $y/D = 3$ plane is 48.4%, predicted by the Standard $k - \varepsilon$ Low-Re model.

As more data is being extracted from the LES simulation more detailed comparisons can be carried looking at the turbulent kinetic energy budget. In future work, the turbulence production rate and the turbulence eddy viscosity will be compared to LES data to better understand the RANS model deficiencies. Besides, the current comparison shows that the $k - \varepsilon$ model is preferred for this scenario when considering the smaller error and lower computational cost. However, as the current simulation is a relatively simple configuration without involving multi-jet interaction and density effect, additional validation efforts are being dedicated to more complex scenarios. Once the hierarchical validation process is completed, best practice guidelines on the use of turbulence models for jet mixing in the upper plenum will be recommended.

CHAPTER VII

Validation of Turbulence Models: HiRJET

7.1 Introduction

The occurrence of thermal stratification in reactor plenums or safety components has attracted great attention because of its important role in determining mixing and heat removal rate or its potential to cause thermal-hydraulic instabilities and thermal fatigue in the reactor internals. Improving models prediction of buoyant flow including stratification would lead to a more accurate estimation of safety margins. In the past decades, experimental investigations and modeling efforts have been dedicated to the understanding and prediction of this phenomenon. Literature reviews have been reported in Ref. [127] and Ref. [122], with the first review summarizing the work conducted until the late 2000s and the second one providing an update over the past decade.

Computational Fluid Dynamics (CFD) models based on Reynolds-Averaging Navier-Stokes (RANS) equations have been widely used for nuclear safety applications. However, accurate prediction of thermal stratification using RANS models remains a challenge [122, 168]. These turbulence models require closure relations to model the turbulent fluxes (i.e., the correlation between velocity and scalar fluctuations - $\overline{u_j'\phi'}$) that appear in the Reynolds-averaged scalar transport equation (here Einstein's notation is being used):

$$\frac{\partial \mathit{\Phi}}{\partial t} + U_j \frac{\partial \mathit{\Phi}}{\partial x_j} = \mathit{\Gamma} \frac{\partial^2 \mathit{\Phi}}{\partial x_j^2} - \frac{\partial \overline{u_j'\phi'}}{\partial x_j} \tag{7.1}$$

where $\mathit{\Phi}$ is the mean scalar field (e.g., density, temperature or species concentration), U_j is the mean velocity component in the jth direction, and u'_j and ϕ' are the j velocity component and scalar fluctuations, respectively.

A commonly deployed approximation for turbulent fluxes is the Simple Gradient Diffusion Hypothesis (SGDH), which relates the turbulent fluxes to the gradient of the mean scalar field. The SGDH relation is given by:

$$-\overline{u'_j\phi'} = \mathit{\Gamma}_t \frac{\partial \mathit{\Phi}}{\partial x_j} \tag{7.2}$$

where $\mathit{\Gamma}_t$ is a turbulent diffusion coefficient. While widely used, Equation 7.2 is known to under-perform in several scenarios, including but not limited to situations where large density gradients are present [169, 170, 171, 172, 173, 174]. Several more sophisticated models have been developed [175]. However, due to their inherent complexity and lack of consensus on the values of the model coefficients, implementation of these more complex models has been limited to academic codes and are only partially available in CFD commercial codes [174, 161]. As a result, SGDH remains the prevailing model in CFD codes. High-resolution experimental data of buoyancy-driven stratification flows is still needed for further development and validation of CFD RANS models and to inform the best practice for using these models in related phenomena.

As has been summarized in [122], several research facilities have been built aimed at investigating thermal stratification and providing high-resolution data for code development and validation, including but not limited to, the SUPERCAVNA experiments carried out by CEA [176], the Gallium Thermal-hydraulic Experiment (GaTE) facility funded through a DOE NEUP and operated at Kansas State university [177] and the thermal stratification testing facility (TSTF) operated at the University of Wisconsin [178], the experiments on the Upper Plenum of the MONJU Reactor Vessel by Japan Atomic Energy Agency (JAEA) [179]. Experimental data from these facilities have been leveraged to validate the existing turbulence models. Ref. [180] used CFD code CFX-11 in combination with the SST $k-\omega$ model to simulate the stratification in the vertical mixing test facility (VeMix). Good qualitative agreement between experimental data and CFD simulations was found. In Ref. [174], three turbulence models, namely, Low-Re k–ε, elliptic-blended k–ε, and (SST) k–ω models were used to simulate the temperature stratification using STAR-CCM+. CFD simulations were compared to the experimental results from the TJWF facility at the University of Tennessee, Knoxville. It was reported that the Low-Re k–ε and SST k–ω models tended to predict more diffusive stratification. The experimental data obtained from the MONJU reactor was widely used to validate different CFD codes, as is summarized in Ref. [166]. Due to the complex geometry of the upper plenum of the MONJU reactor vessel, the moving up rate of the thermal stratification front was mainly influenced by the unclearly-defined boundaries, i.e., the shape of the flow hole edge, instead of the standard $k-\varepsilon$ model being used. Ref. [181] compared the calculations using the JAEA CFD code AQUA with the experimental data and found that the algebraic stress model gave the best predictions for the stratification interface in water and sodium. Ref. [182] studied the thermal stratification in water and sodium tests using three CFD codes (AQUA, STAR-CD, and FLUENT) with different RANS turbulence models (Standard k–ε, RNG $k-\varepsilon$, and Reynold Stress Transport model). With higher-order discretization schemes being used, different codes were confirmed to be applicable to evaluating the basic behaviors of thermal stratification. In addition, an assessment of the mesh configuration showed using 2D fine mesh, the results from 3D simulation could be reproduced. No remarkable difference was observed using the different turbulence models, and the discrepancy was inferred from the difference in the evaluation of turbulent viscosity.

This work aims to validate the existing RANS turbulence models using these newly-obtained high-resolution experimental and DNS data. In particular, CFD RANS simulations using the Standard $k-\varepsilon$ model (SKE) and the Reynolds Stress Transport (RST) model have been carried out to replicate the stratification phenomena observed in the HiRJet experiments.

In this work, the predictive capabilities of these two models have been assessed by comparing the characteristics of the stratification front, i.e., front speed, maximum density gradient, and front thickness obtained with the RANS simulations, with that of the experiments and the DNS simulations. Correctly predicting these quantities is of great importance since the propagation and stratification of the interface, along with the magnitude of the temperature gradient, were considered the dominant factors that affect thermal loading, and determine the performance of passive safety systems [182, 183, 184].

7.2 Test Parameters and Uncertainty Quantification

Buoyant flows are categorized by the Reynolds Number *Re* (Eq. 7.3) and the Richardson Number *Ri* (Eq. 7.4). These dimensionless quantities were calculated based on the inlet flow conditions according to the following formulas [182, 147]:

$$Re = \frac{\rho_{\mathrm{in}} U_{\mathrm{o}} L_{\mathrm{o}}}{\mu_{\mathrm{in}}} \tag{7.3}$$

$$Ri = g L_{\mathrm{o}} \frac{|\rho_{\mathrm{in}} - \rho_{\mathrm{a}}|}{\rho_{\mathrm{in}}} / U_{\mathrm{o}}^2 \tag{7.4}$$

where U_{o} is the nominal velocity, L_{o} the characteristic length (i.e., the jet diameter D), g the acceleration due to gravity, and the subscripts "in" and "a" indicate the inlet and ambient quantities, respectively. For the experiment, the nominal velocity was the inlet average velocity, and the inlet diameter was selected as the characteristic length. Tap water and sugar aqueous solution (made with DI water) with a concentration of 4 weight percent (wt%) was used to achieve 1.5% density differences (DD).

In this thesis, two cases are selected for validation purposes. The fluid properties at the time of the measurements are provided in Table 7.1, along with the flow conditions for the experiments discussed in the present paper. Case 1 corresponds to light fluid injected into the tank pre-filled with heavy fluid, creating a downward-propagating front, while case 5 corresponds to heavy fluid injected into the tank pre-filled with light fluid, creating an upward-propagating front. These two scenarios can be representative of the stratification phenomena that are often seen in reactor applications.

Table 7.1: Summary of the flow conditions and fluid properties.

	Q_o (GPM)	U_o (m/s)	Re[-]	Ri [-]
Case 1 (1.5% DD)	2.50	0.1391	5020	0.289
Case 5 (-1.5% DD)	2.50	0.1391	4660	0.286
	ρ_in (kg/m^3)	μ_in $(10^{-3} Pa \cdot s)$	ρ_a (kg/m^3)	μ_a $(10^{-3} Pa \cdot s)$
Case 1 (1.5% DD)	999	1.05	1014	1.15
Case 5 (-1.5% DD)	1014	1.15	999	1.05

To quantify the uncertainty of the WMS measurements, let's assume the readings for the high (tap water) and low (DI+sugar solution) conductivity fluids from the calibration measurements are U_1 and U_2, respectively. The concentration field $\varphi(t)$ is expressed as [6]:

$$\varphi(t) = \frac{U(t) - U_1}{U_2 - U_1} \tag{7.5}$$

where $U(t)$ is the instantaneous reading in the experiment. Based on the error propagation [185], the uncertainty $\delta\varphi(t)$ on the sensor measurement can be expressed as:

$$\delta\varphi(t) = |\varphi(t)| \left(\frac{(\frac{\delta_{U(t)}}{U(t)})^2 + (\frac{\delta_{U_1}}{U_1})^2}{(1 - U_1/U(t))^2} + \frac{(\frac{\delta_{U_1}}{U_1})^2 + (\frac{\delta_{U_2}}{U_2})^2}{(1 - U_1/U_2)^2} \right)^{1/2} \tag{7.6}$$

where δ_{U_1}/U_1, δ_{U_2}/U_2, $\delta_{U(t)}/U(t)$ are the coefficient of variations. The first two terms, δ_{U_1}/U_1 and δ_{U_2}/U_2, can be obtained through the calibration measurement. However, the third term $\delta_{U(t)}/U(t)$ can not be directly measured during the transient since, at each time snapshot t, only one data point is available for each location. It is reasonable to assume that the coefficient of variation $\delta_{U(t)}/U(t)$ will be bounded by $\delta_{U_1}/U_1 < \delta_{U(t)}/U(t) < \delta_{U_2}/U_2$ [185]. To estimate the total uncertainty, the third term is thus taken to be the average of the two limits, which gives:

$$\frac{\delta_{U(t)}}{U(t)} = \frac{1}{2}(\frac{\delta_{U_1}}{U_1} + \frac{\delta_{U_2}}{U_2}) \tag{7.7}$$

By examining the time-dependent uncertainty distribution using Eq. 7.6 and 7.7, the maximum observed uncertainty on the concentration field through the whole transient process is less than 1.5%.

7.3 DNS Simulations

The data generated by DNS simulating Cases 1 and 5 are included to provide complementary information additional to the experimental data. The DNS simulating stratification in HiRJet test section was performed as part of an effort within the IRP-NEAMS-1.1 to expand the multi-fidelity data base for density stratification research [15, 16]. The DNS was performed using the spectral element method (SEM)-based Navier-Stokes solver NekRS [186], which can leverage Graphical Processing Units (GPU) in the modern high-performance computing (HPC) facilities to achieve considerable speedup compared to its predecessor Nek5000. This brings particular advantage for large-scale simulations of transient flows that span across several minutes to an hour.

The setup of the DNS cases included in this work is summarized in Table 7.2. Incompressible Navier-Stokes equations and the transport equation of concentration scalar were solved in the DNS. The Boussinesq approximation was adopted for the buoyancy treatment, where only linear variability of the density with respect to the concentration scalar is retained. In DNS, the computational domain is discretized into N_e curvilinear hexahedral spectral elements and the solution within is expanded as the tensor product of 7^{th} order Lagrangian polynomials collocated on the Gauss-Lobatto Legendre (GLL) quadrature points on each direction. The estimated resolution in the jet and the bulk of the mixing enclosure is $(\Delta r_{wall}, \Delta r_{cl}, \Delta x) = (0.5, 6.0, 15.0)$ and $(\Delta y, \Delta z, \Delta x) = (6.0, 6.0, 15.0)$ where $\Delta r_{wall}, \Delta r_{cl}$ are the grid point spacing on the wall, center-line of the jet and $\Delta x, \Delta y, \Delta z$ are that along the jet-parallel, horizontal transverse and the vertical direction, respectively.

To ensure consistency with the experiment, the time-varying Dirichlet boundary condition based on the small WMS density reading was enforced for the concentration scalar at the inlet of the computational domain(same position as the small WMS). The nearest neighbor rule was applied to spatially assign the concentration values to the finer DNS mesh, and the inlet concentration profiles are held constant until the corresponding time of the next WMS reading is reached. Readers are advised to the reference paper for further details of the simulation and boundary condition setup.

Table 7.2: Summary of the case setup of the data source DNS cases [15, 16]

	Case 1 (1.5% DD)	Case 5 (-1.5% DD)
Governing equations	Incompressible Navier-Stokes	
Buoyancy treatment	Boussinesq approximation	
Number of spectral elements	1,361,440	877,148
Transient span covered	403.2 seconds (28%)	906.6 seconds (64.7%)
Total GPU-hours spent [187]	40,800	62,640

The DNS solution was exported every 0.1 seconds. The DNS data included in this work is based on further down-sampling of the full-resolution solution onto a coarser grid. Details of the comparison with experimental data and RANS simulations will be provided in Section 7.5.

7.4 CFD RANS Simulations

A CFD model was developed in STAR-CCM+ to perform simulations and assess the performance of current CFD RANS models. In this section, the mesh development, mesh convergence study, time step convergence study, and boundary conditions are discussed.

7.4.1 Computational Domain

The computational fluid domain was created using the CAD module embedded in Siemens STAR-CCM+ version 15.06.007. Taking advantage of the symmetry of the system, only half of the tank was modeled. This strategy has often been adapted for studying thermal stratification phenomena for the sake of saving computational time, as can be found in [181, 182, 175, 188].

The modeled geometry is shown in Figure 7.1. The middle nozzle on the side of the tank was used as the inlet, and the middle nozzle on the bottom was used as the outlet, consistent with the configuration of the experiment. The nozzles that remained closed during the experiments were not modeled in the simulation. These two simplifications helped reduce the computational costs for the transient simulations. Figure 7.1 indicates the locations of the inlet and outlet, as well as the coordinate system used for the analysis.

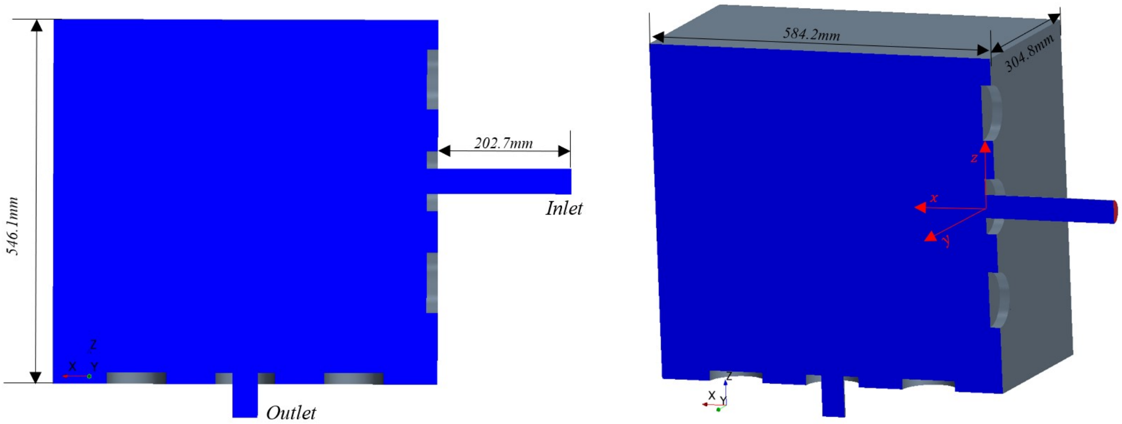

(a) Side View

(b) Angled view

Figure 7.1: Computational domain of the HiRJet facility used for CFD simulations.

7.4.2 Simulation Settings

The density variations were modeled using the multi-component model, which solves Equation 7.1 for the mass fraction of one component. The turbulent flux in Equation 7.1 was solved using the SGDH reported in Equation 7.2. The diffusion coefficient in the equation is directly related to the deployed turbulence model through the relation

$$\mathit{\Gamma}_t = \frac{\mu_t}{\sigma_t} \tag{7.8}$$

where μ_t is turbulent eddy viscosity and σ_t is the turbulent Schmidt number σ_t. While there is currently no consensus on the best option for σ_t [189], the turbulent Schmidt number in the simulation was kept as the default constant value for validation purposes [161]. In the present work, two turbulence models, namely the Standard $k - \varepsilon$ (SKE) model, and the Reynolds Shear Stresses (RST) model, were assessed since these two models serve as good representatives of the isotropic and anisotropic turbulence models, respectively, as well as have been of interest in the application of prediction on thermal stratification [166, 181, 182]. Detailed descriptions of both models can be found in Ref. [161].

7.4.3 Mesh Size Sensitivity Study

Grid and time step sensitivity analyses were conducted to ensure that the obtained CFD results were not dependent on the mesh size or on the integration time step. The mesh analysis for the HiRJet facility, originally introduced in [90], is revisited in this section. Expanding upon the insights provided in [90], this section underscores the continued suitability of the developed mesh for the RST model.

The grid sensitivity analysis was first carried out by comparing the velocity magnitude and the Turbulent Kinetic Energy (TKE) profiles for different grid sizes Δx. Due to the rectangular geometry of the fluid domain, trimmer (hexahedron) volume cells were utilized. Tap water was used as the working fluid in the simulation, with a constant inlet mass flow rate. The velocity field for this steady state scenario along the axis of symmetry is shown in Figure 7.2a. The study in Ref. [182] showed that the spatial mesh arrangement in the gravitational direction around the thermal stratification interface was essential to correctly capture the behavior of the interface. Therefore, a systematical grid refinement in the vertical direction has been conducted in this work. Three meshes were used for the sensitivity analysis, a fine mesh with a base size Δx of 3 mm, an intermediate mesh with a base size of 4 mm, and a coarse mesh with a 5 mm base size. The grid refinement factors κ, defined as the ratio of the local mesh size between meshes, are 1.25 and 1.33, respectively, which is close to the empirical value of 1.3 recommended in Ref. [190].

Additionally, each mesh was divided into three regions with increasing degrees of refinement: the highest refinement, with mesh size Δx_f, was used along the jet core and shear regions to resolve the largest velocity gradients. The intermediate refinement region, with mesh size Δx_m, followed the high refinement region where the velocity gradients were less severe. The rest of the flow domain was kept at base size Δx. In Figure 7.2b the three refinement regions can be identified. The darkest region represents the finest mesh (near the inlet), and the lighter regions indicate the coarser part of the mesh. Details about the three meshes used for the mesh sensitivity analysis are provided in Table 7.3. The coarse mesh inlet boundary has a total of 30 cells ($\Delta x_f = 1.25mm$).

The normalized velocity magnitude U^* (normalized by the inlet velocity) and the normalized TKE k^* (normalized by the square of inlet velocity) profiles obtained with the three meshes tested are shown in Figure 7.3. Note that the spatial axes were scaled by the nozzle diameter D (38 mm). The velocity magnitude profiles at $x^* = 1, 11$ (Figures 7.3a and 7.3b) indicate that the velocity fields do not vary significantly by further decreasing Δx_f. The TKE profiles shown in Figure 7.3c indicate that there is a larger discrepancy between profiles at the peaks at $z^* = \pm 0.5$ (where the largest gradients occur). Furthermore, in Figure 7.3d, the discrepancies occur throughout the profile; however, these profiles only differ by at most 3%. With these differences in mind and the computational cost required for the different meshes, the intermediate grid size ($\Delta x_f = 1.00mm$) was determined to capture the flow dynamics well.

Table 7.3: HiRJet mesh information

Mesh	Δx(mm)	$\Delta x_m = \frac{\Delta x}{2}$(mm)	$\Delta x_f = \frac{\Delta x}{4}$(mm)	Total Cells (million)
1	4	2.0	1.00	3.20
2	5	2.5	1.25	6.15
3	3	1.5	0.75	14.5

The transient mesh convergence study was performed with a scenario where a light fluid is injected into a tank full of heavy fluid (LIH injection). Consistently, an upward jet

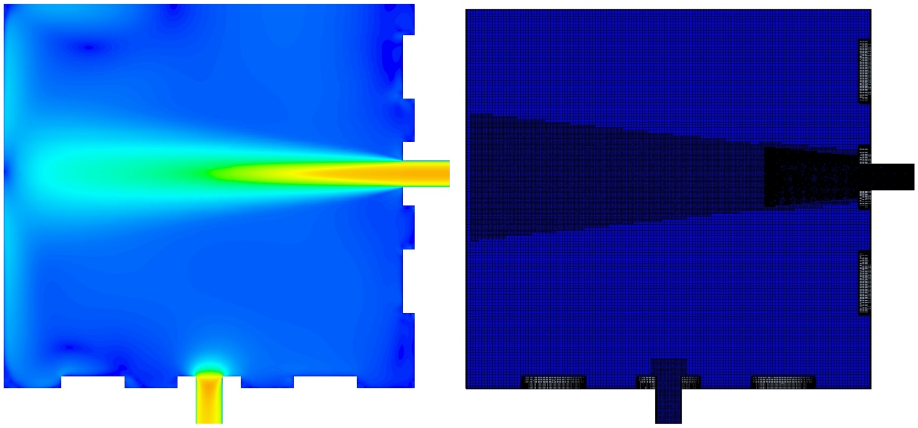

(a) Steady-state velocity field

(b) Mesh for the steady state simulation

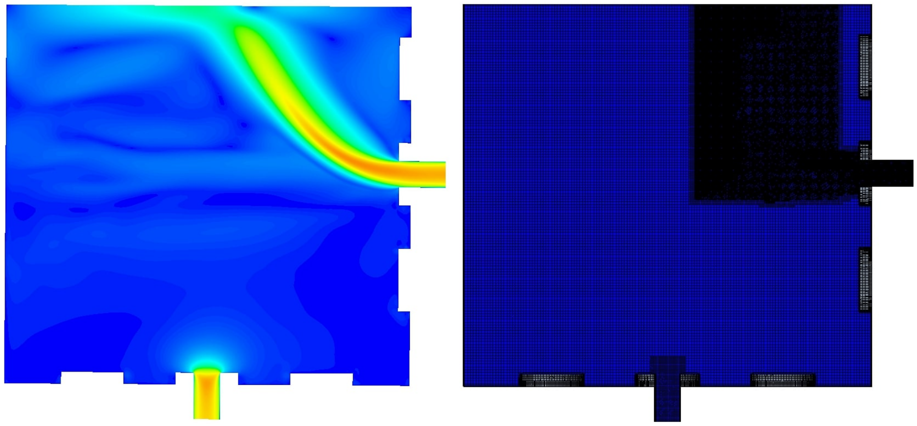

(c) Velocity field of the transient simulation

(d) Mesh for the steady state simulation

Figure 7.2: Velocity fields and meshes along the symmetrical xz-plane for steady-state and transient simulations.

curvature occurs, as shown in Figure 7.2c. Later in the transient, as the inlet fluid mixes with the surrounding environment, the effect of buoyancy on the jet consequently decreases and the jet slowly returns to a horizontal trajectory. To cover the varying jet trajectory, the mesh refinement in the computational domain was modified as shown in Figure 7.2d. Only the regions where the highest velocity and density gradients occur (i.e., near the inlet) were refined to resolve the largest gradients in the flow field. The computational mesh was modified for the heavy into light fluid injection (HIL injection) such that the finer grid followed the downward curvature of the jet.

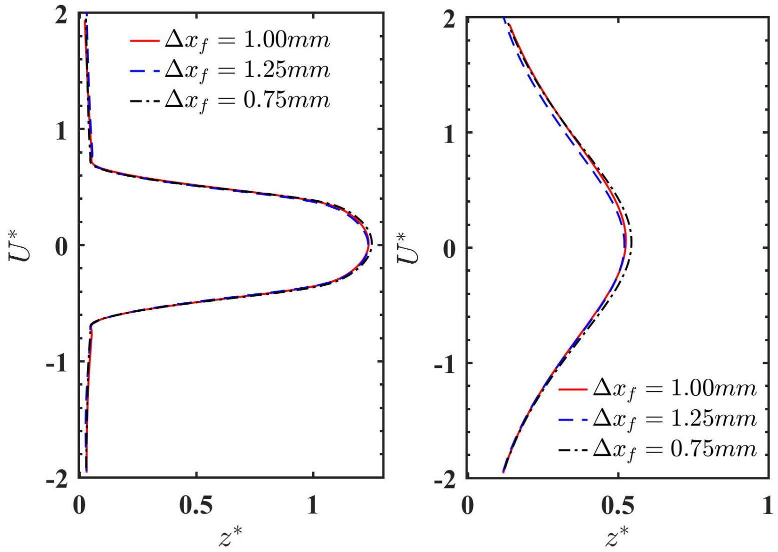

(a) $U^*(x^* = 1, y^* = 0)$ (b) $U^*(x^* = 11, y^* = 0)$

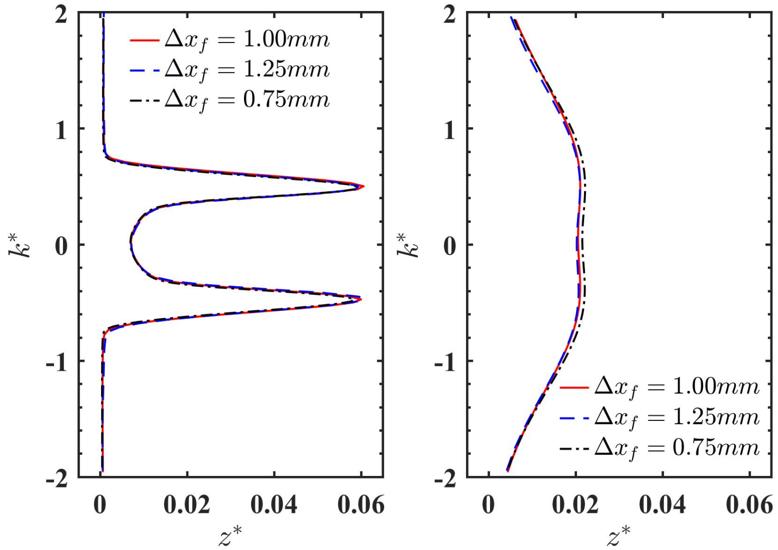

(c) $k^*(x^* = 1, y^* = 0)$ (d) $k^*(x^* = 11, y^* = 0)$

Figure 7.3: Velocity and TKE profiles for different grids: (a) Velocity profiles at $x^* = 1$; (b) Velocity profiles at $x^* = 11$; (c) TKE profiles at $x^* = 1$; (d) TKE profiles at $x^* = 11$. The velocity profile is normalized by the inlet velocity U_o, and the TKE profile is normalized by the square of the inlet velocity U_o^2.

7.4.4 Time Step Sensitivity Study

Before discussing the time-step sensitivity study, a discussion of density normalization is necessary. To compare the propagation of the stratified density fronts over time, the density was nondimensionalized according to:

$$\rho^* = a + \frac{(\rho - \rho_{\min})(b - a)}{\rho_{\max} - \rho_{\min}} \tag{7.9}$$

where ρ^* and ρ are the nondimensionalized and original densities, respectively, and a and b are arbitrary numbers to restrict the range of the scaled density to the $[a, b]$ interval. The convention used to indicate a sugar solution (heavy fluid) and tap water (light fluid) is $\rho^* = 1$ and $\rho^* = 0$, respectively; Thus, $\rho^*(x^*, y^*, z^*) = 1$ at time $t = 0s$ for the experiments where light fluid is injected into a heavy fluid (LIH).

For the time step sensitivity study, the dimensionless density over time with time steps $\varDelta t = 0.01, 0.05, 0.25, 1.25s$ at one location below the inlet ($z^* = -5$) and another above the inlet ($z^* = +5$) were analyzed. Furthermore, the convergence within the time steps was assessed by verifying that the residuals reached an asymptote (i.e., the residuals do not change further with more inner iterations within the time step), and the values of the residuals were below 10^{-6}. The results are shown in Figure 7.4. The dimensionless density for all $\varDelta t$ followed the same trends; however, the largest observable deviations occurred only on the plots for $\varDelta t = 1.25s$. The investigation in Ref.[182] also showed that the time step was not affecting the simulation results. Based on these observations, $\varDelta t = 0.25s$ was determined to be the time step size for the transient simulation.

So far, the sensitivity study has shown good mesh and time step size independence using the standard $k - \varepsilon$ model. In the literature, it is often reasonably assumed that the mesh validated under one of the 2-equation models can be applied directly to other turbulence models when the mesh is sufficiently fine [182, 173]. However, since more equations and transport terms are numerically solved to resolve the Reynolds stress tensor in the RST model [161], it is inferred that the RST model would experience more numerical diffusion under the same mesh setup. To verify that the selected mesh and time step size are suitable for the RST model, the quantity of interest, i.e., the concentration distribution in the large

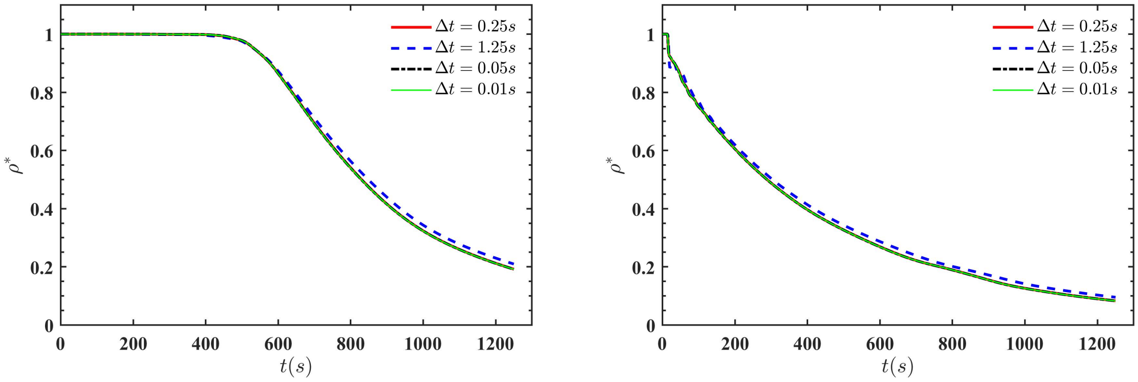

(a) $\rho^*(x^* = 3, z^* = -5, t)$ (b) $\rho^*(x^* = 3, z^* = 5, t)$

Figure 7.4: Propagation of density fronts under various time step sizes at two z^* locations on the symmetrical plane: (a) $\rho^*(x^* = 3, z^* = -5, t)$; (b) $\rho^*(x^* = 3, z^* = 5, t)$;

WMS plane, is further investigated using the RST model with two different mesh setups. Specifically, the RST model simulations for case 1 were run using mesh $\Delta x_f = 1.00$ mm and $\Delta x_f = 1.25$ mm, respectively. The distribution of the dimensionless density along three different vertical lines ($x^* = 5, x^* = 7.5$, and $x^* = 12.5$) on the large WMS plane is plotted in Figure 7.5. It can be seen from the plot that the distributions of the dimensionless density at different times and locations are nearly identical between the two mesh setups, indicating good mesh independence when using the RST model. Therefore, to assess the performance of turbulence models, a time step of $\Delta t = 0.25s$, with the intermediate mesh described in Table 7.3, was utilized in this work.

7.4.5 Boundary and Initial Conditions

The boundary of the inlet in the simulation was set as velocity inlet, and the outlet boundary was set to be an outlet. The rest of the surfaces were set to be wall boundaries. The initial tank was set to be quiescent with $I = 1\%$ turbulence intensity. A priori-simulation with a different intensity value $I = 0.05$ has shown that the initial turbulence intensity did not affect the later transient build-up of the density field since there was a long transient ($\sim 100s$) before the injected fluid reached the inlet. The last key step for the simulation setup is the time-dependent inlet boundary condition. With the WMS experimental data,

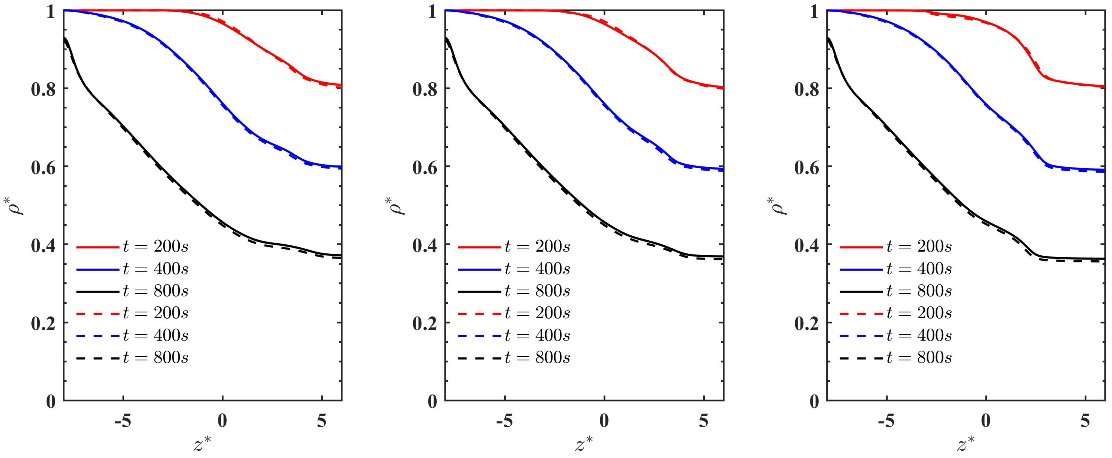

(a) $\rho^*(x^* = 5)$ (b) $\rho^*(x^* = 7.5)$ (c) $\rho^*(x^* = 12.5)$

Figure 7.5: Dimensionless density distribution from RST model at three different vertical slices on the large WMS plane: (a) $\rho^*(x^* = 5)$; (b) $\rho^*(x^* = 7.5)$;(c) $\rho^*(x^* = 12.5)$. Solid line: $\Delta x_f = 1.00mm$; Dashed line: $\Delta x_f = 1.25mm$.

accurate boundary conditions for the time and spatial-dependent density distribution in the inlet cross-section are available for simulations. Figure 7.6 shows snapshots of the inlet density distribution at different times during an LIH injection. As a reminder for the LIH injection, the main tank was filled with heavy fluid (DI + sugar solution), and light fluid (tap water) was injected into the main tank through the inlet. Figure 7.6a shows that the light fluid (tap water) has not arrived at the inlet WMS at t = 84s. At t = 94s (Figure 7.6b) stratified flow is present in the inlet cross-section, while at t = 104s (Figure (Figure 7.6c) the light fluid occupies a larger proportion of the inletWMS. The WMS data show that the inlet density distribution is non-uniform in space. This non-uniformity in the inlet boundary condition is an important effect to take into account in the CFD simulations. The WMS data were therefore converted into a time-dependent 2D inlet density profile for the inlet boundary condition of the CFD simulation.

In addition to the inlet density profile, the inlet velocity profile along with turbulent parameters also need to be specified. Steady-state velocity measurements were measured with LDV. Since the density field is non-uniformly distributed during the experiment, the transient velocity field at the inlet would be expected to deviate from the steady-state (fully

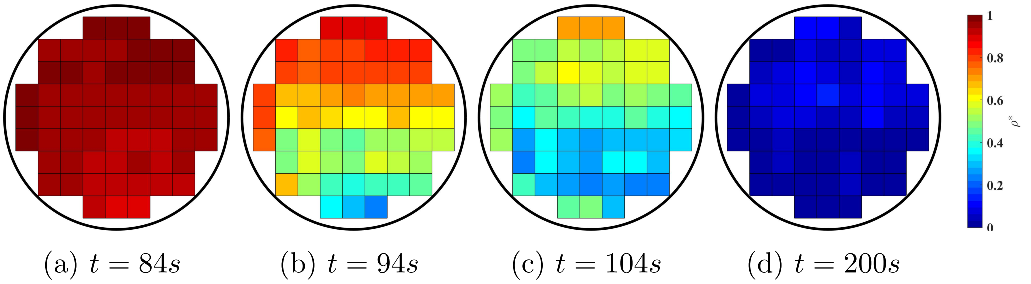

(a) $t = 84s$ (b) $t = 94s$ (c) $t = 104s$ (d) $t = 200s$

Figure 7.6: The transient dimensionless density distribution from the inlet WMS at four different times. A value of zero (blue) indicates the light fluid, and a value of one (red) indicates the heavy fluid.

developed) distributions. To investigate the influence of the velocity profiles on the propagation of the stratified front in the main tank, two cases were run while keeping the total mass flow rate constant, one case characterized by a fully developed turbulent velocity profile, and a second case with a distorted velocity profile (see Figure 7.7a and Figure 7.7b respectively). Two simulations were then run using the time-dependent inlet density distribution as measured by the inlet WMS and a constant inlet velocity profile corresponding to the two profiles reported in Figure 7.7a and Figure 7.7b respectively. The results obtained with these two cases are compared using the density distribution on the large WMS plane through three 1-D vertical slices at $x^* = 5, 7.5$, and 12.5, respectively, shown in Figure 7.8. The density distributions obtained at three different times ($t = 151s, t = 351s$, and $t = 901s$ respectively) are nearly the same for these two cases. Based on the results, it is concluded that the effect of the inlet velocity profile on the density stratification in the tank is negligible. Therefore, for the final simulations, a fully developed velocity profile is used as the inlet condition.

7.5 Results and Discussion

7.5.1 Visualization of the Transient Dimensionless Density Field

Figure 7.9 shows time snapshots of the transient dimensionless density field for case 1 (LIH injection) and case 5 (HIL injection), respectively, obtained with the CFD RANS simulations. Note that the colormap has been filtered with a low-pass filter for case 1 and a

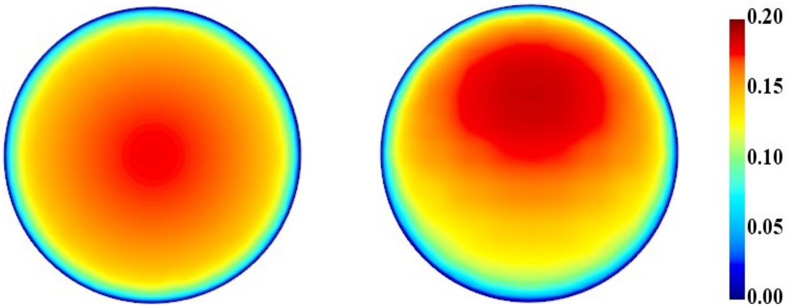

(a) Fully-developed (b) Distorted

Figure 7.7: Assumptions on the inlet velocity profile. (a) fully-developed; (b) distorted.

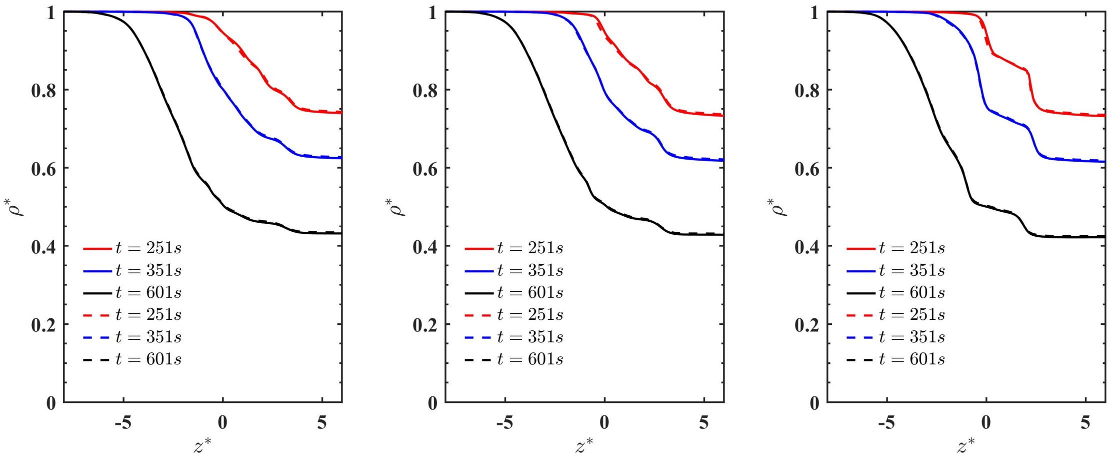

(a) $\rho^*(x^* = 5)$ (b) $\rho^*(x^* = 7.5)$ (c) $\rho^*(x^* = 12.5)$

Figure 7.8: Propagation of density fronts overtime on the large WMS plane with different inlet velocity profiles. (a) $\rho^*(x^* = 5)$; (b) $\rho^*(x^* = 7.5)$;(c) $\rho^*(x^* = 12.5)$. Solid line: full-developed; Dashed line: distorted.

high-pass filter for case 5 to facilitate the visualization. The opacity increases from maximum to minimum for the low-pass filter, and vice versa for the high-pass filter [161].

As seen from Figure 7.9a, when light fluid flows into the tank filled with heavy fluid, the jet bends upwards under the buoyancy effect. The light fluid, therefore, accumulates on the top of the tank first. As such, the dimensionless density field, after the low-pass filter, is seen in the top region of the tank at the early stage of the transient (see Figure 7.9a, snapshot at 200s). The density front then propagates gradually downwards while mixing with the tank fluid. For case 5 shown in Figure 7.9b, instead, where heavy fluid flows into the tank filled with light fluid, the jet bends downward due to higher body force acting on the jet. Therefore, mixing happens near the bottom region of the tank first. Accordingly, the density front is seen in the bottom region of the tank at the early stage of the transient. In this scenario (see Figure 7.9b, snapshot at 250s), an upward-moving front has been correctly predicted.

To visualize the propagation of the stratified fronts, the dimensionless density fields on the large WMS plane (as shown by the meshed sheet in Figure 7.9) are presented in Figure 7.10 and Figure 7.11, respectively. In both figures, three snapshots of the 2D normalized density distribution are reported. The results from the SKE simulation are reported in the first column, and the results from the RST model and the experiments are reported in the second and third columns, respectively. Note that the 2-D area over which WMS experimental data is available is smaller than the simulation area (i.e., the WMS does not cover the entire 2D cross-section of the tank).

7.5.1.1 Low-to-high injection: case 1

Comparing the simulations to the experimental data at t =251s, it can be seen that both RANS models successfully predict the occurrence of a thin mixing region. The location of the stratification front, which in this paper is defined as the location where dimensionless density equals 95%, has been captured well by the SKE model through visual comparison, while the RST model predicts a faster propagation of the stratified front, therefore a stronger mixing. Both models and the experiment show that the stratified front remains stable as it propagates downward.

7.5.1.2 High-to-low injection: case 5

In this case, the location of the stratification front, which is defined as the location where the dimensionless density equals 5%, has been captured well by the SKE model and the RST model through visual comparison in the early stage ($t = 251$). As the mixing develops, the RST model predicts a faster traveling front speed, i.e, a higher location of the stratified

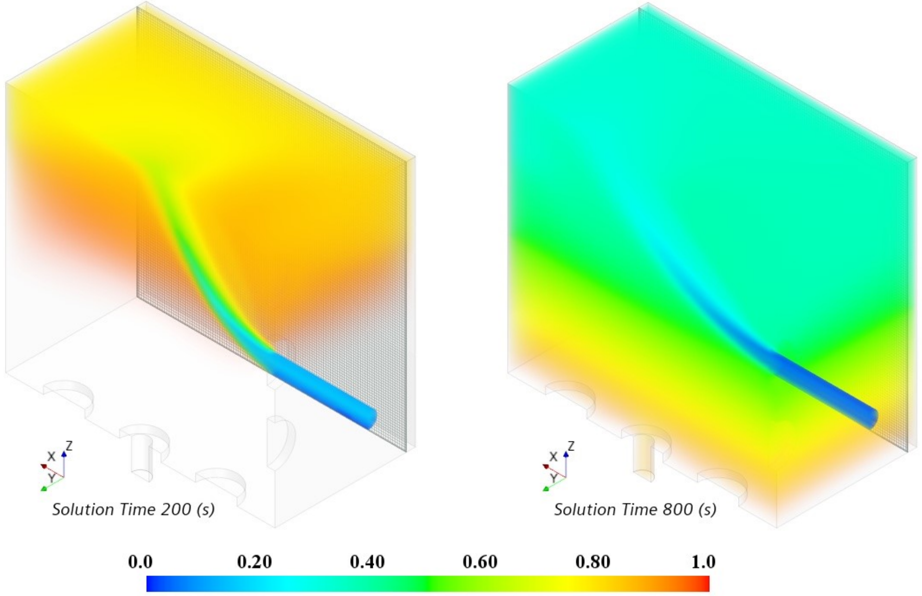

(a) $\tilde{\rho}^*(x^*, y^*, z^*, t)$ of case 1 (LIH)

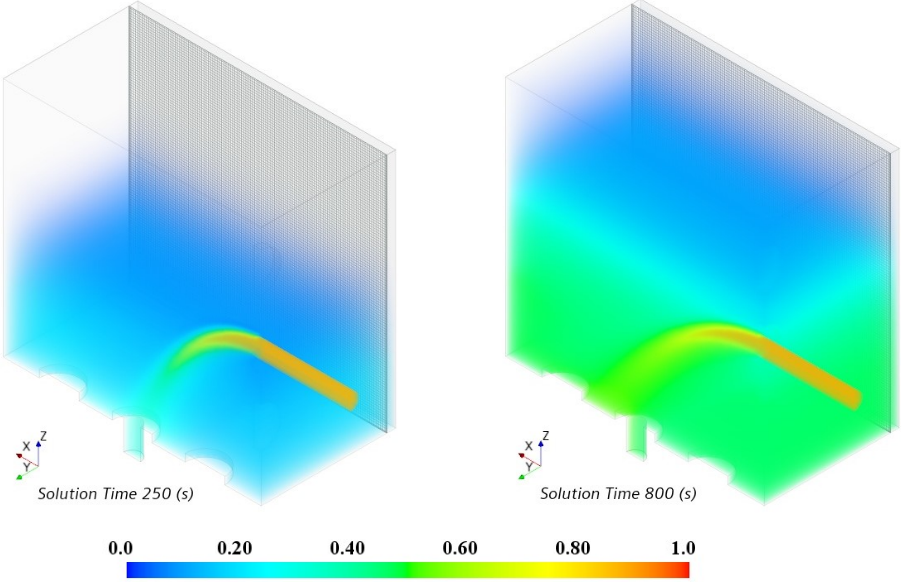

(b) $\tilde{\rho}^*(x^*, y^*, z^*, t)$ of case 5 (HIL)

Figure 7.9: Visualization of the dimensionless density field from simulations for case 1 and case 5. (a) $\tilde{\rho}^*$ for case 1 with a low-pass filter on the colormap; (b) $\tilde{\rho}^*$ for case 5 with a high-pass filter on the colormap. The meshed sheet shows the location of the measurement location of the largeWMS.

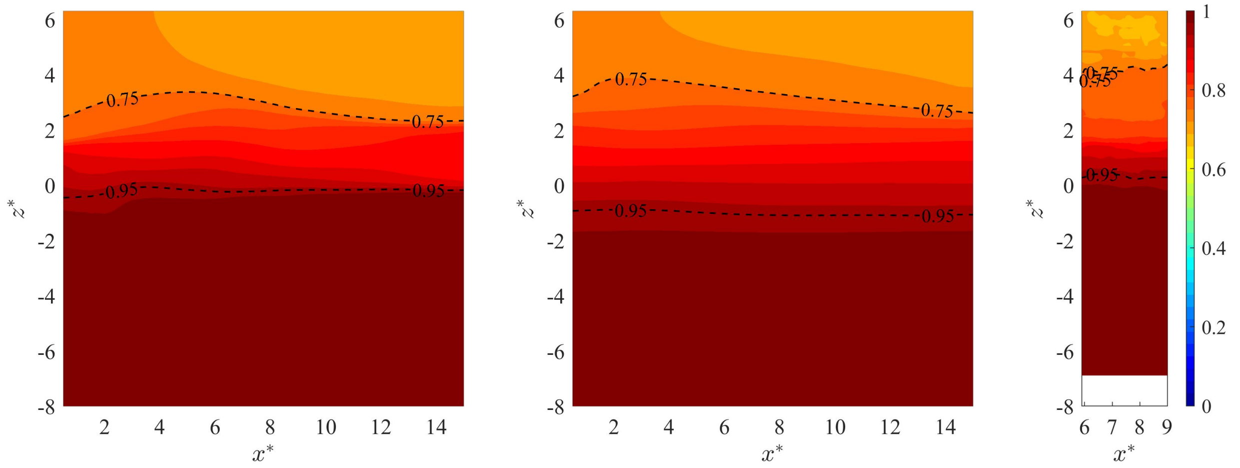

(a) $\rho^*(x^*, y^* = -7.5, z^*, t = 251s)$ for case 1, from left to right: SKE, RST, and exp.

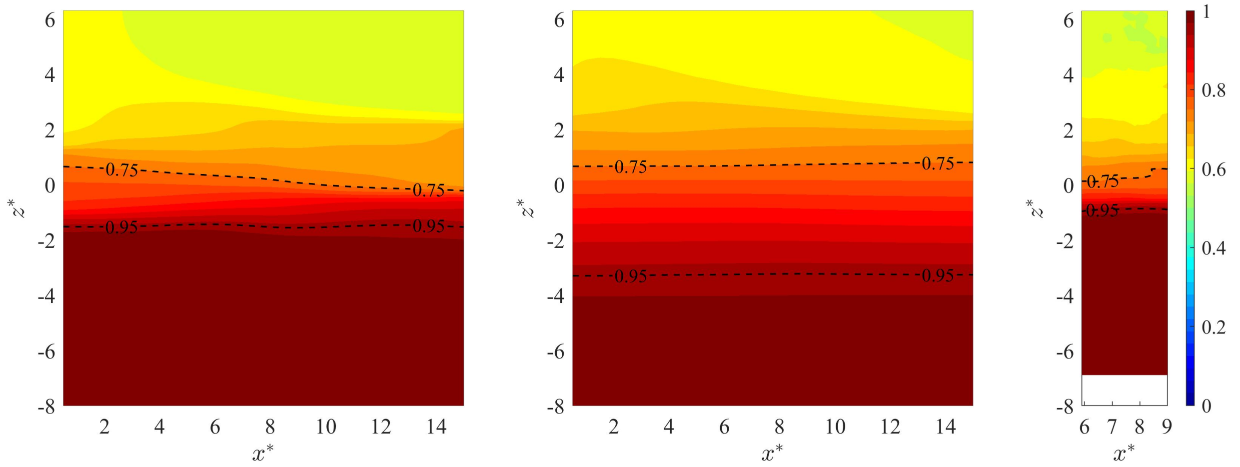

(b) $\rho^*(x^*, y^* = -7.5, z^*, t = 351s)$ for case 1, from left to right: SKE, RST, and exp.

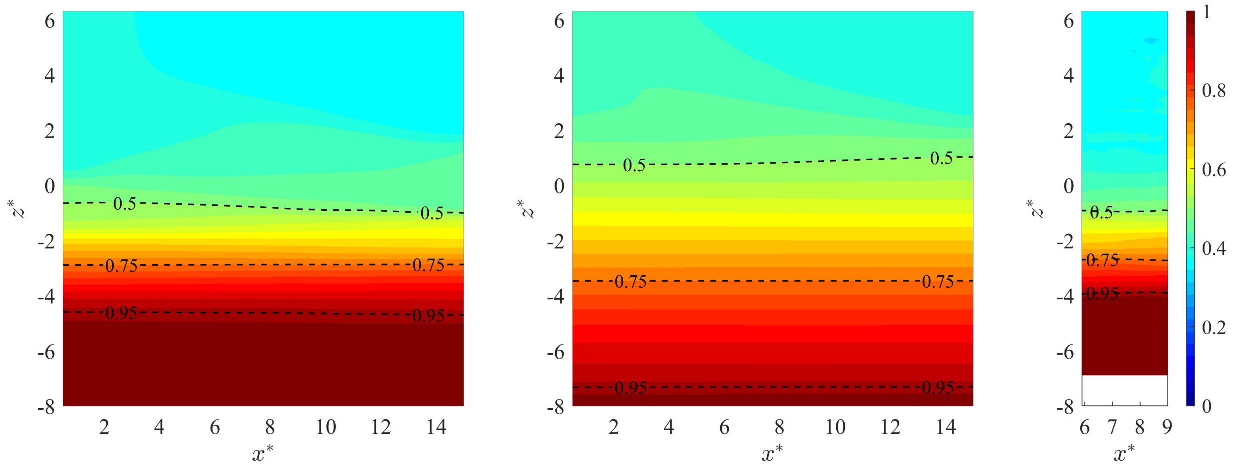

(c) $\rho^*(x^*, y^* = -7.5, z^*, t = 601s)$ for case 1, from left to right: SKE, RST, and exp.

Figure 7.10: Propagation of density fronts for case 1 at three different times (t = 251s, t = 351s, and t = 601s) on the large WMS plane: SKE (first column), RST (second column), and experiments (third column).

font, while the SKE still gives a reasonably well-predicted front location compared to the experiments through visual comparison.

7.5.2 Quantification of the Density Stratification

In this subsection, the density distribution and the quantities of interest for the stratified fronts from the simulations are presented and compared to the experimental and DNS data.

7.5.2.1 Comparison of density profiles

To directly compare the density distribution quantitatively, a time-dependent density profile $\overline{\rho^*}(z^*, t)$ is defined as:

$$\overline{\rho^*}(z^*, t) = \frac{1}{l_{x^*}} \int \rho^*(x^*, z^*, t) dx^* \tag{7.10}$$

where l_{x^*} is the width of the largeWMS. Figure 7.12 presents the profiles from the RANS simulation, experiments, and DNS simulations at different times. The shading for each color represents 3σ at a particular point and time, showing the corresponding fluctuation at each horizontal location. It can be seen from Figure 7.12 that the density distribution predicted by the SKE model has a relatively good agreement with the DNS and experiment. In contrast, the RST model is more diffusive, especially in the later stages of the transient.

7.5.2.2 Quantification of the stratified fronts

For thermal stratification, it is important to quantify the process with regard to the front propagation speed, the thickness of the stratified layer, and the density gradients. The first metric of interest is the position of the leading edge of the density front, or mixing front $Z_f^*(x^*, t)$. The mixing front location is calculated as the position of $\rho^* = 95\%$ in the LIH injections and $\rho^* = 5\%$ in the HIL injection. This metric helps to identify the regions where mixing starts. The second metric of interest is the position of the maximum gradient of

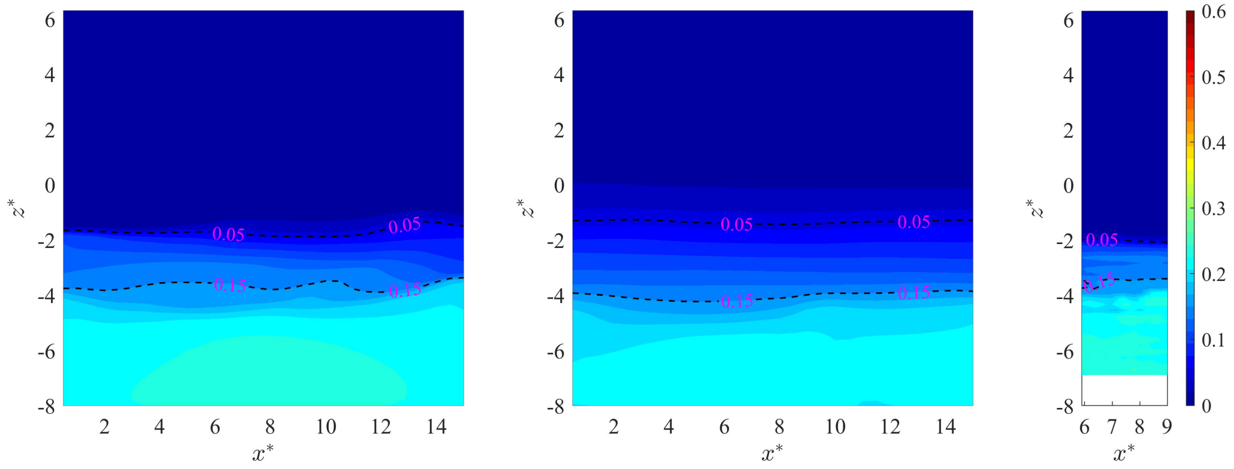

(a) $\rho^*(x^*, y^* = -7.5, z^*, t = 251s)$ for case 5, from left to right: SKE, RST, and exp.

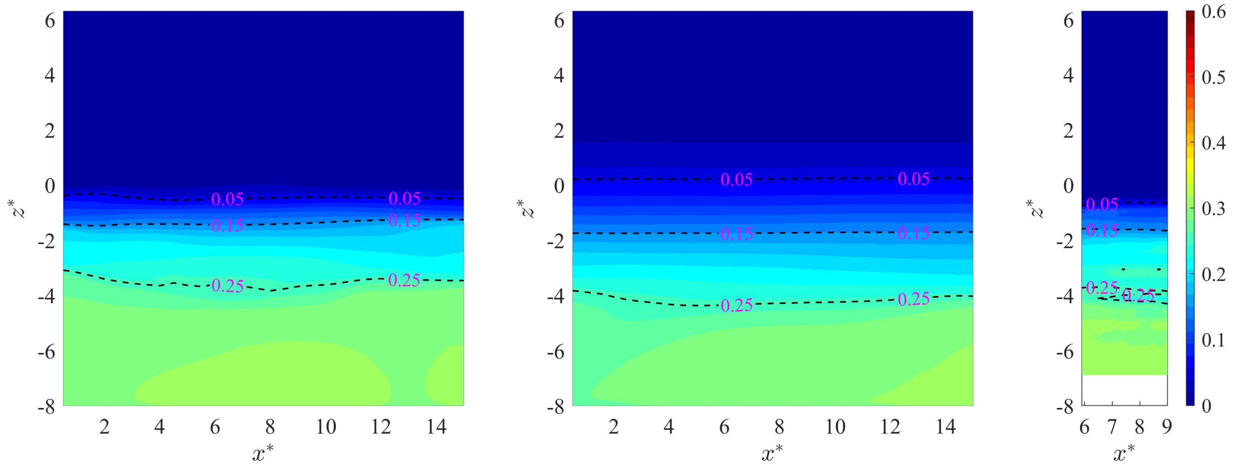

(b) $\rho^*(x^*, y^* = -7.5, z^*, t = 351s)$ for case 5, from left to right: SKE, RST, and exp.

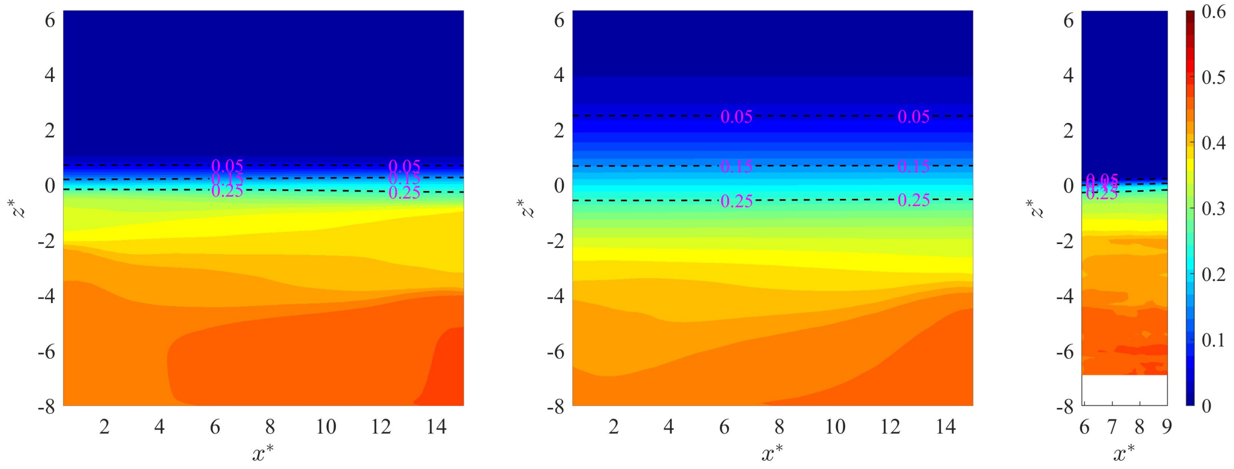

(c) $\rho^*(x^*, y^* = -7.5, z^*, t = 601s)$ for case 5, from left to right: SKE, RST, and exp.

Figure 7.11: Propagation of density fronts for case 5 at three different times (t = 251s, t = 351s, and t = 601s) on the large WMS plane: SKE (first column), RST (second column), and experiments (third column).

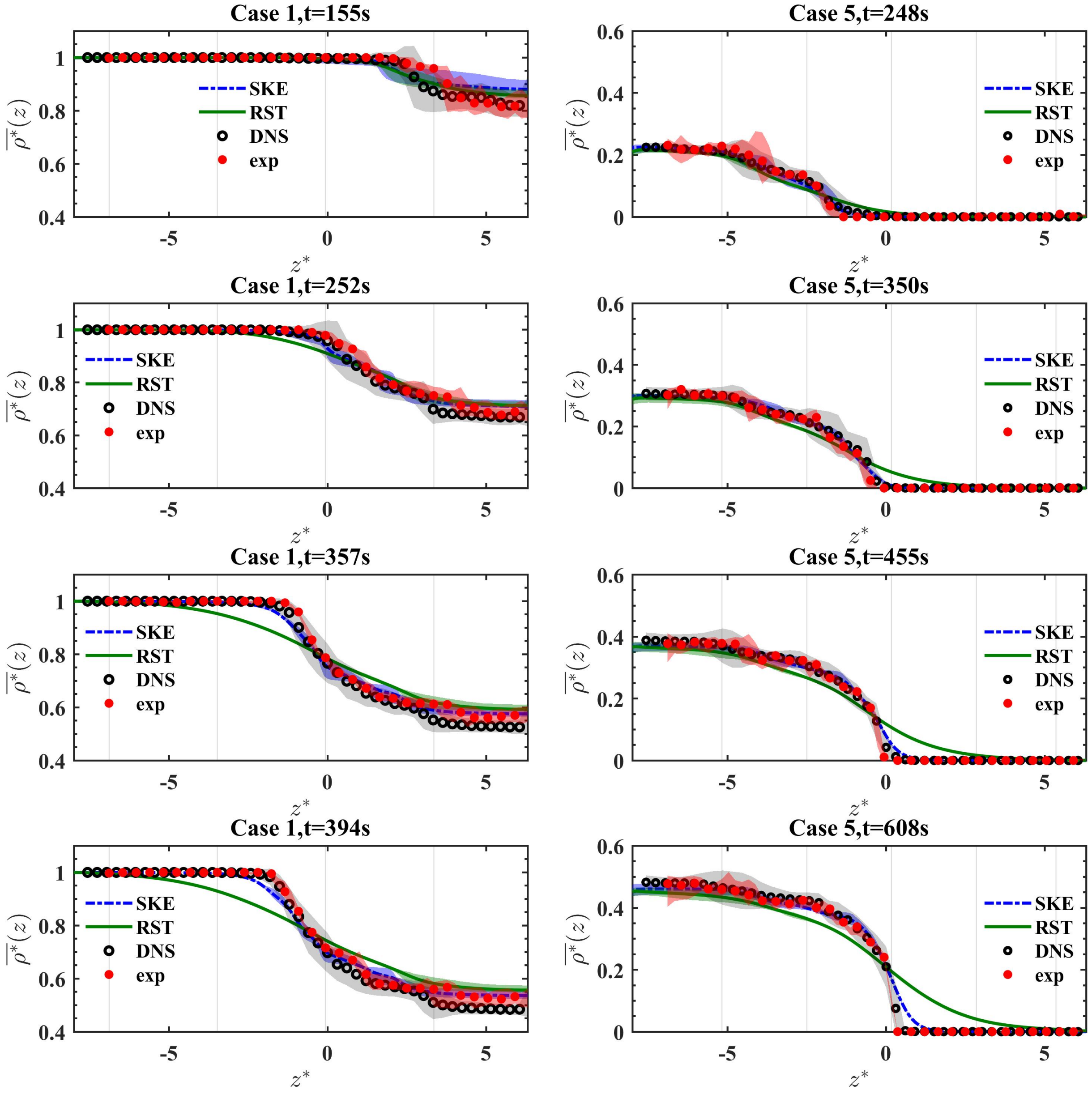

Figure 7.12: Dimensionless density profiles $\overline{\rho^*}(z^*, t)$ for case 1 and case 5 at four different times.

the dimensionless density field, or the stratified front $Z_m^*(x^*, t)$, which is found through the derivative of the dimensionless density, $\partial\rho^*/\partial z^*(x^*, t)$. Since this definition is susceptible to local fluctuation on the profile, the stratified front is found by fitting the experimental and simulation data with a Sigmoid curve (S curve) of 95% confidence interval and then finding the location of the maximum dimensionless density gradient on the fitted curve. The definition of the sigmoid curve is given by:

$$S^*\left(z^*\right) = \frac{a}{\left(1 + e^{-c(z^*-z_0)}\right)} + b \tag{7.11}$$

where z_0, a, b, and c represent the shift, maximum value, minimum value, and decay rate of the sigmoid function. The corresponding gradient can then be written as:

$$\frac{\partial S^*}{\partial z^*} = \frac{ace^{-c(z^*-z_0)}}{\left(1 + e^{-c(z^*-z_0)}\right)^2} \tag{7.12}$$

The positions of the mixing front Z_f^* and of the maximum gradient Z_m^* define the third metric, namely the thickness of the stratified front. The half thickness of the front is defined as the distance between the first metric and the second metric, which gives insight into the magnitude of mixing occurring.

7.5.2.3 Comparison of the quantities of interest

The quantities of interest are averaged over the horizontal coordinate using the same approach as in Eq. 7.10. The time-trace of the average mixing front position $\overline{Z}_f^*(t)$, average stratified front position $\overline{Z}_m^*(t)$, and the magnitude of maximum gradient $\overline{d\rho^*/dz_m^*}(t)$ can be obtained. In Figure 7.13, the time traces of these quantities of interest for the large WMS plane are reported.

Looking at Figure 7.13a, both models predicted the mixing front $\overline{Z}_f^*(t)$ well in the early stages of the transient (i.e., before 200s for both cases). This shows that the simulations have predicted the accurate arrival time of the injected fluid at the measurement locations, thanks to the well-monitored inlet boundaries. As the stratification builds up and develops, it can be seen from Figure 7.13a that the traveling speed of the mixing front tends to be slightly over-predicted by the SKE model, while the RST model predicts an even faster speed. However, Figure 7.13b shows that the stratified front $\overline{Z_m^*}(t)$ has been well-predicted by both models. This finding agrees well with the finding in Ref. [181, 182], in which the interface height was shown to be reasonably well-captured by both the SKE and RST models. Based on these two metrics, the thickness of the mixing region can be inferred to be slightly over-predicted by the SKE model and largely over-predicted by the RST model. This is further validated by examining the maximum gradient values of the stratified front shown in Figure 7.13c. The over-mixing predicted by these two models has led to a smaller maximum gradient value, as compared to the experimental and DNS data.

7.5.2.4 Comparison of the turbulent/molecular Flux

It can be concluded from both cases that the simulations over-predicted the front mixing, regardless of the injection schemes. The RST model showed a stronger over-prediction of the mixing compared to the SKE model. The discrepancy in the model behavior can be examined by looking into the predicted turbulent diffusion coefficient, which depends on the estimation of the turbulent viscosity [182]. Figure 7.14 shows the average turbulent viscosity profile normalized by the molecular viscosity of the tank fluid. The vertical lines represent the front positions, and the length of the arrow indicates the front thickness in each plot. For case 1 (LIH), it can be seen that both models predicted high turbulent viscosity above the inlet jet nozzle ($z/D > 0$), where the jet spreading effect dominated during the transient. On the contrary, the high magnitude of turbulent viscosity predicted by both models was near the bottom of the tank for case 5 (HIL), where the injected jet flow disturbed the tank fluid strongly. At each time snapshot, the turbulent viscosity predicted by the RST model was generally larger than that from the SKE model at the mixing front region, which caused a stronger mixing force, thus, a thicker front for all the cases. It is noticeable that for the

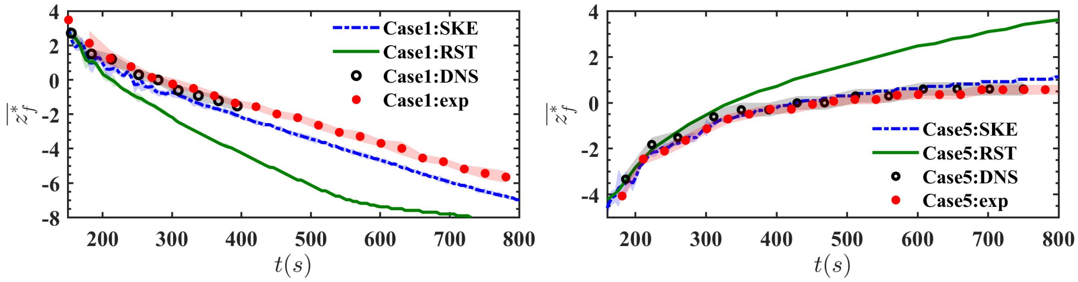

(a) Mixing front $\overline{Z_f^*}(t)$. Left: case 1, right: case 5.

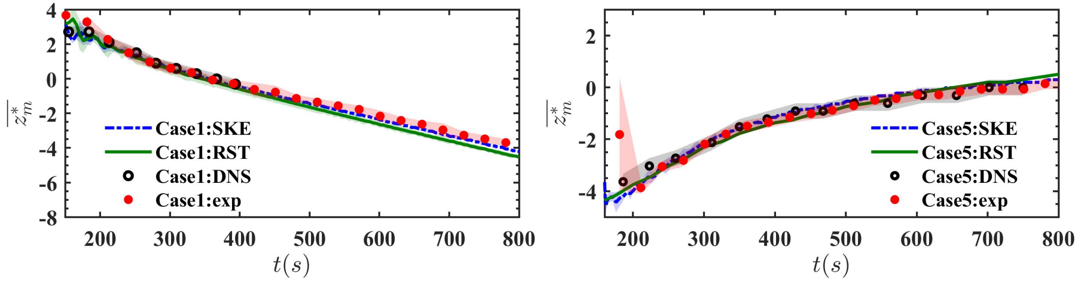

(b) Stratified front $\overline{Z_m^*}(t)$. Left: case 1, right: case 5.

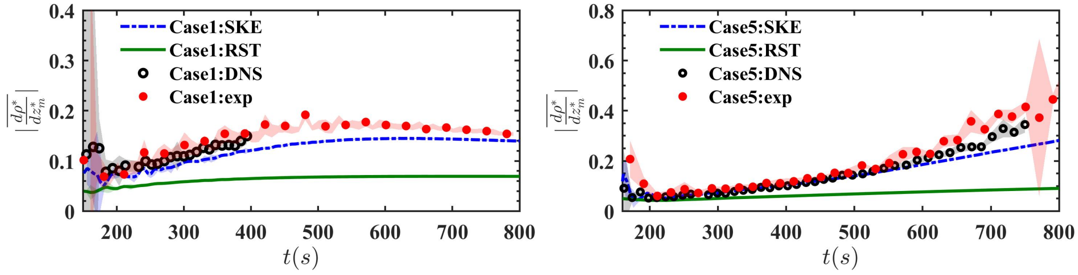

(c) Maximum gradient value $\overline{|\frac{d\rho^*}{Z_m^*}|}(t)$. Left: case 1, right: case 5.

Figure 7.13: Comparison of quantities of interest for stratified fronts between RANS, experiments, and DNS.

SKE model, a steep transition from turbulent flow to laminar flow was predicted, i.e., the turbulent viscosity transits quickly to zero away from the fluid accumulation region. For the anisotropic RST model, instead, the flow returns to a laminar state slowly. Further examination of the turbulent statistics reveals that higher values of k^* were predicted by the RST model compared to the SKE model, especially in the transition from turbulent to the laminar region, which has caused this over-prediction of turbulent viscosity in the RST model. The over-prediction of the turbulent kinetic energy has also been observed in Ref. [173], in which a higher turbulent production was reported than the experimental data for the turbulent round jet flow. For this work, efforts are currently undertaken to extract data from DNS to provide a quantitative comparison of the turbulent kinetic energy and turbulent viscosity with the RANS simulations to help facilitate an understanding of the RANS models' deficiency. Further improvement on the models' performance can focus on examining the appropriateness of the model coefficients to provide correct turbulent viscosity as well.

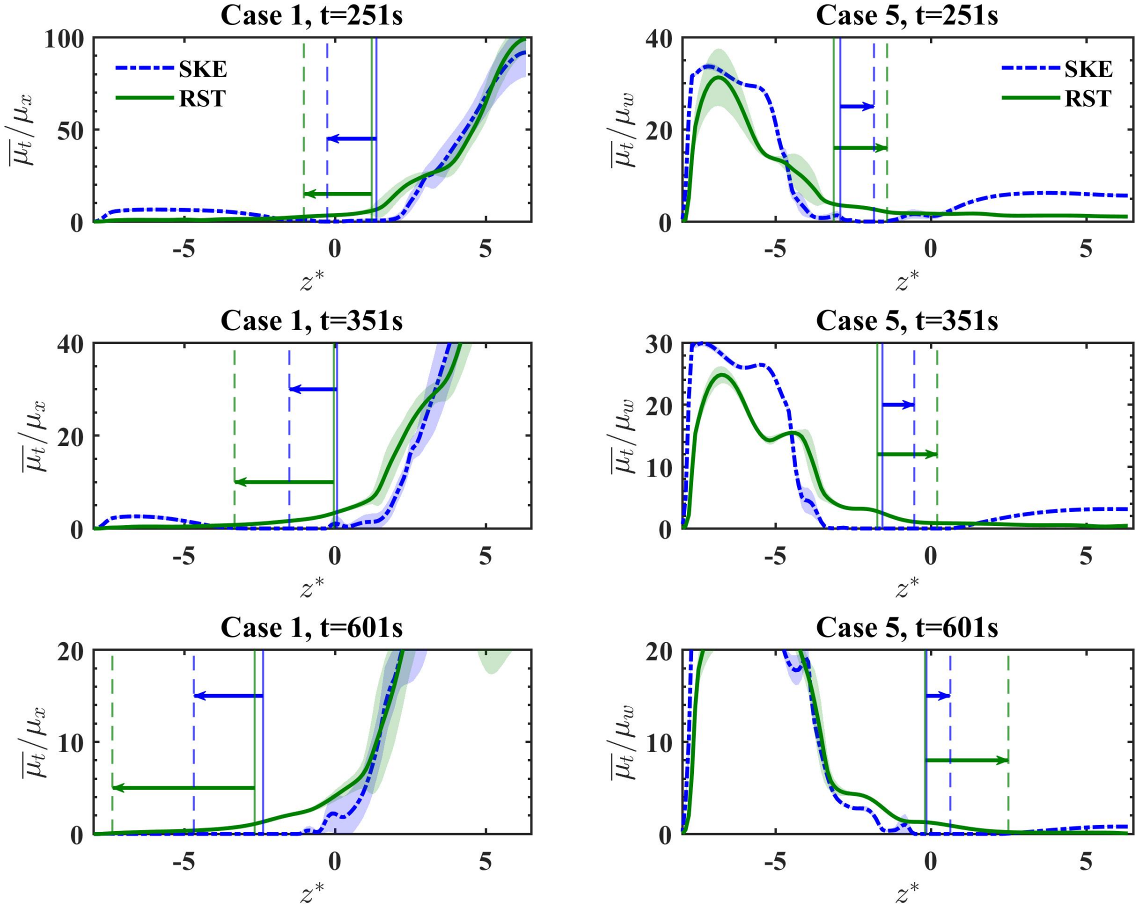

(a) Case 1 (LIH)

(b) Case 5 (HIL)

Figure 7.14: Comparison of turbulent viscosity distribution for simulations.

7.6 Conclusions and Future Work

This chapter aimed to establish if turbulence models were capable of correctly predicting stratification phenomena and to identify the RANS model that gives optimum results. To establish a high-resolution, high-fidelity database for supporting CFD model validation and development, experiments on the HiRJet facility have been conducted with Reynolds numbers near 5,000 and Richardson numbers near 0.29. The boundary conditions and fluid properties were accurately measured, and the process of time-dependent density stratification on a 2D plane was captured with the aid of theWMS. Meanwhile, DNS simulations on the HiRJet facility were also conducted in parallel to the experimental campaign to provide complementary data on stratification.

CFD RANS simulations using the Standard $k-\varepsilon$ model (SKE) and the Reynolds Stress Transport (RST) model have been carried out to predict two selected cases: case 1 with a downward-moving front and case 5 with an upward-moving front. The visualization of the density field propagation first showed that both models have correctly predicted a stratification layer between two fluids. When comparing the dimensionless density profiles, it was found that the RST model predicted a more diffusive front. In contrast, the results from the SKE model were reasonably well matched with the DNS and experiments. The predictive capabilities of these two models were then quantitatively accessed by comparing the front characteristics, i.e., the mixing front and the stratified front, with that of the experiments and the DNS. It is inferred that the thickness of the mixing region was slightly over-predicted by the SKE model and largely over-predicted by the RST model. As such, the same trend was also observed for the maximum density gradient. Further analysis of the turbulent statistics revealed that the turbulent viscosity was over-predicted by the RST model due to the over-prediction of the turbulent kinetic energy, compared to the SKE model.

As a continuing effort to support the further validation and development of CFD models for buoyancy-driven flow with stratified fronts, the measurements of the HiRJet facility are actively undertaken to expand the database to cover a wider range of Re and Ri numbers. DNS simulations on the HiRJet facility are also parallelly conducted to provide high-fidelity data in conjunction with the experimental results. Further validation of the CFD models will include more turbulent models to inform the best practice for simulating stratified flows.

CHAPTER VIII

Conclusions and Future Work

8.1 Conclusions

This thesis aims to address two challenges in thermal hydraulics for HTGRs, encompassing the necessity to develop reliable models for predicting heat transfer and fluid flow, along with the requirement for advanced instrumentation and sensors to monitor the coolant's behavior and identify any anomalies or malfunctions. In Chapter I, we provide the research background and mottivation for this thesis. Before delving into the specific technical work, Chapter II provides a summary of the measurement techniques and computational methods used for the study.

One of the significant and original contributions of the present dissertation was the development of a novel acoustic flow meter, aimed at addressing the need of flow meters suitable for use in harsh environments, given the characteristics of HTGRs. A system based on corrugated pipes has been considered a potential candidate and proposed in Chapter III. The viability of such a system has been investigated through both experiments and simulations. The experimental study conducted within the present dissertation has revealed that the peak frequency of the acoustic wave emitted by the pipe increases with the airflow rate, but not monotonically; Additionally, it has been confirmed that adding a smooth pipe downstream or upstream of the corrugated section causes a shift in the acoustic wave frequency under the same airflow rate conditions, which could be exploited for the simultaneous application of multiple acoustic flow-meters in close proximity. A prototype of the acoustic flow meter has been proposed based on these experimental observations, and the proposed design has recently been awarded a US patent [191]. Furthermore, URANS simulations have been validated against experimental data as well as Large Eddy Simulations (LES). It was shown that URANS simulations are able to successfully capture the physics of whistling, and the velocity-frequency dependence. However, the simulation accuracy needs further improvement, as it tends to underpredict the peak frequency.

The second original and significant contribution of the present dissertation was the establishment of a high-resolution database, aimed at shedding light on mixing and stratification phenomena relevant for HTGRs, and at providing suitable data for the validation of CFD models. This effort was accompanied by CFD simulations to assess the performance of current CFD models.

Chapter IV provides an overview of mixing in large enclosures and discusses the framework of model validation and development. This involves leveraging the results of high-resolution experiments and LES/DNS to inform the development of lower-fidelity models. Two separate-effect experimental facilities with well-defined boundaries were used in this dissertation and are described in Chapter IV.

Firstly, the Michigan Multi-jet Gas-mixture Dome (MiGaDome) facility, scaled down to 1/12th from the upper plenum geometry of the Modular High-Temperature Gas Reactors (HTGRs) design, was designed and built. The facility is aimed at the investigation of multi-jet interactions in a domed enclosure using optical measurements such as Laser Doppler Velocimetry (LDV) and Particle Image Velocimetry (PIV). Secondly, the High-Resolution Jet (HiRJet) facility was employed to investigate the propagation of stratified fronts in a body of fluid using Wire-Mesh Sensor (WMS) units. High-fidelity simulations have also been conducted in parallel with the two experimental facilities to expand the database, partly supported by colleagues.

Chapter V is dedicated to high-resolution experimental datasets focusing on mixing in large enclosures and thermal stratification, utilizing the MiGaDome and HiRJet facilities. In the MiGaDome facility, a comprehensive exploration of various injection schemes was conducted. Findings from single air jet injections revealed that the normalized statistics of the jet exhibit asymptotic behavior as the Reynolds number increases. Analysis of the 2D budgets for the momentum equation indicated a minor contribution of turbulent diffusion near the enclosure's surface, where strong convection occurs due to impingement. For two jets without density variations, time-averaged flow fields obtained through ensemble averaging illustrated the formation of a down-wash fountain flow due to wall jet impingement in even injection cases, while an anticlockwise recirculation formed in the case of uneven injection (TJb). An initial examination of density effects on two-jet interactions showcased increased intricacy in the flow pattern with evolving density effects. Regarding multi-jets, it was observed that the flow field for the three-jet injection case resembles that of the six-jet injection when all inlets have the same Reynolds number.

For HiRJet, the study focused on the propagation of stratified fronts with different injection schemes, resulting in eight test cases. It was observed that the thickness of the stratified front changes considerably depending on whether the high density fluid is injected above or below the low density fluid...[here you should add the conclusions from the HIRJET experimental observations]

Datasets from the two separate effect facilities have been readily available for model validation and development. Experiments from the MiGaDome facility have recently been chosen as the benchmark data for the first annual nuclear thermal hydraulics competition held by the American Society of Thermal and Fluids Engineers (ASTFE), demonstrating the relevance of the measured data.

In Chapter VI, an isothermal single-jet case for the MiGaDome facility has been selected as a validation effort for the RANS models. Both high-resolution experiments and high-fidelityLESsimulation of the MiGaDome have been used to validate the four turbulent models: Standard $k-\varepsilon$ Low-Re model, Realizable $k-\varepsilon$ model, Reynolds stresses transport model, and $k-\omega$(SST) (Low-Re Damping) model. A quantitative comparison first demonstrated the high accuracy of theLESdata. An error quantification showed that the Standard $k-\varepsilon$ Low-Re model had best predicted the velocity, with only 6.6% error on the vertical plane and 5.3% error on the horizontal plane. The largest deviation is seen for the $k-\omega$(SST) (Low-Re Damping) model. For the turbulence kinetic energy, the four turbulence models predicted the profiles with similar magnitude of error. The lowest mean error on the vertical plane is predicted by the Reynolds stresses transport model, with a value of 36%. The lowest mean error on the horizontal plane is 48.4%, predicted by the Standard $k-\varepsilon$ Low-Re model.

In Chapter VII aimed to establish if turbulence models were capable of correctly predicting stratification phenomena and to identify the model that gives optimum results based on the HiRJet facility. Results from high-resolution experiments and high-fidelityDNSsimulation of the HiRJet have been used. CFD RANS simulations using the Standard $k-\varepsilon$ model (SKE) and the Reynolds Stress Transport (RST) model have been carried out to predict two selected cases: case 1 with a downward-moving front and case 5 with an upward-moving front. The visualization of the density field propagation first showed that both models have correctly predicted a stratification layer between two fluids. When comparing the dimensionless density profiles, it was found that the RST model predicted a more diffusive front. In contrast, the results from the SKE model were reasonably well matched with theDNSand experiments. The predictive capabilities of these two models were then quantitatively accessed by comparing the front characteristics, i.e., the mixing front and the stratified front, with that of the experiments and the DNS. It is inferred that the thickness of the mixing region was slightly over-predicted by the SKE model and largely over-predicted by the RST model. As such, the same trend was also observed for the maximum density gradient. Further analysis of the turbulent statistics revealed that the turbulent viscosity was over-predicted by the RST model due to the over-prediction of the turbulent kinetic energy, compared to the SKE model.

8.2 Future work

In this thesis, an innovative practical solution for measuring the HTGR's in-core flow rate has been proposed, leveraging the flow-acoustics interactions in a corrugated pipe. Future endeavors should be dedicated to a systematic experimental campaign aimed at refining the flow meter geometry to optimize its flow-frequency response. Furthermore, exploration into the application of machine learning techniques to predict the flow rate based on the frequency spectrum, rather than solely relying on peak frequency, is a promising avenue for further investigations. A comprehensive proposal detailing these advancements has been submitted to the Department of Energy, marking the next phase of this innovative research.

In addition, a high-resolution experimental database has been established to explore mixing in large enclosures and thermal stratification, featuring well-defined initial and boundary conditions. To further enhance understanding, several future investigations are recommended. Firstly, the primary focus on a vertical plane in measuring the MiGaDome facility prompts a call to explore crossflow between jets through measurements on a horizontal plane, adding depth to the analysis. Secondly, in the MiGaDome facility's frequency study, future work should involve time-resolved measurements to extend the cutoff frequency, facilitating the examination of flow dynamics beyond the current limit, if hardware permits. Lastly, a more systematic study on flow mixing with density effects in the MiGaDome facility, encompassing both velocity and density field measurements, would significantly contribute to comprehending the intricacies of flow dynamics. For the HiRJet facility, future efforts should be dedicated to expanding the database to encompass a broader range of flow rates and density variations. Regarding the validation effort on the RANS models, future work anticipates expanding the scope of investigated cases and extracting a more comprehensive set of information from LES and DNS to gain deeper insights into model deficiencies. This expanded analysis will contribute to the refinement of best practices for effectively utilizing turbulence models.

APPENDIX

APPENDIX A

Examination of Data Repeatability

When dealing with complex high-resolution instrumentation, such as PIV, the quality of the measured data is subjected to several factors, including but not limited to seeding particle intrusiveness, statistics, postprocessing, etc. The experimentalists can reasonably quantify uncertainties raised by some of these factors. However, the setup uncertainties (laser alignment, etc.) are very difficult to quantify and can be much larger than all other uncertainties [192]. Nunez et. al [90] conducted several repeated PIV measurements and showed that laser misalignment could result in the measurement falling off the uncertainty bar. The recommended approach is to check the repeatability and reproducibility when compiling CFD-grade databases. With *repeatability*, we intend the ability to repeat the experiments at the same conditions (flow rates, temperatures, etc.). With *reproducibility*, we intend the ability to reproduce the same experimental data [192]. We will access the data repeatability and reproductivity (R&R) from the MiGaDome and HiRJet facilities in the following. Note that even though a database involves a test matrix, repeating all the measurement conditions will be cumbersome and unnecessary. Here, the R&R will be examined by looking into one of the specific experimental cases and assuming the same level of data quality can be achieved for other cases with the same experimental and post-processing procedures strictly followed.

A.1 Examination on the MiGaDome facility

The selected experimental case involves a single air jet injection into the test section. The experimental conditions are summarized in Table A.1. The experiment was conducted at $Re = 4097$ and with a recording frequency of $f = 15Hz$. To examine the R & R, the measurements were repeated three times:

- Cond#1: Measurement on a symmetry plane (P1).
- Cond#2: Measurement on the left half of the symmetry plane (P2).
- Cond#3: A repeated measurement of Cond#2.

The measurement was first conducted on a symmetry plane (P1). Then, the PIV system was realigned and recalibrated into the left half of the symmetry plane (P2) and repeated twice. The three measurements were then processed using the same procedure to obtain time-averaged statistics. Figures A.1- A.2 show the profiles of the first- and second-order statistics at two locations ($y/D = 2, 4$). Overall, all the quantities show a good overlap between different experimental setups.

Table A.1: Boundary conditions and recording information for the R&R measurements

Condition	#1	#2	#3
Gas	Air	Air	Air
Mass flow rate $\dot{m}$(kg/s)	2.596	2.596	2.596
Reynolds number Re	4097	4097	4097
Recording rate f(Hz)	15	15	15
# of image pairs	3390	3389	6778
Recording plane	P1	P2	P2

A.2 Examination on the HiRJet facility

The selected experimental case involves injecting a light fluid from the horizontal middle pipe into the tank filled with heavy fluid (Case 1). Two repeated runs were conducted and

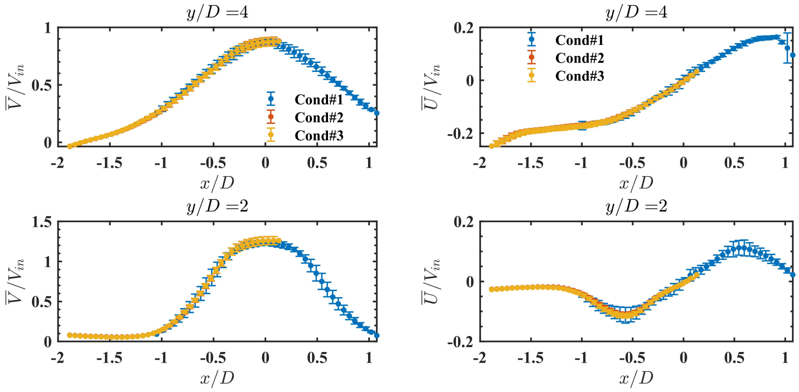

(a) Streamwise velocity (b) Transverse velocity

Figure A.1: R&R of the normalized first-order statistics.

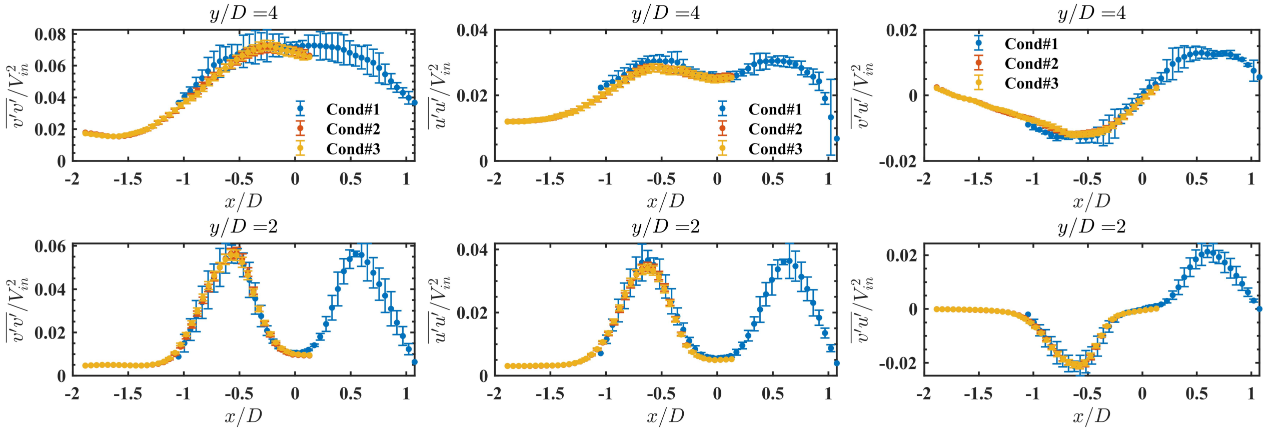

(a) Streamwise Reynolds stress (b) Lateral Reynolds stress (c) Reynolds shear stress

Figure A.2: R&R of the normalized second-order statistics.

compared. Figures A.3 and A.4 show the snapshots of the normalized instantaneous density field and the average profiles. It can be seen from the results that the experiments can be well-repeated.

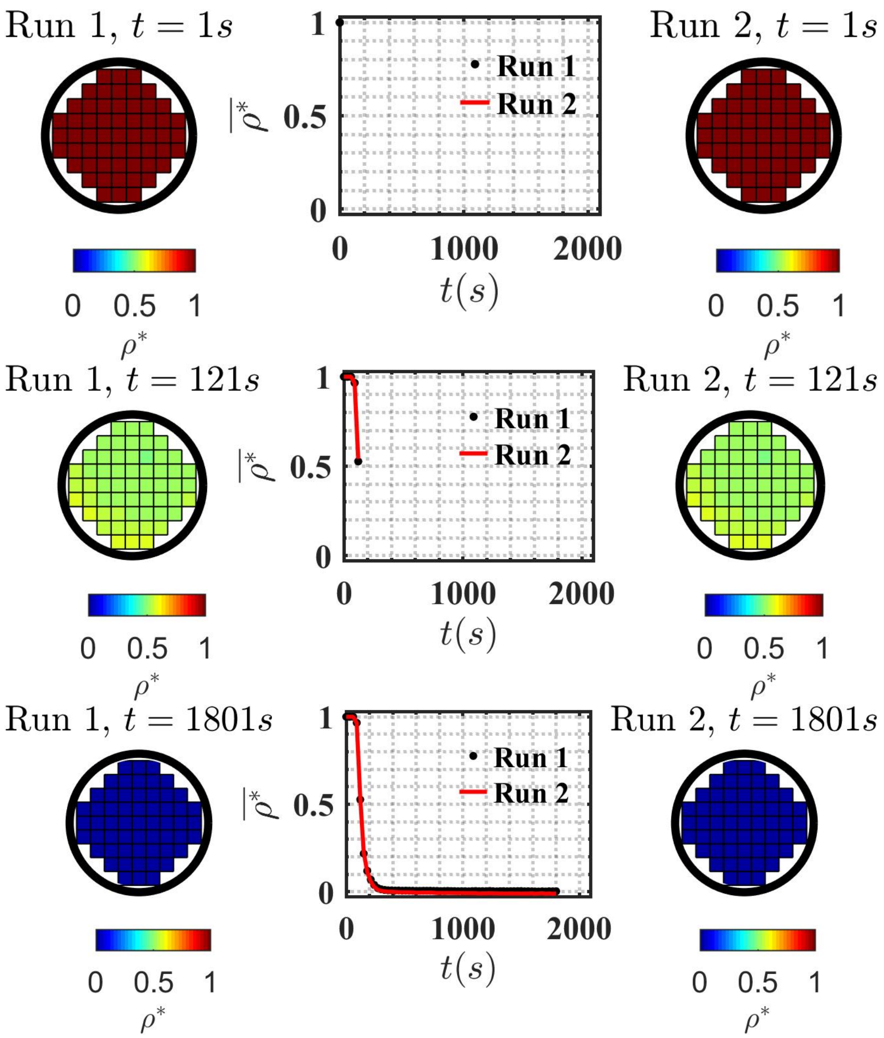

Figure A.3: R&R of the normalized inlet density field and the averaged profiles.

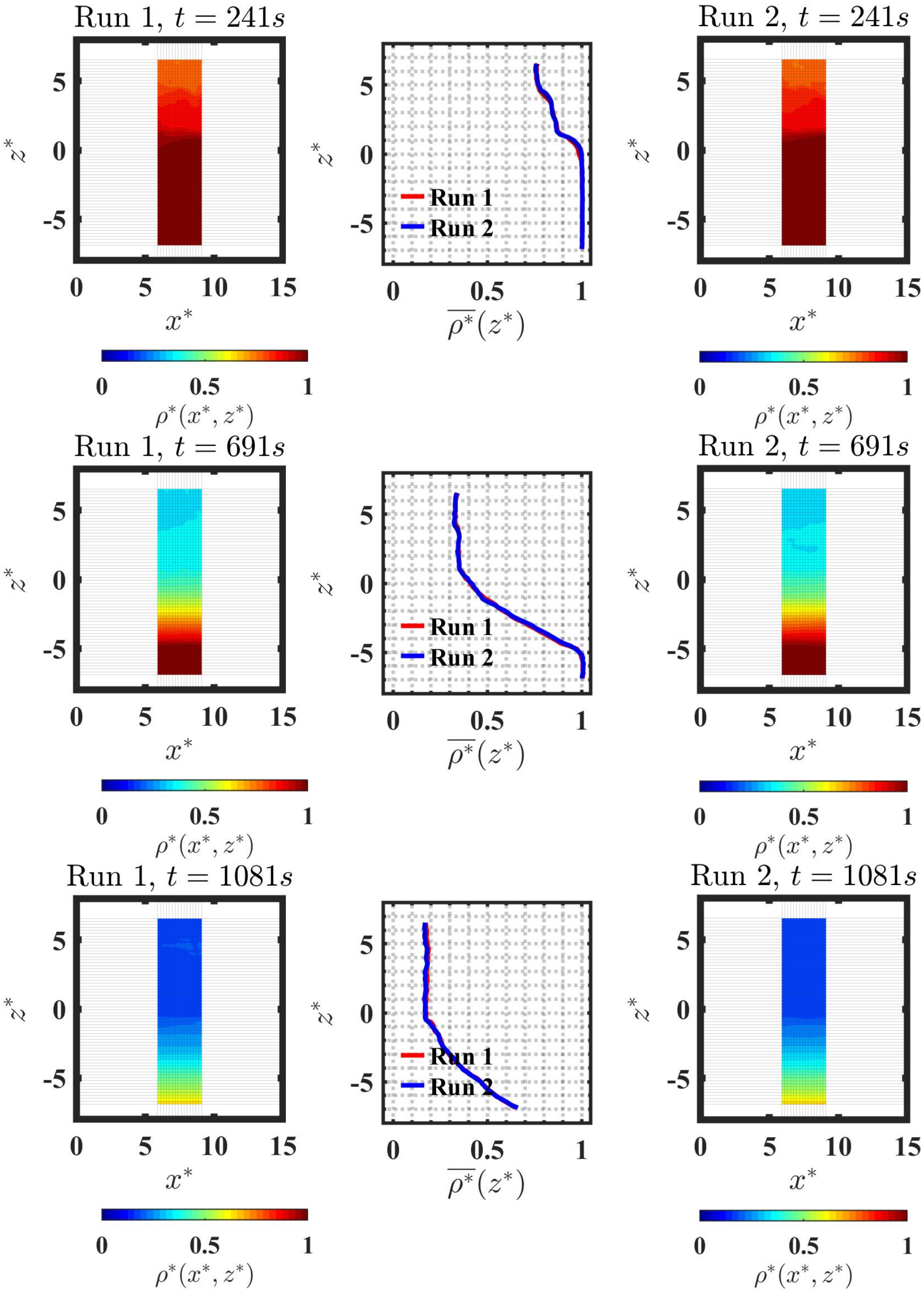

Figure A.4: R&R of the normalized large-sensor density field and the averaged profiles.

BIBLIOGRAPHY

BIBLIOGRAPHY

[1] Generation IV International Forum. Very high temperature reactor (vhtr). viii, 2

[2] Thomas Hicks. Modular htgr safety basis and approach. Technical report, Idaho National Lab.(INL), Idaho Falls, ID (United States), 2011. viii, 6

[3] Richard R Schultz, Hans Gougar, Prasad Vegendla, Aleksandr Obabko, and Justin Thomas. Identification and characterization of thermal fluid phenomena associated with selected operating/accident scenarios in modular high temperature gas-cooled reactors. Technical report, Idaho National Lab.(INL), Idaho Falls, ID (United States), 2017. viii, 7, 60

[4] LaVision®. Laser doppler velocimetry (ldv). `https://www.digitalimagecorrelation.com/en/techniques/ldv-pdi`. Accessed: 2024–03–29. viii, 11

[5] Seika Digital Image Corporation. PIV Principle, Year. viii, 12, 13

[6] H-M Prasser, Arnd Böttger, and Jochen Zschau. A new electrode-mesh tomograph for gas–liquid flows. *Flow measurement and instrumentation*, 9(2):111–119, 1998. viii, 14, 15, 16, 127

[7] IdealSimulations ®. Turbulence models in cfd. `https://www.idealsimulations.com/resources/turbulence-models-in-cfd/`. Accessed: 2024–03–29. viii, 24

[8] E. Merzari, A. Iskhakov, I A. Bolotnov, N T. Dinh, E. Baglietto, A. Manera, D. Shaver, and Y. Hassan. Building a multiscale framework: An overview of the neams thermal-hydraulics integrated research project. *Proceedings of the 20th International Topical Meeting on Nuclear Reactor Thermal Hydraulics (NURETH-20)*, 08 2023. ix, 52, 53

[9] A Manera, A S. Iskhakov, V C. Leite, J. Mao, C. Tai, V. Vishwakarma, R. Wiser, E. Baglietto, I A. Bolotnov, N T. Dinh, Y. Hassan, V. Petrov, and E. Merzari. Neams irp challenge problem 3: Mixing in large enclosures and thermal stratification. *Proceedings of the 20th International Topical Meeting on Nuclear Reactor Thermal Hydraulics (NURETH-20)*, 08 2023. Under Review. ix, 53, 54

[10] Holger Martin. Heat and mass transfer between impinging gas jets and solid surfaces. In *Advances in heat transfer*, volume 13, pages 1–60. Elsevier, 1977. ix, 55

[11] Gréard J Poitras, André Babineau, Gilles Roy, and L-E Brizzi. Aerodynamic and heat transfer analysis of a impinging jet on a concave surface. *International Journal of Thermal Sciences*, 114:184–195, 2017. ix, 56

[12] Jung-Yang San and Jenq-Jye Chen. Effects of jet-to-jet spacing and jet height on heat transfer characteristics of an impinging jet array. *International journal of heat and mass transfer*, 71:8–17, 2014. ix, 57

[13] H Glaser. Untersuchungen an schlitz-und mehrdüsenanordnungen bei der trocknung feuchter oberflächen durch warmluftstrahlen. *Chemie Ingenieur Technik*, 34(3):200–207, 1962. ix, 57

[14] Victor Coppo Leite, Elia Merzari, Jiaxin Mao, Victor Petrov, and Annalisa Manera. High-fidelity simulation of mixing phenomena in large enclosures. *Nuclear Science and Engineering*, pages 1–18, 2023. x, 108, 109, 114

[15] C. Tai, J. Mao, V. Petrov, A. Manera, and I A. Bolotnov. Study of stable stratification in hirjet facility with direct numerical simulation. *Nuclear Science and Engineering*, 2022. Under Review. xii, 61, 105, 128, 129

[16] C. Tai, H. Yuan, E. Merzari, and I A. Bolotnov. High fidelity simulation of the light-to-dense stratification transient in the hirjet facility. *Proceedings of the 20th International Topical Meeting on Nuclear Reactor Thermal Hydraulics (NURETH-20)*, 08 2023. Under Review. xii, 61, 128, 129

[17] International Atomic Energy Agency. Nuclear power in the world today, 2021. 1

[18] Keisuke Sadamori. Nuclear power in a clean energy system. In *Annales des Mines-Responsabilité et environnement*, pages 122–126. Cairn/Softwin, 2020. 1

[19] International Atomic Energy Agency. Nuclear power and climate change: 2018. `https://www.iaea.org/sites/default/files/19/02/nuclear-power-and-climate-change.pdf`, 2019. Accessed on May 5, 2023. 1

[20] Nuclear Energy Institute (NEI). Types of reactors. https://www.nei.org/advantages/types-of-reactors. 1

[21] International Atomic Energy Agency (IAEA). Nuclear power reactors in the world. https://www.iaea.org/pris/. 1

[22] International Atomic Energy Agency (IAEA). Nuclear energy series: Advanced reactors information system. https://aris.iaea.org/, 2021. 1

[23] Andrey N Zrodnikov, Stanislav A Subbotin, Nikolay N Ponomarev-Stepnoy, Soeren Kliem, and Kalle Maekelae. Safety analysis of high-temperature gas-cooled reactor using passive cooling systems. *Nuclear Engineering and Design*, 376:179–189, 2021. 3

[24] Lee Nelson. Integration of high-temperature gas-cooled reactors into industrial process applications. Technical report, Idaho National Lab.(INL), Idaho Falls, ID (United States), 2009. 3

[25] Mark F Ruth, Owen R Zinaman, Mark Antkowiak, Richard D Boardman, Robert S Cherry, and Morgan D Bazilian. Nuclear-renewable hybrid energy systems: Opportunities, interconnections, and needs. *Energy Conversion and Management*, 78:684–694, 2014. 3

[26] William J Nuttall. Nuclear energy for sustainable development: a review of its potential and challenges. *Proceedings of the Institution of Mechanical Engineers, Part A: Journal of Power and Energy*, 224:275–289, 2010. 3

[27] K Jensen, V Ignatiev, O Khoruzhii, A Kunitsa, K Mikityuk, V Murogov, E Osipov, L Ponomarev, and V Sadovskii. The htr-mhr project at okb gidropress. In *Proceedings of the International Conference on the Next Generation of Nuclear Power Technology (NGNP 2008)*, 2008. 3

[28] Fu Li, Kun Chen, Xiaojin Huang, Liang Li, Jianping Li, Bing Liu, Binglin Liu, Yongjun Luo, Wei Shen, Wenxi Tian, , et al. The china institute of atomic energy very high temperature reactor. *Nuclear Engineering and Design*, 285:70–78, 2015. 3

[29] US Department of Energy. Next generation nuclear plant (ngnp) project, 2021. 3

[30] Alexander J Huning, Sriram Chandrasekaran, and Srinivas Garimella. A review of recent advances in htgr cfd and thermal fluid analysis. *Nuclear Engineering and Design*, 373:111013, 2021. 3, 5

[31] Sydney J Ball. Next generation nuclear plant phenomena identification and ranking tables (pirts) volume 1: Main report. Technical report, Oak Ridge National Lab.(ORNL), Oak Ridge, TN (United States), 2008. 3, 4

[32] Sydney J Ball, M Corradini, Stephen Eugene Fisher, R Gauntt, G Geffraye, Jess C Gehin, Y Hassan, David Lewis Moses, John-Paul Renier, R Schultz, et al. Next generation nuclear plant phenomena identification and ranking tables (pirts) volume 2: Accident and thermal fluids analysis pirts. Technical report, Oak Ridge National Lab.(ORNL), Oak Ridge, TN (United States), 2008. 3

[33] Andrew C Kadak. The status of the us high-temperature gas reactors. *Engineering*, 2(1):119–123, 2016. 3, 5

[34] Sunming Qin, Minseop Song, Stefan Hans Vietz, Cam Binh T Pham, Mitchell A Plummer, and Gerhard Strydom. High-temperature gas-cooled reactor research survey and overview: Preliminary data platform construction for the nuclear energy university program. Technical report, Idaho National Lab.(INL), Idaho Falls, ID (United States), 2022. 4, 5, 60

[35] Anas Alwafi, Thien Nguyen, Yassin Hassan, and NK Anand. Time-resolved particle image velocimetry measurements of a single impinging jet in the upper plenum of a scaled facility of high temperature gas-cooled reactors. *International Journal of Heat and Fluid Flow*, 76:113–129, 2019. 6, 59, 76, 93

[36] VC Leite, E Merzari, J Mao, V Petrov, and A Manera. High-fidelity simulation of mixing phenomena in large enclosures. *Proc. Int. Topl. Mtg. Advances in Thermal Hydraulics (ATH 2022)*, pages 12–16, 2022. 9, 32, 61, 68

[37] Cheng-Kai Tai. *Knowledge Gap-driven Simulation Strategy Development based on Direct Numerical Simulation of Mixed Convection Flows.* PhD thesis, North Carolina State University, 2023. 9, 32, 61, 68

[38] A Manera, AS Iskhakov, VC Leite, Jiaxin Mao, C Tai, V Vishwakarma, R Wiser, E Baglietto, IA Bolotnov, NT Dinh, et al. Neams irp challenge problem 3: Mixing in large enclosures and thermal stratification. *Proc. 20th Int. Topl. Mtg. Nuclear Reactor Thermal Hydraulics (NURETH-20)*, 2023. 9

[39] Franz Durst, Adrian Melling, and James H Whitelaw. Principles and practice of laser-doppler anemometry. *NASA STI/Recon Technical Report A*, 76:47019, 1976. 11

[40] Ronald J Adrian. Particle-imaging techniques for experimental fluid mechanics. *Annual review of fluid mechanics*, 23(1):261–304, 1991. 12

[41] Markus Raffel, Christian E Willert, Jürgen Kompenhans, et al. *Particle image velocimetry: a practical guide*, volume 2. Springer, 1998. 12

[42] LaVision. Product manual for davis 8.2. 1.48998: Flowmaster, 2014. 13, 14

[43] Casey Tompkins, Horst-Michael Prasser, and Michael Corradini. Wire-mesh sensors: A review of methods and uncertainty in multiphase flows relative to other measurement techniques. *Nuclear Engineering and Design*, 337:205–220, 2018. 14, 15

[44] HF Velasco Peña and OMH Rodriguez. Applications of wire-mesh sensors in multiphase flows. *Flow measurement and instrumentation*, 45:255–273, 2015. 15, 17

[45] Ragna Kipping, Rosmer Brito, Eckhard Scheicher, and Uwe Hampel. Developments for the application of the wire-mesh sensor in industries. *International Journal of Multiphase Flow*, 85:86–95, 2016. 15

[46] MJ Da Silva, E Schleicher, and U Hampel. Capacitance wire-mesh sensor for fast measurement of phase fraction distributions. *Measurement Science and Technology*, 18(7):2245, 2007. 15

[47] Weerin Wangjiraniran. *Study on multi-dimensional characteristics of two-phase flow using wire mesh tomography.* PhD thesis, Tokyo Institute of Technology, 2004. 15

[48] Horst-Michael Prasser and Richard Häfeli. Signal response of wire-mesh sensors to an idealized bubbly flow. *Nuclear Engineering and Design*, 336:3–14, 2018. 15, 16, 21

[49] Corey E Clifford, Nolan E MacDonald, Horst-Michael Prasser, and Mark L Kimber. Robust computational framework for wire-mesh sensor potential field calculations. *Flow Measurement and Instrumentation*, 67:107–117, 2019. 15

[50] Hengwei Zhang, Yao Xiao, and Hanyang Gu. Numerical investigations of the accuracy of conductivity wire-mesh sensors. *Nuclear Engineering and Design*, 345:148–156, 2019. 16

[51] Jae Won Lee, Hyun Heo, Dong Kee Sohn, and Han Seo Ko. Experimental and numerical study on bubble behaviour using electrostatic model around wire–mesh sensor. *Chemical Engineering Science*, 248:117170, 2022. 16

[52] CY Wang. Exact solutions of the steady-state navier-stokes equations. *Annual Review of Fluid Mechanics*, 23(1):159–177, 1991. 23

[53] AW Vreman and Johannes GM Kuerten. Comparison of direct numerical simulation databases of turbulent channel flow at reτ= 180. *Physics of Fluids*, 26(1), 2014. 24

[54] Stephen B Pope and Stephen B Pope. *Turbulent flows*. Cambridge university press, 2000. 25, 93

[55] Athony Leonard. Energy cascade in large-eddy simulations of turbulent fluid flows. In *Advances in geophysics*, volume 18, pages 237–248. Elsevier, 1975. 25

[56] Hao Lu and Christopher J Rutland. Structural subgrid-scale modeling for large-eddy simulation: A review. *Acta Mechanica Sinica*, 32:567–578, 2016. 25

[57] Yacine Addad, Ulka Gaitonde, Dominique Laurence, and Stefano Rolfo. Optimal unstructured meshing for large eddy simulations. *Quality and reliability of large-eddy simulations*, pages 93–103, 2008. 26

[58] Iztok Tiselj, Cedric Flageul, and Jure Oder. Direct numerical simulation and wall-resolved large eddy simulation in nuclear thermal hydraulics. *Nuclear Technology*, 206(2):164–178, 2020. 26

[59] Jun Fang, Joseph J Cambareri, Mengnan Li, Nadish Saini, and Igor A Bolotnov. Interface-resolved simulations of reactor flows. *Nuclear Technology*, 2019. 26

[60] Elia Merzari, Paul Fischer, Misun Min, Stefan Kerkemeier, Aleksandr Obabko, Dillon Shaver, Haomin Yuan, Yiqi Yu, Javier Martinez, Landon Brockmeyer, et al. Toward exascale: overview of large eddy simulations and direct numerical simulations of nuclear reactor flows with the spectral element method in nek5000. *Nuclear Technology*, 206(9):1308–1324, 2020. 26, 108

[61] EMJ Komen, A Mathur, F Roelofs, E Merzari, and I Tiselj. Status, perspectives, and added value of high fidelity simulations for safety and design. *Nuclear Engineering and Design*, 401:112082, 2023. 26

[62] Osborne Reynolds. Iv. on the dynamical theory of incompressible viscous fluids and the determination of the criterion. *Philosophical transactions of the royal society of london.(a.)*, pages 123–164, 1895. 26

[63] David C Wilcox et al. *Turbulence modeling for CFD*, volume 2. DCW industries La Canada, CA, 1998. 26

[64] User Guide. Starccm+ version 2020.1. *SIEMENS simcenter*, 2020. 28

[65] T-H Shih, William W Liou, Aamir Shabbir, Zhigang Yang, and Jiang Zhu. A new k-epsilon eddy viscosity model for high reynolds number turbulent flows: Model development and validation. Technical report, National Aeronautics and Space Administration, 1994. 30

[66] UDF Manual. Ansys fluent 12.0. *Theory Guide*, page 67, 2009. 30

[67] Sydney J Ball, David Eugene Holcomb, and SM Cetiner. Htgr measurements and instrumentation systems. *ORNL/TM-2012/107, Oak Ridge, TN: Oak Ridge National Laboratory*, 2012. 33

[68] W Burstyn. Eine neue pfeife (a new pipe). *Z. Tech. Phys.(Leipzig)*, 3:179–180, 1922. 33

[69] P Cermak. Über die tonbildung bei metallschläuchen mit eingedrücktem spiralgang (on the sound generation in flexible metal hoses with spiraling grooves). *Phys. Z*, 23:394–397, 1922. 33

[70] Frank S Crawford. Singing corrugated pipes. *American Journal of Physics*, 42(4):278–288, 1974. 34

[71] Maria Eva Amorim, Teresa Delmira Sousa, P Simeão Carvalho, and Adriano Sampaioe Sousa. A simple experiment to explore standing waves in a flexible corrugated sound tube. *The Physics Teacher*, 49(6):360–362, 2011. 34

[72] B Rajavel and MG Prasad. Acoustics of corrugated pipes: a review. *Applied Mechanics Reviews*, 65(5), 2013. 34, 37

[73] Oleksii Rudenko, Güneş Nakiboğlu, Ad Holten, and Avraham Hirschberg. On whistling of pipes with a corrugated segment: Experiment and theory. *Journal of Sound and Vibration*, 332(26):7226–7242, 2013. 34

[74] AC van Eckeveld, J Westerweel, and C Poelma. Mitigation of whistling in vertical corrugated pipes by liquid addition. *Experiments in Fluids*, 58(9):1–14, 2017. 34

[75] AC van Eckeveld, J Westerweel, and C Poelma. Silencing corrugated pipes with liquid addition-identification of the mechanisms behind whistling mitigation. *Journal of Sound and Vibration*, 484:115495, 2020. 34

[76] JW Elliott. Corrugated pipe flow. *Lecture Notes on the Mathematics of acoustics*, pages 207–222, 2005. 37, 41

[77] V Debut, J Antunes, and M Moreira. Experimental study of the flow-excited acoustical lock-in in a corrugated pipe. *ICSV14, Cairns, Australia*, 2007. 38

[78] AC van Eckeveld. *Silencing corrugated pipes: Whistling mitigation by liquid addition to vertical corrugated pipe flow.* PhD thesis, Delft University of Technology, 2019. 38

[79] G Nakiboğlu, SPC Belfroid, J Golliard, and Avraham Hirschberg. On the whistling of corrugated pipes: effect of pipe length and flow profile. *Journal of Fluid Mechanics*, 672:78–108, 2011. 38

[80] Y Nakamura and N Fukamachi. Sound generation in corrugated tubes. *Fluid Dynamics Research*, 7(5-6):255–261, 1991. 38

[81] Hee-Chang Lim and Faran Razi. Experimental study of flow-induced whistling in pipe systems including a corrugated section. *Energies*, 11(8):1954, 2018. 41

[82] Mihaela Popescu and Stein Johansen. Acoustic wave propagation in low mach flow pipe. In *46th AIAA Aerospace Sciences Meeting and Exhibit*, page 63, 2008. 44, 45, 47, 49

[83] B Rajavel and MG Prasad. Parametric studies on acoustics of corrugated tubes using large eddy simulation (les). *Noise Control Engineering Journal*, 62(4):218–231, 2014. 44

[84] Rajeev K Jaiman, Owen H Oakley, and J Dean Adkins. Cfd modeling of corrugated flexible pipe. In *ASME 2010 29th International Conference on Ocean, Offshore and Arctic Engineering*, pages 661–670. American Society of Mechanical Engineers Digital Collection, 2010. 44

[85] Gunes Nakiboglu, Oleksii Rudenko, Avraham Hirschberg, Joachim Golliard, and Nestor Gonzalez Diez. On the higher hydrodynamic modes and the onset of whistling in self-sustained cavity oscillations. In *19th AIAA/CEAS Aeroacoustics Conference*, page 2155, 2013. 44

[86] Joachim Golliard, Néstor González-Díez, Stefan Belfroid, Güneş Nakiboğlu, and Avraham Hirschberg. U-rans model for the prediction of the acoustic sound power generated in a whistling corrugated pipe. In *ASME 2013 Pressure Vessels and Piping Conference*. American Society of Mechanical Engineers Digital Collection, 2013. 44

[87] Alessandro Petruzzi and Francesco D'Auria. Thermal-hydraulic system codes in nulcear reactor safety and qualification procedures. *Science and Technology of Nuclear Installations*, 2008, 2008. 52

[88] Jiaxin Mao, Sunming Qin, Victor Petrov, and Annalisa Manera. Rans simulations of turbulent round jets in the presence of density difference and comparison with high-resolution experimental data. *Nuclear Science and Engineering*, 2021. 52

[89] V Petrov, A Manera, et al. Validation of star-ccm+ for buoyancy driven mixing in a pwr reactor pressure vessel. In *NURETH-14: 14th International Topical Meeting on Nuclear Reactor Thermal Hydraulics, Toronto, Ontario (Canada)*, 2011. 52

[90] Daniel Nunez. *High-Resolution Experiments of Momentum-and Buoyancy-Driven Flows for the Validation and Advancement of Computational Fluid Dynamics Codes.* PhD thesis, University of Michigan, 2020. 52, 65, 87, 131, 157

[91] Srinath V Ekkad and Prashant Singh. A modern review on jet impingement heat transfer methods. *Journal of Heat Transfer*, 143(6), 2021. 54, 56

[92] Liaqat Hussain, Muhammad Mahabat Khan, Manzar Masud, Fawad Ahmed, Zabdur Rehman, Łukasz Amanowicz, and Krzysztof Rajski. Heat transfer augmentation through different jet impingement techniques: A state-of-the-art review. *Energies*, 14(20):6458, 2021. 54

[93] N Zuckerman and N Lior. Jet impingement heat transfer: physics, correlations, and numerical modeling. *Advances in heat transfer*, 39:565–631, 2006. 54, 58

[94] Mrinal Kaushik, Rakesh Kumar, and G Humrutha. Review of computational fluid dynamics studies on jets. *American Journal of Fluid Dynamics*, 5(3A):1–11, 2015. 54

[95] N Kayansayan and S Küçüka. Impingement cooling of a semi-cylindrical concave channel by confined slot-air-jet. *Experimental Thermal and Fluid Science*, 25(6):383–396, 2001. 54

[96] William K George. The self-preservation of turbulent flows and its relation to initial conditions and coherent structures. *Advances in turbulence*, 3973, 1989. 55

[97] N Souris, H Liakos, and M Founti. Impinging jet cooling on concave surfaces. *AIChE journal*, 50(8):1672–1683, 2004. 55

[98] Javad Taghinia, Md Mizanur Rahman, and Timo Siikonen. Cfd study of turbulent jet impingement on curved surface. *Chinese Journal of Chemical Engineering*, 24(5):588–596, 2016. 55

[99] RE Mayle, MF Blair, and FC Kopper. Turbulent boundary layer heat transfer on curved surfaces, 1979. 56

[100] Dennis Cooper, DC Jackson, Brian Edward Launder, and GX Liao. Impinging jet studies for turbulence model assessment—i. flow-field experiments. *International Journal of Heat and Mass Transfer*, 36(10):2675–2684, 1993. 56, 59

[101] C Cornaro, AS Fleischer, and Richard J Goldstein. Flow visualization of a round jet impinging on cylindrical surfaces. *Experimental Thermal and Fluid Science*, 20(2):66–78, 1999. 56

[102] Mansoo Choi, Han Seoung Yoo, Geunyoung Yang, Joon Sik Lee, and Dong Kee Sohn. Measurements of impinging jet flow and heat transfer on a semi-circular concave surface. *International Journal of Heat and Mass Transfer*, 43(10):1811–1822, 2000. 56, 59

[103] Janice A Fitzgerald and Suresh V Garimella. Visualization of the flow field in a confined and submerged impinging jet. Technical report, Univ. of Wisconsin, Milwaukee, WI (US), 1997. 56

[104] Suresh V Garimella and RA Rice. Confined and submerged liquid jet impingement heat transfer, 1995. 56

[105] KR Saripalli. Visualization of multijet impingement flow. *AIAA Journal*, 21(4):483–484, 1983. 57

[106] Jr-Ming Miao, Chen-Yuan Wu, and Ping-Hei Chen. Numerical investigation of confined multiple-jet impingement cooling over a flat plate at different crossflow orientaions. *Numerical Heat Transfer, Part A: Applications*, 55(11):1019–1050, 2009. 58

[107] Yuan Fang, Shengfei Wang, Wang Xiong, Yili Yang, Shengsheng Lin, Fenglei Niu, and Xiaowei Jiang. Experimental study of heat transfer in the complex space of small steel containment with a steam jet. *Annals of Nuclear Energy*, 166:108822, 2022. 58

[108] C De Walsche and F de Cachard. Experimental investigation of condensation and mixing during venting of a steam/non-condensable gas mixture into a pressure suppression pool, 2000. 58

[109] Nolan Anderson, Yassin Hassan, and Richard Schultz. Analysis of the hot gas flow in the outlet plenum of the very high temperature reactor using coupled relap5-3d system code and a cfd code. *Nuclear Engineering and Design*, 238(1):274–279, 2008. 58

[110] Shine-Zen Kuhn, Hwan Kook Kang, and Per F Peterson. Study of mixing and augmentation of natural convection heat transfer by a forced jet in a large enclosure. *J. Heat Transfer*, 124(4):660–666, 2002. 58

[111] O Auban, Robert Zboray, and D Paladino. Investigation of large-scale gas mixing and stratification phenomena related to lwr containment studies in the panda facility. *Nuclear Engineering and Design*, 237(4):409–419, 2007. 58

[112] Glenn E McCreery and Keith G Condie. Experimental modeling of vhtr plenum flows during normal operation and pressurized conduction cooldown. Technical report, Idaho National Lab.(INL), Idaho Falls, ID (United States), 2006. 58

[113] Shiyong Yao, Yong Guo, Nan Jiang, and Junjie Liu. An experimental study of a turbulent jet impinging on a flat surface. *International Journal of Heat and Mass Transfer*, 83:820–832, 2015. 59

[114] Kui-Soon Kim. An experimental study on the flow and heat transfer characteristics of an impinging jet. *KSME Journal*, 7(3):258–271, 1993. 59

[115] Mark J Tummers, Jeroen Jacobse, and Sebastiaan GJ Voorbrood. Turbulent flow in the near field of a round impinging jet. *International Journal of Heat and Mass Transfer*, 54(23-24):4939–4948, 2011. 59

[116] Mouhammad El Hassan, Hassan Hassan Assoum, Vaclav Sobolik, Jérôme Vétel, Kamel Abed-Meraim, André Garon, and Anas Sakout. Experimental investigation of the wall shear stress and the vortex dynamics in a circular impinging jet. *Experiments in fluids*, 52(6):1475–1489, 2012. 59

[117] Amina Meslem, Vaclav Sobolik, Florin Bode, Kodjovi Sodjavi, Yassine Zaouali, Ilinca Nastase, and Cristiana Croitoru. Flow dynamics and mass transfer in impinging circular jet at low reynolds number. comparison of convergent and orifice nozzles. *International Journal of Heat and Mass Transfer*, 67:25–45, 2013. 59

[118] Juliana BR Loureiro and AP Silva Freire. Wall shear stress measurements and parametric analysis of impinging wall jets. *International journal of heat and mass transfer*, 55(23-24):6400–6409, 2012. 59

[119] Tianqi Guo, Matthew J Rau, Pavlos P Vlachos, and Suresh V Garimella. Axisymmetric wall jet development in confined jet impingement. *Physics of Fluids*, 29(2):025102, 2017. 59

[120] ERTAN Baydar and YÜCEL Ozmen. An experimental investigation on flow structures of confined and unconfined impinging air jets. *Heat and mass transfer*, 42(4):338–346, 2006. 59

[121] H Sohn, JY Yang, HS Lee, and BJ Park. Sensing solutions for assessing and monitoring of nuclear power plants (npps). In *Sensor Technologies for Civil Infrastructures*, pages 605–637. Elsevier, 2014. 60

[122] Zeyun Wu, Cihang Lu, Sarah Morgan, Sama Bilbao y Leon, and Matthew Bucknor. A status review on the thermal stratification modeling methods for sodium-cooled fast reactors. *Progress in Nuclear Energy*, 125:103369, 2020. 60, 61, 123, 124

[123] YI Chang, PJ Finck, C Grandy, J Cahalan, L Deitrich, F Dunn, D Fallin, M Farmer, T Fanning, T Kim, et al. Advanced burner test reactor preconceptual design report. Technical report, Argonne National Lab.(ANL), Argonne, IL (United States), 2008. 60

[124] Y Ieda, I Maekawa, T Muramatsu, and S Nakanishi. Experimental and analytical studies of the thermal stratification phenomenon in the outlet plenum of fast breeder reactors. *Nuclear engineering and design*, 120(2-3):403–414, 1990. 60

[125] Timothy L Norman and Shripad T Revankar. Jet-plume condensation of steam–air mixtures in subcooled water, part 1: Experiments. *Nuclear Engineering and Design*, 240(3):524–532, 2010. 60

[126] Michel Y Haller, Cynthia A Cruickshank, Wolfgang Streicher, Stephen J Harrison, Elsa Andersen, and Simon Furbo. Methods to determine stratification efficiency of thermal energy storage processes–review and theoretical comparison. *Solar Energy*, 83(10):1847–1860, 2009. 61

[127] Haihua Zhao and Per F Peterson. An overview of modeling methods for thermal mixing and stratification in large enclosures for reactor safety analysis, 2010. 61, 123

[128] Jiaxin Mao, Shuai Che, Victor Petrov, and Annalisa Manera. Benchmark experiments for turbulent mixing in the scaled-down upper plenum of high-temperature gas-cooled reactors under accident scenario. *Nuclear Science and Engineering*, 2023. 61

[129] J Mao, V Petrov, and A Manera. High-resolution experiments on flow mixing in the scaled-down upper plenum of high-temperature gas-cooled reactors under accident scenario. *Proc. Int. Topl. Mtg. Advances in Thermal Hydraulics (ATH 2022)*, pages 12–16, 2022. 61

[130] Victor Coppo Leite, Elia Merzari, Jiaxin Mao, Victor Petrov, and Annalisa Manera. High-fidelity simulation of mixing phenomena in large enclosures. *Nuclear Science and Engineering*, 2023. 61

[131] Jiaxin Mao, Zachary Welker, Daniel Nunez, , and Annalisa Petrov, Victor Manera. Validation of rans-based turbulence models against high-resolution experimental data for buoyancy-driven flow with stratified fronts. *Proceedings of the 19th International Topical Meeting on Nuclear Reactor Thermal Hydraulics (NURETH-19)*, 2022. 61

[132] S Che, J Mao, X Sun, A Manera, and V Petrov. Design of high-resolution experiments for extended lofc accidents in htgrs. *Proceedings of the 19th International Topical Meeting on Nuclear Reactor Thermal Hydraulics (NURETH-19)*, 2022. 63

[133] E Deri, B Cariteau, and D Abdo. Air fountains in the erosion of gaseous stratifications. *International journal of heat and fluid flow*, 31(5):935–941, 2010. 64

[134] J Mi, DS Nobes, and GJ Nathan. Influence of jet exit conditions on the passive scalar field of an axisymmetric free jet. *Journal of Fluid Mechanics*, 432:91–125, 2001. 64

[135] AD Birch, DR Brown, MG Dodson, and JR Thomas. The turbulent concentration field of a methane jet. *Journal of Fluid Mechanics*, 88(3):431–449, 1978. 64

[136] Victor Petrov, Daniel Nunez, John Downing, Akshay Dave, and Annalisa Manera. High resolution experiments of velocity and concentration fluctuations in a jet flow. *Nuclear Engineering and Design*, 312:361–374, 2017. 65

[137] Zilong Wang, Hua Zhang, Binlin Dou, Huajie Huang, Weidong Wu, and Zhiyun Wang. Experimental and numerical research of thermal stratification with a novel inlet in a dynamic hot water storage tank. *Renewable Energy*, 111:353–371, 2017. 66

[138] YC Li, F Li, X Cheng, and YH Yang. Experimental investigation on the temperature distribution in the cavity pool of ex-vessel cooling system. *Annals of Nuclear Energy*, 53:90–98, 2013. 66

[139] Jose Fernandez-Seara, Francisco J Uhı, Jaime Sieres, et al. Experimental analysis of a domestic electric hot water storage tank. part ii: dynamic mode of operation. *Applied thermal engineering*, 27(1):137–144, 2007. 66

[140] Anthony T Patera. A spectral element method for fluid dynamics: laminar flow in a channel expansion. *Journal of computational Physics*, 54(3):468–488, 1984. 68

[141] J Mao, V Petrov, and A Manera. High-resolution experiments on flow mixing in the scaled-down upper plenum of high-temperature gas-cooled reactors under accident scenario. *Proceedings of the International Topical Meeting on Advances in Thermal Hydraulics 2022 (ATH'22)*, 2022. 72, 111

[142] Sunming Qin. *High-Resolution Experiments and Computations on Mixing of Turbulent Buoyant Round Free Jets in Uniform and Stratified Environments.* PhD thesis, University of Michigan, 2020. 72, 87

[143] MO Iqbal and FO Thomas. Coherent structure in a turbulent jet via a vector implementation of the proper orthogonal decomposition. *Journal of Fluid Mechanics*, 571:281–326, 2007. 76

[144] Hachimi Fellouah and Andrew Pollard. The velocity spectra and turbulence length scale distributions in the near to intermediate regions of a round free turbulent jet. *Physics of Fluids*, 21(11):115101, 2009. 76

[145] Gu Xu and Robert Antonia. Effect of different initial conditions on a turbulent round free jet. *Experiments in fluids*, 33(5):677–683, 2002. 76

[146] J. Mao, S. Che, V. Petrov, and A. Manera. Benchmark experiments for turbulent mixing in the scaled-down upper plenum of high-temperature gas-cooled reactors under accident scenario. *Nuclear Science and Engineering*, 2023. 82, 88, 90

[147] Duo Xu and Jun Chen. Experimental study of stratified jet by simultaneous measurements of velocity and density fields. *Experiments in fluids*, 53(1):145–162, 2012. 82, 126

[148] Daniel Flórez-Orrego, Walter Arias, Diego López, and Héctor Velásquez. Experimental and cfd study of a single phase cone-shaped helical coiled heat exchanger: an empirical correlation. In *Proceedings of the 25th international conference on efficiency, cost, optimization, simulation and environmental impact of energy systems*, pages 375–394, 2012. 82

[149] Stephen B Pope. Turbulent flows. *Measurement Science and Technology*, 12(11):2020–2021, 2001. 86, 90

[150] Kunihiko Taira, Steven L Brunton, Scott TM Dawson, Clarence W Rowley, Tim Colonius, Beverley J McKeon, Oliver T Schmidt, Stanislav Gordeyev, Vassilios Theofilis, and Lawrence S Ukeiley. Modal analysis of fluid flows: An overview. *Aiaa Journal*, 55(12):4013–4041, 2017. 87

[151] Peter Welch. The use of fast fourier transform for the estimation of power spectra: a method based on time averaging over short, modified periodograms. *IEEE Transactions on audio and electroacoustics*, 15(2):70–73, 1967. 87

[152] Claude E Shannon. Communication in the presence of noise. *Proceedings of the IEEE*, 72(9):1192–1201, 1984. 87

[153] J. Mao, V. Petrov, and A. Manera. High-resolution experiments on flow mixing in the scaled-down upper plenum of high-temperature gas-cooled reactors under accident scenario. *Proceedings of the International Topical Meeting on Advances in Thermal Hydraulics 2022 (ATH2022)*, 06 2022. 87, 88

[154] Benedikt Krohn, Sunming Qin, John Downing, Victor Petrov, and Annalisa Manera. An experimental study of local self-similarity in the mixing transition of a turbulent free jet. *Nuclear Science and Engineering*, 193(1-2):171–184, 2019. 87

[155] Saya Lee and Yassin A Hassan. Experimental study of flow structures near the merging point of two parallel plane jets using piv and pod. *International Journal of Heat and Mass Transfer*, 116:871–888, 2018. 90

[156] Adelya Khayrullina, Twan van Hooff, Bert Blocken, and GJF van Heijst. Piv measurements of isothermal plane turbulent impinging jets at moderate reynolds numbers. *Experiments in Fluids*, 58(4):1–16, 2017. 90

[157] CG Ball, H Fellouah, and A Pollard. The flow field in turbulent round free jets. *Progress in Aerospace Sciences*, 50:1–26, 2012. 92

[158] Guichao Wang, Fan Yang, Ke Wu, Yongfeng Ma, Cheng Peng, Tianshu Liu, and Lian-Ping Wang. Estimation of the dissipation rate of turbulent kinetic energy: A review. *Chemical Engineering Science*, 229:116133, 2021. 93

[159] George Keith Batchelor. *The theory of homogeneous turbulence.* Cambridge university press, 1953. 93

[160] Hendrik Tennekes, John Leask Lumley, Jonh L Lumley, et al. *A first course in turbulence.* MIT press, 1972. 93

[161] Siemens. Star-ccm+ 15.06. 007 user guide, 2020. 93, 124, 131, 135, 139

[162] Stephen K Robinson. Coherent motions in the turbulent boundary layer. *Annual review of fluid mechanics*, 23(1):601–639, 1991. 93

[163] J Mao, V Petrov, A Manera, and W Strasser. Geometry and boundary specifications of the migadome facility for the first annual astfe nuclear thermal hydraulics cfd competition, 2023. 99

[164] Nadine Aubry, Philip Holmes, John L Lumley, and Emily Stone. The dynamics of coherent structures in the wall region of a turbulent boundary layer. *Journal of fluid Mechanics*, 192:115–173, 1988. 102

[165] Julien Weiss. A tutorial on the proper orthogonal decomposition. In *AIAA aviation 2019 forum*, page 3333, 2019. 102

[166] H Ohira, Y Xu, U Bieder, K Velusamy, H Mochizuki, S Choi, Y Shvetsov, T Sofu, J Thomas, S Monti, et al. Benchmark analyses of sodium natural convection in the upper plenum of the monju reactor vessel. In *Int. Conf. Fast Reactors and Related Fuel Cycles: Safe Technologies and Sustainable Scenarios–FR*, volume 13, pages 4–7, 2013. 105, 125, 131

[167] V. Vishwakarma, J. Mao, V. Petrov, and A. Manera. Experimental analysis of the propagation of stratified fronts using wire-mesh sensor. *Nuclear Engineering and Design*, 2024. Under preparation. 105

[168] Ling Zou, Daniel Nunez, and Rui Hu. Development and validation of sam multi-dimensional flow model for thermal mixing and stratification modeling. Technical report, Argonne National Lab.(ANL), Argonne, IL (United States), 2020. 123

[169] Daniel P Combest, Palghat A Ramachandran, and Milorad P Dudukovic. On the gradient diffusion hypothesis and passive scalar transport in turbulent flows. *Industrial & engineering chemistry research*, 50:8817–8823, 2011. 124

[170] Rodney O Fox. *Computational models for turbulent reacting flows.* Cambridge university press, 2003. 124

[171] [Z. Warhaft. Passive scalars in turbulent flow. *Annual Review of Fluid Mechanics.*, 32:203 – 240, 1999. 124

[172] Bassam A Younis, Charles G Speziale, and Timothy T Clark. A rational model for the turbulent scalar fluxes. *Proceedings of the Royal Society A: Mathematical, Physical and Engineering Sciences*, 461(2054):575–594, 2005. 124

[173] Jiaxin Mao, Sunming Qin, Victor Petrov, and Annalisa Manera. Rans simulations of turbulent round jets in the presence of density difference and comparison with high-resolution experimental data. *arXiv preprint arXiv:2301.06001*, 2023. 124, 135, 148

[174] Lane B Carasik, Frédéric Sebilleau, Simon P Walker, and Yassin A Hassan. Numerical simulations of a mixed momentum-driven and buoyancy-driven jet in a large enclosure for nuclear reactor severe accident analysis. *Nuclear Engineering and Design*, 312:161–171, 2017. 124, 125

[175] Rajesh Kumar and Anupam Dewan. Urans computations with buoyancy corrected turbulence models for turbulent thermal plume. *International Journal of Heat and Mass Transfer*, 72:680–689, 2014. 124, 130

[176] R Vidil, D Grand, and F Leroux. Interaction of recirculation and stable stratification in a rectangular cavity filled with sodium. *Nuclear Engineering and Design*, 105(3):321–332, 1988. 124

[177] Brendan Ward, Broderick Sieh, and Hitesh Bindra. Experimental measurement of liquid metal flow fields in a scaled sfr upper plenum. In *18th International Topical Meeting on Nuclear Reactor Thermal Hydraulics (NURETH-18)*, 2019. 124

[178] James A Schneider and Mark H Anderson. Thermal stratification in a pool-type geometry. Technical report, university of Wisconsin Madison, 2019. 124

[179] Makoto Shibahara, Takashi Takata, and Akira Yamaguchi. Numerical study on thermal stratification phenomena in upper plenum of lmfbr "monju". *Nuclear Engineering and Design*, 258:226–234, 2013. 124

[180] Marco Jose Da Silva, Sebastian Thiele, Thomas Höhne, Roman Vaibar, and Uwe Hampel. Experimental studies and cfd calculations for buoyancy driven mixing phenomena. *Nuclear engineering and design*, 240(9):2185–2193, 2010. 125

[181] Toshiharu Muramatsu and Hisashi Ninokata. Investigation of turbulence modelling in thermal stratification analysis. *Nuclear engineering and design*, 150(1):81–93, 1994. 125, 130, 131, 147

[182] Shuji Ohno, Hiroshi Ohki, Akihiro Sugahara, and Hiroyuki Ohshima. Validation of a computational simulation method for evaluating thermal stratification in the reactor vessel upper plenum of fast reactors. *Journal of nuclear science and technology*, 48(2):205–214, 2011. 125, 126, 130, 131, 135, 147

[183] Yoshio Shimakawa, Shigeo Kasai, Mamoru Konomura, and Mikio Toda. An innovative concept of the sodium-cooled reactor to pursue high economic competitiveness. *Nuclear Technology*, 140(1):1–17, 2002. 126

[184] Hideki Kamide. Study on thermal stratification in a compact reactor vessel of advanced sodium cooled reactor. In *Proc. Fifth Korea-Japan Symp. on Nuclear Thermal Hydraulics and Safety, Jeju, Korea, Nov. 26-29, 2006*, 2006. 126

[185] Glenn F Knoll. *Radiation detection and measurement*. John Wiley & Sons, 2010. 127

[186] Paul Fischer, Stefan Kerkemeier, Misun Min, Yu-Hsiang Lan, Malachi Phillips, Thilina Rathnayake, Elia Merzari, Ananias Tomboulides, Ali Karakus, Noel Chalmers, and Tim Warburton. Nekrs, a gpu-accelerated spectral element navier–stokes solver. *Parallel Computing*, 114:102982, 2022. 128

[187] Sudharshan S Vazhkudai, Bronis R De Supinski, Arthur S Bland, Al Geist, James Sexton, Jim Kahle, Christopher J Zimmer, Scott Atchley, Sarp Oral, Don E Maxwell, et al. The design, deployment, and evaluation of the coral pre-exascale systems. In *SC18: International Conference for High Performance Computing, Networking, Storage and Analysis*, pages 661–672. IEEE, 2018. 129

[188] T Sofu. Parametric analysis of thermal stratification during the monju turbine trip test. Technical report, American Nuclear Society, 555 North Kensington Avenue, La Grange Park, IL . . . , 2012. 130

[189] Yoshihide Tominaga and Ted Stathopoulos. Turbulent schmidt numbers for cfd analysis with various types of flowfield. *Atmospheric Environment*, 41(37):8091–8099, 2007. 131

[190] Ishmail B Celik, Urmila Ghia, Patrick J Roache, and Christopher J Freitas. Procedure for estimation and reporting of uncertainty due to discretization in cfd applications. *Journal of fluids Engineering-Transactions of the ASME*, 130(7), 2008. 132

[191] Mustafa S. Cetiner, Trevor K. Howard, Annalisa Manera, Victor Petrov, and Jiaxin Mao. Method and system to measure gas flow. 11 2023. 152

[192] A Manera and V Petrov. Best practices for cfd grade experiments and recent developments in high-resolution measurement techniques. In *18th International Topical Meeting on Nuclear Reactor Thermal Hydraulics, NURETH-18, Portland, OR, USA*, 2019. 157